LEABHARLANN CHOLÁISTE NA TRÍONÓIDE, BAILE ÁTHA CLIATH | TRINITY COLLEGE LIBRARY DUBLIN
Ollscoil Átha Cliath | The University of Dublin

Terms and Conditions of Use of Digitised Theses from Trinity College Library Dublin

Copyright statement

All material supplied by Trinity College Library is protected by copyright (under the Copyright and Related Rights Act, 2000 as amended) and other relevant Intellectual Property Rights. By accessing and using a Digitised Thesis from Trinity College Library you acknowledge that all Intellectual Property Rights in any Works supplied are the sole and exclusive property of the copyright and/or other IPR holder. Specific copyright holders may not be explicitly identified. Use of materials from other sources within a thesis should not be construed as a claim over them.

A non-exclusive, non-transferable licence is hereby granted to those using or reproducing, in whole or in part, the material for valid purposes, providing the copyright owners are acknowledged using the normal conventions. Where specific permission to use material is required, this is identified and such permission must be sought from the copyright holder or agency cited.

Liability statement

By using a Digitised Thesis, I accept that Trinity College Dublin bears no legal responsibility for the accuracy, legality or comprehensiveness of materials contained within the thesis, and that Trinity College Dublin accepts no liability for indirect, consequential, or incidental, damages or losses arising from use of the thesis for whatever reason. Information located in a thesis may be subject to specific use constraints, details of which may not be explicitly described. It is the responsibility of potential and actual users to be aware of such constraints and to abide by them. By making use of material from a digitised thesis, you accept these copyright and disclaimer provisions. Where it is brought to the attention of Trinity College Library that there may be a breach of copyright or other restraint, it is the policy to withdraw or take down access to a thesis while the issue is being resolved.

Access Agreement

By using a Digitised Thesis from Trinity College Library you are bound by the following Terms & Conditions. Please read them carefully.

I have read and I understand the following statement: All material supplied via a Digitised Thesis from Trinity College Library is protected by copyright and other intellectual property rights, and duplication or sale of all or part of any of a thesis is not permitted, except that material may be duplicated by you for your research use or for educational purposes in electronic or print form providing the copyright owners are acknowledged using the normal conventions. You must obtain permission for any other use. Electronic or print copies may not be offered, whether for sale or otherwise to anyone. This copy has been supplied on the understanding that it is copyright material and that no quotation from the thesis may be published without proper acknowledgement.

Pulse Injection Metalorganic Chemical Vapour Deposition of selected magnetic metal oxides

A thesis to the University of Dublin in application for the degree of Doctor of Philosophy

Anna Zukova

School of Chemistry
University of Dublin
Trinity College
October 2008

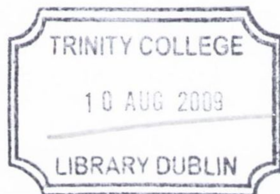

THESIS
8758

Declaration

This thesis is submitted by the undersigned to the University of Dublin, Trinity College for the examination of Doctorate of Philosophy. Except as otherwise indicated, the author carried out the work described herein alone and has not submitted as an exercise for a degree in any other university.

I agree that the library may lend or copy this thesis freely on request.

Abbreviations

AC	Alternating current
AFM	Atomic Force Microscopy
BMP	Bound Magnetic Polaron
CVD	Chemical Vapour Deposition
CCVD	Catalytic Chemical Vapour Deposition
DC	Direct current
DMS	Diluted Magnetic Semiconductor
ESAVD	Electrostatic Spray Assisted Vapour Deposition
EDAX	Energy Dispersive Analysis of X-ray's
FM	Ferromagnetic
FMS	Ferromagnetic Semiconductor
FWHM	Full width at half maximum
GMR	Giant magnetoresistance
H_C	Coercive Field
ITO	Indium Tin oxide
LPCVD	Low Pressure Chemical Vapour Deposition
MTJ	Magnetic tunnel junction
MR	Magnetoresistance
MOCVD	Metalorganic Chemical Vapour Deposition
MBE	Molecular Beam Epitaxy
$M(tmhd)_n$	Metal Tetramethylheptanodionate
$M(acac)_n$	Metal acethyl acetonate
MFM	Magnetic Force Microscopy
M_S	Saturation magnetisation
M_R	Remanence
NM	Nonmagnetic
PI MOCVD	Pulse Injection Metalorganic Chemical Vapour Deposition
PLD	Pulsed Laser Deposition
RKKY	Ruderman-Kittel-Kasuya-Yoshida
RT	Room temperature
RMS	Roughness mean square
Ra	Roughness average

RIXS	Resonant Inelastic X-ray Scattering
SEM	Scanning Electron Microscopy
SIMS	Secondary Ion Mass Spectroscopy
SQUID	Superconducting Quantum Interference Device
Tdep	Deposition temperature
TMR	Tunnelling magnetoresistance
T_C	Curie temperature
TEM	Transmission Electron Microscopy
TGA	Thermogravimetric Analysis
TM	Transition metal
TPA	Thermal Pressure Analysis
UV	Ultraviolet
VSM	Vibrating Sample Magnetrometry
XAS	X-ray absorption spectroscopy
XPS	X-ray Photoemission Spectroscopy
XRD	X-ray diffraction
XRR	X-ray Reflectivity

Acknowledgements

First of all I would like to thank my supervisor, Prof. Yurii Goun'ko for providing me with such an interesting work and also for his guidance and support over the past four years. Also thank you Dr. Sebastiaan van Dijken for helpful conversations on the subject of IO and ZnO. It was also from his contract that I was financed for my research.

Very big thank you to all Yurii's group: Gemma, Michelle, Mick, Maciek, Ian, Joe & Joe, Amro, Renata, Steven, Serina, Aine and Arunas. Thank you guys for being so nice and friendly, without you these four years would be empty. Special thank you to Joe for Raman measurements and also Ian for the conductivity measurements. Also I wanted to thank to my best friend Renata who supported me through those four years and helped me with those last minute EDX measurements! Thank you to Dr. Arunas Teiserskis for being so helpful and patient sharing office with me. His practical and experimental knowledge of PI MOCVD reactor was very helpful. It is also because of Arunas I came to Ireland and met my supervisor.

I would also like to thank everybody in School of Chemistry who helped in realisation of this work: Neal for helping me with SEM and EDAX measurements, Satheesh for XAS measurements. I also want to thank Patsy and Martin for helpful advises, its been pleasure working with you guys.

Special thanks to all in School of Physics and particularly Prof. Mike Coey for use of many of their facilities and equipment such as XRD, AFM, MFM, SQUID and many other. It is hard to express how thankful I am to all guys in Prof. Mike Coey group for practical advises and all the help: Venki for SQUID measurments, Lucio, Karsten and Jonathan for imparting much of their XRD knowledge, Zhu for his help with AFM and MFM measurements. Thank you all: Marita, Plamen, Robbie, Peter and Cathy.

Also thank you to my friend Karina for moral support during the hardest times of my PhD. Being now in a final stage of her own PhD she knows what it means to be a PhD sudent!

I want also to thank to my family for support and help. It's hard to imagine I would be able to come to Ireland without your help. And I can finally answer your question – yes, it all over now☺.

Finally I would like to thank my boyfriend Liam for his tremendous patience and encouragement during my PhD and particularly during thesis writing. I know it's been a very difficult time for both of us and everything like, finishing my PhD, moving into new house and looking for a new job all came up at the same time.

I could not forget to thank to Liam's family: Catherine, John, Margaret and Marian. They have been so patient when during my visits in their house all they could see of me is the back screen of my laptop. I also found your house very inspiring and a lot of my chapters were completed there in Morenane.

Summary

The main aim of this project is to prepare oxide based DMS and ferrimagnetic oxide layers for potential application in new generation spintronic devices. This work involves the preparation of Co-doped ZnO, Cr-doped In_2O_3 and also ferrimagnetic Fe_3O_4 and $CoFe_2O_4$ thin films using PI MOCVD and investigation of their morphology, structure and magnetic properties. The new approach of growing thin films in external magnetic field is also developped in this work. It is anticipated that the external magnetic field can be used to tune the magnetic properties of the films during their growth and apply it for the preparation of spintronic devices.

Chapter 1 gives an introduction into spintornic devices and also reviews the properties and potentials of known diluted magnetic semiconductor materials. All up to date theories explaining magnetism in diluted magnetic semiconductors are also discussed in Chapter 1. Also discussed are different thin film preparation techniques.

All experimental procedures and techniques, which are used to characterise the prepared thin films are given in Chapter 2. Some of them include X-ray diffraction (XRD), magnetisation measurements, Raman measurements, Scanning Electron Microscopy (SEM) and Atomic Force Microscopy (AFM).

In Chapter 3 the preparation of Co-doped ZnO films is discussed. In order to determine the best experimental conditions for the preparation of Co-doped ZnO films, undoped ZnO films were prepared under various deposition conditions. Carefully examining prepared ZnO films by the means of XRD and SEM we were able to estimate the best deposition conditions. The next step involved doping ZnO films with Co. Careful examinations using XRD, elemental analysis, X-ray photoemission spectroscopy (XPS) and Secondary Ion Mass Spectroscopy (SIMS) analysis were performed on the thin films that exhibited room temperature ferromagnetism to exclude the possibility of secondary phases, which could contribute to the observed ferromagnetism. Second part of this chapter includes deposition of Co-doped ZnO films in external magnetic field. The structural, crystalline and magnetic properties of as deposited films are then carefully examined and compared when films are grown in and without external magnetic field.

The preparation of another oxide based DMS system: Cr-doped In_2O_3 is described in Chapter 4. Similar to Co-doped ZnO films, structural and crystalline properties of In_2O_3 films are carefully examined by variety of techniques in order to

ascertain the absence of secondary phase or possible ferromagnetic impurities. The magnetic properties of the films are then evaluated. The effects of vacuum annealing and external magnetic field on structural and magnetic properties of the films are also examined.

Chapters 5 and 6 are dealing with preparation of ferrimagnetic oxides Fe_3O_4 and $CoFe_2O_4$ respectively. Fe_3O_4 and $CoFe_2O_4$ films were prepared by PI MOCVD technique on different substrates and at different deposition conditions, in and without external magnetic field. The crystalline, structural and magnetic properties of the films are examined. One of the most interesting finds of this thesis is that magnetic properties of Fe_3O_4 and $CoFe_2O_4$ films could be tuned by external magnetic field during the film growth. It is expected that this approach can be used for the preparation of new generation spintronic devices.

Finally Chapter 7 details the conclusions of this work and also further studies to be carried out with some other prepared thin films. In summary a number of materials with intriguing magnetic properties have been prepared by PI MOCVD technique. It is expected that this research and some of our materials could be utilised in the field of spintronics.

Table of Contents

	Page
Chapter 1. Introduction	1
1.1. Spin electronics	1
1.1.1. Mechanism of spintronic and devices	1
1.1.2. Materials for spintronics	5
1.2. Semiconductors	6
1.2.1. Simple band structure	7
1.2.2. Intrinsic semiconductors	9
1.2.3. Extrinsic semiconductors	11
1.3. Magnetic semiconductors	12
1.4. Diluted magnetic semiconductors	13
1.4.1. Theories of ferromagnetism in DMS oxides	14
1.4.2. III-V DMS	16
1.4.3. Metal oxide based DMS	17
1.4.3.1. ZnO based DMS	20
1.4.3.2. In_2O_3 based DMS	25
1.5. Other magnetic oxides	28
1.5.1. Fe_3O_4	29
1.5.2. $CoFe_2O_4$	30
1.5.3. Co_3O_4	31
1.5.4. Mn_3O_4	31
1.6. CVD	32
1.6.1. Pulsed Injection Metal Organic Chemical Vapour Deposition (PI MOCVD)	38
1.7. Aims and Objectives of this work	39
References	41

Chapter 2. Experimental 53

2.1. Starting materials 53

2.1.1. Metalorganic precursors and solvents 53

2.1.1.1. $Zn(tmhd)_2$ 53

2.1.1.2. $Co(tmhd)_2$ 54

2.1.1.3. $In(acac)_3$ 54

2.1.1.4. $In(tmhd)_3$ 54

2.1.1.5. $Cr(acac)_3$ 55

2.1.1.6. $Fe(tmhd)_3$ 55

2.1.1.7. $Mn(tmhd)_3$ 55

2.1.2. Substrates 56

2.2. Sample preparation techniques 56

2.2.1. PI MOCVD 56

2.2.2. PI MOCVD with 1T magnet 59

2.3. Characterisation techniques 61

2.3.1. X-ray Diffraction 61

2.3.2. X-ray Reflectivity 65

2.3.3. White Light Interferometry 67

2.3.4. Atomic Force Microscopy 68

2.3.5. Magnetic Force Microscopy 68

2.3.6. Scanning Electron Microscopy 69

2.3.6.1 Energy Dispersive Analysis of X-rays 70

2.3.7. SIMS and XPS 71

2.3.8. Optical Spectroscopy 71

2.3.9. Raman Spectroscopy 72

2.3.10. SQUID 74

2.3.11. Vibrating sample magnetrometry 74

References 75

Chapter 3. Co-doped ZnO films 76

3.1. Introduction 76

3.2. Deposition of undoped ZnO films 78

3.2.1. Precursor characterisation and screening 79
3.2.2. Studies of the influence of deposition temperature 79
3.2.3. The influence of oxygen concentration 82
3.3. Co-doped ZnO films 84
3.3.1. Preparation of Co-doped ZnO films 84
3.3.2. Characterisation of the films 85
3.3.2.1. Film composition 85
3.3.2.1.1 X-ray absorption spectroscopy 88
3.3.2.2. X-ray diffraction 91
3.3.2.3. Morphology of the films 97
3.3.2.4. Magnetic properties of the films 99
3.3.2.4.1. SQUID magnetometer measurements 99
3.3.2.4.2. VSM magnetometer measurements 104
3.4. Co-doped ZnO films grown in magnetic field 106
3.4.1. Preparation of Co-doped ZnO films in magnetic field 106
3.4.2. Characterisation of Co-doped ZnO films 107
3.4.2.1. X-ray diffraction 107
3.4.2.2. Film composition 111
3.4.2.3. Morphology of the films 112
3.4.2.4. Magnetic properties 114
3.5. Conclusions 116
References 118

Chapter 4. Cr-doped In_2O_3 films 121
4.1. Introduction 121
4.2. Cr-doped In_2O_3 films 121
4.2.1. Preparation of Cr-doped In_2O_3 films 122
4.2.2. Characterisation of the Cr-doped In_2O_3 films 123
4.2.2.1. X-ray diffraction 123
4.2.2.2. Morphology of Cr-doped In_2O_3 films 127
4.2.2.3. Composition of Cr-doped In_2O_3 films 131
4.2.2.4. Optical properties of Cr-doped In_2O_3 films 137

4.2.2.5. Magnetic properties of Cr-doped In_2O_3 films 138
4.2.2.5.1. Effect of vacuum annealing on magnetic and structural properties 142
4.2.2.5.2. Conductivity measurements 143
4.2.2.5.3. Structural properties and morphology of annealed films 144
4.2.2.5.4. Magnetic properties of annealed films 147
4.3. Growth of Cr-doped In_2O_3 films in magnetic field 150
4.3.1. Preparation of Cr-doped In_2O_3 films in magnetic field 150
4.3.2. Characterisation of the Cr-doped In_2O_3 films grown in magnetic fields 151
4.3.2.1. Composition of Cr-doped In_2O_3 films 152
4.3.2.2. X-ray diffraction analysis 153
4.3.2.3. Morphology of Cr-doped In_2O_3 films 158
4.3.2.4. Magnetic properties of Cr-doped In_2O_3 films 160
4.4. Conclusions 162
References: 164

Chapter 5. Deposition and investigation of Fe_3O_4 oxide layers 166
5.1. Introduction 166
5.2. Preparation of Fe_3O_4 films 167
5.3. Investigation of Fe_3O_4 films 169
5.3.1 Thickness of the Fe_3O_4 films 169
5.3.2. X-ray diffraction studies 170
5.3.2.1. Crystalline properties of Fe_3O_4 on Al_2O_3 170
5.3.2.2. Growth of Fe_3O_4 on MgO substrate 176
5.3.3. Raman spectroscopy studies 180
5.3.4. Investigation of surface microstructure 182
5.3.4.1. SEM 182

5.3.4.2. AFM 187
5.3.5. Magnetic force microscopy 188
5.3.6. Magnetisation measurements 190
5.3.6.1. Fe_3O_4 grown on Al_2O_3 substrate 191
5.3.6.2. Fe_3O_4 films grown on MgO substrate 195
5.4. Conclusions 199
References 200

Chapter 6. Deposition and investigation of $CoFe_2O_4$ layers 203
6.1. Introduction 203
6.2. Preparation of $CoFe_2O_4$ films 204
6.3. Characterisation of $CoFe_2O_4$ films 205
6.3.1. Thickness measurements 205
6.3.2. X-ray Diffraction studies 206
6.3.2.1. Co concentration influence 206
6.3.2.2. Deposition temperature influence 209
6.3.3. EDAX measurements 212
6.3.4. Raman spectroscopy studies 213
6.3.5. Investigation of surface microstructure 214
6.3.5.1. SEM 214
6.3.5.2. AFM microscopy 216
6.3.6. Magnetic force microscopy 217
6.3.7. Magnetisation measurements 218
6.3.7.1. Co concentration influence on magnetic properties 219
6.3.7.2. Deposition temperature influence on magnetic properties 221
6.3.7.2.1. Magnetic properties of $CoFe_2O_4$ on MgO substrate 225
6.4. Conclusions 227
References 230

Chapter 7. Conclusions and Future Work 232

7.1. Conclusions 232

7.2. Future work 234

7.2.1. Preparation of Mn_3O_4 films 243

7.2.2. Preparation of Co_3O_4 films 235

References 237

Chapter 8. Appendices 238

Publications 241

Figures and Tables

Chapter 1. Introduction

Fig. 1.1 Spin dependent scattering, for the explanation of the GMR effect. Only minority (spin down) electrons are scattered. Unscattered majority (spin up) electrons cause a short circuit effect, appearing for parallel alignment of the magnetisation (a) but not for antiparallel alignment (b)

Fig. 1.2 Illustration of spin accumulation effect

Fig. 1.3 Johnson transistor

Fig. 1.4 Band diagrams for a) an insulator, b) a semiconductor and c) metal. The parabola at the bottom represents the valence band and conduction band at the top. Shading represents the carrier population

Fig. 1.5 Simple band structure

Fig. 1.6 Different types of semiconductors: a) magnetic semiconductor, b) diluted magnetic semiconductor, c) not-magnetic semiconductor

Fig. 1.7 Crystal structure of ZnO

Fig. 1.8 Magnetic moment of In_2O_3 films doped with different transition metals expressed in μ_B / dopant metal

Fig. 1.9 Schematic illustration of the key CVD steps during deposition

Fig.1.10 One-dimensional model of oxidation of silicon

Table 1.1 Summary of the magnetic properties of some GaN-based DMS

Table 1.2 Summary of the magnetic properties of the oxide-based DMS

Table 1.3 Potential magnetic phases observed in transition metal doped oxide DMS

Table 1.4 Summary of reported magnetic properties of ZnO based DMS

Chapter 2. Experimental

Fig. 2.1 Structure of $M(tmhd)_n$

Fig. 2.2 Schematic diagram of PI MOCVD reactor

Fig. 2.3 Schematic diagram of PI MOCVD reactor with 1 Tesla magnet

Fig. 2.4 X-ray diffraction in Bragg-Brentano $\theta/2\ \theta$ geometry

Fig. 2.5 Graphic presentation of ω scan

Fig. 2.6 Graphic presentation of ϕ scan in Shultz geometry

Fig. 2.7 Possible features with explained sources in X-ray reflectivity curve, from Philips Panalytical

Fig. 2.8 Principal scheme of SEM

Fig. 2.9 Energy-level diagrams of Rayleigh scattering, Stokes Raman Scattering and anti-Stokes Raman scattering

Table 2.1 Important substrate parameters for the deposition of the films

Chapter 3. Co-doped ZnO films

Fig. 3.1 X-ray diffractogram of the ZnO films deposited at different temperatures. Inset shows magnified ZnO (002) reflection at 34.422°; * indicates Al_2O_3 (0001) reflections

Fig. 3.2 Thickness (black symbols) and FWHM (blue symbols) of the ZnO films as a function of deposition temperature

Fig. 3.3 X-ray diffractogram of ZnO (002) diffraction as a function of oxygen concentration

Fig. 3.4 AFM images of ZnO films at different O_2 concentrations. The scale size of a square is 10μm

Fig. 3.5 Comparison of SIMS, XPS and EDAX measurements for Co-doped ZnO films on Al_2O_3 (0001) and Al_2O_3 ($1\underline{1}02$) substrates

Fig. 3.6 SIMS depth profile of the 20% Co-doped ZnO film on Al_2O_3 ($1\underline{1}02$) substrate

Fig. 3.7 XPS spectra of Co 2p electrons of Co-doped ZnO films with different Co concentrations

Fig. 3.8 2% Co doped ZnO: Co 2p XAS. Magnetic sample is in red crosses; nonmagnetic sample is shown in blue circles

Fig. 3.9 O 2p XAS spectra for 2% Co doped magnetic film (red), non-magnetic film (blue), and undoped ZnO (black)

Fig. 3.10 O *K* X-ray emission spectrum for 2% Co-doped non-magnetic and magnetic ZnO films

Fig. 3.11 XRD θ-2θ spectra of ZnO films with different Co concentrations, grown on Al_2O_3 (0001) and Al_2O_3 $(1\bar{1}02)$ substrates showing good crystalline quality even for highest Co concentration in precursor solution

Fig. 3.12 Detailed XRD θ-2θ scan for ZnO films with 10% and 20% Co concentrations, grown on Al_2O_3 $(1\bar{1}02)$ substrate. No presence of metallic Co clusters at 76.7° 2θ is seen in the scan

Fig. 3.13 The change of c and a lattice parameters in Co-doped ZnO films on Al_2O_3 (0001) as a function of Co concentration

Fig. 3.14 The change of c and a lattice parameters in Co-doped ZnO films on Al_2O_3 $(1\bar{1}02)$ as a function of Co concentration

Fig. 3.15 AFM images of Co-doped ZnO films for 1% and 5% Co on Al_2O_3 (0001) and Al_2O_3 $(1\bar{1}02)$ substrates

Fig. 3.16 SEM images of Co-doped ZnO films on Al_2O_3 $(1\bar{1}02)$ substrate

Fig. 3.17 Magnetisation curve of undoped ZnO film

Fig. 3.18 Magnetisation curve of 2% Co-doped ZnO film, grown on Al_2O_3 $(1\bar{1}02)$ substrate. Diamagnetic contribution of sapphire substrate is subtracted. The inset shows the same data at smaller magnetic fields indicating a small remanence of about 10%

Fig. 3.19 Magnetisation curves for 1% Co-doped ZnO film on c-cut sapphire substrate. The red squares were measured immediately after deposition and the black squares were recorded 270 days later

Fig. 3.20 Variation of the magnetic saturation moment with time for 1% Co-doped ZnO films on Al_2O_3 (0001) (black circles) and Al_2O_3 $(1\bar{1}02)$ (red squares). The solid lines indicate fits to the data with $m(t)/m(t=0) = (1+1)^{-0.162}$

Fig. 3.21 Magnetic saturation moment as a function of Co doping concentration for ZnO films on Al_2O_3 $(1\bar{1}02)$ [(a) and (b)] and Al_2O_3 $(1\bar{1}02)$ [(c) and (d)]

Fig. 3.22 In-plane VSM magnetisation curves at different temperatures for a 2% Co-doped ZnO film on Al_2O_3 $(1\bar{1}02)$. The curve in the lower right panel and the red circle in the main frame were measured after cooling from 900K

Fig. 3.23 X-ray diffraction analysis of Co-doped ZnO films grown in and without magnetic field showing very similar crystalline structure of the films independent on Co concentration or application of external magnetic field

Fig. 3.24 The change of *c* and *a* lattice parameters in Co-doped ZnO films grown Al_2O_3 substrate as a function of Co concentration

Fig. 3.25 EDAX spectrum of 15% Co-doped ZnO film showing the presence of Co and Zn elements in a film. Al peak is appearing in all spectra due to Al_2O_3 substrate

Fig. 3.26 Co concentration in Co-doped ZnO films versus Co concentration in precursor solution for the films grown in and without external magnetic field, showing smaller Co content in a film

Fig. 3.27 SEM micrographs for Co-doped ZnO films with different Co concentrations. The left column represents films grown without external magnetic field and the right column represents films grown in 1T external magnetic field. The images are given with Co concentration increasing from top to bottom from 0, 2,5,10,15, and 20%

Fig. 3.28 SQUID magnetisation curves for Co-doped ZnO films grown in and without magnetic field

Table 3.1 Deposition conditions for ZnO grown at different temperatures

Table 3.2 Deposition conditions for Co-doped ZnO films

Table 3.3 Average crystallite size calculated for Co-doped ZnO films with different Co concentrations

Table 3.4 Deposition conditions for Co-doped ZnO films

Table 3.5 Summary of important parameters evaluated from XRD analysis for Co-doped ZnO films

Chapter 4. Cr-doped In_2O_3 films

Fig. 4.1 XRD spectra for Cr-doped In_2O_3 films on Al_2O_3 (0001) at different deposition temperatures

Fig. 4.2 XRD spectra for Cr-doped In_2O_3 films on Al_2O_3 $(1\bar{1}02)$ at different deposition temperatures

Fig. 4.3 Variation of a lattice parameter of Cr-doped In_2O_3 films with deposition temperature

Fig. 4.4 SEM images of Cr-doped In_2O_3 films on Al_2O_3 $(1\bar{1}02)$ substrate deposited at different temperatures

Fig. 4.5 SEM images of Cr-doped In_2O_3 films on Al_2O_3 (0001) substrate deposited at different temperatures

Fig. 4.6 SEM cross-section image for Cr-doped In_2O_3 film on Al_2O_3 (0001) grown at 750°C

Fig. 4.7 The variation of Cr-doped In_2O_3 films thickness with growth temperature

Fig. 4.8 AFM images of the Cr-doped In_2O_3 films deposited at 750°C. Left image- film grown on Al_2O_3 (0001), and right image for the film grown on Al_2O_3 $(1\bar{1}02)$ substrate

Fig. 4.9 Typical EDAX analysis spectra for Cr-doped In_2O_3 films grown on Al_2O_3 substrate

Fig. 4.10 Variation of Cr concentration in the 2% Cr-doped In_2O_3 films with deposition temperature

Fig. 4.11 XPS spectra of the Cr2p core level in the Cr-doped In_2O_3 films

Fig. 4.12 SIMS depth profile as a function of milling time for 2% Cr-doped In_2O_3 film grown at 600°C on Al_2O_3 $(1\bar{1}02)$ substrate

Fig. 4.13 SIMS depth profile as a function of milling depth for 2% Cr-doped In_2O_3 film grown at 700°C on Al_2O_3 (0001) substrate

Fig. 4.14 Optical transmission spectra of 2%Cr-doped In_2O_3 grown at different temperatures

Fig. 4.15 SQUID magnetisation curve for 2%Cr-doped In_2O_3 film grown at 700°C on Al_2O_3 (0001) substrate. Inset in the figure shows magnetisation curve of undoped In_2O_3 film

Fig. 4.16 Saturation magnetisation of Cr-doped In_2O_3 films expressed in μ_B/Cr atom as a function of deposition temperature, the inset shows the variation of absolute magnetic moment for Cr-doped In_2O_3 films as a function of deposition temperature

Fig. 4.17	Hysterisis curve for the Cr-doped In_2O_3 film grown at 700ºC, graph inside shows magnified area of the hysterisis curves
Fig. 4.18	The variation of out of plane and in plane saturation magnetisation with time for Cr-doped In_2O_3 films deposited at 550ºC and 750ºC
Fig. 4.19	Current (I) versus applied voltage in vacuum annealed Cr-doped In_2O_3 film showing the linear dependence as expected from Ohm's law
Fig. 4.20	Comparison of XRD spectra for Cr-doped In_2O_3 grown at 600ºC and 700ºC before and after annealing in vacuum
Fig. 4.21	SEM micrographs of Cr-doped In_2O_3 films before and after annealing in vacuum
Fig. 4.22	SQUID magnetisation data for Cr-doped In_2O_3 grown at 600ºC, a) prior to annealing, b) immediately after vacuum annealing, c) 2 weeks after vacuum annealing, d) 2 months after vacuum annealing, e) 6 months after vacuum annealing, f) magnetisation data of the film grown at 700ºC
Fig. 4.23	SQUID magnetisation measurement for Cr-doped In_2O_3 film after annealing in O_2
Fig. 4.24	XRD pattern (left) and SEM micrograph (right) of the Cr-doped In_2O_3 film after annealing in O_2
Fig. 4.25	Variation of Cr concentration in a film as a function of Cr concentration in precursor solution for Cr-doped In_2O_3 films
Fig. 4.26	XRD patterns for Cr-doped In_2O_3 films with different Cr concentrations and grown in and without 1T magnetic field
Fig. 4.27	The calculated lattice parameter of Cr-doped In_2O_3 films for different Cr concentrations
Fig. 4.28	SEM micrographs of Cr-doped In_2O_3 films with different Cr concentrations grown in and without magnetic field
Fig. 4.29	Room temperature SQUID magnetisation of Al_2O_3 substrate
Fig. 4.30	SQUID magnetisation data for 6 and 12% Cr-doped In_2O_3 films grown on c-cut sapphire substrate in and without magnetic field
Table 4.1	Deposition conditions for Cr-doped In_2O_3 films
Table 4.2	The average crystallite size calculated using Scherrer formula for Cr-doped In_2O_3 film grown at different temperatures

Table 4.3 Calculated coercive fields for Cr-doped In_2O_3 films grown at different temperatures

Table 4.4 Deposition conditions for Cr-doped In_2O_3 films grown in PI MOCVD equipped with 1 Tesla magnet

Table 4.5 The average crystallite size calculated using Scherrer formula for Cr-doped In_2O_3 film for different Cr concentrations in precursor solution for the grown in and without magnetic field

Chapter 5. Deposition and investigation of Fe_3O_4 oxide layers

Fig. 5.1 XRD patterns (θ-2θ) of Fe_3O_4 films grown on Al_2O_3 at different deposition temperatures

Fig. 5.2 The comparison of XRD patterns of Fe_3O_4 films grown in and without magnetic field on Al_2O_3 substrate, showing similar crystalline structure

Fig. 5.3 XRD patterns of the Fe_3O_4 films grown on Al_2O_3 sapphire in $Ar+H_2$

Fig. 5.4 The variation of lattice parameter (a) with deposition temperature for the Fe_3O_4 films grown on Al_2O_3 substrate in Ar atmosphere

Fig. 5.5 Typical XRD pattern for the Fe_3O_4 film grown on (100) MgO substrate and Fe_3O_4 (511) reflection for the films grown at different temperature in and without external magnetic field (b) Figure 5.6 Phi scan performed for Fe_3O_4 (511) reflection, grown at 450°C showing four reflections

Fig. 5.7 The change of a lattice parameter with deposition temperature of Fe_3O_4 films on MgO substrate grown in Ar atmosphere

Fig. 5.8 Raman spectrum of Fe_3O_4 films, where * indicates substrate peaks, numbers in red indicate the approximate positions for Fe_3O_4 phase and in black indicate α-Fe_2O_3 phase

Fig. 5.9 SEM micrographs of the Fe_3O_4 films on Al_2O_3 substrate grown in Ar atmosphere, showing different morphology of the films grown at different temperatures. The images in the left row are corresponding to films grown without magnetic field and in the right row in 1T external magnetic field

Fig. 5.10 SEM micrographs of the Fe_3O_4 films on MgO (100) substrate grown in Ar atmosphere. The films in the left row are grown without magnetic field and in the right row in 1T external magnetic field

Fig. 5.11 SEM micrographs for the Fe_3O_4 films grown in $Ar+H_2$ atmosphere

Fig. 5.12 AFM images of Fe_3O_4 films grown at 550°C on Al_2O_3 and MgO substrates. The dimensions of the square are $2\mu m$

Fig. 5.13 MFM images for the Fe_3O_4 films grown in different conditions

Fig. 5.14 Hysteresis curves of the Fe_3O_4 films grown in and without external magnetic field on Al_2O_3. The blue line indicates the effect of cooling the film in 1T external magnetic field

Fig. 5.15 The M_S and μ_B/f.u. values versus deposition temperature for the films on Al_2O_3 grown

Fig. 5.16 The M_S values of the Fe_3O_4 films versus film thickness (number of pulses)

Fig. 5.17 Hysteresis curves for Fe_3O_4 films on MgO substrate grown in and without external magnetic field. The blue line indicates the effect of cooling the film in 1T external magnetic field

Fig. 5.18 Hysteresis curves of the Fe_3O_4 film with magnetic field applied parallel to the film plane (black squares) and perpendicular to the film plane (red squares)

Fig. 5.19 The M_S and μ_B/f.u. values versus deposition temperature for the films on MgO, grown in and without external magnetic field

Table 5.1 General deposition conditions for Fe_3O_4 films

Table 5.2 The average thickness of Fe_3O_4 films grown in different deposition conditions

Table 5.3 The experimental values of FWHM, *a* lattice parameter and effective out-of-plane strain for Fe_3O_4 films grown in and without magnetic field at different temperatures

Table 5.4 The experimental values of FWHM, *a* lattice parameter and effective out-of-plane strain for the Fe_3O_4 films grown with different pulse numbers

Table 5.5 The average grain size calculated for Fe_3O_4 films grown on Al_2O_3 substrate

Table 5.6 The FWHM, rocking curve, *a* lattice parameter, effective out-of-plane strain and average grain size values of the Fe_3O_4 films on MgO substrate

Table 5.7 The estimated Ra for the Fe_3O_4 films grown on c-cut sapphire substrate in Ar atmosphere

Table 5.8 The magnetic properties of Fe_3O_4 films grown on Al_2O_3 at different deposition parameters

Table 5.9 The magnetic properties of Fe_3O_4 films grown on MgO at different deposition parameters

Chapter 6. Deposition and investigation of $CoFe_2O_4$ layers

Fig. 6.1 Thickness of $CoFe_2O_4$ films versus deposition temperature for the films grown in and without external magnetic field on Al_2O_3 (0001)

Fig. 6.2 X-ray diffraction of $CoFe_2O_4$ films grown at 600°C on Al_2O_3 with different Co concentrations in precursor solution

Fig. 6.3 X-ray diffraction patterns for $CoFe_2O_4$ films grown on Al_2O_3 substrate at different temperatures

Fig. 6.4 X-ray diffraction of $CoFe_2O_4$ (511) reflection grown on (100) MgO substrate at 600°C in and without external magnetic field. The inset is showing phi scan around $CoFe_2O_4$ (511) reflection evidencing the epitaxial relation between film and MgO substrate

Fig. 6.5 Variation of Co concentration in the film with Co concentration in precursor solution for $CoFe_2O_4$ films grown on Al_2O_3 substrate. Red triangle denotes Co concentration for the film grown in 1T on Al_2O_3 substrate and blue square for the films grown on MgO substrate

Fig. 6.6 Raman spectrum of $CoFe_2O_4$ films, where * denotes substrate peaks, numbers denote the approximate positions for $CoFe_2O_4$ phase

Fig. 6.7 SEM micrographs of $CoFe_2O_4$ films grown at different deposition temperature in and without external magnetic field

Fig. 6.8 AFM images of $CoFe_2O_4$ films grown on MgO substrate

Fig. 6.9 Magnetic domain structure of $CoFe_2O_4$ films grown at 600°C. The scale is $2\mu m$

Fig. 6.10 Hysteresis curves for $CoFe_2O_4$ films grown in and without magnetic

field on Al_2O_3 substrate with 10 and 40% Co

Fig. 6.11 M_s values of $CoFe_2O_4$ films grown with different Co concentrations with and without external magnetic field

Fig. 6.12 M_S of $CoFe_2O_4$ grown at different deposition temperature with and without external magnetic field

Fig. 6.13 Hysteresis loops showing the influence of magnetic field on magnetic properties of $CoFe_2O_4$ films grown on Al_2O_3 substrate at different deposition temperatures

Fig. 6.14 Shows quite similar hysteresis curves for $CoFe_2O_4$ films with magnetic field applied perpendicular and parallel to the films surface

Fig. 6.15 a) Hysteresis curves for $CoFe_2O_4$ films with magnetic field applied parallel and perpendicular to the film surface, showing huge magnetic anisotropy effect; b)

Table 6.1 General deposition conditions for $CoFe_2O_4$ films

Table 6.2 Summary of experimental values of FWHM, *a* lattice parameter, effective out-of-plane strain and average grain size for $CoFe_2O_4$ films grown with different Co concentrations on Al_2O_3 substrate. The [1] indicates the main peak, and [2] indicates the splitting (222) peak

Table 6.3 Summary of experimental values of FWHM, *a* lattice parameter, effective out-of-plane strain and average grain size for $CoFe_2O_4$ films grown at different temperatures on Al_2O_3 and MgO substrates

Table 6.4 The magnetic properties of $CoFe_2O_4$ films grown on Al_2O_3 with different Co concentrations

Table 6.5 Summary of the magnetic properties for $CoFe_2O_4$ films grown on Al_2O_3 and MgO substrates at different deposition temperatures

Chapter 7. Conclusions and Future Work

Fig. 7.1 X-ray diffraction patterns of Mn_3O_4 films grown at 600°C on Al_2O_3 (0001) substrate from two different precursors showing similar crystalline quality independent on the precursor choice or presence of external magnetic field

Fig. 7.2 SEM micrographs of Mn_3O_4 films prepared in (right image) and without (left image) external magnetic field (1T), showing similar surface morphology

Fig. 7.3 X-ray diffraction patterns of Co_3O_4 films showing good crystalline quality, independent on the presence of external magnetic field

Fig. 7.4 SEM microhraphs of Co_3O_4 films prepared in and without external magnetic field

Chapter 8. Appendices

Appendix 1 AFM images of Cr-doped In_2O_3 films deposited on Al_2O_3 (0001) substrate at different deposition temperatures

Appendix 2 AFM images of Cr-doped In_2O_3 films deposited on Al_2O_3 $(1\underline{1}20)$ substrate at different deposition temperatures

Appendix 3 SEM micrographs of Fe_3O_4 films on Al_2O_3 (0001) grown at 550°C in Ar atmosphere with different number of pulses

Chapter 1: Introduction

1.1. Spin electronics

Electron spin was known about for most of the 20th Century, but until recent time, conventional electronic systems have ignored the spin of the electron using a charge of the electron as a basis for information processing. However, employing of independent families of current carriers with opposite spin polarization could open the way for realisation of whole new generation of semiconductor spin transfer electronic devices, also known as spintronics [1]. Spintonics exploit the spin dependent electronic properties of magnetic materials in semiconductors [2]. Two of the most successful technologies in last years have created the Si integrated circuit industry and the data storage industry based on hard magnetic materials. Even though integrated circuits include high speed signal processing and excellent reliability, but the memory elements are volatile, i.e., when the power is switched off the stored information is lost, as data stored as charge in capacitors. At the same time, magnetic memory technologies are not volatile since they employ ferromagnetic materials, which have remanence. Spintronics are expected to combine both features: the charge and the spin of the electrons. The discovery of giant magneto resistance (GMR) of the Fe/Cr magnetic multilayers in 1988 [3, 4] opened the large research field of spintronics. Ten years after the discovery of GMR all hard drives included GMR based read heads. This was a significant improvement in data density and more important have demonstrated the potential of applications for spintronics. Another spintronics effect is the tunnelling magneto resistance (TMR) observed in magnetic tunnel junctions (MTJ). Non-volatile random access magnetic memories including MTJs as the storage element using low power consumption could be another great application of spintronics.

1.1.1. Mechanism of spintronics and devices

The technical basis of spintronics first appeared in 1936 when Mott suggested that current in bulk ferromagnets is carried by two independent ‘spin channels’ consisting of electrons with spin-up and spin-down charge carriers [5]. This is a first and the simplest

spintronic device possible. It is a two terminal passive device, also known as a 'spin valve'. Its simplest form consists of magnetic trilayers, in which a layer of nonmagnetic metal (NM) is sandwiched between two layers of ferromagnetic (FM) metal [3, 4]. As two spin channels pass through the magnetically orientated FM layer they experience a different resistance. Parallel alignment of FM layers gives low resistance (Fig.1a) and antiparallel alignment high resistance (Fig.1b).

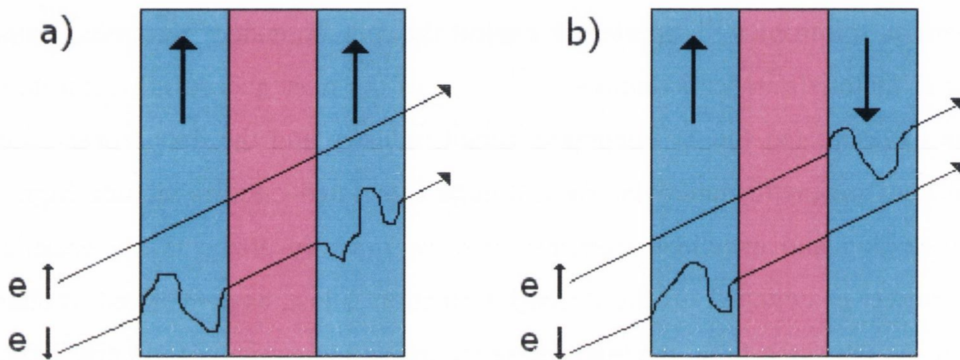

Fig. 1.1 Spin dependent scattering, for the explanation of the GMR effect. Only minority (spin down) electrons are scattered. Unscatered majority (spin up) electrons cause a short circuit effect, appearing for parallel alignment of the magnetisation (a) but not for antiparallel alignment (b)

Therefore, the resistance of the stack is dependent on the field applied. This is called a magnetoresistive effect and first was discovered in Fe/Cr/Fe trilayers by Baibich [3]. The magnetoresistance (MR) can be presented by the equation:

$$MR = \frac{R\uparrow\downarrow - R\uparrow\uparrow}{R\uparrow\downarrow} \quad (1)$$

Where, $R\uparrow\downarrow$ and $R\uparrow\uparrow$ are the resistances of the anti-aligned and aligned states of FM layers. Note, that MR expressed by equation (1) cannot be more than 100%.

Magnetic information is encoded onto the carrier population by the first FM layer (the polariser) and transferred to the second FM layer (the analyser). In the other words,

spin electronic devices work by transferring spin information from one part of the device to another. At the interface between FM and NM materials, the contribution of each spin channels changes. Let's assume, if the conductivity in FM layer is larger for spin up electrons, then the larger part of spin flux is carried by spin up channel. While, NM is symmetric and both spin channels contribute equally to the current. Due to the incoming and outgoing currents, in both sides of the interface, the density of spin-up and spin-down electrons is out of equilibrium. This effect is known as spin accumulation (Fig.1.2). Any spin flip scattering will preferentially scatter a spin-up to a spin-down until equilibrium has been restored. Although, information is mediated by the electrical carriers and it decays on some characteristic length scale known as spin diffusion length (λ_{sd}), which is the average distance diffused by a carrier before spin flipping occurs. Spin diffusion length is given by the equation:

$$\lambda_{sd} = \sqrt{\frac{\lambda \upsilon_F \tau_{\uparrow\downarrow}}{3}} \qquad (2)$$

Where λ is the mean free path of the carriers, υ_F is the Fermi velocity and $\tau_{\uparrow\downarrow}$ is the spin-flip time. The spin diffusion length is dependent on the mean free path, so a large number of scattering sites such as defects or impurities tend to reduce λ_{sd}. For example, λ_{sd} reduces from about 1 μm for pure silver, to roughly 100 Å for silver with 3% of added gold impurity [6]. Therefore, in order to exploit these spin electronics, the physical dimensions of the structures should be smaller than spin diffusion length.

Another quantity we can derive from the mechanisms of spintronics is the polarisation - the extent to which the population of one channel exceeds the population of the other channel - and it is defined as the difference in carrier concentration at the Fermi surface divided by the sum of carriers:

$$P = \frac{n\uparrow - n\downarrow}{n\uparrow + n\downarrow} \qquad (3)$$

where $n_\uparrow$, $n_\downarrow$ are the carrier concentrations for the up and down channels, respectively.

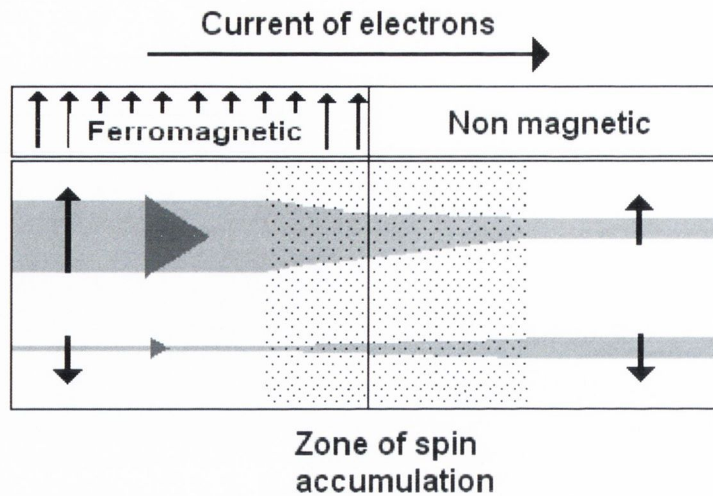

Fig. 1.2 Illustration of spin accumulation effect .[7]

The aim for future spintronic devices is the realization of three-terminal devices, such as the metal-spin transistor (Fig.1.3). In a spin transistor an additional contact is added to the central layer and conditions at terminal 3 may be set by adjusting conditions at terminals 1 and 2, as in conventional electronic three terminal devices [8]. The difference between electronic devices is that these conditions are switchable by applying an external magnetic field.

Another step of realization of spintronic devices is hybrid spin electronics, combination of conventional semiconductors with spin asymmetric conducting materials. Although, to make a full use of hybrid spin electronic devices a spin dependent transport should be exploited in semiconductors itself.

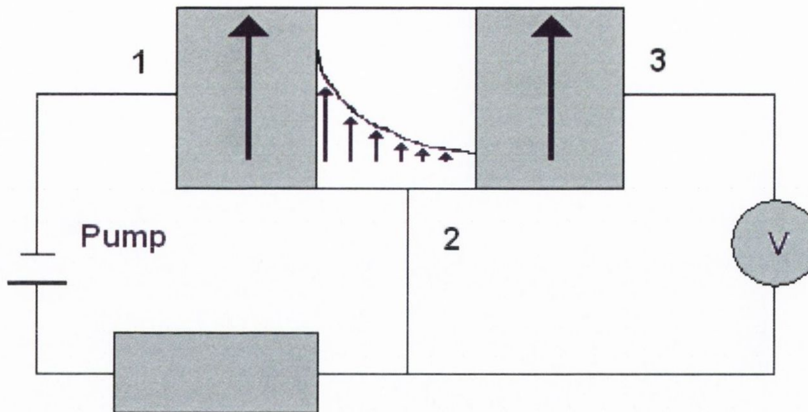

Fig. 1.3 Johnson transistor

1.1.2. Materials for spintronics

Conventional Si, Ge or GaAs semiconductors widely used in industry do not posses ferromagnetic properties, thus can not be used in spintronics. Existing magnetic devices exploiting GMR, such as read heads or magnetic data storage devices are based largely on ferromagnetic metals, iron, cobalt and nickel and their alloys. Current spin valves, for example, use CoFe or NiFe layers with Cu as a spacer. Although, the conduction electrons in the 3d ferromagnets are not fully spin polarized, for example, in 3d ferromagnets in the diffusive limit, the spin polarization is always positive and close to 40%. [9]. In addition, due to dissimilar materials properties of a metal and semiconductor, spin injection efficiency in diffusive transport regime is low, unless material is nearly 100% spin polarized, i.e. half metallic. For practical applications of spintronics the development of new class materials is essential. There are a number of essential requirements for achieving practical spintronic devices:

1) Spin dependent transport. It is essential for spintronics to have two independent spin channels with different transport properties. Non-magnetic materials, such as semiconductors do not exhibit this property.
2) High Curie temperature (T_C). For the integration of spintronic devices into semiconductor based electronics, they will have to operate at practical temperatures, i.e. room temperature or higher.

3) Large spin diffusion lengths and high mobilities. The spin diffusion length needs to be large enough to survive spin orientation during operation of spintronic device.
4) For device fabrication, *n*- and *p*- type semiconductors are required. The ability to control carrier concentration in semiconductors can be useful for spintronic devices.

Based on the criteria listed above the ideal material should be inexpensive, non-volatile and non-toxic, compatible with common semiconductor materials (Si, GaAs) and have high T_C. For these reasons, there is a great interest in developing high T_C ferromagnetic semiconductor, which combines the properties of ferromagnetic and semiconducting systems. High T_C diluted magnetic semiconductor (DMS) that will be discussed in chapter 1.4 would satisfy all requirements listed above.

In the next chapter, a brief introduction into semiconductor materials and their properties will be given.

1.2. Semiconductors

Originally, semiconductors were defined as materials that have conductivity between metals and insulators. This means that resistance of semiconductors can be varied over eleven orders of magnitude, in the range between 10^2 and 10^{-9} Ω/cm. Although, a more advanced definition of semiconductors, which explains variation of conductivity, reads: A semiconductor is a solid state material, which is insulating at low temperatures and has a measurable electronic conductance at higher temperature. The electronic conductivity is due to the well-defined chemical composition, which does not change in high electric fields or due to some influence from outside the solid state material [10].

In the middle of the periodic system – between the metals and the insulators there is a group of elemental semiconductors (group IV). The most important group IV semiconductors are Si and Ge. Semiconductors can also be binary compounds of groups III and V elements, like GaAs and InP, or binary combinations of group II and VI elements, like ZnS and CdTe. These materials tend to have the same or very similar structures in their solid state, because of the same number of the electrons involved in the

bonding. At absolute zero temperature (T = 0 K), all electrons are bound to their atoms, so there are no electrons involved in the current flow. This means, that semiconductors are insulators at low temperatures.

1.2.1. Simple band structure

Depending on the conductivity materials can generally be classified as conductors, semiconductors and insulators. Each category can be understood of as having a conduction band of electrons (i.e. electrons involved in the conduction processes) and a valence band, whose electrons are involved in the binding of the material (Fig.1.4).

It is very easy to explain how semiconductors work by introducing simple band structure (Fig 1.5). At absolute zero temperature, when semiconductor is insulating all states in the valence band are occupied and conduction band is empty. At any temperature above zero, electrons can absorb some form of energy i.e. lattice vibrations, photons and etc., and electron bond can break. Thus, electron becomes a free charge carrier capable of conducting electrical current. In the place of electron there is a hole left, which is immediately filled with other valence electrons from surrounding bonds. Therefore, hole is also considered to be a free charge carrier of positive sign, which contribute to the electrical conductivity of the semiconductor. This process of free electron formation, illustrated in Figure 1.5-1 is called electron-hole pair generation. The opposite process, when after some time electron will jump into another broken bond in the crystal, cancelling the hole is called electron-hole recombination (Fig. 1.5-2). The energy difference between the valence and conduction band, the forbidden energy zone is called energy gap. Energy gap is the most important parameter for semiconductors, as it determines which energy needs to be absorbed to generate charge carriers.

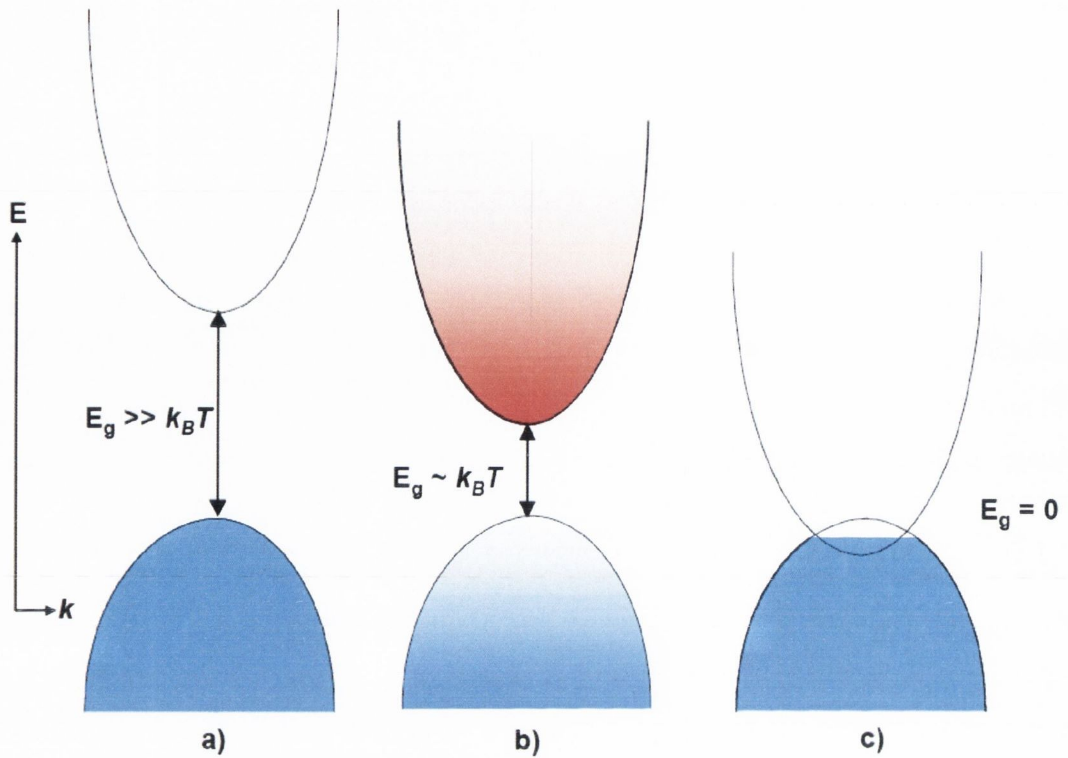

Fig. 1.4 Band diagrams for a) an insulator, b) a semiconductor and c) metal. The parabola at the bottom represents the valence band and conduction band at the top. Shading represents the carrier population [9].

For instance, in insulating materials, the energy required to promote an electron is larger than the thermal energy of the electron and thus the conduction band is empty. Therefore, the material has no charge carriers available for the conductions and is insulating. In the metal, the bands are overlapping, so any free electrons in a valence band a free to populate the conduction band, enabling electrical conductivity in the material. While in semiconductors, the conduction band does not overlap the valence band, but the gap is narrow enough for thermal or optical activation process to enable charge carriers in the conduction band. Usually, the band gap, E_g, in semiconductors is of the order of 1eV.

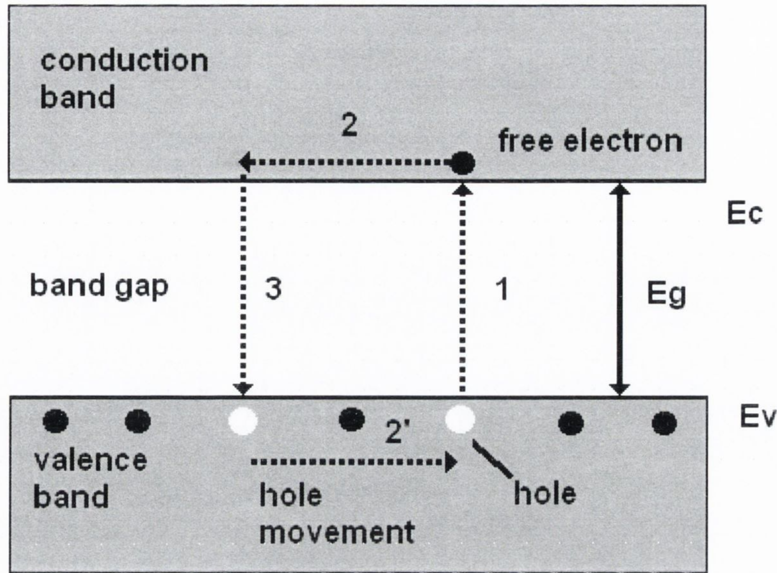

Fig. 1.5 Simple band structure [11]

1.2.2. Intrinsic semiconductors

Pure semiconductor materials are called intrinsic semiconductors as their properties are intrinsic to the material itself. In intrinsic semiconductors, free charge carriers are generated exclusively by the process of electron-hole generation. Therefore, the concentration of electrons in equilibrium equals to the concentration of holes. For an evaluation of the conductivity of semiconductors the number of charge carriers (i.e. charge carriers distribution) has to be calculated. The charge carrier distribution is the product of the number of electron states per unit energy per unit volume, which is known as the density of states, and the fraction of occupied states at each energy, which is given by Fermi function. Electrons and holes occupy states near the band edges with parabolic dispersion relations. For electrons near the lower edge of the conduction band the density of states D (E) is found to be:

$$D_C(E) = \frac{4\pi(2m_c^*)^{3/2}}{h^3}\sqrt{E - E_C} \tag{4}$$

and, accordingly for holes near the valence band edge:

$$D_V(E) = \frac{4\pi(2m_v^*)^{3/2}}{h^3}\sqrt{E_V - E} \qquad (5)$$

where, m_c^* and m_v^* are the effective masses of electrons and holes, respectively. Knowing density of states for electrons and holes we can calculate the density of electrons in the conduction band:

$$n = N_C \exp\left[-\frac{E_C - E_F}{kT}\right] \qquad (6)$$

and density of holes in the valence band:

$$p = N_V \exp\left[-\frac{E_F - E_V}{kT}\right] \qquad (7)$$

Where, E_F is called the Fermi energy or Fermi level. It is the energy where the probability of a state being occupied by an electron or a hole is one half. N_C and N_V are called the effective density of states for the conduction band and for the valence band, respectively. n and p depend only on the temperature and the kind of semiconductor, but not on hole or electron densities. In intrinsic semiconductor the electron density equals to the hole density and the name intrinsic carrier density n_i^2 is given:

$$np = n_i^2 \qquad (8)$$

This equation is called the semiconductor equation and it is very important in the study of semiconductors and it is an example of the chemical law of mass action. Semiconductor equation holds for any n and p as long as thermal equilibrium is satisfied. Dividing two equations for n and p we can determine E_F:

$$E_F = \frac{E_C + E_V}{2} + \frac{3}{4} kT \ln\left(\frac{m_v^*}{m_c^*}\right) \quad (9)$$

This equation shows that Fermi level for intrinsic semiconductor is at the average of E_C and E_V, when $m_c^* \neq m_v^*$. When p ≠ n, then the Fermi level shifts towards the band with majority carriers.

1.2.3. Extrinsic semiconductors

An extrinsic semiconductor is defined as a semiconductor in which controlled amounts of dopant or impurity atoms have been added. In extrinsic semiconductor the electron and hole concentrations are different, so the electrical properties of extrinsic semiconductor is different form intrinsic. One type of carrier will predominate in extrinsic semiconductor. Impurities that cause the increase of electron concentration are called donors. If concentration of electrons in semiconductor is higher than concentration of holes semiconductor is called an n-type. By adding acceptor impurities the hole concentration in semiconductor becomes higher than electron concentration and semiconductor is called p-type. Adding donor or acceptor impurity atoms to a semiconductor will change the distribution of electrons and holes in the material, and will also change the position of the Fermi level. For a donor, say, the energy needed to excite the electron to the conduction band is the donor ionization energy E_d. As the charge neutrality condition in the system has to preserve we can write:

$$p + N_d^+ = n + N_a^- \quad (10)$$

where p and n are intrinsic hole and electron concentrations, N_d^+ and N_a^- are the concentrations of ionized donors and acceptors, respectively. If the concentrations of impurities are not too high almost all of them will be ionized at room temperature. So it can be assumed that the concentrations of ionized impurities are equal to the total concentration. For n-type semiconductor, the concentration of ionized donors is given as:

$$N_d^+ = N_d\left[1 - \frac{1}{1+\frac{1}{2}\exp[(E_d - E_F)]/kT}\right] \quad (11)$$

Similarly, for p-type semiconductor, for known concentration of N_a that introduces an energy level E_a within the band gap, the concentration of ionized acceptors will be:

$$N_a^+ = \frac{N_a}{1+4\exp[(E_a - E_F)/kT]} \quad (12)$$

Using a charge neutrality equation for n-type and p-type semiconductors the Fermi level F_E can be determined.

$$E_C - E_F = kT\ln\left(\frac{N_c}{N_a}\right) \quad (13)$$

For n-type semiconductor the Fermi level places in between the donor band and conduction band. And consequently, for p-type semiconductors:

$$E_F - E_V = kT\ln\left(\frac{N_v}{N_a}\right) \quad (14)$$

1.3. Magnetic semiconductors

The first wave of research on spintronics began with the observation that there was a number of outstanding phenomena associated with the interplay between ferromagnetic phenomena and semiconducting properties in $CrBr_3$, EuO and other europium and manganese based chalcogenides [12]. These materials have been strictly termed as ferromagnetic semiconductors as they exhibit a long-range ferromagnetic order at some finite temperature [13]. In these materials, the ferromagnetic behaviour is due to the nearest-neighbours spin-spin interactions. Even if there is a strong interaction between carriers in the bands of the semiconductor, this interaction gives the opportunity to tune the magnetic properties through the carrier density [14]. The problem with

ferromagnetic semiconductors (FMS) was their low Curie temperature, T_C, which would rarely break 100 K. For any practical application, it has always been understood that a Curie temperature of well above 300 K, room temperature, would be needed. These FMS dropped out of favour due to their inability to push the Curie temperature higher than 100 K and also preparation difficulties.

1.4. Diluted magnetic semiconductors

The most common class of materials that would qualify as ferromagnetic semiconductors is the diluted magnetic semiconductors (DMS). A DMS typically consist of a nonmagnetic semiconductor doped with a several atomic percent of some open shell transition metal (usually 3d metals), so that they combine magnetic and semiconducting properties. Such compound is an alloy between nonmagnetic semiconductor and magnetic material, as shown in Figure 1.6. A true DMS is one in which the magnetic dopant spins retain their remanent alignment under the influence of spin-polarized free carriers. Free carriers could be introduced into system either by magnetic dopants or by some secondary electronic dopant. Also, it is generally believed that it is necessary to achieve a single phase DMS in order to realise useful devices. In DMS it is the polarized carriers that carry the spin information. In case, if precipitates or clusters which responsible for ferromagnetism are present and carriers do not mediate magnetic interaction, then the practical usefulness of such materials in spintronics is under question. The development of reliable high T_C diluted magnetic oxides with large spin polarization at room temperature and above, and electrically tunable magnetic and electronic properties might pay a role in future spintronic devices.

In the early period of searching the best candidates for spintronic devices the most common and intensively studied DMS were II-VI compounds, such as CdTe, ZnSe, CdS, CdSe and etc., doped with transition metal atoms, usually Mn [15]. Often such magnetic semiconductors are difficult to grow and have low T_C. Also, they are incompatible with common semiconductor materials such as Si and GaAs.

The quest to achieve room temperature carrier induced ferromagnetism has motivated significant efforts on wide band gap semiconductors such as GaN and ZnO.

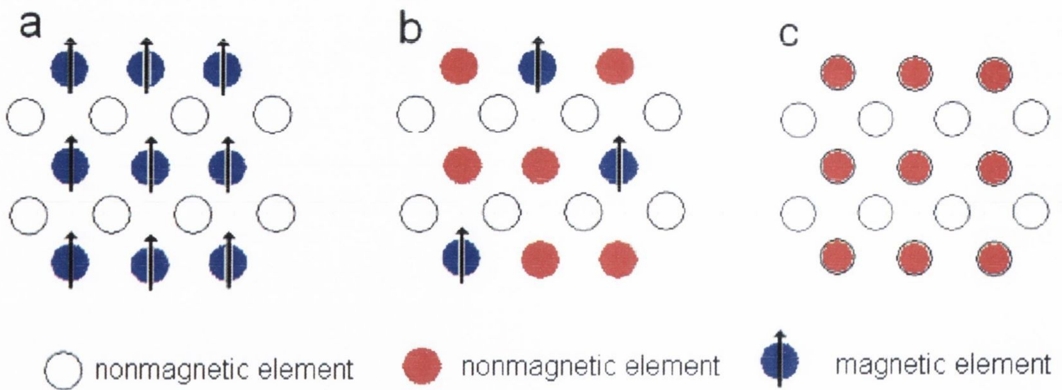

Fig. 1.6 Different types of semiconductors: a) magnetic semiconductor, b) diluted magnetic semiconductor, c) not-magnetic semiconductor

1.4.1. Theories of ferromagnetism in DMS oxides

There have been a lot of successful experiments carried out on transition metal doped oxides. Despite the experimental success a fundamental description of ferromagnetism in oxides remains incomplete. Dietl *et al.* [16] have applied Zenere's model for ferromagnetism. It implies, that exchange interactions between carriers and localized spins can explain the ferromagnetic transition temperature in III-V and II-VI compound semiconductors. There are three limiting cases of carrier mediated exchange: the Ruderman-Kittel-Kasuya-Yoshida (RKKY) interaction, Zener carrier mediated exchange (mean field model) and Zener double exchange.

The basic idea behind the RKKY interaction is based on the exchange coupling between the magnetic ion and the conduction band electrons. The conduction electron is magnetised in the vicinity of the magnetic ion, with polarisation decaying with distance from the magnetic ion in an oscillatory manner. The oscillation causes an indirect superexchange interaction between two magnetic ions on the nearest or next to the nearest magnetic neighbours. This coupling may result in a ferromagnetic or antiferromagnetic interaction of the moments.

The mean field Zener model has been successful in explaining the transition temperatures observed in p- (Ga,Mn)As and (Zn,Mn)Te. Compared to the RKKY interaction the mean field Zener model takes into account the anisotropy of the carrier

mediated exchange interaction associated with the spin-orbit coupling in the host material.

Finally, the Zener double exchange model was first proposed to explain the experimentally observed ferromagnetism in the doped manganites [17], like $La_{1-x}A_xMnO_3$, with A = Ca, Sr, or Ba. In the double exchange mechanism magnetic ions in different charge states couple with each other by virtual hopping of the electron from one ion to the other. In the case of DMS, in the ferromagnetic configuration, introducing carriers in the d band can lower the band energy. In this case the 3d electron in the partially occupied 3d orbital of the transition metal is allowed hop to the 3d orbital of the neighbouring transition metal if they have parallel magnetic moments.

Other basic classes of models for the ferromagnetism in the absence of the ferromagnetic clusters or second phases include the bound magnetic polaron and virtual transition. Most of the theories describing ferromagnetism in DMS materials assume that the transition metal ions (typically Mn^{+2}) are randomly substituted on the cation sites where they act as acceptors.

The concept of bound magnetic polarons (BMPs) in connection with magnetic semiconductors was first introduced to explain the low temperature metal-insulator transition in oxygen deficient EuO [14]. The BMPs are formed by the alignment of the spins of many transition metal ions with weakly bound carriers such as exitons within the polaron radius. The localised holes of the polarons act on the transition metal impurities surrounding them and produce an effective magnetic field and align all spins. As temperature decreases the interaction distance grows. Neighbouring magnetic polarons overlap and interact via magnetic impurities forming clusters of polarons. Ferromagnetism is observed then the size of such clusters is equal to the size of the sample. The polaron model is applicable for both p- and n- type semiconductors [18].

Virtual excitations were suggested by Litvinov and Dugaev [19]. According to them virtual excitations from the magnetic impurity levels to the valence band or the ligand orbitals could produce the p-d exchange needed for the ferromagnetism in the absence of large density of free carriers.

1.4.2. III-V DMS

In the 1990's the application of new crystal growth techniques such as molecular-beam epitaxy (MBE) renewed interest and progressed the development of ferromagnetic DMS. Most efforts were focused on III-Mn-V compound semiconductors such as $Ga_{1-x}Mn_xAs$ and $In_{1-x}Mn_xAs$, which are *p*-type and exhibit ferromagnetic ordering. Ferromagnetic ordering in these materials is commonly believed to be induced by carrier mediated interactions between the magnetic atoms, but the precise mechanism is still to be clarified. However, the highest T_C reported for $Ga_{1-x}Mn_xAs$, has a maximum value of 172 K [20]. Reported T_C for $In_{1-x}Mn_xAs$ is even lower, reaching only ~61 K [21]. This is a significant limiting factor for practical applications of these DMS in spintronic devices.

Table 1.1 Summary of the magnetic properties of some GaN-based DMS

Compound	TM content, (%)	Substrate (or bulk)	Fabrication method	Growth temperature (°C)	Post annealing (°C)	T_C, (K)	Notes	Reference
(Ga,Mn)N	1 – 2	p- GaN	Solid state diffusion		250-800	220-230	Ferromagnetic	[22]
(Ga,Mn)N	3	c-sapphire	MBE	580-720		940	Ferromagnetic	[23]
(Ga,Mn)N	7	c-sapphire	MBE	865		10-25	Ferromagnetic	[24]
(Ga,Mn)N	1 – 3	p-GaN	Ion implantation	350	700-1000	250	Ferromagnetic	[25]
(Ga,Mn)N	2	Bulk	Ammonothermal & resublimation	1200-1250		>425	Para + ferromagnetic	[26]
(Ga,Mn)N	7 - 14	4H-SiC (0001)	MBE	710		750	Ferromagnetic, from Mn clusters	[27]
(Ga,Cr)N	3	Bulk	Sodium flux growth	750		280	Ferromagnetic	[28]
(Ga,Fe)N	10	p-GaN	Implantation		700-900	>350	Ferromagnetic	[29]
(Ga,Mn)N	7	4H-SiC (0001)	MBE	710			Spin-glass	[30]
(Ga,Co,V)	3 - 5	p-GaN	Ion	350	5 min at		V:	[31]

N			implantation		700		paramagnetic, Co: spin glass	
(Ga,Cr)N	3 - 5	p-GaN	Ion implantation	350	5 min at 700	>300	Ferromagnetic	[31]
(Ga,Mn)N	1 – 3	p-GaN	Ion implantation	350	5 min at 700	>300	Ferromagnetic	[32]

The search for a new DMS was given a jump-start in 2000 after theoretical predictions made by Dietl *et al.* [16]. His calculations based on the Zener mean field model of ferromagnetism predicted above RT T_C in wide band gap semiconductors; such as 5 % Mn doped p-type GaN and p-ZnO with acceptor concentrations of 3.5 x 10^{20} cm^{-3}. This discovery has triggered a great experimental and theoretical activity aiming to understand the properties of these materials. Das *et al.* [33] showed by first-principle calculations that Cr-doped GaN can also be ferromagnetic with T_C as high as 900 K which was also observed experimentally [34]. In the case of Mn-doped GaN a formation of ferromagnetic secondary phases, such as Mn_4N [35], Mn_3GaN [36] and Mn_2Ga [37] have to be taken into consideration. As a result, some report on RTFM [38], while others have concluded that material is paramagnetic [39]. The question is whether the material is intrinsically ferromagnetic or it is GaN with clusters, precipitates or secondary phases that are responsible for the observed magnetic properties. List of recently reported magnetic properties of GaN-based DMS is presented in Table 1.1.

1.4.3. Metal oxide based DMS

The theoretical prediction and observation of RT ferromagnetism in oxides doped with transition metals is one of the most interesting and provocative scientific developments of the early 21st century. In fact, one of the 125 critical unanswered scientific questions posted in Science magazine asks: *"Is it possible to create diluted magnetic semiconductors that work at room temperature?"* [40]

Recently several oxide-based DMS have received much attention. In particular the Co-doped TiO_2 system received much attention after Matsumoto *et al.* [41] first reported ferromagnetism with $T_C \sim$ 650K. Following theoretical prediction by Dietl *et al.* [16] a lot of work was also focused on ZnO based system. Many researchers have grown

ZnO doped with the entire series of 3d transition metal atoms (Sc, V, Cr, Mn, Fe, Co, Ni and Cu) and rare earth elements that have partially filled f states (Eu, Gd, Er). Some of them reported high RT ferromagnetism [42, 43], while others report observation of paramagnetic or spin-glass behavior in their films [44].

Recently, reviews have also appeared on experimental status of SnO_2, Cu_2O and In_2O_3. In_2O_3 became another intensively studied transparent oxide after discovery of RT ferromagnetism in Cr-doped In_2O_3 observed by Philip *et al.* [45]. A summary of different types of oxide DMS is given in the Table 1.2.

Table 1.2 Summary of the magnetic properties of the oxide-based DMS

Compound	**TM content, (%)**	**Substrate (or bulk)**	**Fabrication method**	**Growth temperature (°C)**	**Post annealing**	**T_C, (K)**	**Notes**	**Reference**
ZnO:Mn	36	c-sapphire	PLD	600		N/A	Spin-glass	[46]
ZnO:Co	3-5	c-sapphire	PLD	300-700		N/A	Spin-glass	[47]
ZnO:(Co,Fe)	<15	SiO_2/Si	Magnetron sputtering	600	600, for 10 min. in vac.	>300	Ferromagnetic	[48]
ZnO:Co	3-5	Bulk	Ion implantation		700,5 min. under O_2	>300	Co precipitates	[49]
Anatase TiO_2:Co	<8	$LaAlO_3$, $SrTiO_3$	PLD	677-727		>400	Ferromagnetic	[41]
Rutile TiO_2:Co	5	r-sapphire	PLD	700		>400	Ferromagnetic	[50]
Anatatse TiO_2Co	3-12	SiO_2/Si	MOCVD	400-500	700, 1h in vacuum	>300	Ferromagnetic	[51]
Anatase TiO_2:Co	4	$SrTiO_3$	PLD	600			Co metal clusters	[52]
Cu_2O:Mn	5	$MgAl_2O_4$	PLD	300-700		48	Mn_3O_4 precipitates	[53]
SnO_2:Co	5	r-sapphire	PLD	700		650	Ferromagnetic	[54]
SnO_2:(Mn,Sb)	5-34	r-sapphire	PLD	300-600		N/A	Paramagnetic	[55]

It is very important to distinguish true ferromagnetic semiconductor from those semiconductors, which merely show magnetic properties. These weak magnetic properties could come from phase separation leading to magnetic secondary phase formation. Table 1.3 shows some potential second phases which could form during the growth of transition metal doped DMS. Nonmagnetic semiconductors with the presence of ferromagnetic secondary phases my also exhibit an anomalous Hall effect, indicating an internal magnetic force on free carriers [56, 57], however, any spin polarization in the majority carrier band is not controllable in a way is useful in spintronic devices. Thus, such materials might be referred to as semiconductors, which are ferromagnetic, which is different from true ferromagnetic semiconductors. Failing to distinguish between these two different classes of materials has led to a lot of confusion in a field of DMS.

Table 1.3 Potential magnetic phases observed in transition metal doped oxide DMS

Phase	Nature of magnetism	Curie temperature (T_c) or Neel temperature (T_N), K	Reference
Co	Ferromagnetic	1373	[49]
Cr	Antiferromagnetic	311	[58]
Fe	Ferromagnetic	1040	[58]
Mn	Antiferromagnetic	100	[58]
Ni	Ferromagnetic	627	[58]
Cu clusters	Antiferromagnetic	154	[59]
CoO	Antiferromagnetic	291	[44, 60]
MnO	Antiferromagnetic	116	[61]
MnO_2	Antiferromagnetic	92	[62]
Mn_2O_3	Antiferromagnetic	76	[62]
Mn_3O_4	Ferromagnetic	43	[62]
Mn_3O_4 (hausmanitte)	Ferrimagnetic	40	[63]
CuO	Antiferromagnetic	230	[59]
(Zn,Mn)Mn_2O_4	Ferrimagnetic	40	[64]
$ZnFe_2O_4$ (invert spinel)	Ferromagnetic		[65]
$(Zn,Fe)_3O_4$	Ferromagnetic	440	[44]

In the next chapters a detailed review on recent status in the field of ZnO and In_2O_3 based DMS will be presented.

1.4.3.1. ZnO based DMS

ZnO occurs in nature as the mineral zincite. ZnO crystallises in a hexagonal wurtzite structure shown in Figure 1.7. The zinc atoms are nearly in the position of hexagonal close packing. Every oxygen atom lies within a tetrahedral group of four zinc atoms. The wurtzite lattice constants of ZnO are $a=3.24$ *Å* and $c=5.19$ *Å*.

Amongst the most important characteristics of ZnO is the large band gap of *3.37eV* at room temperature, a unique combination of piezoelectric, conducting, thermal and optical properties. ZnO has electron n-type conductivity naturally (due to oxygen vacancies), but p-type conductivity can also be induced. Until now the most commonly employed techniques for the growth of ZnO films were PLD, MBE, magnetron sputtering and MOCVD.

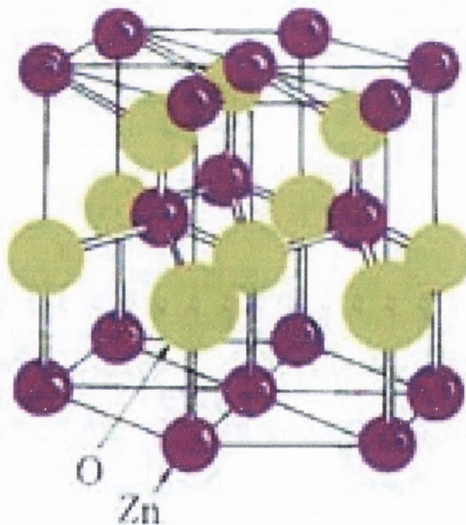

Fig. 1.7 Crystal structure of ZnO [66]

The search for novel magnetic materials, with ideally large spin polarization, high T_C has triggered an intense activity on doping nonmagnetic semiconducting oxides with magnetic ions. The choice of oxide was motivated by the prediction by Dietl *et al.* in Mn-doped ZnO with T_C above 300K. ZnO is a particularly promising candidate for the

application of spinronics, due to its long spin lifetime [67]. Also, spintronics applications based on ZnO would benefit from the use of ZnO in optoelectronic devices. Although, theoretical predictions suggested room temperature ferromagnetism in p-type doped ZnO, unfortunately realisation of p-type ZnO is quite difficult. Following Dietl's work, Sato *et al.* performed an ab initio calculations and found ferromagnetism in n-type ZnO doped with the entire series of transition metal ions, such as Co, Cr, Fe, Ni, V, but predicted no ferromagnetism for Mn doped ZnO [68]. These predictions are consistent with experimental results, where ferromagnetism is not observed in n-type Mn- doped ZnO. As for example, in the first experiment on Mn-doped ZnO performed by Fukumura *et al.* [46] where an antiferromagnetic behaviour was indicated for ZnO films doped with 36 % Mn using PLD technique. However, ferromagnetism is observed in Sn implanted n-type Mn-doped ZnO. Although, it is not clear what role the Sn dopant plays in enabling ferromagnetism in Mn-doped ZnO. Han *et al.* [64] observed ferromagnetic behaviour in polycrystalline Mn-doped ZnO films prepared by solid state reaction. It was later concluded that $(Zn,Mn)Mn_2O_4$ is responsible for the observed ferromagnetic transition. The bulk sample of Mn-doped ZnO without second phase precipitate showed paramagnetic bechaviour. In contrast to these results ferromagnetism has also been observed in Mn-doped ZnO. For example, Jung *et al.* [61] observed ferromagnetism in MBE grown ZnO films doped with 10 % and 30 % Mn, although T_C was only 30 and 45 K for 10 % and 30 % Mn doped samples respectively. Kim *et al.* [69] also reported T_C = 30-40 K for 10 and 30% Mn-doped ZnO, deposited on Si substrate by sol-gel. The equilibrium solubility limit of Mn in ZnO has been determined to be ~ 13 % [70]. However, due to the non-equilibrium nature of the different thin film growth techniques, solubility of up to ~ 35 % have been obtained, while maintaining wurtzite structure [46, 61, 71-74]. After conducting numerous experiments it was found that lower Mn dopant concentrations lead to better magnetic properties. While ferromagnetic ordering has been reported for Mn concentrations between 2.2 and 30 % [42, 43, 61, 75], both the magnetic moment per Mn ion and the ferromagnetic T_C seems to decrease with increasing Mn concentration.

The substrate temperature during the growth and the annealing temperature have a significant influence on the magnetic interactions. It was generally observed that lower

temperatures, typically ≤ 400 °C, seem to be favourable of obtaining ferromagnetic samples [42, 61, 75, 76], which turned paramagnetic after annealing at higher temperatures.

Oxygen partial pressure is believed to have crucial influence on magnetic properties of magnetically doped ZnO films. A low oxygen partial pressure favours the formation of oxygen vacancies that dope the system with electrons. Although, it has been recently proposed that oxygen vacancies might stabilize a secondary ferromagnetic phase of ZnMnO [77].

First experimental work on Co-doped ZnO was carried out by Ueda *et al.* [60]. He used PLD to grow ZnO doped with Co, Mn, Cr and Ni. Only Co-doped ZnO was found to be ferromagnetic with T_C of ~ 280- 300 K, however reproducibility in the ferromagnetism was less than 10 %. The possibility of formation of magnetic secondary phases could not be ruled out as only X-ray diffraction (XRD) was used to characterise the films. XRD is known to be quite insensitive to the secondary phases.

Following this report thin Co-doped ZnO films have been grown by different groups and using various growth techniques like: PLD [47, 78-81], magnetron sputtering [82, 83], sol-gel [84] and others.

Different thermal solubility of Co in ZnO was reported. Prellier *et al.* [79] found that solubility limit in his PLD grown samples is 10 %. Park *et al.* [85] observed the formation of Co nanoclusters for the concentrations more than 12 % in samples grown by sol-gel and rf magnetron sputtering techniques. In other report [84] formation of Co_3O_4 phase was observed for dopant concentrations above 25 %.

The influences of substrate temperature and oxygen pressure were studied in [47]. It was concluded that films deposited at lower temperature (≤ 600 °C) and higher oxygen pressure (≥ 10^{-5} Torr) had a homogeneous distribution of Co. Secondary phases formed at higher temperature and lower oxygen pressure. As for magnetic properties, the films grown at lower temperature were paramagnetic. At higher temperatures mixed phases of wurtzite ZnO, rock salt CoO and hexagonal Co phases formed and ferromagnetism was observed.

The presence of a magnetic moment in Co-doped ZnO was confirmed by several groups [48, 49, 79, 80, 84], but without any consistency in a magnitude of magnetic moments.

The measured values of saturation magnetisation spread over a wide range, from 0.56 μ_B/Co [84] to 2.6 μ_B/Co [78].

These controversial results raise questions about the origin and the intrinsic nature of ferromagnetism in Co doped ZnO. While the origin of the ferromagnetic phase is well established for most of the semiconductors ($Ga_{1-x}Mn_xAs$ [86], $Zn_{1-x}Mn_xTe$ [87], Mn_xGe_{1-x} [88]), it is still debated for Co-doped ZnO. The question of whether the Co-doped ZnO really is a high temperature magnetic semiconductor remains open. It may be that n-type carriers associated with lattice defects play a critical role in ferromagnetism. To avoid antiferromagnetic ordering, the concentration of magnetic cations 'x' must lie below the cation nearest neighbour percolation threshold x_c, which is $\approx$ 0.17 for the wurtzite structure [78].

In addition to the large number of experiments focused on Mn and Co-doped ZnO there have been numerous reports on V [74, 78, 89], Cr [60, 78, 90], Fe [48, 60, 74, 78] and Ni [60, 74, 78] doped ZnO films. Table 1.4 summarizes published reports of magnetism in a transition metal doped ZnO.

Table 1.4 Summary of reported magnetic properties of ZnO based DMS.

Compound	TM content, (%)	Substrate (or bulk)	Fabrication method	Growth temperature (°C)	Post annealing Temperature (°C)	T_C, (K)	Notes	Reference
ZnO:Mn	<35	c-sapphire	PLD	600		N/A		[91]
ZnO:Mn	36	c-sapphire	PLD	600		N/A	Spin-glass	[46]
ZnO:Mn	1-36	c-sapphire	PLD	610			Paramagnetic	[72]
ZnO:Mn	0-30	c-sapphire	PLD	600		>30-45	Ferromagnetic	[61]
ZnO:Mn	<4	Bulk	Sintered	500-700		>425	Ferromagnetic	[42]
ZnO:Mn	2.21	Fused quartz	pellets PLD	400		>425	Ferromagnetic	[42]
ZnO:Mn	4-9	c-sapphire		200-380		>400	Ferromagnetic	[92]
ZnO:Mn	7	a-sapphire,	Reactive sputtering	400			Paramagnetic	[93]
ZnO:Mn	3; 20	GaAs (001)	Sputtering	500-600				[43]
ZnO:Mn,Sn	0-30	Bulk	Sputtering Implantation		700,5 min. RTA in N_2	250	Ferromagnetic	[94]
ZnO:Mn,Sn	Mn 30,	c-sapphire	PLD	400-600		>300	Ferromagnetic	[95]

	Sn<1							
ZnO:Co (Mn,Cr, or Ni)	5-25	c-sapphire	PLD	350-600		280-300	Co: Ferromagnetic	[60]
ZnO:(Mn,Co)	2-15		Crystalline precursor			N/A	Antiferromagnetic	[96]
ZnO:(Mn,Co)	<5		Melt growth		700, 5 min in O_2	N/A	Paramagnetic	[97]
ZnO:Co	3-5	Bulk ZnO	Ion implantation		RTA 700, 1min in O_2		Co nanocrystals	[49]
ZnO:Co	0-25	c-sapphire	Sol-gel	<350		>350	Ferromagnetic	[84]
ZnO:Co	1.5	c-sapphire	PLD	650		>300	Ferromagnetic	[80]
ZnO:Co,Al	4-12	Glass	Rf sputtering			>350	Ferromagnetic	[83]
ZnO:Co	2-50	c-sapphire	PLD	300-700			Spin-glass	[47]
ZnO:Co	10	ZnO	PLD				Antiferromagnetic	[98]
ZnO:Co	<35	r-sapphire	MOCVD	300-650	500, 20 min in vacuum	>350	Ferromagnetic	[99]
ZnO:Co,Fe	<15	SiO_2/Si	Magnetron sputtering	600		>300	Ferromagnetic	[48]
ZnO:Cu,Fe	Fe<7 Cu<1	Bulk	Solid state Reaction	897	600, 10min at 10^{-5} torr	550	Ferromagnetic	[100]
ZnO:Ni	1-25	c-sapphire	PLD	300-700			Super para- or ferromagnetic	[101]
ZnO:V	5-15	r-sapphire	PLD	300			Ferromagnetic	[89]
ZnO:Mn	10	r-sapphire	PLD	650		>350	Ferromagnetic	[102]
ZnO:Mn,Cu	Mn: 10, Cu:5	r-sapphire	PLD	650		400	Ferromagnetic	[102]
ZnO: Sc,Ti,(V,Fe, Co,Ni)	5	r-sapphire	PLD	600		>300	Ferromagnetic	[78]

As seen from Table 4, work on magnetically doped ZnO has resulted in a range of different results. This controversy could rise due to the range of growth methods and

conditions and inadequate material characterisation. In order to get a clear picture, well characterised magnetically doped oxides of high structural quality must be prepared and carefully studied.

1.4.3.2. In_2O_3 based DMS

In_2O_3 is n-type transparent semiconducting oxide material with a wide band gap of ~ 3.6 eV. In general, undoped In_2O_3 films are insulators in the stoichiometric form. The conductivity of pure oxide layers can be improved to the level of doped layers (such as highly conducting Sn-doped In_2O_3) by controlling the density of oxygen vacancies, each of which donate two electrons to the conduction band. In_2O_3 occurs in two crystal structures: body-centered cubic, with a = 10.118 Å and rhombohedral, with a = 5.478 Å and c = 14.51 Å [103]. All deposited In_2O_3 films show cubic crystal structure, with only few exceptions being reported on rhombohedral In_2O_3 [104].

In_2O_3 is very important material for microelectronic applications. It is widely used for transparent electrodes in electronic devices, such as liquid crystal displays [105], solar cells [106], and barrier layer in tunnel junctions [107], as a sensing material in gas sensors [108] and in nanowire technology [109]. Since In_2O_3 is so widely used in semiconductor industries, it should be a good challenge to achieve FM in this oxide.

In_2O_3 films have been prepared using various deposition techniques like vacuum evaporation [110, 111], sputtering [107, 112, 113], spray pyrolysis [114-116], atomic layer deposition [117], thermal oxidation [118], ion assisted deposition [119], PLD [120-122], ultrasonic CVD [123] and sol-gel [124]. MOCVD was also successfully used for the deposition of In_2O_3 [125].

Magnetism was first reported in thin In_2O_3 films in 1999 by Zhang *et al.* [126] for granular films of Fe clusters in In_2O_3 matrix. The Fe formed clusters in the material, which were superparamagnetic at room temperature and ferromagnetic below 50K.

Later Shim et al. observed ferromagnetism in Mn and Fe-doped In_2O_3 films, prepared by sol-gel process [127]. No ferromagnetism was observed for Co dopant.

In 2005 Yoo et al. [128] presented evidence of room temperature ferromagnetism in Cu co-doped $(In_{1-x}Fe_x)O_3$ bulk samples. Solubility of Fe was up to 20% in the host In_2O_3. A high magnetic moment of up to ~ 6 μ_B was reported for this system. From XRD and TEM only small amounts, about 1% of Fe_3O_4 impurity phase for dopant concentrations

above 10% were observed. Authors claim that impurity phases such as Fe_3O_4 or $CuFe_2O_4$ are not responsible for the observed moment, as T_C of 750 K differs slightly from two possible impurity phases.

This report was soon followed by experiment of He *et al.* [65] with discovery of room temperature ferromagnetism in 2% Cu co-doped $(In_{1-x}Fe_x)O_3$ (x = 0.1 and 0.15). The films also had T_C = 750 K and exhibited an anomalous Hall effect. The resistivity of the films was $\rho \approx 6 \times 10^{-3}$ Ωcm and a carrier concentration of $n \approx 5 \times 10^{-19}$ cm^{-3}.

Later Brize *et al.* [129] exploited Mn and Cu for substitution of In in In_2O_3 grown on MgO substrates by PLD. The authors found that Mn doping does not bring any enhancement to the ferromagnetism of the In_2O_3 films and Cu doping degrades enormously the magnetic ordering of the films.

Peleckis *et al.* observed room temperature ferromagnetism in Fe and Mn co-doped In_2O_3 samples prepared by solid state reaction [130]. In contrast to the already reported data [128], only the Fe only doped sample was paramagnetic at room temperature. The Mn only doped sample was ferromagnetic below T_C = 46 K. Fe and Mn co-doped samples were ferromagnetic at room temperature with maximum saturation moment of 0.35 μ_B/ (Fe+Mn) and 0.98 μ_B/ (Fe+Mn) at 300 and 10 K, respectively, for dopant concentrations 4% of Fe and 6 % of Mn. High temperature ferromagnetism was also observed by the same group in Ni-doped In_2O_3 and Ni, Sn co-doped In_2O_3 [131] with the magnetic moments of 0.03 – 0.06 μ_B/Ni and 0.1 μ_B/Ni at 300 and 10K, respectively. Enhanced room temperature ferromagnetism was also observed in polycrystalline $(In_{0.9}Fe_{0.1-x}Ni_x)_2O_3$ samples [132] with magnetic moments of 0.28 μ_B/ (Fe+Ni), 0.453 μ_B/ (Fe+Ni) and 0.442 μ_B/ (Fe+Ni) for x = 0.02, 0.04, 0.06, respectively, which is much higher as compared to [131]. Hong *et al.* [133] have doped In_2O_3 with a range of transition metals (V, Cr, Fe, Co and Ni) and found them all to be ferromagnetic at room temperature (Fig. 1.8). In addition, same author also observed room temperature ferromagnetism in undoped In_2O_3 when deposited on MgO substrates [134].

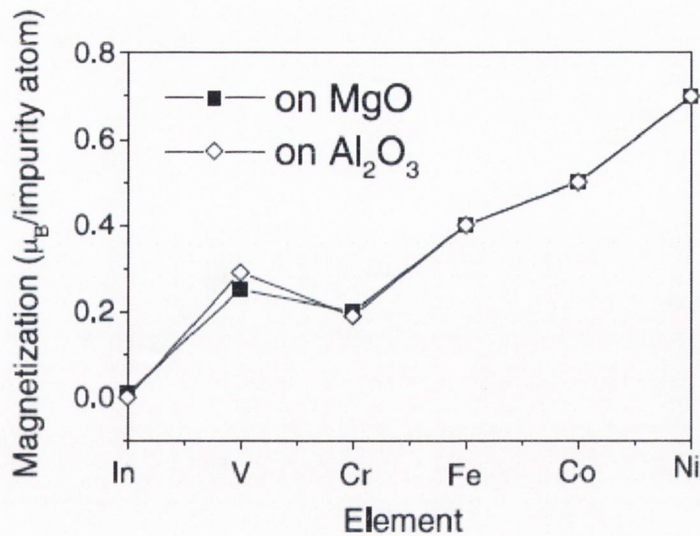

Fig. 1.8 Magnetic moment of In_2O_3 films doped with different transition metals expressed in μ_B / dopant metal, after [133].

The search for an ideal magnetic semiconductor with high T_C and tunable ferromagnetic behaviour over a wide range of doping is crucial for developing spin-based devices. Recently, J. Philipp *et al.* [45] found a set of unique properties in Cr-doped In_2O_3 prepared by reactive sputtering. Authors observed that In_2O_3 films doped with 2 % Cr exhibit room temperature ferromagnetism with T_C of up to 850-930K. Most importantly, both the electronic and magnetic phases of the films can be controllably tuned by the oxygen defect concentration. By changing oxygen partial pressure during the growth of the films it was found that ferromagnetic metallic phase is observed when the films are highly oxygen deficient, whereas reducing the defect concentration results in the ferromagnetic semiconducting state. Nearly stoichiometric films showed a paramagnetic insulating phase. Another advantage of this system is that Cr has a large magnetic moment in the ionic state and it is antiferromagnetic in the bulk, thus ruling out the ferromagnetism if Cr metal segregation occurs. In addition, it is not trivial to form any ferromagnetic secondary phases of Cr oxide. Soon after this report P. Kharel *et al.* [135] have also prepared Cr-doped In_2O_3 both in thin film and bulk forms using sol-gel. Similar to J. Philipp *et al.* [45] room temperature ferromagnetism was observed in both samples but only after vacuum annealing, suggesting a carrier mediated model for the

ferromagnetism, in which the ferromagnetism is produced by n-type carriers that arise from oxygen vacancies in the samples.

Cr was also used to dope Sn-doped In_2O_3 (ITO) up to 20% without formation of secondary phases confirmed by XRD and high resolution TEM [136]. PLD grown films were room temperature ferromagnetic and semiconducting with conductivity changing from n-type to p-type at about 15% mol Cr doping. Authors claimed that observation of anomalous Hall effect proved intrinsic nature of carrier mediated ferromagnetism in Cr-doped ITO films.

Other 3d metals like Fe [137], Co [138] and Mn [139] were also used to dope into ITO. For the Mn and Co doping films were found to be room temperature ferromagnetic and exhibited anomalous Hall effect. Although, in the case of Co dopant there is an evidence that two magnetic subsystems, interacting nanoclusters (of Co metal and Co-rich ITO) and a ferromagnetic matrix are present in ITO films doped with 30 atomic % of Co. Doping of Fe into ITO films have resulted in magnetic and electric properties which systematically varied with oxygen partial pressure . PLD grown films were paramagnetic and semiconducting at 1 and 5 Pa, ferromagnetic and semiconducting at 10^{-1} Pa and ferromagnetic and metallic at 10^{-2} and 10^{-3} Pa. These results are similar to those reported in [135] and [45].

1.5. Other magnetic oxides

Another spintronic effect which gave rise to a large number of experimental and theoretical studies is well known as TMR. Large TMR effects were obtained when using special magnetic materials (the so called half-metals). Half metals have a finite density of states at a Fermi level for one spin direction and a gap for the other spin direction. Many materials that were believed to have this unusual electronic structure were magnetic oxides. For example, CrO_2 was found to be one of the materials having electrons of a single spin at the Fermi energy with polarisation values in the range of 85-100% by electronic structure diagrams of Goodenough [140]. Half metallic character was also found in double-exchange oxides such as Fe_3O_4 in 1984 [141] and manganites in 1996 [142]. Positive spin polarisation of 90 % was reported for manganites [143] and a maximum TMR of 83 % found in $La_{2/3}Sr_{1/3}MnO_3/SrTiO_3/La_{2/3}Sr_{1/3}MnO_3$ MJTs. This discovery has

triggered an active research on magnetic oxides and oxide tunnel junctions in order to get high TMR effects.

Many of known half-metals have a low T_C, thus can not be used in practical devices as spin polarisation declines with temperature. To achieve a typical operating temperature range of – 50 to 120° C, it is necessary to have a T_C in excess of 500 K. The one half-metal which actually meets this requirement is Fe_3O_4.

1.5.1. Fe_3O_4

Magnetite is one of the oldest known magnetic materials. It is ferrimagnetic with a T_C of 858K. Fe_3O_4 crystallises in the spinel structure whose tetrahedral A sites are occupied by Fe^{3+} ions and octahedral B sites by a mixture of Fe^{2+} and Fe^{3+} ions. As in most spinel ferrites the ferromagnetism arises from the strong antiferromagnetic coupling between the A and B sublattices. Within the B sublattice the Fe ions are coupled ferromagnetically. This gives a net spin moment of 4 μ_B per formula, since Fe^{3+} ($3d^5$) and Fe^{2+} ($3d^6$) have spin moments of 5 μ_B and 4 μ_B, respectively.

At room temperature Fe_3O_4 is a bad conductor. It was reported [144] that metallic behaviour occurs in the temperature range of ~ 300 – 800K. Below room temperature, the resistivity is thermally activated with a transition to a charge-ordered insulating state occurring below the Verwey transition temperature ($T_V \approx 120$K).

Many groups were growing Fe_3O_4 by a large number of deposition techniques such as sputtering [145], MBE [146] and PLD [147]. Magnetic properties of thin Fe_3O_4 films are usually different from those of the bulk. It was found that magnetisation is often lower and harder to saturate [145, 148]. Films usually have higher electrical resistivity and sometimes show a disappearance of Verwey transition [149, 150].

Spin polarisation of Fe_3O_4 was measured by spin-polarised photoemission spectroscopy and is found to be negative, ranging from – 40% to – 80% [151, 152]. Although, spin-polarisation values found from spin-dependent tunnelling experiments are very different. Positive polarisation of up to 50 % was found in TMR experiments [153-155] but negative was also observed [156].

Other spintronics devices based on Fe_3O_4 have also been fabricated, these include magnetic tunnel transistors with a magnetite emitter [157] and current-in-plane GMR structures [158, 159].

There have been limited efforts to integrate Fe_3O_4 into semiconductor structures in order to fabricate devices that would exploit its spintronics properties [160-163]. The surface and interface properties of Fe_3O_4 are still under investigation to understand spin-polarisation measurements. So far, the potential of Fe_3O_4 for spintronic devices has not been exploited.

1.5.2. $CoFe_2O_4$

$CoFe_2O_4$ is a ferrimagnet and belongs to the spinel structure ferrite materials. It crystallises in the same inverse cubic spinel structure as Fe_3O_4 in which the octahedral B sites are occupied by eight Co^{2+} and eight Fe^{2+} cations, while the tetrahedral A sites are occupied by eight Fe^{3+}. Co^{2+} ions on the B sites give rise to large anisotropies [148]. Although, $CoFe_2O_4$ has the same crystal structure as Fe_3O_4 it is a hard magnetic material with a saturated magnetic moment of 3.7 μ_B per formula.

High coercivety, good chemical stability, high resistance, relatively high saturation magnetisation of $CoFe_2O_4$ has found various magnetic applications such as magnetic recording and magneto-optical devices [164, 165].

Recently, $CoFe_2O_4$ has been studied as a potential magnetic candidate for multiferroic composites fabricated in bulk composites, polycrystalline bilayers or multilayers [166-169].

Multiferroics is a new family of materials in the field of spintronics. These are multifunctional materials with two or more ferroic properties like ferromagnetic, ferroelectric, ferroelastic or ferrotoroidic. For example, magnetoelectric multiferroics in which ferromagnetic and ferroelectric orders coexist with magnetoelectric coupling between them open the possibility of controlling the polarisation by a magnetic field or the magnetisation by an electric field [170]. An extrinsic magnetoelectric effect has been observed in the bulk multiferroic composites consisting of ferroelectric $BaTiO_3$ and piezomagnetic $CoFe_2O_4$ [171].

1.5.3. Co_3O_4

Co forms two stable oxides: CoO and Co_3O_4. Co_3O_4 is stable at lower temperatures and has a normal spinel structure (AB_2O_4 type) where Co^{2+} occupy the tetrahedral *A* sites and Co^{3+} occupy the octahedral *B* sites.

Co oxide based ceramics have attractive magnetic properties and their films and multilayers have been studied for decades and still motivate research and development efforts [172]. Coatings of Co_3O_4 can be used as solar-selective absorbers and as protective layers [173]. Thin films of Co_3O_4 may be useful as buffer layers on Si substrates for the oriented growth of functional ferroelectric and sureconducting oxides [173]. More recently, Co_3O_4 have been studied in the context of next generation of Li-ion batteries [173]. The phenomenon of anodic electrochromism of cobalt oxide allows potential application as a counter electrode in electrochromic devices [174].

We plan to deposit cobalt oxide films and to study their structure, morphology and magnetic response. We also plan to demonstrate the potential of PI MOCVD equipped with external magnet as an alternative technique to film deposition methods.

1.5.4. Mn_3O_4

Hausmannite, Mn_3O_4 is known to crystallise in the normal spinel structure with tetragonal distortion elongated along the *c*-axis, with lattice parameters $a = b = 5.765$Å and c = 9.442Å. Manganese ions are placed on the tetrahedral *A*-site (Mn^{2+}) and octahedral *B*-site (Mn^{3+}), which corresponds to the normal spinel structure. The oxygen octahedra are tetragonally distorted due to the Jahn-Teller effect on Mn^{3+} ions [175]. At 1160°C Mn_3O_4 experiences Jahn-Teller transition (JTT) [176]. This is the first order phase transition accompanied by the significant lattice distortion. Above this temperature the structure becomes cubic. Also, Mn_3O_4 shows ferromagnetic long-range order when the temperature is below the T_C (46K).

The stable and well-known Mn oxides are MnO, Mn_3O_4, Mn_2O_3 and MnO_2. Their magnetic, transport and optical properties are closely related to their structures, crystalline quality and stoichiometry [177]. Manganese oxides are of great interest due to their wide applications in electrode and alloy materials [178]. Furthermore, if structural and

physical properties of the films could be controlled well, it would be possible to fabricate multilayer Mn oxides with different structures and properties, such as ferromagnetic and antiferromagnetic behaviours. These have potential applications in magnetic storage and sensor devices [178].

Most of the studies on magnetic properties of Mn_3O_4 have been performed on the bulk samples [177]. On the other hand, the properties of the thin films can be essentially different from those of the bulk due to the strain effects. Moreover, there is very little information on magnetic properties of Mn_3O_4 films. In this work we plan to adopt PI MOCVD technique to grow thin films of Mn_3O_4 and to study their magnetization and phase transition temperature, as well as the effects of interface and crystal quality on magnetization.

1.6. CVD

One of the best methods to produce multicomponent epitaxial oxides is chemical vapour deposition (CVD). The industrial exploitation of CVD can be traced back to a patent by de Lodyguine in 1883 who had deposited W onto carbon lamp filaments through the reduction of WCl_2 by H_2. However, it is only in the past 40 years that a considerable in-depth understanding of the process and an increase in the application of CVD has been made. In the early 70s CVD had attained significant success in the manufacturing of electronic semiconductors and protective coatings for electronic circuits. Today CVD technology has found increasing importance in the fields of aerospace, military, science and engineering. It is well suited for the preparation of many advanced products, including bulk materials, as well as composites, coatings and films.

In CVD the substrates are immersed in the gas stream and so-called boundary layer are developed near the substrate surface. The boundary layers are defined as the region near the substrate surface where the gas stream velocity, the concentration of the vapour species and the temperature are not equal to those in the main gas stream.

In general, the CVD process involves the following key steps. Each of these steps may be rate-limiting in the absence of thermodynamic limitations. The plausible rate-limiting steps are as follows:

1) Transport of the gaseous reactants to the boundary layer surrounding the substrate (free and forced convection)
2) Transport of the gaseous reactants across the boundary layer to the surface of the substrate (diffusion and convection)
3) Adsorption of the reactants on the surface of the substrate
4) Chemical reactions (Gaseous reactants undergo gas phase reaction and form intermediate species, for example at high temperature above the decomposition temperature of intermediate species inside the reactor, homogeneous gas phase reaction can occur where the intermediate species undergo decomposition and/ or chemical reaction forming powders and volatile by-products in the gas phase. In the other case, at temperatures below the dissociation of the intermediate phase, diffusion/convection of the intermediate species across the boundary layer occur, which undergo further steps).
5) Nucleation
6) Desorption of some of the reaction products from the surface of the substrate
7) Transport of the reaction products across boundary layer to the bulk gas mixture
8) Transport of the reaction products away from the boundary layer

The described process is very well illustrated in the below figure:

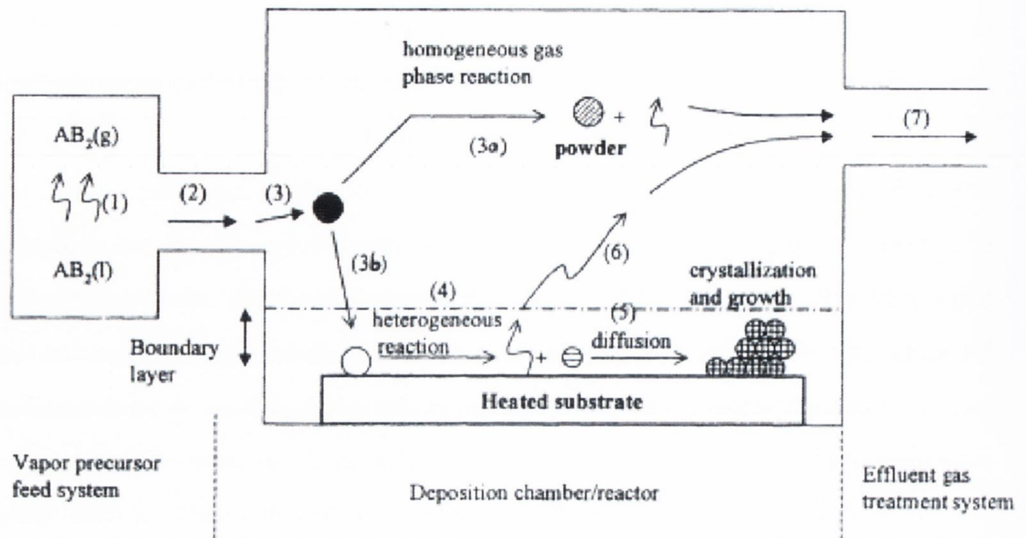

Fig. 1.9 Schematic illustration of the key CVD steps during deposition[179]

The analysis of the CVD processes includes the understanding of the thermodynamics, chemical kinetics and mass transport phenomena. However, thermodynamic calculations only provide basic information as to whatever a process is feasible or not. In addition, thermodynamics can provide guidelines for selecting process conditions based on the equilibrium analysis of the phases and the amount of the solid and gaseous species present in the CVD system. A more precise and accurate analysis of the CVD reactor system requires the consideration of the chemical kinetics and mass transport phenomena.

The kinetics of a CVD process involves chemical reactions in the gas phase, on the substrate surface, chemisorption and desorption.

The rate of mass transport is dependent on the concentration of reactants, thickness of the boundary layer, diffusivity of active species. These factors are influenced by the deposition temperature, pressure, gas flow rate, and geometry of the reactor.

A well-established model for thermal oxide growth has been proposed by Deal and Grove[180] in the middle of the 60's and because of its simplicity it is still applied frequently. One reason for this simplicity is that the whole physics of the oxidation process is contained in two so-called Deal-Grove parameters, which must be extracted

from experiments. Furthermore, it is assumed that the structure is one-dimensional. Therefore, the model can only be applied to oxide films grown on plane substrates. Grove's model is a simplified approach to predict the growth rate of films, which assumes that reaction rate flux depends linearly on the surface concentration. The model also neglects the effect of any temperature gradients on the gas phase mass transfer.

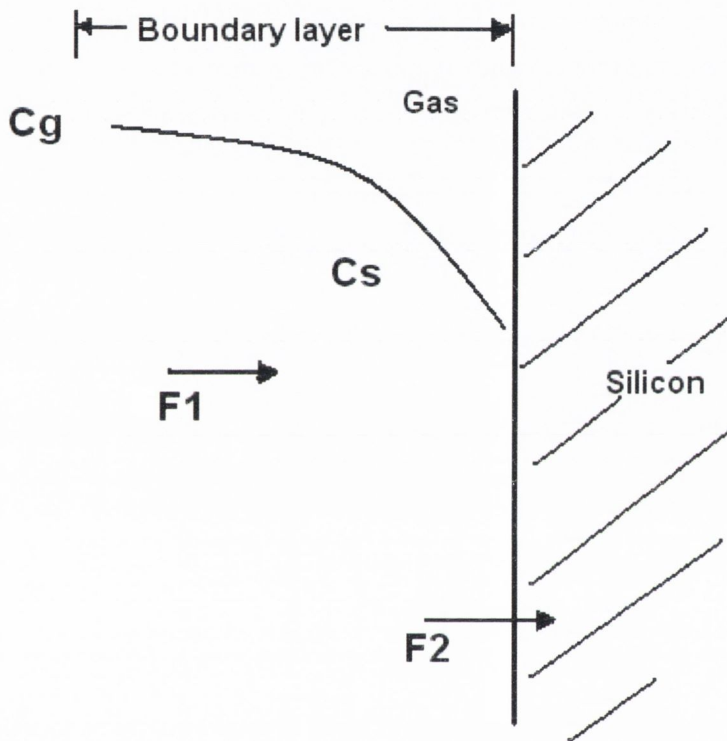

Fig. 1.10 One-dimensional model of oxidation of silicon

If one assumes that the oxidation process is dominated by the inward movement of the oxidant species, the transported species must go through the following stages:

(1) It is transported from the bulk of the oxidizing gas to the outer surface of oxide, where it is adsorbed (not shown in the figure)

(2) It is transported across the oxide film towards silicon.

(3) It reacts at the interface with silicon and forms a new layer of SiO_2.

Each of these steps can be described as independent flux equation. The flux F_1 represents the diffusion of the oxidants through the oxide layer to the Si-SiO_2 interface, which can be expressed as:

$$F_1 = h_G(C_G - C_S) \tag{15}$$

where h_G is the mass transfer coefficient expressed in cm/sec, C_G is the oxidant concentration near oxide surface at any give time, C_S is the oxidant concentration at the oxide-silicon interface.

The second part of the oxidation process is the flux of oxidants consumed by the xidation reaction at the oxide-silicon interface given by:

$$F_2 = k_S C_S \tag{16}$$

where k_S as the surface reaction rate , expressed in cm/sec, constant, which represents a number of processes occurring at the Si/SiO_2 interface. These may include oxidant ($O^{2-} \rightarrow 2O$), Si-Si bond breaking, and/or Si-O bond formation. The rate at which this reaction takes place should be proportional to the oxidant concentration at the interface C_S.

In the steady conditions the fluxes are equal, which allows expressing them as:

$$F = F_1 = F_2 \tag{17}$$

Equating equations (15) and (16) leads to:

$$C_S = \frac{C_G}{1 + (\frac{k_S}{h_G})} \tag{18}$$

The rate of the oxide growth is proportional to the flux of oxidant molecules and given by:

$$V = \frac{F}{V} = \frac{k_S h_G}{k_S + h_G}(\frac{C_G}{N}) = \frac{k_S h_G}{k_S + h_G}(\frac{C_T}{N})Y \qquad (19)$$

where N is the number of atoms incorporated per unit volume in the films and Y is the mole fraction of the incorporating species.

From equation (19) one can see if mass transfer through gas boundary layer is fast, i.e. $k_S << h_G$, then surface reaction control is achieved, which is temperature sensitive process. When $k_S >> h_G$ the reaction rate is controlled by mass transport, or gas phase diffusion controlled case and not temperature sensitive.

The recent development of CVD variants, such as pulsed injection metal organic vapour deposition (PI MOCVD), electrostatic spray assisted vapour deposition (ESAVD), catalytic chemical vapour deposition (CCVD), low pressure chemical vapour deposition (LPCVP) have been enabled the deposition of multicomponent films with well-controlled stoichiometry and microstructure. The variation of CVD used in this work is known as pulsed injection metalorganic chemical vapour deposition (PI MOCVD). Metalorganic chemical vapour deposition (MOCVD) is a variant of CVD, which has been classified according to the use of metalorganics as precursor. During the deposition process the metalorganic precursors generally undergo decomposition or pyrolysis reactions. In general, metalorganic precursors have lower decomposition or prolysis temperatures than halides, hydrides or halohydrides, which are used in conventional CVD. Thus, enable MOCVD process to perform at a lower deposition temperature than conventional CVD.

MOCVD has been widely used to grow metal oxide films such as ferroelectric (e.g. $PbTiO_3$, $PbZrTiO_3$, $BaTiO_3$) [86, 181], semiconducting (e.g. ZnO) [87] and superconducting (e.g $YBa_2Cu_3O_x$) films [88]. However, the MOCVD of these films is still in its infancy and more suitable metalorganic precursors are yet to be developed for these applications. The influence of process parameters and the deposition mechanism in the oxidising growth environment are still to be understood and optimised.

The synthesis of high quality films requires volatile precursors that will undergo pyrolysis easily. However, the low thermal stability of the metalorganic precursors due to their polymerisation or hydrolysis changes the rate of evaporation with time. This has led to difficulties in controlling the composition of both the vapour phase and films. In addition, the low vapour pressure of some available precursors such as Ba, and earth elements, as well as 'ageing' of the precursors have led to the loss of volatility and formation of residue hence affecting the chemical reaction and resulting in coating reproducibility problems.

1.6.1. Pulsed Injection Metal Organic Chemical Vapour Deposition (PI MOCVD)

To overcome the problems mentioned above, in 1993 Senateur and his group developed a new PI MOCVD method. The main difference of this method from conventional MOCVD was new precursor delivery system. PI MOCVD uses fuel injection principles in thermal motors. The method involves sequential injection of micro amounts (mg) of a metal organic precursor solution into an evaporator through a high-speed microelectrovalve with aid of pressure inert gas inside a container, where the injected solution is flash vaporised. The flow rate is controlled by the fast opening of the valve similar to a fuel injection system. The control is relatively simple and versatile using two computer controlled parameters: injection frequency (1-100Hz) and electrical pulsed width (2-8ms) which controls the number of precursor drops injected with fixed injection parameters (size of each drop, frequency).

The distinct advantages of the pulsed injection MOCVD technique over conventional CVD technique are:

a) The thickness of the layer, coating stoichiometry and the growth rate can be controlled precisely by changing the concentration of the solution, number of pulses, pulse duration and injection frequency. This is especially important for the synthesis of superlattice and multilayers with complex stacking at a nanometer scale level. A mean thickness as low as 0.1 nm can be obtained at each injection by adjusting the valve opening time and solution concentration.

Complex multilayer stacking can be achieved by using few injection sources sequentially.

b) Reservoir with precursor solution is kept at room temperature outside the reactor. This helps to keep the metalorganic precursor stable for a longer time, until it is injected into the evaporation system.

c) Different metalorganic precursors can be used in the same solution. This is very convenient for the growing of multicomponent layers ($La_{1-x}Sr_xMnO_3$, $YBa_2Cu_3O_7$) or doping[182].

d) Reproducibility of the properties of the deposited layers is enhanced using the pulsed injection MOCVD.

A wide range of films can be deposited using the pulsed injection MOCVD method. This technique has the potential to produce integrated structures with different physical properties. For example $SrTiO_3/YBa_2Cu_3O_7$ double layer or $La_{1-x}Sr_xMnO_3/SrTiO_3/YBa_2Cu_3O_7$ trilayers [182], complex stacking of multilayers of crystallised Ta_2O_5/amorphous SiO_2 for optical guides, antireflective layer applications. The precise control of the growth behaviour enables this process to be used in the synthesis of nanometer thin multilayer or oxide superlattice materials for the development of improved piezoelectric actuators, IR detectors and non-volatile memories.

1.7. Aims and objectives of this work

It has been drawing research attention on transparent semiconducting oxides for a long time because of their application in many scientific and industrial areas, such as optical waveguides, conducting gas sensors, transparent conductive electrodes. Recently, transition metal doped semiconducting oxides received much attention after several reports of successful deposition of magnetic thin films [45, 60]. DMS materials, like (Zn,Co)O have a great potential for spintronic devices. The magnetic exchange interaction is these oxides predicted to be mediated by electrons [78], and most experimental data confirms that electrons play a major role. In detail, however, the nature of the magnetism is not clearly understood.

All these potential applications have boosted research related to the growth of high quality semiconducting oxide films by various techniques among which MOCVD occupies a significant place.

The main aim of this project is to develop the deposition of high crystalline quality ZnO and In_2O_3 based DMS films by PI MOCVD technique and investigate their magnetic properties. The scientific and technical objectives of this work are to:

- Develop new PI MOCVD technique for the deposition of samples in an external magnetic field
- Optimize deposition parameters in order to get good crystalline quality transition metal doped ZnO and In_2O_3 films by PI MOCVD technique
- Fully characterize crystalline quality of the films and their morphology using X-ray diffraction and atomic force microscopy (AFM)
- Investigate magnetic properties of the films using vibrating sample magnetrometry (VSM) and superconducting quantum interference device (SQUID) magnetrometry
- Investigate the possible effect of the growth in external magnetic field on magnetic properties of DMS oxides
- Investigate the possible effect of the growth in external magnetic field on selected magnetic oxide films (Fe_3O_4 and $CoFe_2O_4$)

There are several reports on ZnO grown by liquid injection MOCVD[183], however to the best of our knowledge there are no reports on ZnO and In_2O_3 growth using PI MOCVD. Also, no reports were found on the growth of magnetic oxides, such as Fe_3O_4 and $CoFe_2O_4$ using PI MOCVD. We believe that PI MOCVD will give a good opportunity to prepare doped transparent semiconducting oxide films with unique magnetic properties. Earlier papers were published on the growth of ZnO and $YBa_2Cu_3O_4$ films in magnetic field [184, 185]. It has been found that magnetic field changed the morphology and the structure of the films. However, magnetic properties of the DMS films grown in magnetic field have never been investigated. Thus, it is very important to study the effect of growth in external magnetic field on structural and magnetic properties of our DMS films.

Overall, the successful realisation of this project should result in the development of new DMS materials with potential application for spintronics devices. This research should also contribute in better understanding of the nature of magnetism in these systems.

References:

[1] J. F. Gregg, S. M. Thompson, *Electron World and Wireless World* **1994**, 904.

[2] Z. Igor, F. Jaroslav, S. D. Sarma, *Reviews of Modern Physics* **2004**, *76*, 323.

[3] M. N. Baibich, J. M. Broto, A. Fert, F. N. Van Dau, F. Petroff, P. Eitenne, G. Creuzet, A. Friederich, J. Chazelas, *Physical Review Letters* **1988**, *61*, 2472.

[4] G. Binasch, P. Grünberg, F. Saurenbach, W. Zinn, *Physical Review B* **1989**, *39*, 4828.

[5] N. F. Mott, *Proceedings of the Royal Society* **1936**, *153*, 699.

[6] T. Valet, A. Fert, *Physical Review B* **1993**, *48*, 7099.

[7] A. Schuhl, D. Lacour, *Comptes Rendus Physique* **2005**, *6*, 945.

[8] M. Johnson, *Science* **1993**, *260*, 320.

[9] J M D Coey, A. S. Sanvito, *Journal of Physics D: Applied Physics* **2004**, *37*, 988.

[10] Michael Ziese, M. J. Thornton, **2001**.

[11] J. Sribar, J. D. Puksec, **1994**, *1*, 174.

[12] T. Dietl, H. Ohno, *MRS Bulletin* **2003**, *714*.

[13] Y. D. Park, A. T. Hanbicki, S. C. Erwin, C. S. Hellberg, J. M. Sullivan, J. E. Mattson, T. F. Ambrose, A. Wilson, G. Spanos, B. T. Jonker, *Science* **2002**, *295*, 651.

[14] J. B. Torrance, M. W. Shafer, T. R. McGuire, *Physical Review Letters* **1972**, *29*, 1168.

[15] S. Von Molnar, S. Von Molnar, D. Read, *Proceedings of the IEEE* **2003**, *91*, 715.

[16] T. Dietl, H. Ohno, F. Matsukura, J. Cibert, D. Ferrand, *Science* **2000**, *287*, 1019.

[17] C. Zener, *Physical Review* **1951**, *82*, 403.

[18] S. Das Sarma, E. H. Hwang, A. Kaminski, *Physical Review B* **2003**, *67*, 155201.

[19] V. I. Litvinov, V. K. Dugaev, *Physical Review Letters* **2001**, *86*, 5593.

[20] A. M. Nazmul, S. Sugahara, M. Tanaka, *Physical Review B* **2003**, *67*, 241308.

[21] K. Ohtani, H. Sakuma, H. Ohno, *Journal of Crystal Growth* **2003**, *251*, 718.

[22] M. L. Reed, N. A. El-Masry, H. H. Stadelmaier, M. K. Ritums, M. J. Reed, C. A. Parker, J. C. Roberts, S. M. Bedair, *Applied Physics Letters* **2001**, *79*, 3473.

[23] S. Takahiko, S. Saki, Y. Yoshiyuki, S. Ken-ichi, S. Saburo, K. Kouichi, H. Hidenobu, *Vol. 91*, AIP, **2002**, pp. 7911.

[24] E. O. Mark, R. A. Cammy, J. P. Stephen, A. T. Nikoleta, T. M. Kevin, F. H. Arthur, *Applied Physics Letters* **2001**, *79*, 1312.

[25] N. Theodoropoulou, A. F. Hebard, M. E. Overberg, C. R. Abernathy, S. J. Pearton, S. N. G. Chu, R. G. Wilson, *Applied Physics Letters* **2001**, *78*, 3475.

[26] M. Zajac, J. Gosk, E. Grzanka, M. Kaminska, A. Twardowski, B. Strojek, T. Szyszko, S. Podsiadlo, *Journal of Applied Physics* **2003**, *93*, 4715.

[27] S. Dhar, O. Brandt, A. Trampert, L. Daweritz, K. J. Friedland, K. H. Ploog, J. Keller, B. Beschoten, G. Guntherodt, *Applied Physics Letters* **2003**, *82*, 2077.

[28] P. Sang Eon, L. Hyeon-Jun, C. Yong Chan, J. Se-Young, C. Chae Ryong, C. Sunglae, *Applied Physics Letters* **2002**, *80*, 4187.

[29] S. Yoon, K. Young Hae, Y. S. Park, U. Y. Sh, L. Seung Joo, C. S. Park, K. J. Chung, S. J. Yoon, H. J. Kim, W. C. Lee, D. J. Fu, T. W. Kang, X. J. Fan, Y. J. Park, H. T. Oh, *Journal of Applied Physics* **2004**, *95*, 761.

[30] K. H. Ploog, S. Dhar, A. Trampert, *Vol. 21*, AVS, **2003**, pp. 1756.

[31] J. S. Lee, J. D. Lim, Z. G. Khim, Y. D. Park, S. J. Pearton, S. N. G. Chu, *Journal of Applied Physics* **2003**, *93*, 4512.

[32] V. A. Chitta, J. A. H. Coaquira, J. R. L. Fernandez, C. A. Duarte, J. R. Leite, D. Schikora, D. J. As, K. Lischka, E. Abramof, *Applied Physics Letters* **2004**, *85*, 3777.

[33] G. P. Das, B. K. Rao, P. Jena, *Physical Review B* **2004**, *69*, 214422.

[34] H. X. Liu, Y. W. Stephen, R. K. Singh, G. Lin, J. S. David, N. Newman, N. R. Dilley, L. Montes, M. B. Simmonds, *Applied Physics Letters* **2004**, *85*, 4076.

[35] R. Frazier, G. Thaler, M. Overberg, B. Gila, C. R. Abernathy, S. J. Pearton, *Applied Physics Letters* **2003**, *83*, 1758.

[36] K. H. Kim, K. J. Lee, D. J. Kim, H. J. Kim, Y. E. Ihm, D. Djayaprawira, M. Takahashi, C. S. Kim, C. G. Kim, S. H. Yoo, *Applied Physics Letters* **2003**, *82*, 1775.

[37] K. J. Lee, F. C. Yu, J. A. Kim, D. J. Kim, B. G. Kim, Y. H. Kang, H. J. Kim, Y. E. Ihm, *physica status solidi (b)* **2004**, *241*, 1525.

[38] G. Thaler, R. Frazier, B. Gila, J. Stapleton, M. Davidson, C. R. Abernathy, S. J. Pearton, S. Carlos, *Applied Physics Letters* **2004**, *84*, 2578.

[39] R. Moriya, H. Munekata, T. Kondo, A. Oiwa, *Journal of Crystal Growth* **2002**, *237-239*, 1344.

[40] Euditorial, staff, *Science* **2005**, *309*, 82.

[41] Y. Matsumoto, M. Murakami, T. Shono, T. Hasegawa, T. Fukumura, M. Kawasaki, P. Ahmet, T. Chikyow, S.-y. Koshihara, H. Koinuma, *Science* **2001**, *291*, 854.

[42] P. Sharma, A. Gupta, K. V. Rao, F. J. Owens, R. Sharma, R. Ahuja, J. M. O. Guillen, B. Johansson, G. A. Gehring, *Nat Mater* **2003**, *2*, 673.

[43] S. V. Lim, M. C. Jeong, M. H.Ham, a. J. M. Myoung, *Japanese Journal of Applied Physics* **2004**, *43*, L280.

[44] S. Kolesnik, B. Dabrowski, J. Mais, *Journal of Applied Physics* **2004**, *95*, 2582.

[45] J. Philip, A. Punnoose, B. I. Kim, K. M. Reddy, S. Layne, J. O. Holmes, B. Satpati, P. R. LeClair, T. S. Santos, J. S. Moodera, *Nat Mater* **2006**, *5*, 298.

[46] T. Fukumura, J. Zhengwu, M. Kawasaki, T. Shono, T. Hasegawa, S. Koshihara, H. Koinuma, *Applied Physics Letters* **2001**, *78*, 958.

[47] K. Jae Hyun, K. Hyojin, K. Dojin, I. Young Eon, C. Woong Kil, *Journal of Applied Physics* **2002**, *92*, 6066.

[48] C. Young Mok, C. Woong Kil, K. Hyojin, K. Dojin, I. YoungEon, *Applied Physics Letters* **2002**, *80*, 3358.

[49] D. P. Norton, M. E. Overberg, S. J. Pearton, K. Pruessner, J. D. Budai, L. A. Boatner, M. F. Chisholm, J. S. Lee, Z. G. Khim, Y. D. Park, R. G. Wilson, *Applied Physics Letters* **2003**, *83*, 5488.

[50] Y. Matsumoto, R. Takahashi, M. Murakami, T. Koida, X. J. Fan, T. Hasegawa, T. Fukumura, M. Kawasaki, S. Y. Koshihara, H. Koinuma, *Japanese Journal of Applied Physics* **2001**, *40*, L1204.

[51] S. Nak-Jin, Y. Soon-Gil, C. Chae-Ryong, *Applied Physics Letters* **2002**, *81*, 4209.

[52] D. H. Kim, J. S. Yang, K. W. Lee, S. D. Bu, T. W. Noh, S. J. Oh, Y. W. Kim, J. S. Chung, H. Tanaka, H. Y. Lee, T. Kawai, *Applied Physics Letters* **2002**, *81*, 2421.

[53] M. Ivill, M. E. Overberg, C. R. Abernathy, D. P. Norton, A. F. Hebard, N. Theodoropoulou, J. D. Budai, *Solid-State Electronics* **2003**, *47*, 2215.

[54] S. B. Ogale, R. J. Choudhary, J. P. Buban, S. E. Lofland, S. R. Shinde, S. N. Kale, V. N. Kulkarni, J. Higgins, C. Lanci, J. R. Simpson, N. D. Browning, S. Das Sarma, H. D. Drew, R. L. Greene, T. Venkatesan, *Physical Review Letters* **2003**, *91*, 077205.

[55] H. Kimura, T. Fukumura, M. Kawasaki, K. Inaba, T. Hasegawa, H. Koinuma, *Applied Physics Letters* **2002**, *80*, 94.

[56] J. C. Denardin, M. Knobel, X. X. Zhang, A. B. Pakhomov, *Journal of Magnetism and Magnetic Materials* **2003**, *262*, 15.

[57] S. R. Shinde, S. B. Ogale, J. S. Higgins, H. Zheng, A. J. Millis, V. N. Kulkarni, R. Ramesh, R. L. Greene, T. Venkatesan, *Physical Review Letters* **2004**, *92*, 166601.

[58] S. J. Pearton, C. R. Abernathy, D. P. Norton, A. F. Hebard, Y. D. Park, L. A. Boatner, J. D. Budai, *Materials Science and Engineering: R: Reports* **2003**, *40*, 137.

[59] W. H. Brumage, C. F. Dorman, C. R. Quade, *Physical Review B* **2001**, *63*, 104411.

[60] U. Kenji, T. Hitoshi, K. Tomoji, *Applied Physics Letters* **2001**, *79*, 988.

[61] S. W. Jung, S. J. An, Y. Gyu-Chul, C. U. Jung, L. Sung-Ik, C. Sunglae, *Applied Physics Letters* **2002**, *80*, 4561.

[62] S. Kolesnik, B. Dabrowski, *Journal of Applied Physics* **2004**, *96*, 5379.

[63] A. Chartier, P. Dâ€™Arco, R. Dovesi, V. R. Saunders, *Physical Review B* **1999**, *60*, 14042.

[64] S. J. Han, T. H. Jang, Y. B. Kim, B. G. Park, J. H. Park, Y. H. Jeong, *Applied Physics Letters* **2003**, *83*, 920.

[65] H. Jun, X. Shifa, K. Y. Young, X. Qizhen, L. Hyung-Chul, C. Shifan, X. D. Xiang, F. D. Gerald, T. Ichiro, *Applied Physics Letters* **2005**, *86*, 052503.

[66] http://staff.ustc.edu.cn/~bxlin/pic/006.jpg.

[67] S. Ghosh, V. Sih, W. H. Lau, D. D. Awschalom, S. Y. Bae, S. Wang, S. Vaidya, G. Chapline, *Applied Physics Letters* **2005**, *86*, 232507.

[68] K.Sato, H. Katayama_Yioshida, *Japanese Journal of Applied Physics* **2000**, *39*, L555.

[69] Y.-H. Lee, S.-Y. Hyun, Y. M. Kim, I. W. Park, D. H. Kim, S. Y. Ahn, J. S. Kim, *Solid State Communications* **2004**, *131*, 463.

[70] C. H. Bates, W. B. White, R. Roy, *Journal of Inorganic and Nuclear Chemistry* **1966**, *28*, 397.

[71] T. Mizokawa, T. Nambu, A. Fujimori, T. Fukumura, M. Kawasaki, *Physical Review B* **2002**, *65*, 085209.

[72] A. Tiwari, C. Jin, A. Kvit, D. Kumar, J. F. Muth, J. Narayan, *Solid State Communications* **2002**, *121*, 371.

[73] Y. M. Kim, M. Yoon, I. W. Park, Y. J. Park, J. H. Lyou, *Solid State Communications* **2004**, *129*, 175.

[74] J. Zhengwu, T. Fukumura, M. Kawasaki, K. Ando, H. Saito, T. Sekiguchi, Y. Z. Yoo, M. Murakami, Y. Matsumoto, T. Hasegawa, H. Koinuma, *Applied Physics Letters* **2001**, *78*, 3824.

[75] D.S.Kim, S.Lee, C.Min, H.M.Kim, U.Yuldasheva, T.W.Kang, D.Y.Kim, T.W.Kim, *Japanese Journal of Applied Physics* **2003**, *42*, 7217.

[76] Y. W. Heo, M. P. Ivill, K. Ip, D. P. Norton, S. J. Pearton, J. G. Kelly, R. Rairigh, A. F. Hebard, T. Steiner, *Applied Physics Letters* **2004**, *84*, 2292.

[77] D. C. Kundaliya, S. B. Ogale, S. E. Lofland, S. Dhar, C. J. Metting, S. R. Shinde, Z. Ma, B. Varughese, K. V. Ramanujachary, L. Salamanca-Riba, T. Venkatesan, *Nat Mater* **2004**, *3*, 709.

[78] M. Venkatesan, C. B. Fitzgerald, J. G. Lunney, J. M. D. Coey, *Physical Review Letters* **2004**, *93*, 177206.

[79] W. Prellier, A. Fouchet, B. Mercey, S. Ch, B. Raveau, *Applied Physics Letters* **2003**, *82*, 3490.

[80] K. Rode, A. Anane, R. Mattana, J. P. Contour, O. Durand, R. LeBourgeois, *Journal of Applied Physics* **2003**, *93*, 7676.

[81] L. Yan, C. K. Ong, X. S. Rao, *Journal of Applied Physics* **2004**, *96*, 508.

[82] S.-W. Lim, D.-K. Hwang, J.-M. Myoung, *Solid State Communications* **2003**, *125*, 231.

[83] S. G. Yang, S. G. Yang, A. B. Pakhomov, S. T. Hung, C. Y. A. W. C. Y. Wong, *Magnetics, IEEE Transactions on* **2002**, *38*, 2877.

[84] L. Hyeon-Jun, J. Se-Young, C. Chae Ryong, P. Chul Hong, *Applied Physics Letters* **2002**, *81*, 4020.

[85] H. P. Jung, G. K. Min, M. J. Hyun, R. Sangwoo, M. K. Young, *Applied Physics Letters* **2004**, *84*, 1338.

[86] K. Tominaga, Y. Sakashita, H. Nakashima, M. Okada, *Journal of Crystal Growth* **1994**, *145*, 219.

[87] N. D. Kumar, M. N. Kamalasanan, C. Subhas, *Applied Physics Letters* **1994**, *65*, 1373.

[88] C. Sant, P. Gibart, P. Genou, C. Verie, *Journal of Crystal Growth* **1992**, *124*, 690.

[89] H. Saeki, H. Tabata, T. Kawai, *Solid State Communications* **2001**, *120*, 439.

[90] H.J.Lee, S.Y.Jeong, J.Y.Hwang, C.R.Cho, *Europhysics Letters* **2003**, *64*, 797.

[91] P. Koidl, *Physical Review B* **1977**, *15*, 2493.

[92] S. J. Pearton, D. P. Norton, K. Ip, Y. W. Heo, T. Steiner, *Journal of Vacuum Science & Technology B: Microelectronics and Nanometer Structures* **2004**, *22*, 932.

[93] X. M. Cheng, C. L. Chien, *Journal of Applied Physics* **2003**, *93*, 7876.

[94] D. P. Norton, S. J. Pearton, A. F. Hebard, N. Theodoropoulou, L. A. Boatner, R. G. Wilson, *Applied Physics Letters* **2003**, *82*, 239.

[95] M. Ivill, S. J. Pearton, D. P. Norton, J. Kelly, A. F. Hebard, *Journal of Applied Physics* **2005**, *97*, 053904.

[96] G. Lawes, A. S. Risbud, A. P. Ramirez, S. Ram, *Physical Review B (Condensed Matter and Materials Physics)* **2005**, *71*, 045201.

[97] M. H. Kane, K. Shalini, C. J. Summers, R. Varatharajan, J. Nause, C. R. Vestal, Z. J. Zhang, I. T. Ferguson, *Journal of Applied Physics* **2005**, *97*, 023906.

[98] N. Jedrecy, H. J. v. Bardeleben, Y. Zheng, J. L. Cantin, *Physical Review B (Condensed Matter and Materials Physics)* **2004**, *69*, 041308.

[99] A. C. Tuan, J. D. Bryan, A. B. Pakhomov, V. Shutthanandan, S. Thevuthasan, D. E. McCready, D. Gaspar, M. H. Engelhard, J. W. Rogers, Jr., K. Krishnan, D. R. Gamelin, S. A. Chambers, *Physical Review B (Condensed Matter and Materials Physics)* **2004**, *70*, 054424.

[100] S. J. Han, J. W. Song, C. H. Yang, S. H. Park, J. H. Park, Y. H. Jeong, K. W. Rhie, *Applied Physics Letters* **2002**, *81*, 4212.

[101] T. Wakano, N. Fujimura, Y. Morinaga, N. Abe, A. Ashida, T. Ito, *Physica E: Low-dimensional Systems and Nanostructures* **2001**, *10*, 260.

[102] H. Nguyen Hoa, B. Virginie, S. Joe, *Applied Physics Letters* **2005**, *86*, 082505.

[103] ICCD PDF-2 Data Base, JCPDS-Int. Center for Diffraction Data, Pennsylvania, USA, **1994**.

[104] R. D. Shannon, *Solid State Communications* **1966**, *4*, 629.

[105] C. Falcony, J. R. Kirtley, D. J. DiMaria, T. P. Ma, T. C. Chen, *Journal of Applied Physics* **1985**, *58*, 3556.

[106] C. G. Granqvist, *Applied Physics A: Materials Science and Processing* **1993**, *57*, 19.

[107] S. Kasiviswanathan, G. Rangarajan, *Journal of Applied Physics* **1994**, *75*, 2572.

[108] M. B. N. K. E. G. E. H. E. D. V. C. G. Kiriakidis, *physica status solidi (a)* **2001**, *185*, 27.

[109] D.H.Zhang, Z.Q.Liu, Ch.W.Zhou, *MRS Bulletin* **2005**, *828*.

[110] S. Muranaka, *Thin Solid Films* **1992**, *221*, 1.

[111] S. Naseem, I. A. Rauf, K. Hussain, N. A. Malik, *Thin Solid Films* **1988**, *156*, 161.

[112] C. Grivas, D. S. Gill, S. Mailis, L. Boutsikaris, N. A. Vainos, *Applied Physics A* **1998**, *66*, 201.

[113] M. Bender, N. Katsarakis, E. Gagaoudakis, E. Hourdakis, E. Douloufakis, V. Cimalla, G. Kiriakidis, *Journal of Applied Physics* **2001**, *90*, 5382.

[114] M. G. Mikhailov, T. M. Ratcheva, M. D. Nanova, *Thin Solid Films* **1987**, *146*, L23.

[115] M. Girtan, H. Cachet, G. I. Rusu, *Thin Solid Films* **2003**, *427*, 406.

[116] J. Joseph Prince, S. Ramamurthy, B. Subramanian, C. Sanjeeviraja, M. Jayachandran, *Journal of Crystal Growth* **2002**, *240*, 142.

[117] T. Asikainen, M. Ritala, W.-M. Li, R. Lappalainen, M. Leskela, *Applied Surface Science* **1997**, *112*, 231.

[118] V. D. Das, K. Shahil, D. Laxmikant, N. Lakshminarayan, *Journal of Applied Physics* **1996**, *79*, 8521.

[119] C. Jun-Sik, K. Seok-Keun, Y. Ki Hyun, *Journal of The Electrochemical Society* **2000**, *147*, 1065.

[120] O. A. Frederick, I. Hirokazu, I. Tsuguo, Y. Hideki, M. Hiroshi, M. Muneyuki, *Applied Physics Letters* **1999**, *74*, 3059.

[121] E. J. Tarsa, J. H. English, J. S. Speck, *Applied Physics Letters* **1993**, *62*, 2332.

[122] Y. Yuka, S. Nobuyasu, M. Toshiharu, Y. Takehito, *Journal of Vacuum Science & Technology A: Vacuum, Surfaces, and Films* **2000**, *18*, 83.

[123] M. Girtan, *Surface and Coatings Technology* **2004**, *184*, 219.

[124] A. Gurlo, M. Ivanovskaya, A. Pfau, U. Weimar, W. Gopel, *Thin Solid Films* **1997**, *307*, 288.

[125] T. Maruyama, T.Kitamura, *Japanese Journal of Applied Physics* **1989**, *28*, L1096.

[126] L. Zhang, L. S. Zhang, R. Z. Zhang, Y. H. Liu, W. X. Zhang, B. X. Huang, L. M.Mei, *Progress in Natural Science* **1999**, *9*, 353.

[127] I.-B. Shim, C. S. C. S. Kim, *Journal of Magnetism and Magnetic Materials* **2004**, *272-276*, E1571.

[128] K. Y. Young, X. Qizhen, L. Hyung-Chul, C. Shifan, X. D. Xiang, F. D. Gerald, X. Shifa, H. Jun, S. C. Yong, S. D. Preite, E. L. Samuel, T. Ichiro, *Applied Physics Letters* **2005**, *86*, 042506.

[129] V. Brize, J. Sakai, N. Hoa Hong, *Physica B: Condensed Matter* **2007**, *392*, 379.

[130] G. Peleckis, X. L. Wang, S. X. Dou, *Applied Physics Letters* **2006**, *88*, 132507.

[131] G. Peleckis, W. Xiaolin, D. Shi Xue, *Applied Physics Letters* **2006**, *89*, 022501.

[132] X. Li, C. Xia, G. Pei, X. He, *Journal of Physics and Chemistry of Solids* **2007**, *In Press, Corrected Proof.*

[133] Nguyen Hoa Hong, Joe Sakai, Ngo Thu Huong, A. R. a. V. Brizé, *Journal of Physics: Condensed Matter* **2006**, *18*, 6897.

[134] H. Nguyen Hoa, S. Joe, P. Nathalie, B. Virginie, *Physical Review B (Condensed Matter and Materials Physics)* **2006**, *73*, 132404.

[135] P. Kharel, C. Sudakar, M. B. Sahana, G. Lawes, R. Suryanarayanan, R. Naik, V. M. Naik, *Vol. 101*, AIP, **2007**, p. 09H117.

[136] H. S. Kim, S. H. Ji, H. Kim, S.-K. Hong, D. Kim, Y. E. Ihm, W. K. Choo, *Solid State Communications* **2006**, *137*, 41.

[137] T. Ohno, T. Kawahara, M. Murasugi, H. Tanaka, T. Kawai, S. Kohiki, *Journal of Magnetism and Magnetic Materials* **2007**, *310*, e717.

[138] J. Stankiewicz, F. Villuendas, J. Bartolome, J. Sese, *Journal of Magnetism and Magnetic Materials* **2007**, *310*, 2084.

[139] P. John, T. Nikoleta, B. Geetha, S. M. Jagadeesh, S. Biswarup, *Applied Physics Letters* **2004**, *85*, 777.

[140] J. B. Goodenough, *Progress in Solid State Chemistry* **1971**, *5*, 145.

[141] A. Yanase, K. Siratori, *Journal of the Physical Society of Japan* **1984**, *53*, 312.

[142] W. E. Pickett, D. J. Singh, *Physical Review B* **1996**, *53*, 1146.

[143] J. H. Park, E. Vescovo, H. J. Kim, C. Kwon, R. Ramesh, T. Venkatesan, *Nature* **1998**, *392*, 794.

[144] S. Todo, K. Siratori, S. Kimura, *Journal of the Physical Society of Japan* **1995**, *64*, 2118.

[145] D. T. Margulies, F. T. Parker, F. E. Spada, R. S. Goldman, J. Li, R. Sinclair, A. E. Berkowitz, *Physical Review B* **1996**, *53*, 9175.

[146] F. C. Voogt, T. Hibma, G. L. Zhang, M. Hoefman, L. Niesen, *Surface Science* **1995**, *331-333*, 1508.

[147] G. Q. Gong, A. Gupta, G. Xiao, W. Qian, V. P. Dravid, *Physical Review B* **1997**, *56*, 5096.

[148] D. T. Margulies, F. T. Parker, M. L. Rudee, F. E. Spada, J. N. Chapman, P. R. Aitchison, A. E. Berkowitz, *Physical Review Letters* **1997**, *79*, 5162.

[149] W. Eerenstein, T. T. M. Palstra, T. Hibma, S. Celotto, *Physical Review B* **2002**, *66*, 201101.

[150] X. W. Li, A. Gupta, X. Gang, G. Q. Gong, *Vol. 83*, AIP, **1998**, pp. 7049.

[151] D. J. Huang, C. F. Chang, J. Chen, L. H. Tjeng, A. D. Rata, W. P. Wu, S. C. Chung, H. J. Lin, T. Hibma, C. T. Chen, *Journal of Magnetism and Magnetic Materials* **2002**, *239*, 261.

[152] A. M. Bataille, A. Tagliaferri, S. Gota, C. d. Nadai, J. B. Moussy, M. J. Guittet, K. Bouzehouane, F. Petroff, M. Gautier-Soyer, N. B. Brookes, *Physical Review B (Condensed Matter and Materials Physics)* **2006**, *73*, 172201.

[153] P. Seneor, A. Fert, J. L. Maurice, F. Montaigne, F. Petroff, A. Vaures, *Applied Physics Letters* **1999**, *74*, 4017.

[154] A. Ken-ichi, X. W. Shan, *Journal of Applied Physics* **2003**, *93*, 7954.

[155] K. S. Yoon, J. H. Koo, Y. H. Do, K. W. Kim, C. O. Kim, J. P. Hong, *Journal of Magnetism and Magnetic Materials* **2005**, *285*, 125.

[156] L. M. B. Alldredge, R. V. Chopdekar, B. B. Nelson-Cheeseman, Y. Suzuki, *Applied Physics Letters* **2006**, *89*, 182504.

[157] Y. Kap Soo, Y. Jung Yup, K. Ki Woong, K. Ja Hyun, K. Chae Ok, H. Jin Pyo, *Vol. 95*, AIP, **2004**, pp. 6933.

[158] S. van Dijken, X. Fain, S. M. Watts, K. Nakajima, J. M. D. Coey, *Journal of Magnetism and Magnetic Materials* **2004**, *280*, 322.

[159] E. Snoeck, G. Ch, R. Serra, G. BenAssayag, J. B. Moussy, A. M. Bataille, M. Pannetier, M. Gautier-Soyer, *Physical Review B (Condensed Matter and Materials Physics)* **2006**, *73*, 104434.

[160] R. J. Kennedy, P. A. Stampe, *Journal of Physics D: Applied Physics* **1999**, *32*, 16.

[161] Y. X. Lu, J. S. Claydon, Y. B. Xu, D. M. Schofield, S. M. Thompson, *Vol. 95*, AIP, **2004**, pp. 7228.

[162] S. M. Watts, K. Nakajima, S. v. Dijken, J. M. D. Coey, *Vol. 95*, AIP, **2004**, pp. 7465.

[163] D. Reisinger, M. Schonecke, T. Brenninger, M. Opel, A. Erb, L. Alff, R. Gross, *Journal of Applied Physics* **2003**, *94*, 1857.

[164] E. S. Murdock, E. S. Murdock, R. F. Simmons, R. Davidson, *Magnetics, IEEE Transactions on* **1992**, *28*, 3078.

[165] Y. Suzuki, R. B. v. Dover, E. M. Gyorgy, M. P. Julia, V. Korenivski, D. J. Werder, C. H. Chen, R. J. Cava, J. J. Krajewski, W. F. Peck, Jr., K. B. Do, *Applied Physics Letters* **1996**, *68*, 714.

[166] W. H. Wang, X. Ren, *Journal of Crystal Growth* **2006**, *289*, 605.

[167] C.-W. Nan, *Physical Review B* **1994**, *50*, 6082.

[168] Z. Jian-ping, H. Hongcai, S. Zhan, N. Ce-Wen, *Applied Physics Letters* **2006**, *88*, 013111.

[169] K. S. Chang, M. A. Aronova, C. L. Lin, M. Murakami, M. H. Yu, J. Hattrick-Simpers, O. O. Famodu, S. Y. Lee, R. Ramesh, M. Wuttig, I. Takeuchi, C. Gao, L. A. Bendersky, *Applied Physics Letters* **2004**, *84*, 3091.

[170] M. Bibes, A. Barthelemy, *Electron Devices, IEEE Transactions on* **2007**, *54*, 1003.

[171] G. Liu, C.-W. Nan, J. Sun, *Acta Materialia* **2006**, *54*, 917.

[172] L. M. Apatiga, V. M. Castano, *Thin Solid Films* **2006**, *496*, 576.

[173] A. U. Mane, S. A.Shivashankar, *Journal of Crystal Growth* **2003**, *254*, 368.

[174] B. Pejova, A. Isahi, M. Najdoski, I. Grozdanov, *Materials Research Bulletin* **2001**, *36*, 161.

[175] H. X. Xu, S. L. Xu, X. D. Li, H. Wang, H. Yan, *Applied Surface Science* **2006**, *252*, 4091.

[176] O. Y. Gorbenko, I. E. Graboy, V. A. Amelichev, A. A. Bosak, A. R. Kaul, B. Guttler, V. L. Svetchnikov, H. W. Zandbergen, *Solid State Communications* **2002**, *124*, 15.

[177] L. W. Guo, D. P. Peng, H. Makino, K. Inaba, H. J. Ko, K. Sumiyama, T. Yao, *Journal of Magnetism and Magnetic Materials* **2000**, *213*, 321.

[178] L. W. Guo, H. Makino, H. J. Ko, Y. F. Chen, T. Hanada, D. L. Peng, K. Inaba, T. Yao, *Journal of Crystal Growth* **2001**, *227-228*.

[179] K. L. Choy, *Progress in Materials Science* **2003**, *48*, 57.

[180] B. E. Deal, a. A. S. Grove, *Journal of Applied Physics* **1965**, *36*, 3770.

[181] A. Erbil, W. Braun, B. S. Kwak, B. J. Wilkens, L. A. Boatner, J. D. Budai, *Journal of Crystal Growth* **1992**, *124*, 684.

[182] B. Vengalis, V. Plaušinaitiene, A. Abrutis, a. Z. Šaltytė, *Acta Physica Polonica* **2005**, *107*, 286.

[183] H. Li, H. Liu, J. Wang, S. Yao, X. Cheng, R. I. Boughton, *Materials Letters* **2004**, *58*, 3630.

[184] M. Kasuga, T. Takano, S. Akiyama, K. Hiroshima, K. Yano, K. Kishio, *Journal of Crystal Growth* **2005**, *275*, e1545.

[185] Yanwei Ma, Kazuo Watanabe, Satoshi Awaji, a. M. Motokawa, *Applied Physics Letters* **2000**, *77*, 3633.

Chapter 2: Experimental

2.1. Starting materials

2.1.1. Metalorganic precursors and solvents

β-diketonate based precursors were used as a starting materials for the deposition of oxide films. The general structure of metal β-diketonate is presented in Figure 2.1. The main criteria, which have guided the choice of precursors, have been their relatively good thermal stability, high volatility over a wide temperature range, safety and availability.

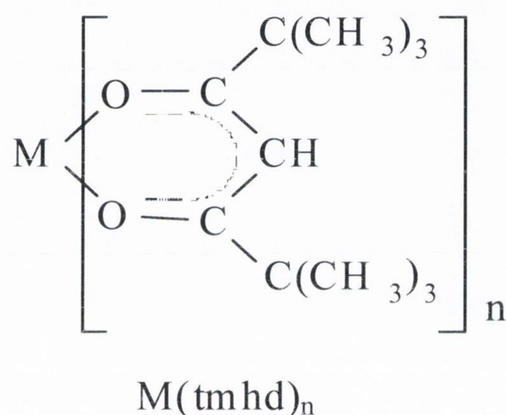

M(tmhd)$_n$

Fig.2.1 Structure of M(tmhd)$_n$

Anhydrous 1,2-Dimethoxyethane 99.5 % was purchased from Sigma-Aldrich and used as a solvent for metalorganic precursors.

Elemental analysis of synthesised precursors was carried out in University College Dublin using an External Analytical CE-440 elemental analyser.

2.1.1.1. Zn(tmhd)$_2$

A 97% purity Zn(tmhd)$_2$ precursor was purchased from Sigma-Aldrich. Additional purification was performed by sublimation in the laboratory. The melting point of Zn(tmhd)$_2$ is 140-144°C [1] and decomposition temperature is 256°C.

2.1.1.2. $Co(tmhd)_2$

$Co(tmhd)_3$ precursor was donated by the Department of General and Inorganic Chemistry of Vilnius University. Melting point for $Co(tmhd)_3$ was found to be in a range of 242-245°C, this is in a good agreement with literature reference [1]. Elemental analysis calculated for $Co(tmhd)_3$ ($CoC_{33}H_{57}O_6$): C, 65.11; H, 9.36; found: C, 59.00; H, 9.03; N, 2.6.

2.1.1.3. $In(acac)_3$

99.9 % purity $Cr(acac)_3$ was purchased from Sigma-Aldrich. Melting point of $Cr(acac)_3$ is in the range of 180-185 °C [2].

2.1.1.4. $In(tmhd)_3$

In_2O_3 films were also grown using $In(tmhd)_3$ precursor. $In(tmhd)_3$ precursor was synthesized according to the procedure described in [1], see equation below. $In(NO_3)_3$ and excess of $NaCH_3COO$ (ratio 1:2) were dissolved in distilled water. An ethanol solution of the β-diketone was added to an aqueous $In(NO_3)_3$ solution.

$$In(NO_3)_3 + NaCH_3COO/H_2O + Htmhd/C_2H_5OH \longrightarrow In(tmhd)_3 \downarrow$$

The $In(tmhd)_3$ was removed by filtration and recrystallized from hexane. 99.9 % purity $In(NO_3)_3$ was obtained from Sigma-Aldrich. 98 % purity Htmhd ligand (β-diketone) was purchased from Fluka. 99.9+ % purity In acetylacetonate ($In(acac)_3$) obtained from Sigma-Aldrich was also used for the deposition of In_2O_3 films.

Analysis calculated for $In(tmhd)_3$ ($InC_{33}H_{57}O_6$): C, 59.63; H, 8.66; N, 0; found: C, 59.69; H, 8.52; N, 0. The melting point of $In(tmhd)_3$ is 167°C [2].

2.1.1.5. $Cr(acac)_3$

99.9 % purity $Cr(acac)_3$ was purchased from Sigma-Aldrich. Melting point of $Cr(acac)_3$ is 214 °C [2].

2.1.1.6. $Fe(tmhd)_3$

$Fe_2(SO_4)_3$ and excess of $NaCH_3COO$ (ratio 1:2) were dissolved in distilled water. An ethanol solution of the β-diketone was added to an aqueous $Fe_2(SO_4)_3$ solution. The $Fe(tmhd)_3$ was removed by filtration and recrystallized from hexane (see equation below).

$$Fe_2(SO_4)_3 + NaCH_3COO/H_2O + Htmhd/C_2H_5OH \longrightarrow Fe(tmhd)_3 \downarrow$$

99.9 % purity $Fe(SO_4)_3$ was obtained from Sigma-Aldrich. Melting point of $Fe(tmhd)_3$ is 163 °C [1].

Analysis calculated for $Fe(tmhd)_3$ ($FeC_{33}H_{57}O_6$): C, 65.44; H, 9.51; N, 0; found: C, 65.52; H, 9.52; N, 0.

2.1.1.7. $Mn(tmhd)_3$

$MnSO_4$ and excess of $NaCH_3COO$ (ratio 1:2) were dissolved in distilled water. An ethanol solution of the β-diketone was added to an aqueous $MnSO_4$ solution. Reaction mixture was stirred until organic layer turned into dark colour and then concentrated NH_4OH solution was added (see equation below). The $Mn(tmhd)_3$ was removed by filtration and purified via sublimation.

$$MnSO_4 + NaCH_3COO/H_2O + Htmhd/CH_3OH \xrightarrow{O_2(air)} \xrightarrow{NH_4OH} Mn(tmhd)_3 \downarrow$$

99.9 % purity $MnSO_4$ was obtained from Sigma-Aldrich. Melting point of $Mn(tmhd)_3$ is 165 °C [1].

Analysis calculated for $Mn(tmhd)_3$ ($MnC_{33}H_{57}O_6$): C, 65.54; H, 9.52; N, 0; found: C, 65.61; H, 9.30; N, 0.

2.1.2. Substrates

In this work monocrystalline (0001) Al_2O_3 (C-cut sapphire), (1$\underline{1}$02) Al_2O_3 (R-cut sapphire) and (100) MgO substrates from Crystal GmbH company were used for the deposition of the films. Substrates were 5×5×0.5 mm^3 squares, polished on both sides. The main advantage of sapphire substrates is their low cost, although there is a significant lattice mismatch between Al_2O_3 (a = 4.754 Å, c = 12.99 Å) and ZnO (a = 3.250 Å, c = 5.213 Å), reaching as much as ~ 32%. In spite of this fact, there are many reports published on highly orientated and even epitaxial zinc oxide films grown on sapphire substrates [3].

MgO is an ideal substrate for epitaxial growth of Fe_3O_4 and $CoFe_2O_4$ due to the small lattice mismatch. Some of the important parameters of the substrates used in this work are presented in Table 2.1.

Table 2.1 Important substrate parameters for the deposition of the films

Substrate orientation, lattice	**Surface structure**	**Lattice parameters (Å)**	**Lattice mismatch with film, %**			
			ZnO hexagonal	**In_2O_3 cubic**	**Fe_3O_4 cubic**	**$CoFe_2O_4$ cubic**
(0001) Al_2O_3 hexagonal	hexagonal	a = 4.758 c = 12.991	Δa/a = -31.8	Δa/a = 0.25	Δa/a = 24.8	Δa/a = 24.7
(1$\underline{1}$02) Al_2O_3 hexagonal	pseudo-square	a = 4.758 b = 5.129	Δa/a = 18 Δb/b = - 0.44	Δa/a = 0.25 Δb/b = -1.36	Δa/a = -11.8 Δb/b = -18.2	Δa/a = -11.8 Δb/b = -18.2
(100) MgO cubic	Square	a = 4.211	—	—	Δa/a = -0.31	Δa/a = -0.36

All substrates were ready to use and no additional cleaning procedures were required.

2.2. Sample preparation techniques

2.2.1. PI MOCVD

The system used in this work is a vertical hot wall stainless steel PI MOCVD reactor equipped with one evaporator. A schematic diagram of PI MOCVD reactor is shown in Figure 2.2.

The method operation principle is as follows: a volatile metalorganic compound or the mixture of several metalorganic compounds is dissolved in organic solvent. Prepared solution is placed into the reservoir, where the argon pressure of 0.5 – 2 atmospheres is build-up. Reservoir is connected to the injector system, which is computer driven. Under the sway of argon pressure minute solution microdoses are injected through the injector system into the reactor's evaporation zone. The microdose is flash-evaporated exposed to the high temperature in evaporation zone. Evaporation temperature has to be higher than the evaporation temperature of the least volatile precursor, but does not have to exceed the decomposition temperature of the precursors. A mixture of complexes and solvent's vapours is transported towards the heated substrate into the deposition zone by the carrier gases ($Ar + O_2$). Oxide layers are formed on a heated substrate during the decomposition reaction. Unreacted vapours and gaseous decomposition products are carried out from the reactor and condensed in a nitrogen trap.

To ensure a good reproducibility of microdose size injector was washed with hexane after each deposition.

The main and the longest stage working with PI MOCVD reactor was optimisation of deposition conditions. The most important factors in PI MOCVD deposition technique which have to be optimised were:

1. Deposition temperature (Tdep) is one of the most important parameters which determines the growth and the properties of the films
2. Temperature gradient near substrate surface, which depends on:
   a) Substrate temperature and substrate position in the furnace
   b) Furnace temperature gradient
   c) Total reactor pressure
   d) Thermal balance (carrier gas temperature, carrier gas flow rate)
   e) Decomposition reactions
3. Carrier gas flow which determines the concentration of precursor vapours near substrate, travelling speed and time the vapours stay in decomposition zone. As a result, carrier gas flow rate influences the precursor decomposition reaction, film composition, growth rate and homogeneity

4. Total gas pressure, influences gas flow rate and vapour concentration
5. Partial oxygen pressure which affects the decomposition rate of precursors and microstructure of the films
6. Carrier gas temperature. Has to be set to avoid the condensation of precursor vapours and to prevent its premature decomposition
7. Evaporation temperature. Has to be sufficiently high to ensure the rapid evaporation of precursor microdose, but not too high to exclude the premature decomposition in evaporation zone
8. Injector parameters, i.e. impulse length and frequency
9. Solution composition (molar ratio of precursors, concentration)

One of the main obstacles during optimisation was that all these factors are very closely related. Changing only one parameter would often result in the change of the other optimisation parameters. The main criteria estimating the parameters influence in this work while approaching the optimal deposition conditions were:

a) If the film growth occurs
b) Film growth rate
c) X-ray diffraction analysis, showing formation of desired phase
d) Film morphology (SEM and AFM)

All these factors and parameters will be discussed in detail in following results chapters.

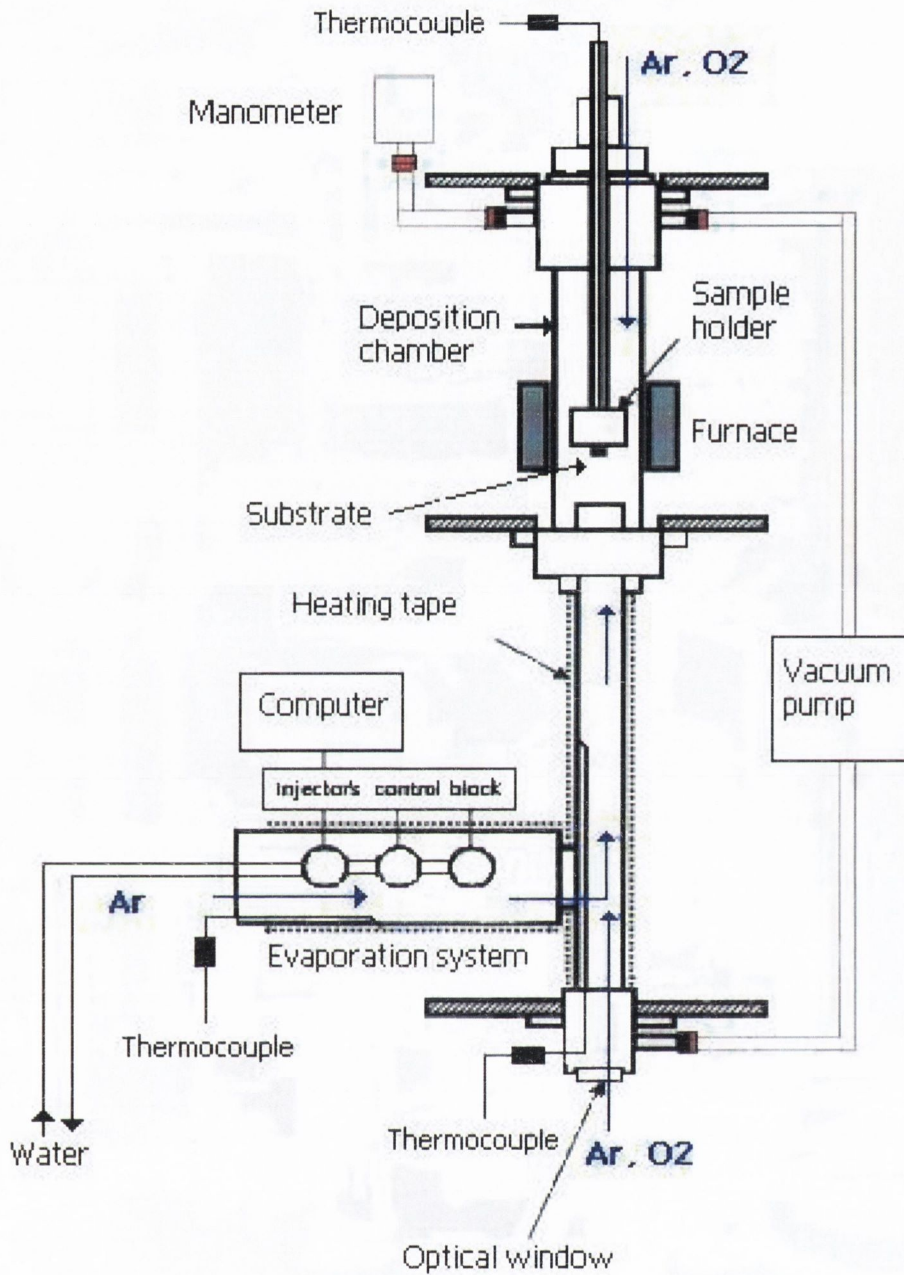

Fig. 2.2 Schematic diagram of PI MOCVD reactor

2.2.2. PI MOCVD with 1T magnet

One of the novelties of this work was construction of PI MOCVD reactor equipped with 1 Tesla permanent magnet (Figure 2.3). The idea behind was that

introduction of magnetic field during the growth of DMS and magnetic films could lead to improved magnetic properties of these films. This idea was supported by previous work on ZnO [4] and $YBa_2Cu_3O_7$ [5] where crystalline and morphological changes were observed when films were grown in high magnetic field, although magnetic properties of these films were never investigated. Improvement of magnetic properties was also found in Fe_3O_4 films [6] grown by magnetron sputtering in magnetic filed of up to 0.3 Tesla.

For the construction of reactor the furnace equipped with water cooling line was placed inside 1 Tesla permanent magnet which had an inside hole of 8 cm in diameter. The furnace cooling has to be very efficient to avoid the overheating of the magnet and thus destroying its magnetic properties. A quartz tube with 3.5 cm in diameter serving as deposition chamber was placed inside the furnace. One additional heater was placed at the top of the vertical tube to keep uniform temperature inside reactor. Magnet introduction resulted in the smaller deposition chamber (3.5 cm in diameter) compared with the previous reactor (10 cm in diameter), thus reducing the dimensions of sample holder to 2 cm rather than 5 cm for the reactor without magnet. The rest of the reactor geometry remained the same. The method operation principle is the same as described in the Chapter 2.2.1.

Magnet specifications allowed switching magnetic field off and on by changing coil directions. When magnet was switched of the remanent field of 0.015T was detected by Hall probe in the centre of magnet, while at the edges of the magnet it was 0.17T. Maximum magnetic field of 1.2T was also detected to be in the very centre of the magnet. For this reason sample holder was adjusted in the deposition chamber so as to be exactly in the centre of the magnet. This distance was never changed when growing films in PI MOCVD reactor equipped with magnet. Magnetic field was oriented perpendicular to the substrate surface.

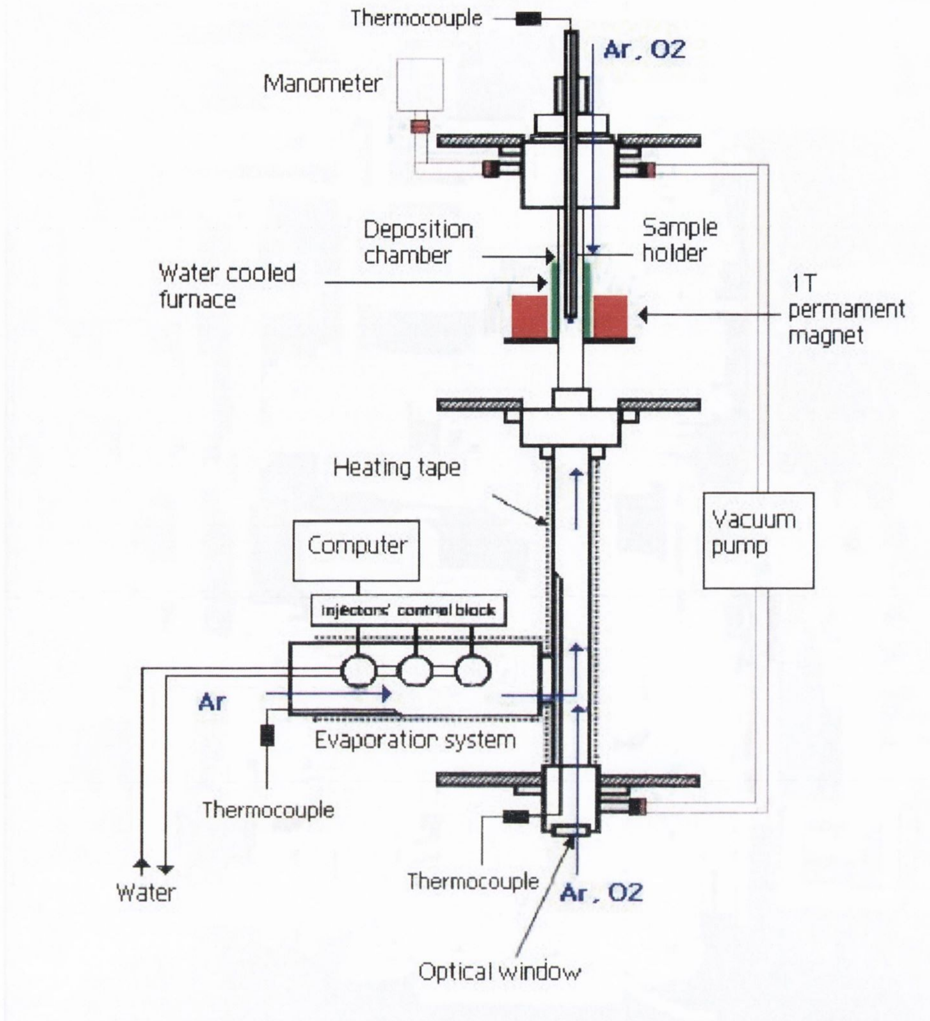

Fig. 2.3 Schematic diagram of PI MOCVD reactor with 1 Tesla magnet.

2.3. Characterisation techniques

2.3.1. X-ray Diffraction

X-ray radiation is the name given to that part of the electromagnetic spectrum that has a wavelength of the order of an angstrom, which is also the order of magnitude of the separation of the atoms in a crystal, thus crystals can diffract the X-rays.

When X-rays interact with a crystalline substance, one gets a diffraction pattern. The X-ray diffraction pattern of a pure substance is like a fingerprint of the substance. The main aim of the XRD is to identify the crystalline phases present in the sample. The phases can be identified by comparison of the sample diffraction pattern with a set of

standard references provided by the Joint Committee on Powder Diffraction Standards (JCPDS) database.

Solid material can be described as amorphous and crystalline. In amorphous materials the atoms arranged in a random way similar to the disorder we find in the liquid. For example, glasses are amorphous materials. While, in crystalline materials atoms are arranged in a regular pattern, and there is a smallest volume element that by repetition in three dimensions describes the crystal. This smallest unit volume element is called a unit cell. About 95% of all solid materials can be described as crystalline.

When an X-ray beam passes through a material its intensity is reduced due to two main effects: absorption and scattering. Absorption phenomena are utilized in various ways, such as X-ray fluorescence analysis. The scattering of X-rays by an atom may occur in either of two ways incoherent and coherent scattering. The interference phenomenon associated with coherent scattering are the basis of X-ray crystallography.

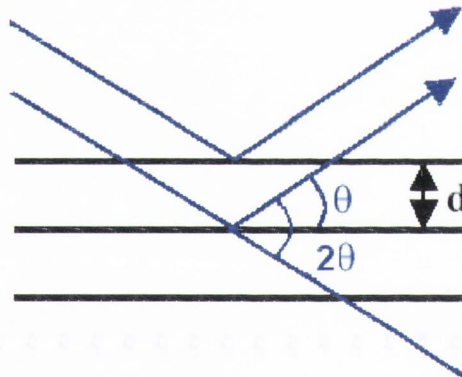

Fig.2.4 X-ray diffraction in Bragg-Brentano $\theta/2\theta$ geometry

X-rays irradiate the sample at an angle θ to the surface plane of the sample. A detector is rotated to $\pi - \theta$ and collects the intensity of the diffracted X-rays (also called $\theta/2\theta$ scan in Bragg-Brentano geometry). The X-rays are diffracted then the Bragg condition is satisfied:

$$n\lambda = 2d \sin\theta \tag{20}$$

θ is the incident angle (2θ is the diffraction angle) and d is the inter-planar spacing (also expressed as d_{hkl}) , as shown in Figure 2.4. Using Bragg equation the d-spacing in the crystal can be calculated. The Bragg condition will be satisfied for one incident angle for each inter-planar distance.

Crystal is a regular three dimensional arrangement of unit cells and it can be regarded as acting as a three dimensional diffraction grating for X-rays. The effect of the grating is to limit the directions in which an observable diffracted beam occurs. Directions of the diffracted X-rays beams depend on the dimensions of the unit cell and their intensities on the nature and disposition of atom within the unit cell. The cell constants, crystal system and space group of the specimen may be determined form the X-ray diffraction pattern. For a cubic crystal system:

$$\frac{1}{d} = \frac{h^2 + k^2 + l^2}{a^2} \tag{21}$$

where a is a cell constant. And for hexagonal system:

$$\frac{1}{d^2} = \frac{4}{3}\left(\frac{h^2 + k^2 + l^2}{a^2}\right) + \frac{l^2}{c^2} \tag{22}$$

In addition to crystal structure and preferential orientation, XRD can be used to estimate the crystallite size in the sample using Scherrer's formula. 1918 Scherrer derived an equation to describe the broadening of a reflection in terms of crystallite size:

$$D = \frac{K\lambda}{\beta \cos\theta} \tag{23}$$

where D is the crystallite size, K is a shape factor, ranging from 0.7 to 1.2 (taken as 0.9), λ is the wavelength of the X-rays (in this thesis, λ = 1.5406 Å) and β is full width at half maximum (FWHM) of the peak. It should also be noted that the error of determination is 20-30%.

From $\theta/2\theta$ scan we can also get information on the specimen texture, i.e. preferred perpendicular to the substrate surface crystallite orientation (found from reflection peak's FWHM).

Omega (ω) scans were also performed. ω scan is used to investigate the orientation of the crystallites perpendicular to the surface of the sample. In omega scan θ and 2θ angles are fixed, thereby satisfying the Bragg condition for only one *d*-spacing, for example (002). The sample is set at a small ω angle regarding to the X-rays incident angle (Figure 2.5) and the change of intensities of the diffracted X-rays is recorded. Resulting reflection intensity change from ω angle is called rocking curve. The FWHM of the rocking curve is a direct measure of the range of orientation present in the irradiated area of the crystal.

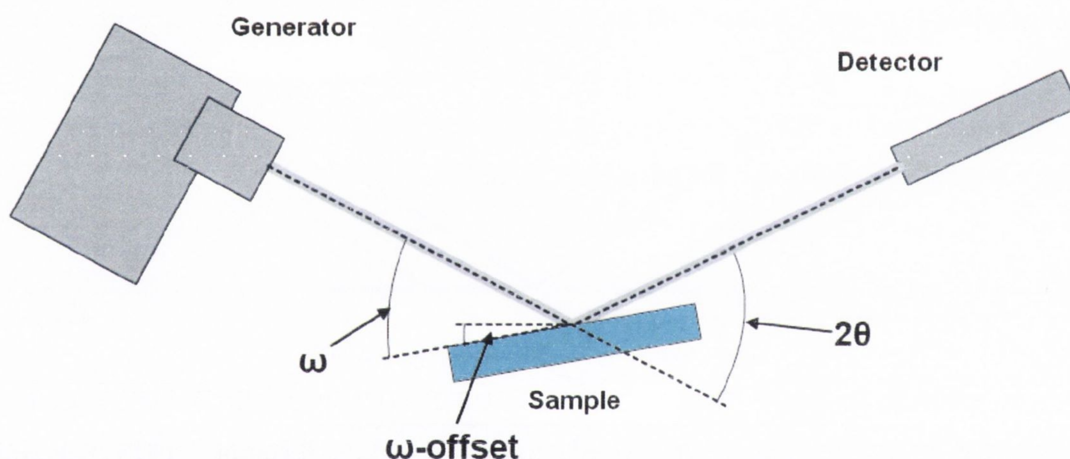

Fig. 2.5 Graphic presentation of ω scan

Schultz geometry was also used in this work to study the orientation (epitaxy) of the crystallites in the sample. In this geometry the sample is rotated at ϕ angle between 0 and 360°, while θ and ψ angles are set for the chosen d_{hkl} spacing, as shown in Figure 2.6. In this geometry a ϕ scan is obtained.

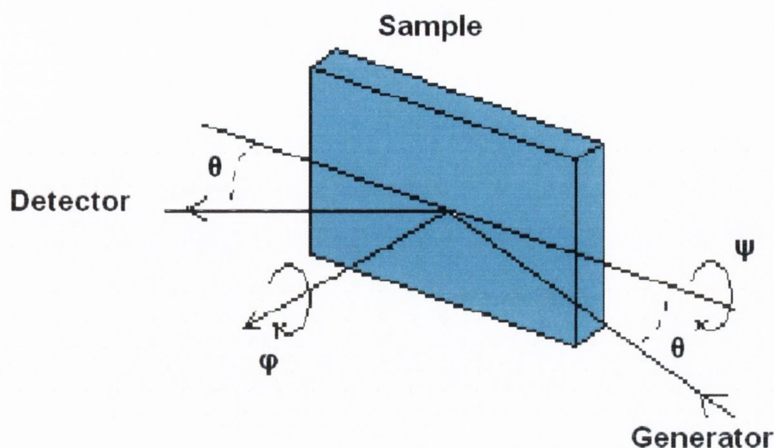

Fig. 2.6 Graphic presentation of ϕ scan in Shultz geometry

In this work a Philips's X'Pert Pro diffractometer with an X'Celerator and PRS Pass detectors and Cu cathode with a wavelength $\lambda_{K\alpha}$ = 1.54056Å was used to characterise the deposited films. The X'Celerator detector is an advanced detector that uses an array of many detectors and performs scans much faster than conventional detectors.

2.3.2. X-ray Reflectivity

X-ray reflectivity (XRR) measurements were performed using a Philips X'Pert Pro diffractometer. XRR allows measuring the thicknesses of up to 200 nm depending on film's roughness and density. Another advantage of XRR is that it is able to indirectly measure the surface and interface roughness of the films. From XRR measurements it is also possible to determine the density of the film (Figure 2.7). The index of refraction n for X-rays is less than one, thus at a critical angle total interaction refraction occurs for the X-ray beam passing from the ambient medium (air) into the thin film. The index of refraction, n, is given by:

$$n = 1 - \delta + i\beta \tag{24}$$

where δ, the dispersion is given by

$$\delta = \frac{r_e \lambda^2}{2\pi} n_e \tag{25}$$

where r_e is the classical electron radius, n_e is the electron density and λ is the wavelength of radiation. The dispersion can be related to the mass density of the material. Thus, this allows us to then relate the critical angle, θ_C, where the beam first begins to penetrate the film, to the mass density, ρ, of the film neglecting β:

$$1 - \delta \approx n_1 \tag{26}$$

$$\cos\theta_C = n_1 / n_{air} \tag{27}$$

$$1 - \frac{\theta_C^2}{2} \approx 1 - \delta_{TIT} \tag{28}$$

where δ_{TIT} is dispersion at critical angle and given by:

$$\delta_{TIT} = \frac{\theta_C^2}{2} = \frac{r_e}{2\pi} N_A \frac{Z - f'}{A} \rho \lambda^2 \tag{29}$$

where N_A is Avogadro number, Z is the number of electrons per atom and f' is a correction term due to the X-ray absorption edge. Thus, we can determine the mass density of the material. The Kiessig fringes that result from interference after the beam has entered the sample can be used to determine the thickness:

$$a_m^2 = a_c^2 + m^2 \frac{\lambda^2}{4t^2} \tag{30}$$

where t is the thickness of the film, m is the order of the fringe and a_m is position of the fringe in radians. Surface roughness can be also determined by modelling the extinction of the reflected intensity and the attenuation of the Kriessig fringes.

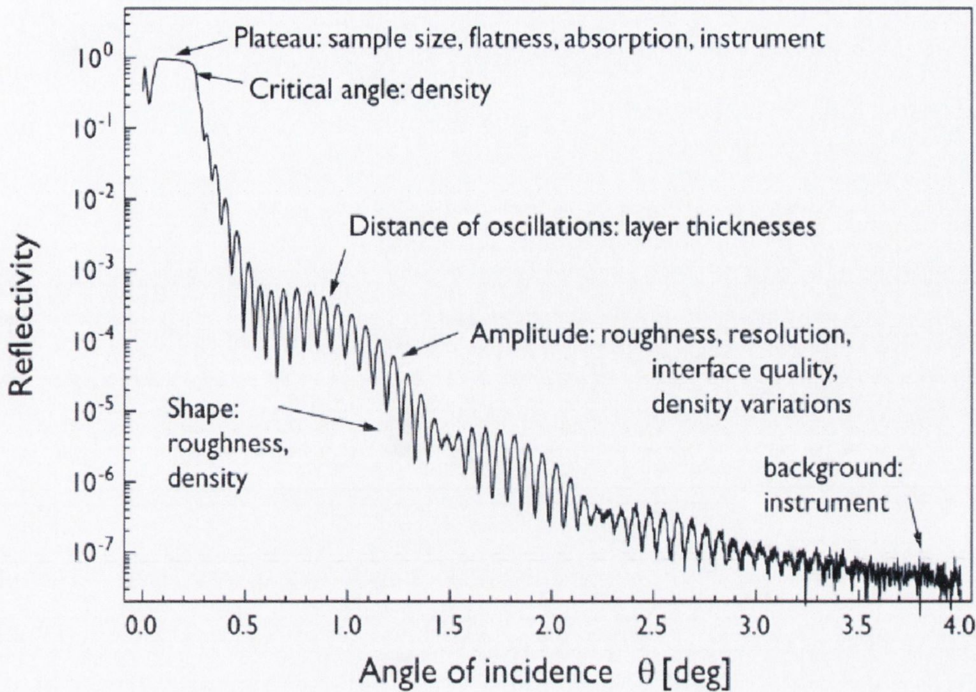

Fig.2.7 Possible features with explained sources in X-ray reflectivity curve, from Philips Panalytical .

XRR measurements were performed by doing $\theta/2\theta$ scan from 0° to 3°. The intensity curves are then modelled using Philips X'Pert Reflectivity software which calculates the optical properties of the layers and fits using a least squares method.

2.3.3. White Light Interferometry

White Light Interferometer was also used for thickness measurements for the samples with thicknesses over 200nm. Measurements were performed using Zygo New View 100 white light interferometer located in Centre of Microscopy and Analysis, Trinity College Dublin. Prior the measurements samples were masked using photoresist and then etched using HF or HCl acid creating a sharp film-substrate step.

Interferometry is a traditional technique in which a pattern of bright and dark lines (fringes) result from an optical path difference between a reference and a sample beam. Incoming light is split inside the interferometer, one beam going to an internal reference surface and the other to the sample. After reflection, the beams recombine inside the

interferometer, undergoing constructive and destructive interference and producing the light and dark fringe pattern. A precision translation stage and a camera together generate a three-dimensional interferogram of the sample, which is stored in the computer memory. The 3D interferogram is then transformed by frequency domain analysis into a quantitative 3D image. The minimum vertical resolution of Zygo New View 100 is 0.1 nm.

Interferometry is a non-contact technique for measuring surface roughness (Ra) on a range of samples. A surface profile is also generated to coincide with the area used for measuring surface roughness.

2.3.4. Atomic Force Microscopy

Atomic force microscopy (AFM, Digital Instruments) was used to study morphology of the samples. This technique does not require any special sample preparation. Using pressurised Ar gas, the dust was removed from the surface of the films, after that, samples were attached to the holder.

AFM measurements were performed using a tapping mode AFM. In tapping mode, it measures topography by tapping the surface with an oscillating tip. This eliminates shear forces, which can damage soft samples and reduce image resolution. As the cantilever bounces vertically, the reflected laser beam is deflected in a regular pattern over photodiode array, generating a sinusoidal electronic signal. The signal is converted to a root mean square (RMS) amplitude value, which is displayed in AC volts on the Tapping Mode output signal meter. The reflected laser beam ("return signal") reveals information about the vertical height of the sample surface, and some characteristics of the sample material itself. These may include elasticity, (hardness) magnetic and/or electric forces present.

2.3.5. Magnetic Force Microscopy

Magnetic force microscopy (MFM, Digital Instruments) was used to study morphology of the ferromagnetic samples. MFM uses the same tapping cantilever as in AFM, although cantilever is equipped with a ferromagnetic tip, which scans the surface

of the ferromagnetic sample. This provides a map of the topology of the sample. The cantilever is then lifted a certain distance from the surface. The scan is repeated without the "tapping" of the surface, keeping a fixed height using the topology recorded in the first scan. Any deflection of the tip during the scan will occur only due to a magnetic interaction between the surface of the film and ferromagnetic cantilever tip. This deflection is measured using a laser and mapped to an image. From the scans performed in this mode it is possible to see magnetic domains of the sample and the size of domains.

2.3.6. Scanning Electron Microscopy

Morphology of the samples was also studied using a scanning electron microscope (SEM, variable pressure Hitachi S-3500N).

The scanning electron microscope accelerates electrons that have been generated by heating a tungsten filament through a many kilovolt potential. The electrons are focused to a beam by magnetic lenses and irradiated onto the sample. The electrons interact with the sample under investigation. The most important interactions of the electrons in SEM are leading to the emission of backscattered electrons, secondary electrons and X-rays.

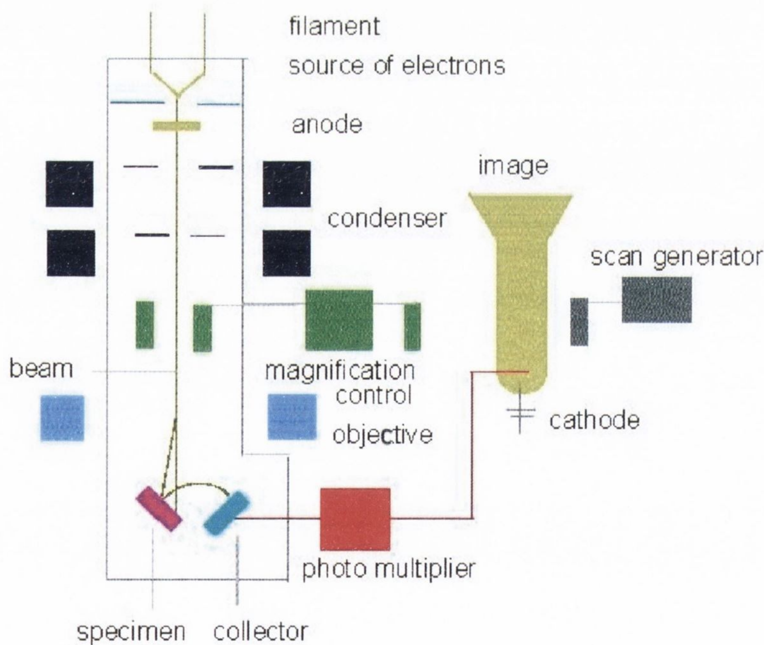

Fig. 2.8 Principal scheme of SEM

Backscattered electrons are formed when the beam electrons encounter the nuclei of atoms within a sample. If they interact at an angle close to that of the incident beam, they may be backscattered. The number of backscattered electrons depends on the atomic number of the atoms in the sample. The higher the atomic number, the more likely electrons will interact with the nuclei. Backscattered electrons can be used to produce an image, which will give details of the specimen in terms of the elements that make it up. Thus, elements with higher atomic numbers will give a brighter image.

Secondary electrons are the most important in the SEM technique. They are formed when the electrons interact with the electrons in the sample, rather than the nucleus. Energy loss is observed during this interaction resulting in a slight deflection in the path of the incoming electrons and the ionisation of the sample electrons. The electrons that exit the sample at lower speed than backscattered electrons are called secondary electrons. Because secondary electrons have a low energy they have to be collected by detector near the surface of the sample, thus giving an impression of the topography of the sample.

2.3.6.1. Energy Dispersive Analysis of X-rays

The X-rays in SEM microscopy are used in a technique called Energy Dispersive Analysis of X-rays (EDAX).

The SEM used for morphology studies was also equipped with (EDAX) elemental analyser. The bombardment of electrons from the beam produces X-rays as well as the backscattered and secondary electrons. Once the secondary electrons are produced, there is a resulting vacancy in the shell (usually the K-shell) of the ionised atom. Then the higher energy electrons from higher outer energy levels can occupy the position with the lower energy thus emitting the excess energy in the form of X-rays. The X-rays produced are characteristic of the element and can be detected and separate into energy spectrum. From the peaks positions and their intensities in the energy spectrum, the elements and their relative abundances in the sample can be found.

Approximately 5 measurements were taken for each of the analysed samples. The error in measurement was determined from the standard deviation of these measurements.

2.3.7. SIMS and XPS

Secondary ion mass spectroscopy (SIMS) and X-ray photoemission spectroscopy (XPS) analysis was performed in the Material Research institute of Vilnius University using RIBER LAS-SIA2000 (SIMS AUGER XPS) analyser. In SIMS a beam of ions is used to sputter the surface and the ionised fragments are monitored using a mass spectrometer. For depth profiling the intensities of these fragments are recorded as a function of erosion depth. Using standards the signal may then be translated into concentration. Quantification in SIMS is generally applicable for measurement of dilute impurities in dilute matrices. The main application of depth profiling SIMS is measurement of dopants and impurities in semiconductor materials. During SIMS analysis, the sample surface is slowly sputtered away. Continuous analysis information as a function obtains composition of depth. Depth resolution of a few Angstroms is possible. High sensitivity mass spectra can be recorded or reconstructed at any depth of the depth profile.

In XPS, the surface is irradiated with X-rays, which excite the photoelectrons. A major advantage of the technique is that the energy spectrum of the photoelectrons is dependent on the precise chemical configuration of the surface atoms and that pronounced chemical shifts are produced in the position of the peaks in spectrum providing information regarding chemical bonds. Chemical bonding will clearly have an effect on both the initial state energy of the atom and the final state energy of the ion created by emission of the photoelectron. So the presence of chemical bonding (and hence, neighbouring atoms) will cause binding energy shifts that can be used to extract information of a chemical nature, such as atomic oxidation state, from the sample surface. For this reason, XPS is also known as Electron Spectroscopy for Chemical Analysis (ESCA).

2.3.8. Optical Spectroscopy

Optical spectrometry measurements were performed using a dual-beam PerkinElmer Lambda 900 Spectrophotometer, which measures transmission for wavelengths ranging from 180-3300nm. To balance the signal difference between two arms transmission was first measured with the sample holders, without any samples.

Effect of the substrate was also determined by measuring transmittance with the substrate loaded in one sample holder. Then measurements were carried on the samples. Analysed sample was placed in one sample holder and the reference substrate in the second sample holder and transmission spectra was obtained in the visible wavelength range from 300-800nm.

2.3.9. Raman Spectroscopy

Raman spectroscopy is named by Indian physicist C. V. Raman who first observed the inelastic scattering phenomenon in 1928 and for it he was awarded the Nobel Prize for Physics in 1930. The Raman Spectroscopy technique is based on the interaction of electromagnetic radiation with a molecule. The interactions of photons with a molecule can yield three phenomena: absorption, emission and scattering. In absorption event, the photon transfers its energy to the molecule, resulting in its transition to a higher energy state. Emission occurs when the molecule drops from a higher energy state to a lower one, and the energy lost in this process is emitted as a photon. Scattering occurs as an immediate effect ($\sim 10^{-14}$ s) of the interaction of the photon with the molecule. The vast majority of scattered photons have exactly the same energy, thus the same wavelength, as the incident photons and are known as Rayleigh scatter. A small portion (approximately 1 in 10^7) of the scattered radiation is shifted to the different wavelengths. The process leading to this inelastic scatter is termed Raman effect. The most of the Raman scattered photons are shifted to the longer wavelengths (Stokes scattering), but a small portion of these photons are shifted to shorter wavelengths (anti-Stokes scattering). Figure 2.8 shows a diagram of scattering effects occurring in Raman. Raman scattering can occur with a change in vibrational, rotational or electronic energy of a molecule.

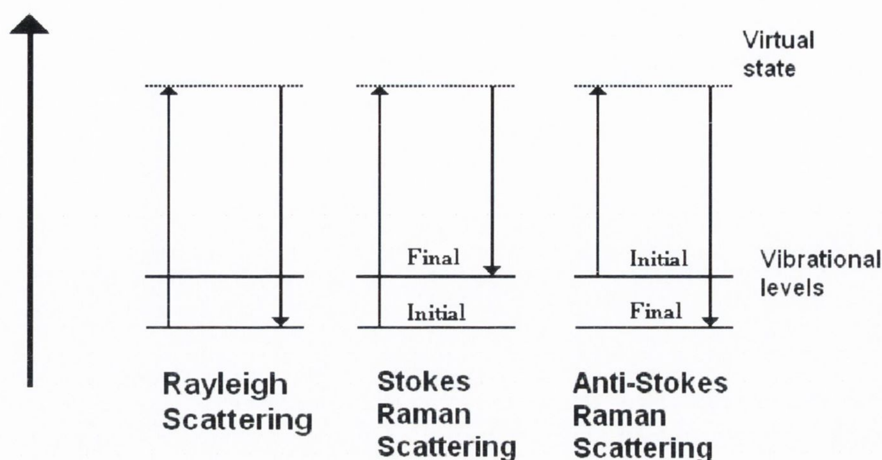

Fig. 2.9 Energy-level diagrams of Rayleigh scattering, Stokes Raman Scattering and anti-Stokes Raman scattering

Stokes scattering is much more common than anti-Stokes scattering because at any given time an electron in the most common temperature range is more likely to be in its lowest energy state, in accordance with Boltzmann distribution. For this reason, it is the measurement of Stokes bands, which are of most importance in Raman spectroscopy. A Raman Spectrum is a plot of the intensity of Raman scattered radiation as a function of its frequency difference from the incident radiation (usually expressed in cm^{-1}). This difference in a frequency is called Raman shift.

The energy of a vibrational mode depends on molecular structure and environment. Atomic mass, bond order, molecular substituents, molecular geometry and hydrogen bonding all affect the vibrational force constant which, in turn dictates the vibrational energy. Vibrational Raman spectroscopy is not limited to intramolecular vibrations. Crystal lattice vibrations and other motions of extended solids are Raman-active. Their spectra are important in such fields as polymers and semiconductors. In the gas phase, rotational structure is resolvable on vibrational transitions. The resulting vibration/rotation spectra are widely used to study combustion and gas phase reactions generally.

Raman spectra were measured with a Renishaw 1000 Micro-Raman system. The laser used was an Ar^+ ion laser (Laser Physics Reliant 150 Select Multi-Line) with an excitation wavelength of 514.5 nm and a typical laser power of 3mW.

2.3.10. SQUID

Magnetic measurements were performed using a Quantum Design MPMS XL magnetometer, which has a SQUID and 5T magnet in its heart. In a SQUID measurements can be performed at the temperatures of 2 - 300K. SQUID is a superconducting quantum interference device, which consists of a superconductor with two parallel Josephson junctions. If a magnetic field is applied perpendicular to the plane of the superconductor, the electrons undergo a different phase shift in the two Josephson junctions, resulting in destructive interference, which yields a field dependent voltage that can be accurately measured. The output voltage of the SQUID is proportional to the moment.

The ferromagnetic moment of the thin DMS films is very small compared to the diamagnetic moment of the much thicker substrate. The film's magnetic moment was obtained by subtracting the substrate's linear diamagnetic moment, using a straight line fit (in Origin program) of the values at higher magnetic field, where the ferromagnetic moment is saturated and does not contribute to the increase of the actual moment of the film.

Before measuring the samples, the dust was removed from the surface. Also silver ink, which is used to attach the film to PI MOCVD sample holder, was removed from the back side of substrate. Then, the corners of quadratic samples were cut off, so that the sample could be fitted into a straw (5mm in diameter). After that, the straw was loaded into the SQUID to perform a scan. Typically, scans were performed at 300K.

2.3.11. Vibrating sample magnetrometry

Magnetisation measurements of up to 900 K were made by vibrating sample magnetrometry (VMS). The applied field of up to 1.1 T was created in the bore of two concentric Hallbach cylinders. Magnetic field can be varied by rotating the cylinders with respect to each other. The magnetisation of the sample is vibrated at a frequency 0f 29.4 Hz and induces a voltage in a set of pick-up coils, which are also located inside the bore. The voltage can be expressed by Faraday's Law:

$$V = -\frac{d\Phi}{dt} \tag{31}$$

The obtained voltage is then referenced against that of a known calibration sample (Ni sphere) and the magnetisation is deduced. The magnetisation of Ni sphere is 55.86 Am^2kg^{-1}.

References:

[1] S. G. Hammond, D. C. Nonhebel, C.-H. S. Wu, *Inorganic chemistry* **1963**, *2*, 73.

[2] STREM, *Vol. 20*, **2004-2006**.

[3] X. Yang, G. Du, X. Wang, J. Wang, B. Liu, Y. Zhang, D. Liu, D. Liu, H. C. Ong, S. Yang, *Journal of Crystal Growth* **2003**, *252*, 275.

[4] M. Kasuga, T. Takano, S. Akiyama, K. Hiroshima, K. Yano, K. Kishio, *Journal of Crystal Growth* **2005**, *275*, e1545.

[5] Yanwei Ma, Kazuo Watanabe, Satoshi Awaji, a. M. Motokawa, *Applied Physics Letters* **2000**, *77*, 3633.

[6] X.-L. Tang, H.-W. Zhang, H. Su, Z.-Y. Zhong, Y.-l. Jing, *Journal of Solid State Chemistry* **2006**, *179*, 1618.

Chapter 3: Co-doped ZnO films

3.1. Introduction

ZnO is a transparent oxide that crystallises in a hexagonal wurtzite structure. In the nature ZnO occurs in the form of white hexagonal crystals or white powder commonly known as zinc white, although, high quality single-crystalline zinc oxide is almost transparent. Bulk ZnO has a density of 5660 kg/m^3. Melting point of ZnO is 1975 °C and decomposition occurs upon melting [1].

ZnO is a very important chemical compound that found a numerous applications in different areas of industry, including pharmacy and cosmetics. ZnO is one of the ingredients in the commercial manufacture of rubber goods. It found the use in the preservation of plantation latex as it reacts with the enzyme responsible for the decomposition. In the production of latex foam ZnO is particularly effective in gelation of the foam with increased stability. ZnO provides a high degree of whiteness and tinting strength in rubber products (surgical gloves) also acting as an effective stabiliser as it is very effectively absorbs the UV. In the plastic industry ZnO is used to increase the heat resistance and mechanical strength of acrylic composites. It contributes to the formation of epoxide resin, while adding ZnO together with aliphatic polyamines imparts higher tensile strength and water resistance. Applications in development for ZnO stabilised polypropylene and high-density polyethylene include safety helmets, stadium seating, insulation, pallets, bags, fiber and filament, agricultural and recreational equipment.

Some of the newer applications of ZnO are used in ceramics, such as electronic glass or low melting glass for metal-to-glass seals. When added to glass ZnO reduces the coefficient of thermal expansion, imparts high brilliance and lustre together with high stability against deformation under stress.

In pharmacy ZnO is mainly used in zinc soap, ointment, dental inlays and food powder. The optical properties of ZnO are used in cosmetics, for example, in creams and powders to protect the skin from absorbing the UV sun rays.

Other applications of ZnO would include such areas as adhesives and sealants, photocopying equipment, paints, metal-protective coatings and many others.

Fabricated in the film form ZnO is a transparent wide band gap semiconductor with a direct energy gap of 3.37 eV at room temperature. ZnO is a strong piezoelectric [2], in which the piezoelectric properties can change the characteristics of potential energy barriers at interfaces. Piezoresistance of ZnO is exploited in metal oxide varistors, which can dissipate large amount of power in a short response times and are commonly found as electrical surge protectors [3]. ZnO has a strong potential for various short-wavelength optoelectronic device applications. In order to explore its optoelectronic properties both high quality n-type and p-type ZnO is necessary.

ZnO thin film usually has N-type conductivity due to electron doping via defects including Zn interstitials (Zn_i), O vacancies (V_O) in the ZnO lattice or different impurities (for example hydrogen), although, the real nature of residual N-type conductivity in undoped ZnO films is still remaining unanswered. Some authors [4] suggested that it is Zn_i rather than V_O is a dominant native shallow donor in ZnO, while others claimed [5, 6] that n-type conductivity in ZnO is only due to hydrogen (H). N-type doping is very easy to achieve, for example, high electron carrier density can be realised by doping ZnO with group III elements (Al, Ga, In) [7, 8].

In contrast, P-type doping of ZnO is difficult to attain. The main difficulties could arise from different causes, like, low solubility of dopant in the host matrix or dopants may be compensated by low-energy native defects. P-type doping in ZnO may be possible by substituting group I elements (Li, Na and K) for Zn sites or group V elements (N, P and As) for O sites. However, due to small atomic, radii group I elements tend to occupy interstitial sites rather than substitutional sites, and therefore, act mainly as donors in ZnO [9]. Moreover, K and Na have significantly larger bond length than ideal Zn-O (1.93 Å), which induces lattice strain and increases the formation of native defects such as vacancies that compensate dopants [10]. All these reasons lead to the difficulties in attaining P-type doping in ZnO. It was predicted that N could be a good candidate for a shallow P-type dopant in ZnO [11], although solubility of N in ZnO is very low. For this reason different growth methods [12-14] and different N sources [12, 14-16] were tried in order to get p-type conductivity in N-doped ZnO. Although, the reproducibility of producing p-type ZnO still remains to be a major problem, which has to be solved before ZnO can be used in optoelectronics applications such as LEDs and laser diodes (LDs).

ZnO is also a promising candidate for spintronics applications. Interest in ZnO-based DMSs was initially generated by the theoretical work of Dietl and co-workers [17]. Their calculations showed Mn-doped ZnO would exhibit above-room-temperature ferromagnetism if the material was grown with substitutional Mn^{+2} ions and sufficiently high levels of some p-type dopant. Recently, Mn-doped ZnO has been showed to be ferromagnetic, but Curie temperature was 250K [18]. Subsequent experiments, on Co-doped ZnO, performed by Ueda *et al*, showed ferromagnetism up to 320K [19]. Several groups have fabricated transition (TM) metal doped ZnO, where TM is Sc [20, 21], Ti [20, 21], V [20-22], Cr [19-21], Mn [19, 20, 23-25], Fe [21], Co [20] [19, 21, 25-28], Ni [19-21, 29] and Cu [20, 21] using different techniques. Although, there is a lot of controversy about the source of ferromagnetism in TM-doped ZnO films found in different reports. Detailed review on recent status in a field of TM-doped ZnO is presented in Chapter 1.4.3.1.

Assuming that ZnO can be made ferromagnetic by doping with TM metals it has the potential to be a highly multifunctional material with coexisting magnetic, semiconducting, electromechanical and optical properties.

This chapter is mostly focused on the deposition and investigation of Co-doped ZnO films. In this work we used PI MOCVD technique to grow Co-doped ZnO. There are several reports on Co-doped ZnO grown by conventional CVD [30, 31], although very few reports have been published on ZnO grown by MOCVD with liquid delivery system [32]. Most of the attention was paid to the optimisation of growth conditions in order to get good crystalline quality of pure ZnO. The next step of the work included doping ZnO with Co in order to investigate its magnetic properties. We also investigated the effect of magnetic field applied during the growth of Co-doped ZnO films. The main aim was to observe the possible changes in structure, morphology and magnetic properties of the Co-doped ZnO films.

3.2. Deposition of undoped ZnO films

The initial work of this project was focused on the deposition of undoped ZnO films. To the best of our knowledge ZnO films have never been deposited using PI MOCVD. Therefore, it was crucial to establish and optimise deposition conditions for achieving good quality crystalline ZnO films before investigating the growth of magnetic

Co-doped ZnO structures. The influence of deposition temperature and oxygen concentration on the growth of ZnO was investigated.

3.2.1. Precursor characterisation and screening

All ZnO films were grown using $Zn(tmhd)_2$ precursor. The advantage of this precursor is that it is highly volatile at higher temperature and stable at room temperature. The melting point of $Zn(tmhd)_2$ is 144°C and boiling point is at 250°C [33]. Respectively, the evaporation temperature of PI MOCVD reactor was selected in the temperature range of 144-250°C, this should allow precursor vapours to travel to the heated substrate and decompose, forming ZnO film. Unfortunately, the premature reactions between Zn-metalorganic compound and the oxidant gas (O_2) were observed under these conditions. This led to the particulates forming in the deposition chamber and as a result no ZnO film was formed on the substrate.

To avoid undesirable premature precursor reactions a TPA study of $Zn(tmhd)_2$ was carried out. TPA showed that at 50 mbar pressure of Ar gas evaporation of $Zn(tmhd)_2$ precursor began at 90°C, which is much lower than the previously chosen evaporation temperature. Relying upon the results obtained from TPA, evaporation temperature for the growth of ZnO was set at 90°C. The resultant growth of ZnO films under different conditions is discussed below.

3.2.2. Studies of the influence of deposition temperature

To investigate the effect of growth temperature ZnO films were grown on Al_2O_3 (0001) substrates at different temperatures. Deposited films were characterised by X-ray diffraction. The main criterion for deposited ZnO films was good crystalline quality. The main deposition conditions are summarised in the Table 3.1.

Table 3.1 Deposition conditions for ZnO grown at different temperatures

Deposition temperature	450-600°C
Evaporation temperature	90°C
Carrier gas flow (Ar + O_2)	1500 ml/min

Reactor pressure	5 mbar
Zn source	$Zn(tmhd)_2$
Solvent	1,2- dimethoxyethane
Solution concentration	0.025 M
Impulse frequency	2 Hz
Microdose mass	4 mg

All films deposited at different temperatures have showed ZnO (002) preferred orientation, as shown in Figure 3.1. ZnO (002) orientation is admitted to be preferred for films grown on Al_2O_3 (0001) substrates due to its lowest surface energy [34].

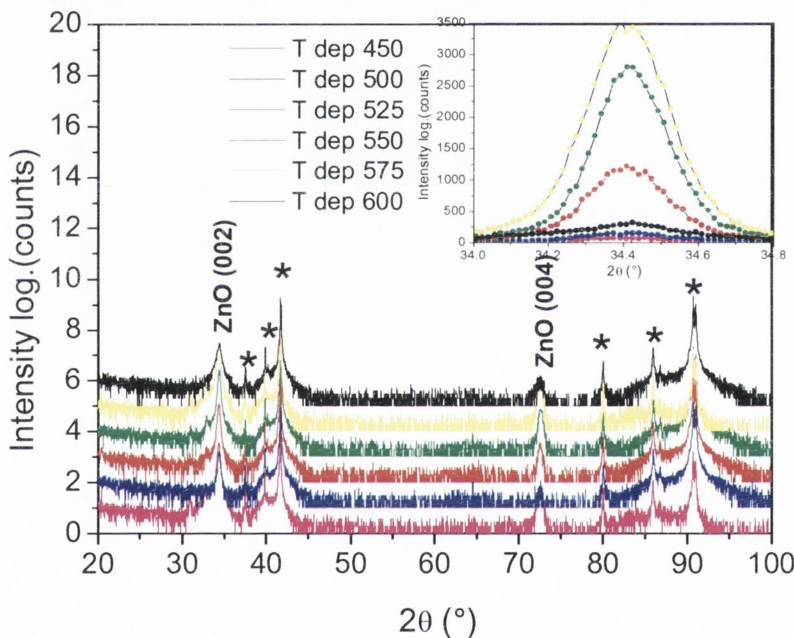

Fig. 3.1. X-ray diffractogram of the ZnO films deposited at different temperatures. Inset shows magnified ZnO (002) reflection at 34.422°; * indicates Al_2O_3 (0001) reflections

Moreover, no significant shift of the (002) diffraction was observed, indicating that residual stress and associated strain may not affect the structural properties of the films (see inset in Figure 3.1.). Films grown at 450°C, 500°C and 600°C showed very poor crystalline quality exhibiting very weak ZnO (002) reflection. As the growth temperature

increases to 575°C, the intensity of the ZnO (002) diffraction peak becomes much stronger. The FWHM value of the films confirmed that the best crystalline quality films were obtained at 550°C with FWHM of ~0.23°, refer to Figure 3.2. Films grown at 450°C, 500°C, and 600°C temperatures had significantly larger FWHM, indicating poorer crystalline quality.

The thickness of the ZnO films was measured using XRR. The change of the film thickness with deposition temperature can be seen in Figure 3.2. The maximum growth rate was found for the sample grown at 550°C, indicating that this temperature is optimal for the decomposition of precursor and growth of the film. We could not estimate the thickness of the films grown at 450°C and 600°C due to its high roughness and low density, which resulted in the absence of fringes in the XRR measurements. For example, the density of the ZnO grown at 600°C was only 4.4 g/cm^3, as compared to the bulk value of 5.6 g/cm^3. The films grown at lower temperatures had significantly higher densities (5.45 ± 0.05 g/cm^3). Similar growth rates were found in some liquid injection MOCVD

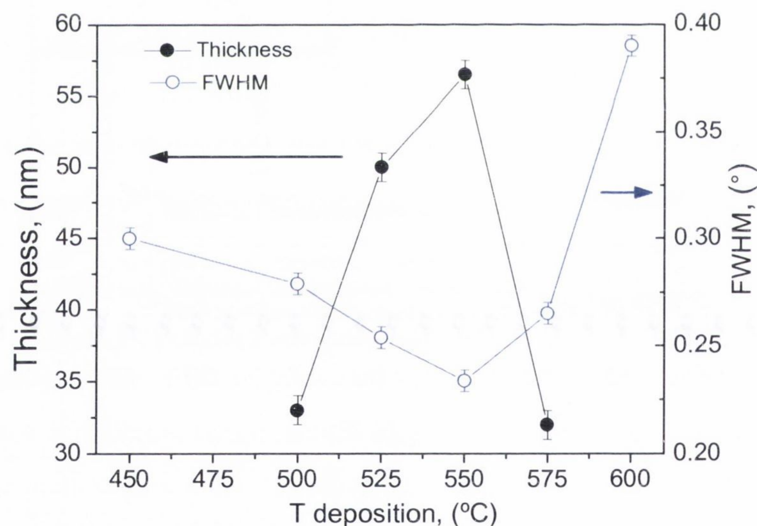

Fig. 3.2. Thickness (black symbols) and FWHM (blue symbols) of the ZnO films as a function of deposition temperature

grown ZnO films [35], with the maximum rate found at 550°C. Above that temperature growth rate rapidly decreased. The decrease in the growth rate was attributed to desorption of ZnO due to its high vapour pressure [35] or decomposition of ZnO [31]. The

low density of our ZnO films grown at 600°C could also be explained by desorption or decomposition of the film.

In summary, it was found that the deposition temperature of 550°C was optimal for the growth of ZnO films. Resultant films showed maximum growth rate, high intensity ZnO (002) reflection with lowest FWHM value. This optimal temperature was used for all further depositions of ZnO films.

3.2.3. The influence of oxygen concentration

To find the optimal oxygen concentration ZnO films were deposited at 550°C at different O_2 content in the carrier gas mixture. O_2 concentration was varied from 0%, 25%, 35% and 50% in total gas mixture. All other deposition conditions are similar as described in Table 3.1.

Again, only the ZnO (002) diffraction peak could be found for all films deposited at different O_2 concentrations, however, no film formation was observed when O_2 concentration was 0%. This means that O_2 is essential to promote the decomposition of the precursor vapours.

ZnO (002) peak intensity increased together with O_2 concentration. The highest peak intensity was found for the films deposited at 50% O_2 in the total gas mixture, indicating that the strongest preferred orientation along the c-axis is obtained (Figure 3.3.). FWHM measured for the (002) diffraction of ZnO decreased with O_2 concentration, also confirming that the better crystalline quality of the films is achieved at 50% O_2.

The average crystallite size of ZnO films formed at different O_2 concentrations was calculated from (222) diffraction using Scherrer formula. For films grown at 20 % O_2 calculated average crystallite size was ~ 35nm, for 35% O_2 it was ~ 42nm and the maximum crystallite size of ~ 53nm was found for 50% O_2. The average surface roughness (Ra) and surface morphology were measured by AFM (Figure 3.4.). In correlation with the increased crystallite sizes, surface roughness also increased from 2.3nm to 6.26 nm with increase in O_2 from 20% to 50%. In addition, formation of larger crystallites at 50% O_2 is also confirmed by AFM.

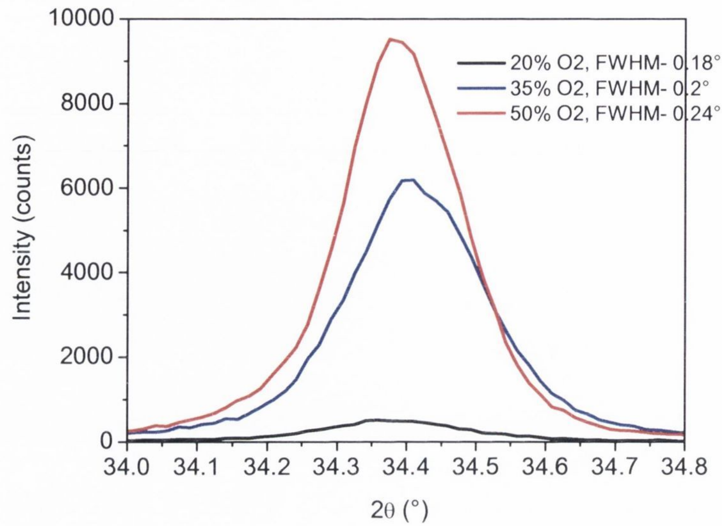

Fig. 3.3. X-ray diffractogram of ZnO (002) diffraction as a function of oxygen concentration

The increase in crystallite size together with surface roughness with O_2 concentration is attributed to an increase in precursor decomposition reaction and consequently increased reaction rate. At these conditions the reaction at the substrate surface becomes diffusion-rate limited, consequently fewer growth centres are formed resulting in the formation of larger crystallites.

XPS analysis of the ZnO film surface showed that oxygen content in the films is noticeably decreasing with decrease in O_2 concentration. Stoichiometric films with Zn/Co = 1 were obtained only for 50% O_2. The Zn/Co ratios of 1.18 and 1.32 were found for the films grown at 35% and 20% O_2 respectively.

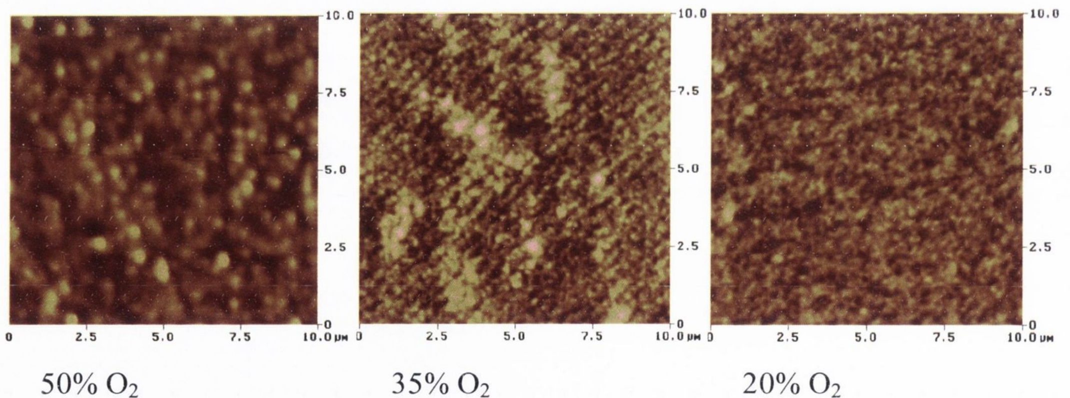

50% O_2 35% O_2 20% O_2

Fig. 3.4. AFM images of ZnO films at different O_2 concentrations. The scale size of a square is 10μm.

Thus, results described in this section showed that ZnO films grown at 50% O_2 were stoichiometric and had best crystalline quality. Oxygen concentration of 50% was selected for the deposition of Co-doped ZnO films.

3.3. Co-doped ZnO films

Ferromagnetism in diluted magnetic oxides is the most interesting new problem in magnetism. The results are found to be very sensitive to the form of the sample and preparation method. Following the original report by Ueda *el al.* [19] there have been a numerous reports on the wide-gap semiconductor ZnO, which exhibit ferromagnetism with Curie point above room temperature, when a few atomic percent of Co [36-39] or another transition element [25, 40] is substituted for ZnO. However, these results are very controversial, for example Ueda *el al.* [19], found that saturation magnetization (M_S) per Co atom in PLD grown Co-doped ZnO films was $2\mu_B$/Co. While, Venkatesan *el al.* [41] found a maximum saturation moment of $2.6\mu_B$/Co in some PLD grown ZnO films doped with 5% of Co, in addition films showed enormous in-plane anisotropy. A very low saturation moment of $0.7\mu_B$/Co was found in some laser ablation grown (Zn,Co)O films [42]. And even smaller moment of $0.56\mu_B$/Co was observed in spin-coated (Zn,Co)O films [40], moreover magnetization curve measured at 350K showed hysteresis loops with the coercive field of 80 Oe in 20% doped sample. In MOCVD deposited (Zn,Co)O films [43], the reported value of moment per Co atom at room temperature ranged from 0.01 to $0.07\mu_B$/Co, and coercive fields were in the range of 100-200 Oe.

3.3.1. Preparation of Co-doped ZnO films

To probe the origin of high-temperature ferromagnetism in Co-doped ZnO thin films systematic variation of magnetism as a function of Co concentration was examined. The main deposition conditions for Co-doped ZnO films are presented in the table below.

10 different coatings were prepared on *c*-cut and *r*-cut sapphire substrates by PI MOCVD. Co concentration in the precursor solution was increased from 1 to 20 mol%

and Zn concentration in solution was maintained to be constant (0.025mol/l). The thickness of the films varied with Co concentration and increased from 59nm to 102nm for 20% Co doping, as measured by white light interferometer.

Table 3.2 Deposition conditions for Co-doped ZnO films

Deposition temperature	550°C
Evaporation temperature	90°C
Carrier gas flow (Ar + O_2)	1500 ml/min
Reactor pressure	5 mbar
Metalorganic precursors	$Zn(tmhd)_2$, $Co(tmhd)_3$
Solvent	1,2- dimethoxyethane
Zn/(Co+Zn) concentration in solution	0.025 mol/l
Co/(Co+Zn) concentration in solution	1, 2, 5, 10, 20%
Impulse frequency	2 Hz
Microdose mass	4 mg
Substrates	Al_2O_3 (0001), Al_2O_3 $(1\underline{1}02)$

3.3.2. Characterisation of the films

3.3.2.1. Film composition

Film composition was examined using three different techniques: EDAX, SIMS and XPS. Co concentration in the film measured by EDAX was found to be only slightly larger than that of the precursor solution (Figure 3.5). Errors were calculated as the average standard deviation using five measurements on each of the samples. Co concentration in a films deposited using 1 and 2% of Co in precursor solution was below detection limit of the instrument.

The Co doping concentration measured by the surface sensitive SIMS and XPS techniques is considerably larger than that obtained by EDAX (Figure 3.5), which for these films can be considered as a bulk technique. For the 1% Co doped ZnO films the signal was too small to be detected by the XPS and SIMS. Significantly higher Co concentration detected by SIMS and XPS suggests that distribution of Co in the films is not uniform. The formation of a Co-rich surface layer is also confirmed by the SIMS depth profile of a 20% Co-doped film shown in Figure 3.6. For this particular film the

surface layer with enhanced Co concentration is about 20nm thick, and the transition from a highly doped surface layer to a film with a substantial lower Co concentration is quite sharp.

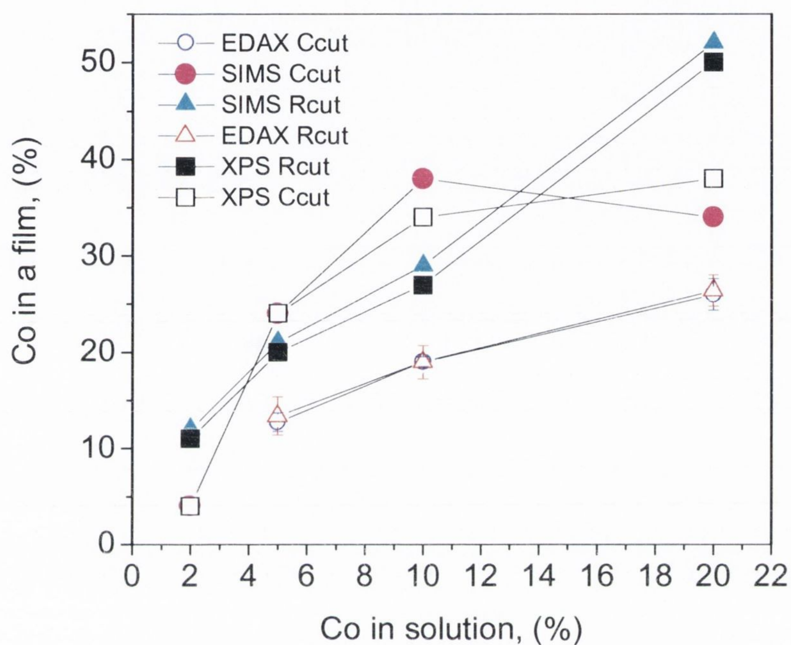

Fig. 3.5. Comparison of SIMS, XPS and EDAX measurements for Co-doped ZnO films on Al_2O_3 (0001) and Al_2O_3 ($1\underline{1}02$) substrates.

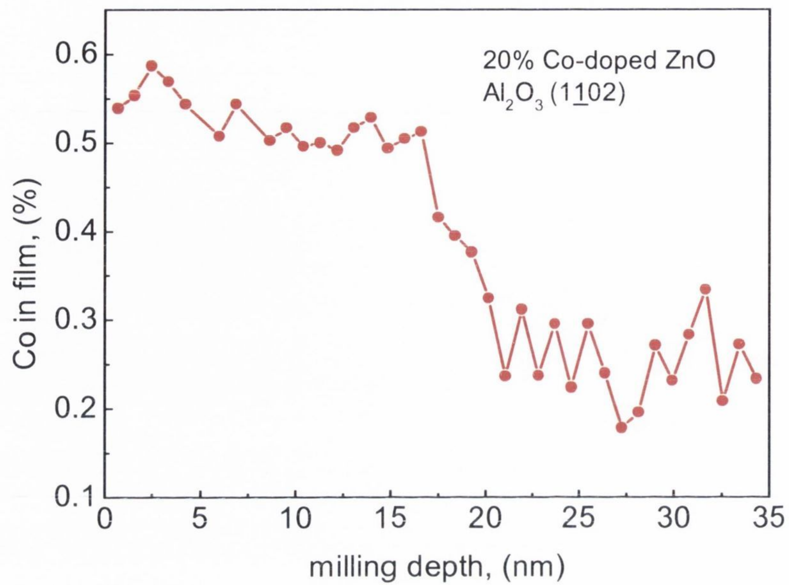

Fig. 3.6. SIMS depth profile of the 20% Co-doped ZnO film on Al_2O_3 (1102) substrate

XPS analysis was also used to characterize the charge state of the Co ions in the films. Figure 3.7, shows the Co 2p electron spectra for Co-doped ZnO films with different doping concentrations. It is expected, that Co^{2+} would incorporate into the wurtzite lattice at Zn^{2+} sites, since the ionic radii of four-coordinate Zn^{2+} and Co^{2+} (0.060 and 0.066nm respectively) differ by only 10%. In addition Co^{2+} is very soluble in ZnO [44]. The Co $2p_{3/2}$ and $2p_{1/2}$ core levels for Co-O bonding are measured at 780.6 eV and 796.3 eV. Indeed, these binding energies are comparable to those of Co^{2+} photoelectrons in CoO and Co_3O_4 [45, 46]. Moreover, two shake-up satellites are visible at higher binding energy. These satellite peaks are typical for Co ions in the divalent Co^{2+} state and are not observed for Co^{3+}. Finally, no maximum is measured at 777.7 eV, the binding energy of metallic Co, and hence the presence of Co clusters can be ruled out. From the XPS analysis we conclude that Co in ZnO wurtzite lattice is present in Co^{2+} state and that metallic Co or other secondary phases do not form during the PI MOCVD growth.

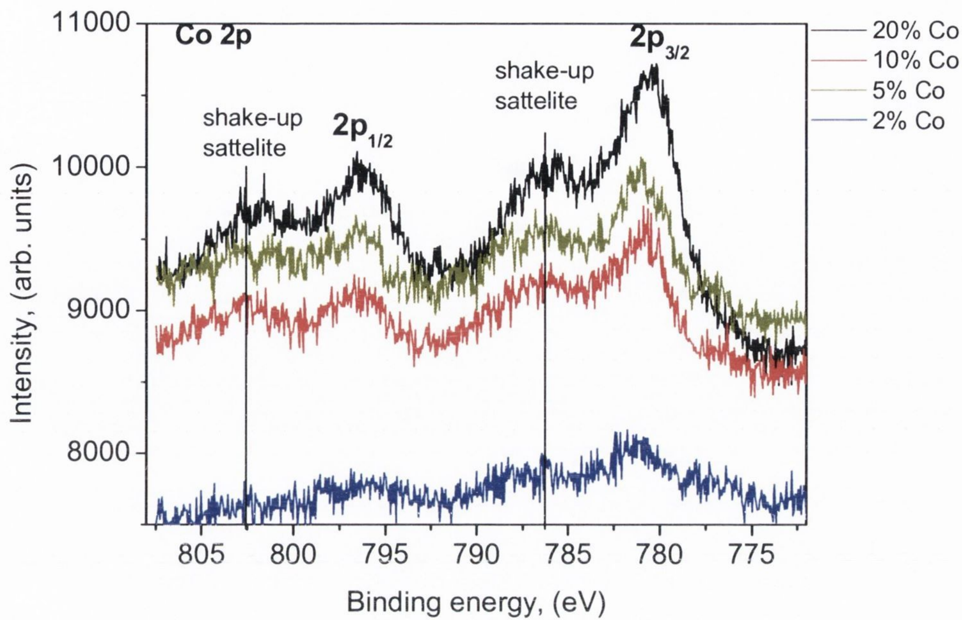

Fig. 3.7. XPS spectra of Co 2p electrons of Co-doped ZnO films with different Co concentrations

3.3.2.1.1. X-ray absorption spectroscopy

Additionally, to probe the vacant states of the conduction band of the Co 2p, O 1s and Zn 2p for the magnetic and non-magnetic samples the X-ray Absorption Spectroscopy (XAS) was performed in Trinity College Dublin. For the best comparison the measurements were performed on undoped ZnO film and 2% Co doped ZnO magnetic and also nonmagnetic samples. The results of the Co *2p* XAS show Co^{2+} ions substituted for Zn ions tetrahedrally coordinated by oxygen anions. The results compared for the 2% Co doped magnetic and 2% Co doped non-magnetic films are shown in Figure 3.8.

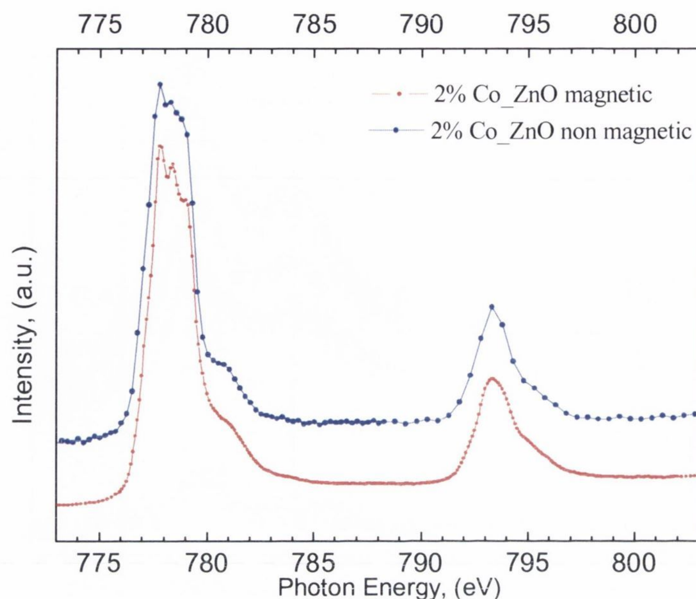

Fig. 3.8. 2% Co doped ZnO: Co 2p XAS. Magnetic sample is in red crosses; nonmagnetic sample is shown in blue circles

The O *2p* XAS spectra of both of these doped films have an additional shoulder close to the threshold of absorption at 531 eV, shown in Figure 3.9. This corresponds to the Co $3dt_2$ states hybridised with O 2p states in the conduction band. However, the magnetic film has another shoulder extending into the below-threshold region of the non-magnetic films, located at 527 eV. It is strongly suggested that these additional states are caused by defects present in the magnetic film and are strikingly similar in character to the features noted in the O *1s* XAS spectra of the PLD grown films[47].

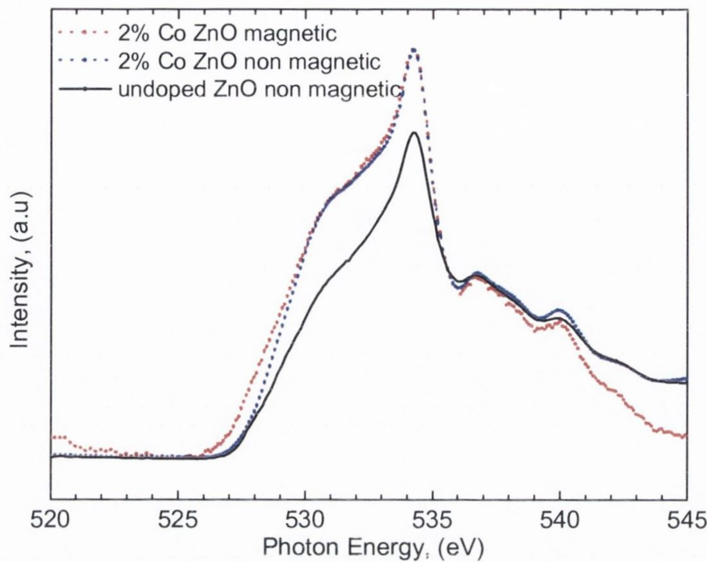

Fig. 3.9 O 2p XAS spectra for 2% Co doped magnetic film (red), non-magnetic film (blue), and undoped ZnO (black)

O *K* Resonant Inelastic X-ray Scattering (RIXS) was also performed to probe the valence band of the Co-doped ZnO and undoped ZnO samples. RIXS analysis of MOCVD grown samples did not show the same degree of 'filling in' of the valley between the Zn 3d states located at 514.0 eV and O 2p states between 516 eV and 518 eV as the PLD grown films[47]. Figure 3.10 shows the emission spectrum obtained for excitation energy of 534.6 eV corresponding to an excitation of a O 1s electron into the states in the first peak of the absorption spectrum. No difference in the emission spectrum is seen for magnetic and non-magnetic Co-doped ZnO. Since the MOCVD grown films were produced at a high oxygen pressure, oxygen vacancy defects are not expected to be present as they are in PLD films grown at very low pressures. This suggests that the role played by the oxygen vacancy defect in the films is not critical. The defects signature seen in the absorption threshold of the O 1s XAS spectra in the both the PLD and MOCVD grown films is more likely associated with ferromagnetic ordering.

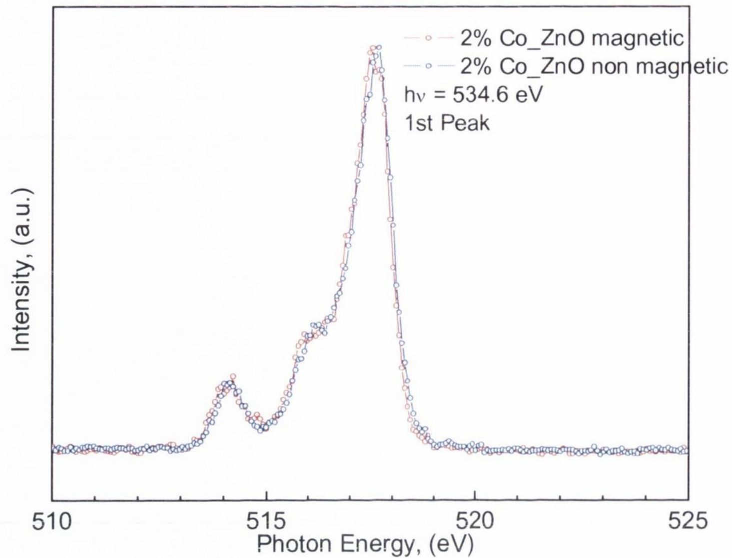

Fig. 3.10. O *K* X-ray emission spectrum for 2% Co-doped non-magnetic and magnetic ZnO films

3.3.2.2. X-ray diffraction

XRD analysis revealed that all Co-doped ZnO films grown on Al_2O_3 (0001) and Al_2O_3 ($1\underline{1}02$) substrates showed good crystalline quality independent on Co concentration. As shown in Figure 3.11, the resultant films exhibit high quality single crystalline (001) and (110) orientations perpendicular to the film plane on Al_2O_3 (0001) and Al_2O_3 ($1\underline{1}02$) substrates respectively. Good film quality was also confirmed by measuring FWHM for rocking curves, which were as low as ~1° and ~0.8° for films on c-cut and r-cut sapphire. In addition, the FWHM of the Co-doped ZnO (002) and (110) reflections and their rocking curves did not change drastically with Co concentration.

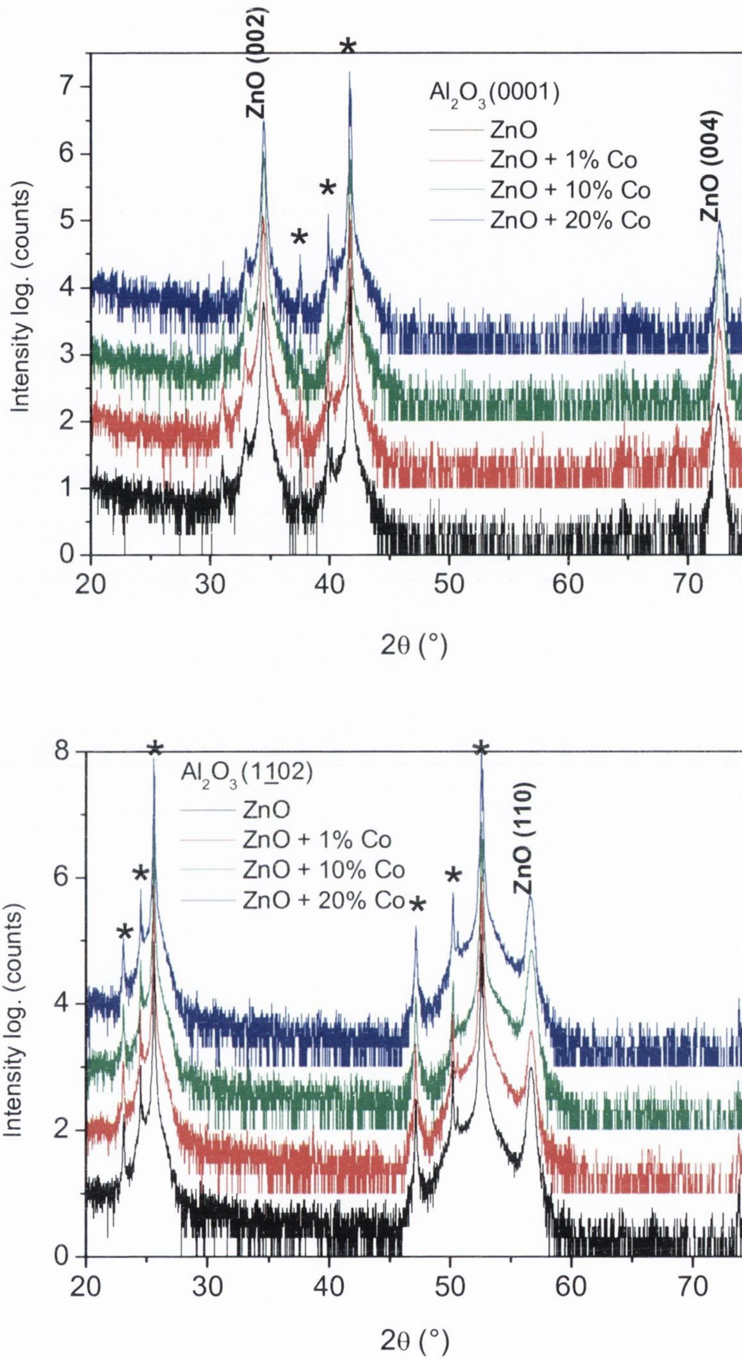

Fig. 3.11. XRD *θ-2θ* spectra of ZnO films with different Co concentrations, grown on Al_2O_3 (0001) and Al_2O_3 (1$\underline{1}$02) substrates showing good crystalline quality even for highest Co concentration in precursor solution

XRD analysis was performed for all of the samples and did not show any presence of secondary phases of CoO, Co_2O_3 or Co_3O_4, or clusters of metallic Co, even for 20% Co concentration. However, it is well known that XRD is not very sensitive for detecting secondary phases, especially if secondary phase clusters are less than 10nm in size. Since all of the above mentioned cobalt oxides are not ferromagnetic, they could not contribute to the room temperature ferromagnetism in Co-doped ZnO. The only possible ferromagnetic secondary phase in Co-doped ZnO system is metallic Co clusters. Some of the magnetron sputtered and pulsed-laser deposited Co-doped ZnO films grown in our laboratory exhibit a small XRD reflection at 76.7°, which indicates the presence of a hexagonal Co (110) phase. For this reasons the detailed measurements with a 25 times larger data collection scans were performed for the 70° $\leq 2\theta \geq$80° (Figure 3.12).

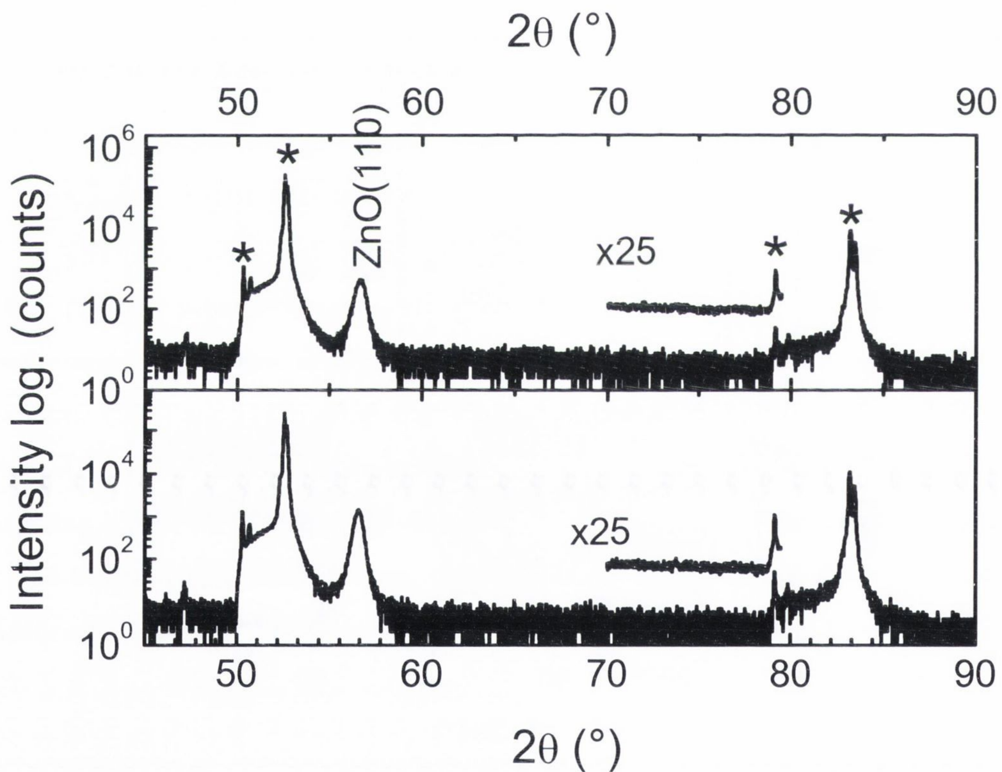

Fig. 3.12. Detailed XRD θ-2θ scan for ZnO films with 10% and 20% Co concentrations, grown on Al_2O_3 (1$\underline{1}$02) substrate. No presence of metallic Co clusters at 76.7° 2θ is seen in the scan

From Figure 3.12 we can see no peak at 76.7 ° even for highest Co concentrations, thus ruling out the possibility of formation of metallic Co clusters in our Co-doped ZnO films.

From the X-ray diffraction it is also possible to calculate Co-doped ZnO film lattice parameters. The *c* parameter of the (001) orientated crystal of ZnO was determined by measuring the (002) *d*-spacing. The bulk value for the 2θ angle of ZnO is 34.426°, which yields a *d*-spacing of 2.603Å, and thus from Bragg's equation a *c* parameter of 5.206Å.

To determine the *a* lattice parameter of (001) ZnO, a (103) *d*-spacing was measured. From the (103) *d*-spacing and *c* parameter, the *a* parameter can be calculated:

$$a = \frac{2d_{103}c}{\sqrt{3}\sqrt{c^2 - 9d_{103}^2}} \tag{27}$$

For (110) orientated ZnO, the *a* parameter was obtained by measuring the (110) *d*-spacing. From the (110) d-spacing with a bulk 2θ value of 56.612°, the *a* parameter is given by $a = 2d$. The c parameter is determined through the *d*-spacing of the (112) plane:

$$c = \frac{2ad_{112}}{\sqrt{a^2 - 4d_{112}^2}} \tag{28}$$

It is well known that the lattice parameter varies with such things, like crystal composition, temperature, pressure, doping level and etc. An increase of Co-doped ZnO lattice parameter is expected with Co concentration due to the substitution of Zn^{2+} by larger Co^{2+} [19, 42].

In our samples, the *a* lattice parameter calculated for undoped ZnO film grown on Al_2O_3 (0001) was much lower (3.1607Å) than that of a bulk ZnO (3.25Å). Such a deviation of lattice parameter of undoped ZnO film from it's bulk value could be due to strain effect caused by significant lattice mismatch ($\Delta a/a = -31.8$). No expected increase in the *a* lattice parameter was observed with Co concentration in ZnO films. In fact, for the films grown at higher Co concentrations the *a* lattice parameter decreased (Figure 3.13, red symbols). Keeping in mind, that Co distribution through the film's thickness is not

uniform and significantly lower at substrate/film interface (refer to Chapter 3.3.2.1) could explain such change in *a* lattice parameter. On the other hand, the *c* lattice parameter for undoped ZnO film was higher than that of bulk ZnO, but sharply decreased with Co concentration. For the films grown on Al_2O_3 (0001) substrate *c* lattice parameter is perpendicular to the substrate surface, thus, associated strain is not that significant as for in plane *a* lattice parameter and would not affect *c* parameter strongly.

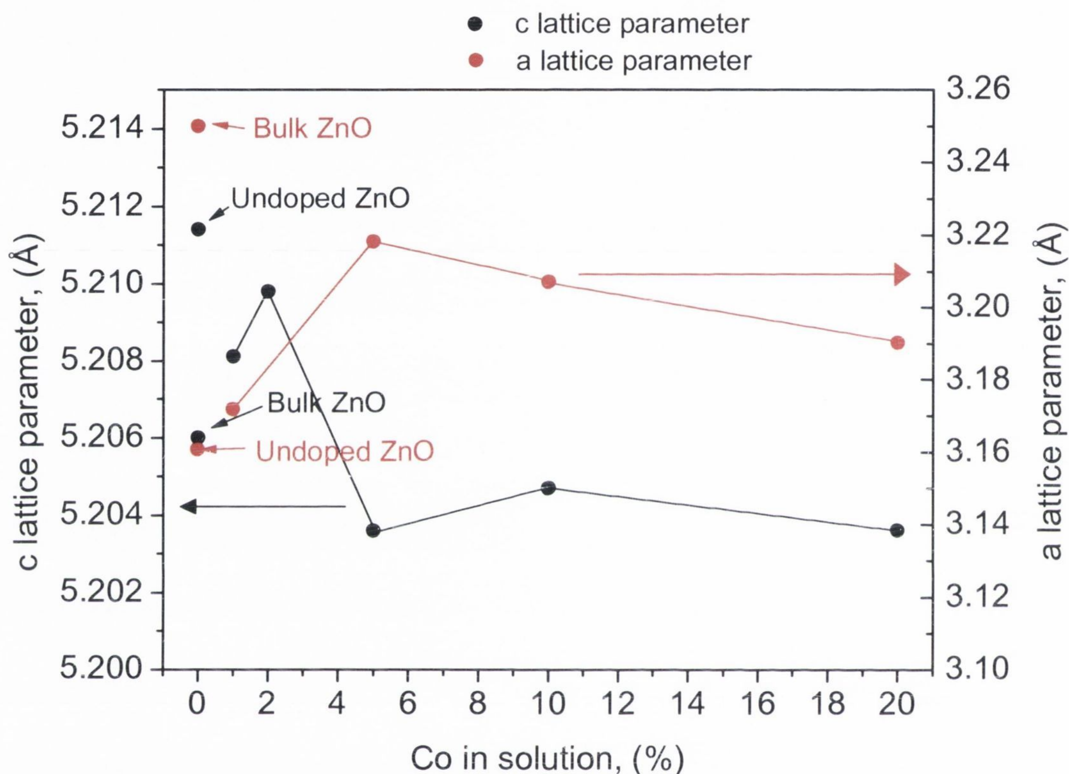

Fig. 3.13.The change of *c* and *a* lattice parameters in Co-doped ZnO films on Al_2O_3 (0001) as a function of Co concentration

Both the *c* and *a* lattice parameters for the undoped ZnO films on Al_2O_3 ($1\underline{1}02$) are lower than those of bulk ZnO. Figure 3.14 shows the change in *a* and *c* lattice parameters in Co-doped ZnO films. No expected increase in *c* lattice parameter was observed with Co concentration up to 5% Co doping. The *a* lattice parameter did not change drastically for up to 10% Co doping, except for sharp increase in it's value for highest Co concentration. Again, the possible explanation for the observed changes in lattice parameters with Co concentration in a film can be associated with the formation of

Co rich surface layer due to diffusion of Co^{2+} ions to the surface of the film, as confirmed by XPS and SIMS analysis.

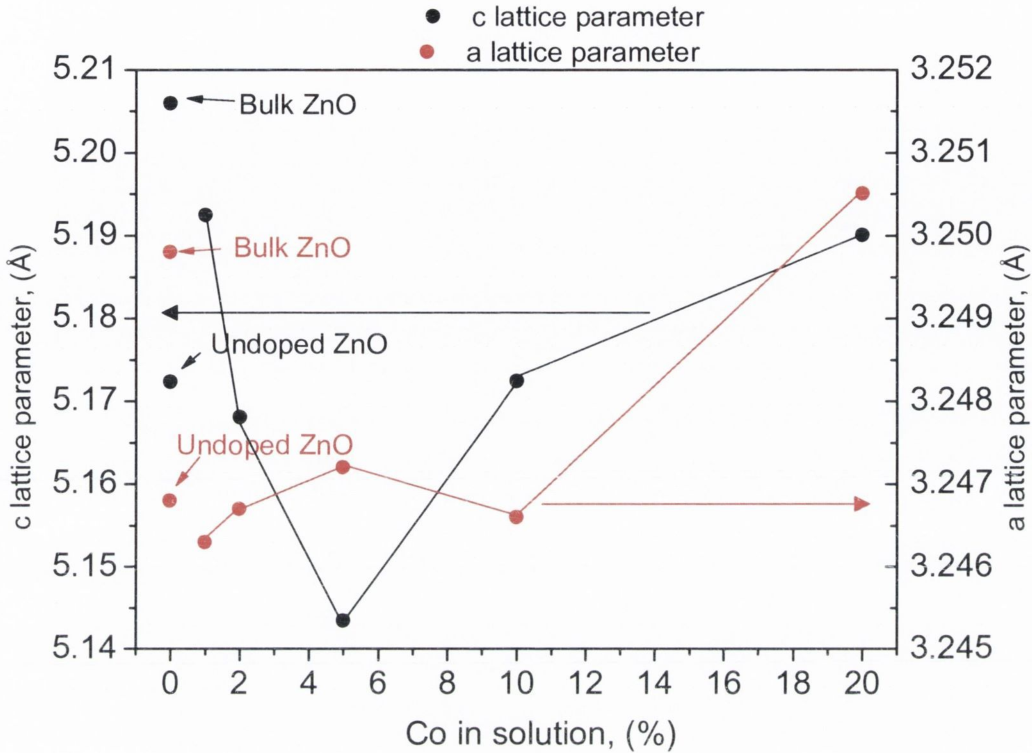

Fig. 3.14. The change of *c* and *a* lattice parameters in Co-doped ZnO films on Al_2O_3 (1$\underline{1}$02) as a function of Co concentration

The change in crystallite size with Co concentration was also studied. Average crystallite size was calculated using Scherrer's formula from (002) reflection for Co-doped ZnO films grown on Al_2O_3 (0001) substrates and (110) reflections for films grown on Al_2O_3 (1$\underline{1}$02) substrates, respectively. We found that when films are grown on Al_2O_3 (0001) the average crystallite size is approximately two times larger than when films are grown Al_2O_3 (1$\underline{1}$02) substrate. It was found that there is no obvious dependence between crystallite size and Co concentration in the films. The calculated values are given in Table 3.3.

Table 3.3 Average crystallite size calculated for Co-doped ZnO films with different Co concentrations

Co concentration in solution (%)	**Average particle size (nm), c-cut sapphire**	**Average particle size (nm), r-cut sapphire**
0	36	21
1	44	21
2	39	24
5	45	25
10	48	20
20	43	19

3.3.2.3. Morphology of the films

The surface of the Co-doped ZnO films was studied using AFM and SEM techniques. Generally, Co-doped ZnO films grown on Al_2O_3 (0001) are rougher than those grown on Al_2O_3 (1$\underline{1}$02) (Figure 3.15). Average film roughness Ra (nm) was found to change with Co concentration from 9.7nm→ 3.2nm→ 17.9nm→ 15.1nm→ 1.4nm on Al_2O_3 (0001) and 4.0nm→ 1.2nm→ 10.4nm→ 2.7nm →3.2nm on Al_2O_3 (1$\underline{1}$02). The change in film's roughness with Co concentration did not have any particular trend, although films doped with 5% Co had highest roughness.

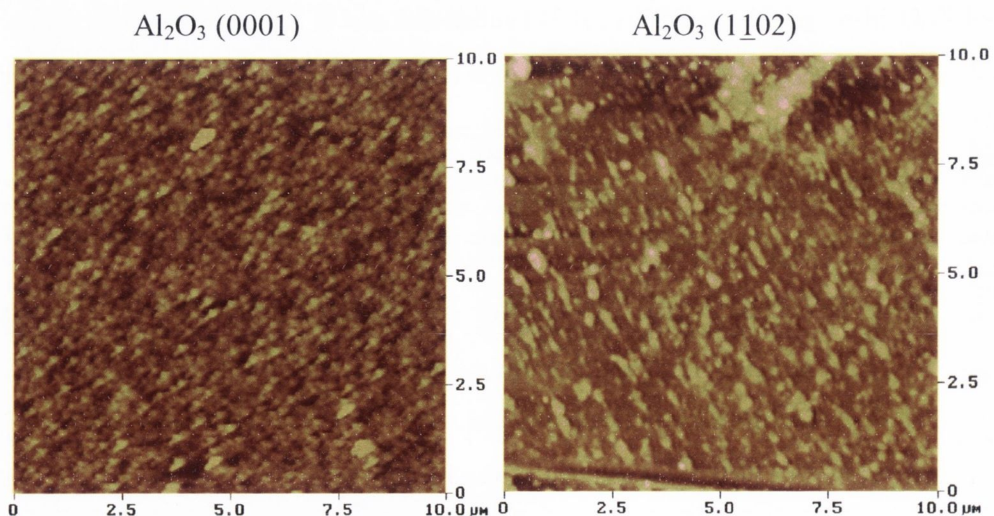

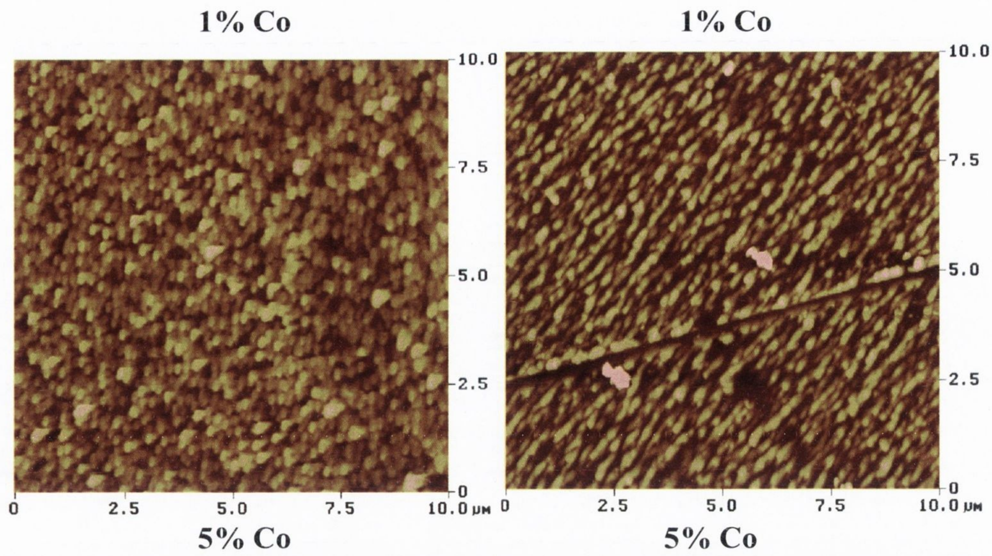

Fig. 3.15. AFM images of Co-doped ZnO films for 1% and 5% Co on Al_2O_3 (0001) and Al_2O_3 $(1\bar{1}02)$ substrates

SEM images taken for the Co-doped ZnO films grown on Al_2O_3 (0001) showed that surface morphology mainly consisted of granules with average size of ~ 90nm (doped with 1-10% Co) (Fig.3.16). Elongated grains were observed for the 5% Co doping. Different surface morphology consisting of plane crystallites was found for 20% Co doped film. The crystallite size estimated from SEM micrographs is in the range of ~40-80nm for the films grown on Al_2O_3 (0001) substrate. These results are in agreement with the average grain size calculated from Scherrer's formula.

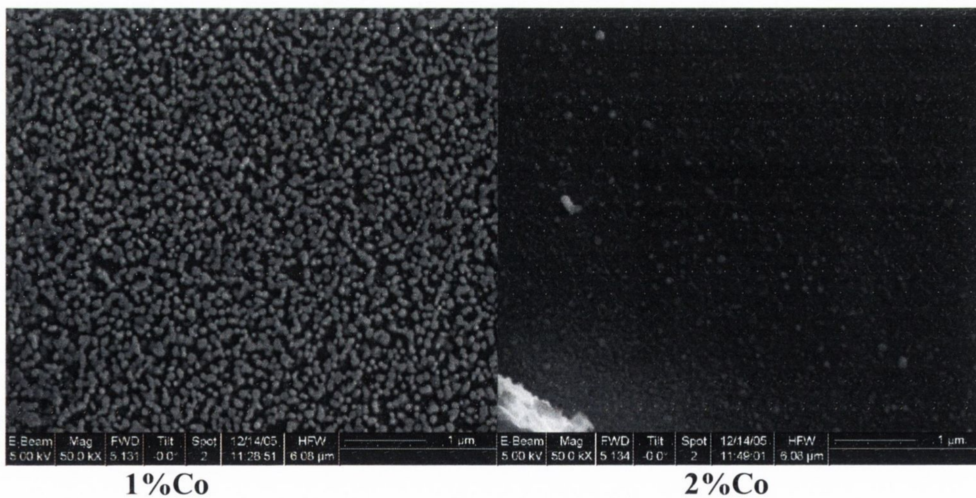

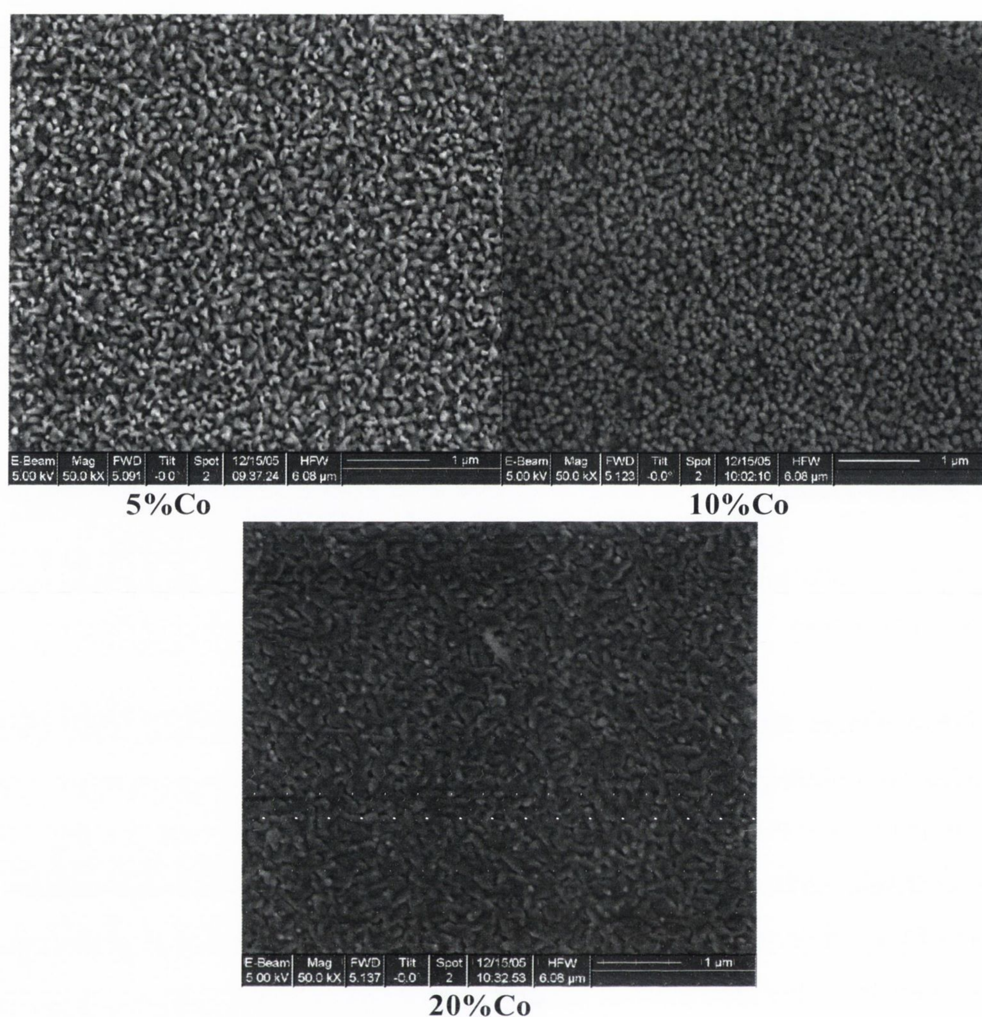

Fig. 3.16.SEM images of Co-doped ZnO films on Al_2O_3 $(1\bar{1}02)$ substrate

3.3.2.4. Magnetic properties of the films

3.3.2.4.1. SQUID magnetometer measurements

Magnetisation measurements were carried out at room temperature in 1T magnetic field. Additionally, magnetisation measurements performed for sapphire substrates showed straight line with negative slope, indicating that the substrate is diamagnetic and free of magnetic impurities. Undoped ZnO films were not ferromagnetic and magnetisation curve showed only diamagnetic contribution from Al_2O_3 substrate (Figure 3.17).

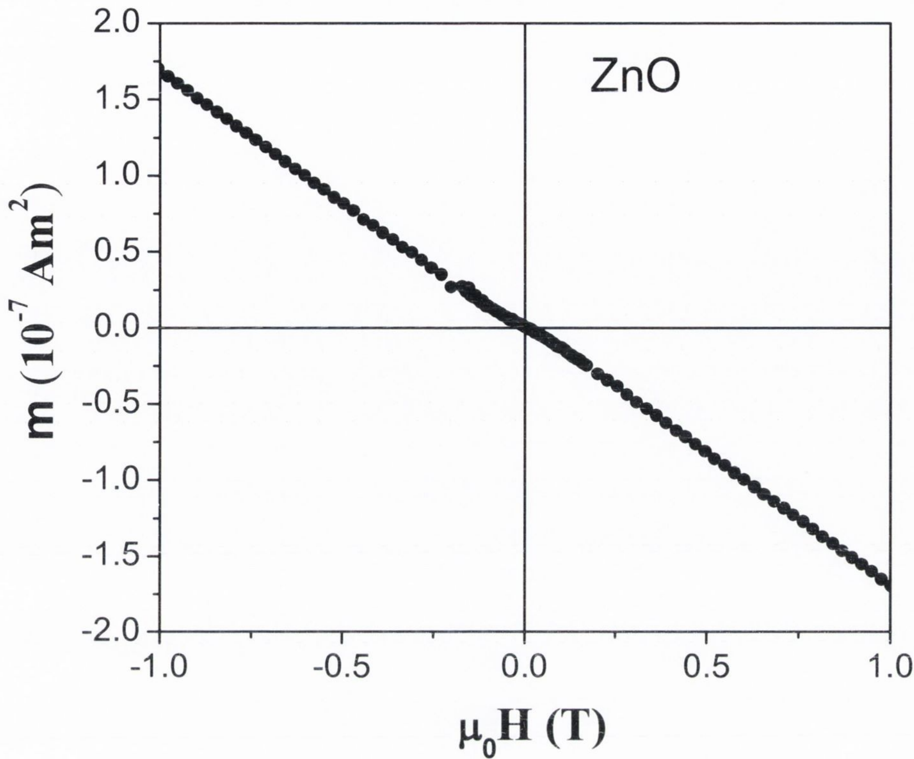

Fig. 3.17.Magnetisation curve of undoped ZnO film

All Co-doped ZnO films grown on Al_2O_3 (0001) and Al_2O_3 ($1\underline{1}02$) substrates showed magnetisation curve at room temperature characteristic for ferromagnetic material (Figure3.18). Moreover, the saturation magnetisation was found to be highly anisotropic. For as deposited samples, the moment is considerably larger when the field is applied perpendicular to the film plane. Anisotropy increased with decreasing Co concentration in the films and magnetic moments differ by a factor of between 1.5 and 4 compared to parallel fields. All films exhibit a small remanence of 10% (given in inset, Figure 3.18) and a saturation field of about 0.5T when the field is applied perpendicular to the film plane. When the field is applied parallel to the film plane, a small high field slope remains. This slope is very small and even for measurements performed at 5T magnetic field a large anisotropy still persists. Based on the extrapolation of the data it was estimated that the parallel saturation field of the as-deposited films is larger than 10T.

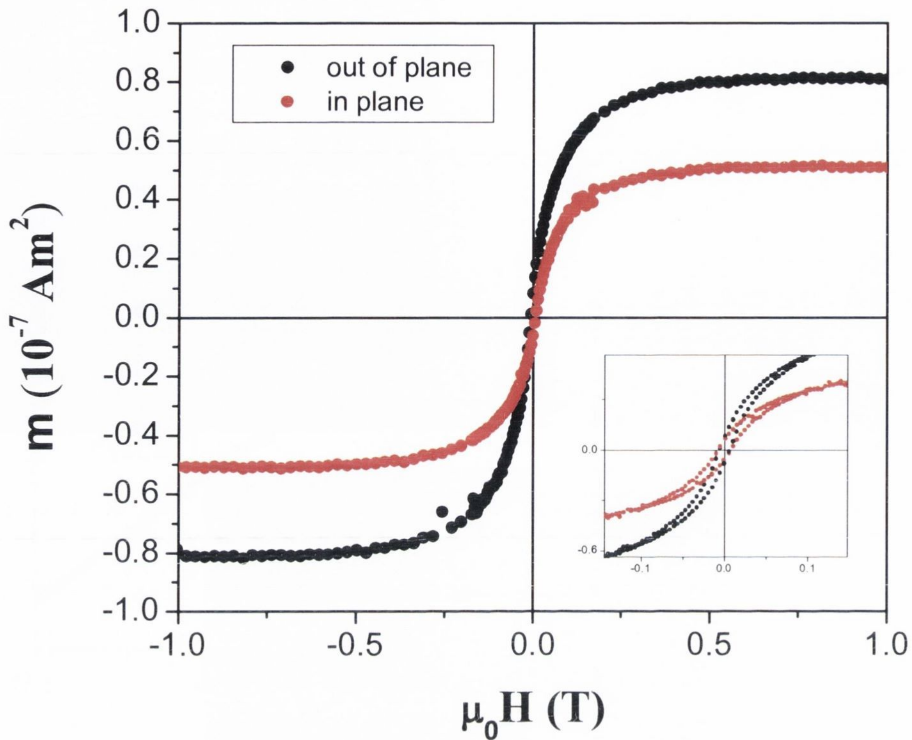

Fig. 3.18. Magnetisation curve of 2% Co-doped ZnO film, grown on Al_2O_3 (1$\underline{1}$02) substrate. Diamagnetic contribution of sapphire substrate is subtracted. The inset shows the same data at smaller magnetic fields indicating a small remanence of about 10%

We also found, that storing samples in open air reduces both the saturation moment (Figure 3.19) and the magnetic anisotropy. After 270 days the film moment is only slightly larger when the magnetic field is applied perpendicular instead of parallel to the film plane (see black squares in Fig.3.19.). For example, for the 1% Co-doped ZnO film on Al_2O_3 (1$\underline{1}$02) the moment decreases from 0.99×10^{-7}Am^2 for as deposited film to 0.39×10^{-7}Am^2 after 270 days. The reasons for decrease of magnetic moment in time are not quite clear, and could possibly arise from the interaction of the films with the ambient conditions (oxidising atmosphere, moisture).

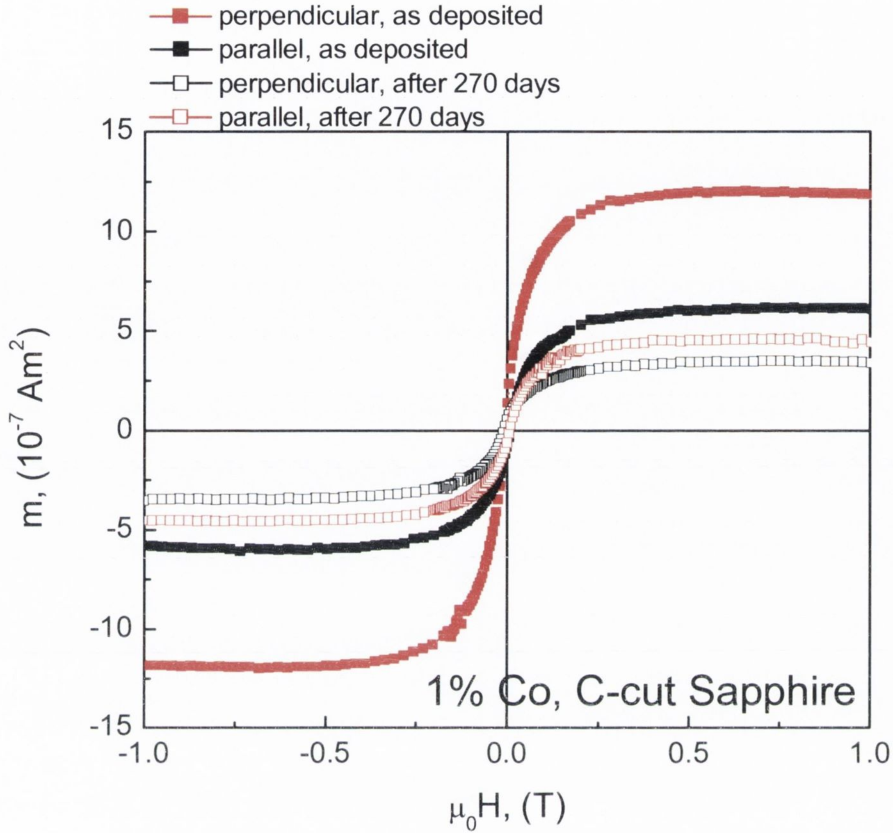

Fig. 3.19. Magnetisation curves for 1% Co-doped ZnO film on c-cut sapphire substrate. The red squares were measured immediately after deposition and the black squares were recorded 270 days later

The moment of Co-doped ZnO films on Al_2O_3 (0001) and Al_2O_3 (1$\underline{1}$02) substrates decays at a similar rate as illustrated in Figure 3.20. Fitting the data in the inset of Figure 3.20 gives a scaling law, $m(t)/m(t=0) = (1+1)^{-0.162}$, for the degradation of the saturation moment.

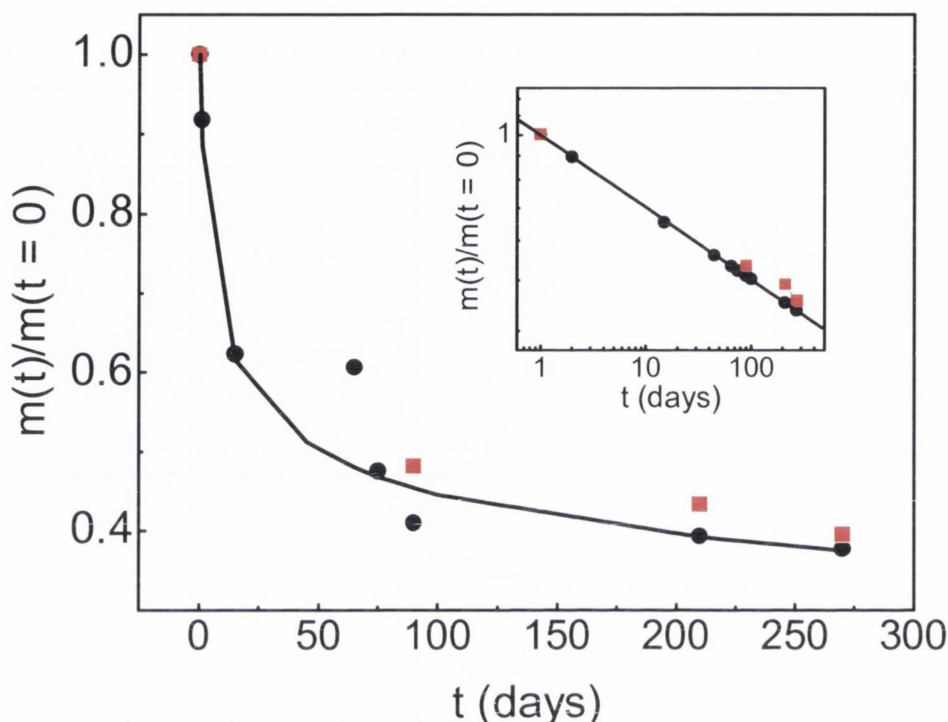

Fig. 3.20. Variation of the magnetic saturation moment with time for 1% Co-doped ZnO films on Al_2O_3 (0001) (black circles) and Al_2O_3 (1_102) (red squares). The solid lines indicate fits to the data with $m(t)/m(t=0) = (1+1)^{-0.162}$

The dependence of saturation magnetisation from Co concentration is summarised in Figure 3.21. The largest moment, a giant m = 18.9μ_B/Co is obtained for the 1% Co-doped ZnO on Al_2O_3 (1_102) substrate. Moreover, the saturation moment of Co-doped ZnO films decreases monotonically with increasing Co concentration irrespective of substrate orientation. One exception is the 1% Co-doped ZnO film on Al_2O_3 (0001) whose magnetic moment is slightly smaller than that of the film with 2% Co (Figure 3.21.(d)). As the 1% Co-doped film on Al_2O_3 (0001) substrate is much thicker (210nm) than the other films with 1% (59nm) and 2% Co (66nm and 69nm on Al_2O_3 (0001) and Al_2O_3 (1_102) respectively), this might suggest that only a relatively thin layer near sapphire/ZnO interface is magnetically active. For example, the 2% Co-doped ZnO films on Al_2O_3 (1_102) and Al_2O_3 (0001) substrates have similar thicknesses and nearly equal

saturation moments of 6.5μ_B/Co and 6.7μ_B/Co. In addition, films doped with 20% Co did not show room temperature ferromagnetism.

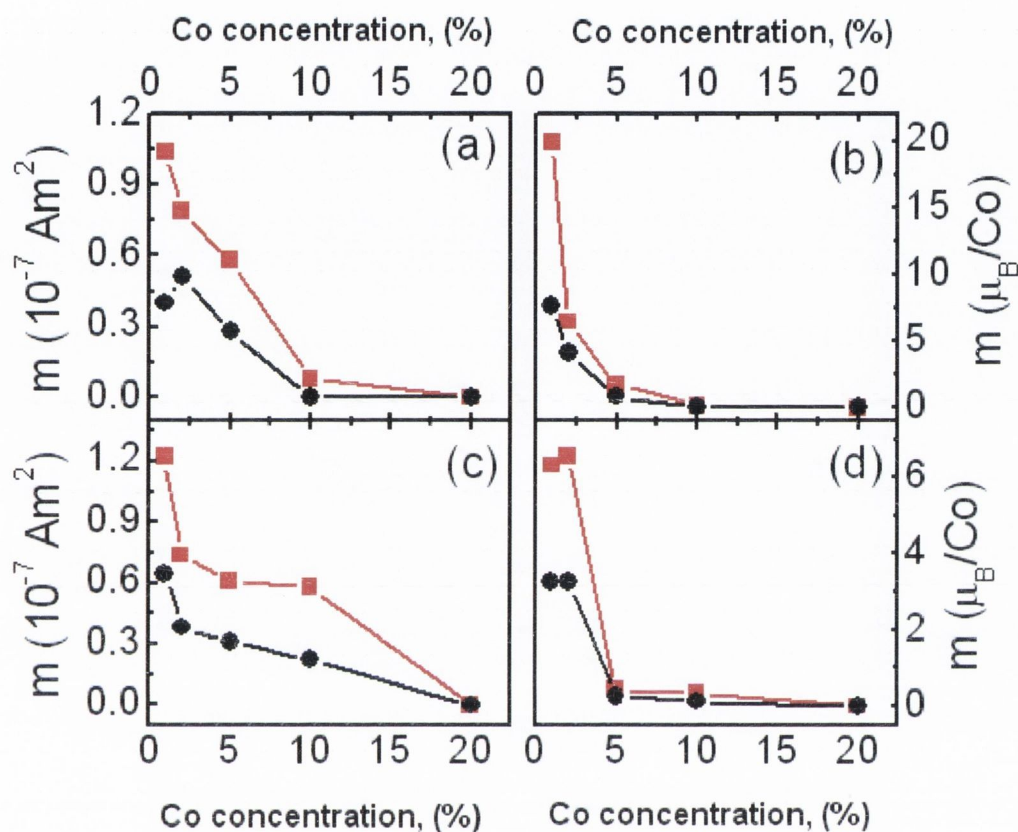

Fig. 3.21. Magnetic saturation moment as a function of Co doping concentration for ZnO films on Al_2O_3 (0001) [(a) and (b)] and Al_2O_3 (1$\underline{1}$02) [(c) and (d)].

3.3.2.4.2. VSM magnetometer measurements

In contrast to SQUID, VSM allows to perform magnetisation measurements at higher temperatures, which enables us to estimate the T_C of the films. Figure 3.22 summarises in-plane magnetisation curves for 2% Co-doped ZnO film on Al_2O_3 (1$\underline{1}$02) substrate at different temperatures with applied magnetic field of 1T. Between 300 and 750K the magnetic moment decreases slightly. Beyond 750K the magnetic moment drops more sharply. The reduction of the magnetic moment at T>750K is irreversible, as

illustrated by the magnetisation curve measured at 300K after cooling the film down from 900K. This clearly indicates that structural and/or electronic modification of the ZnO film occurs above 750K. The fact, that film is still magnetic above 900K demonstrates that the intrinsic magnetic ordering temperature of the as-deposited Co-doped ZnO film well exceeds 900K.

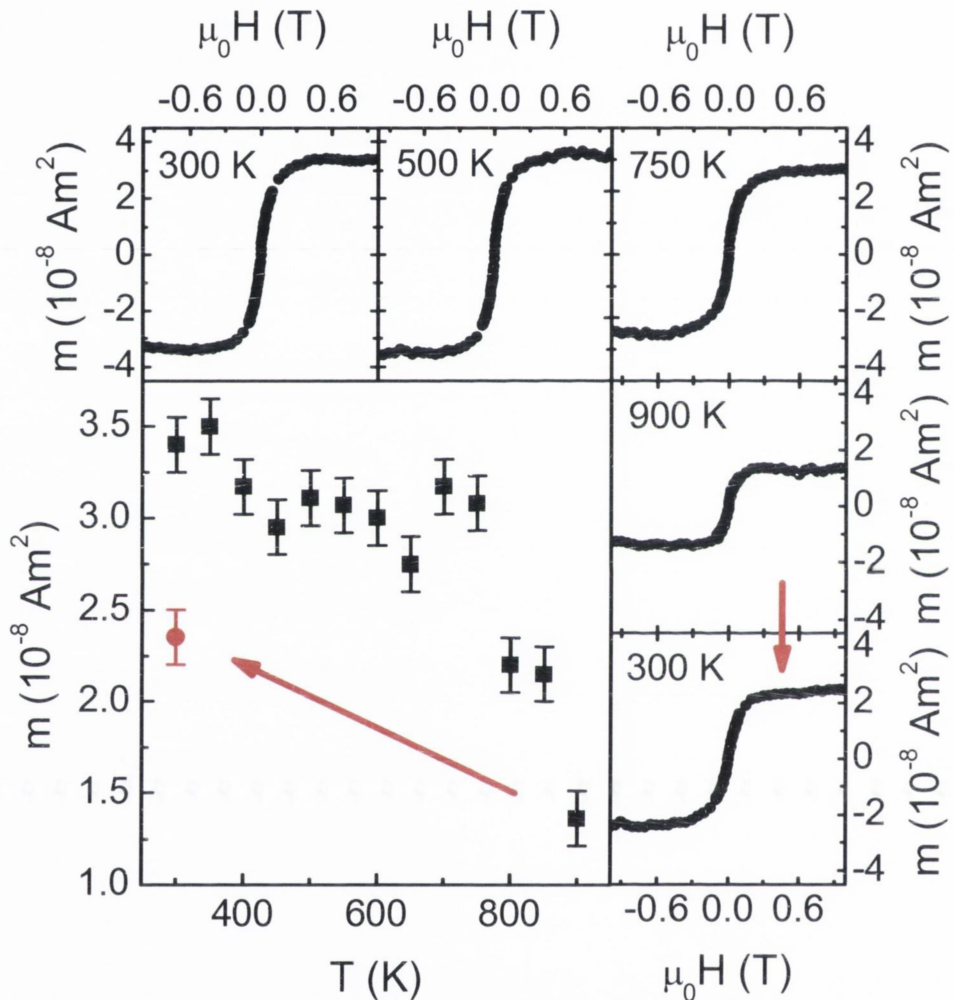

Fig. 3.22. In-plane VSM magnetisation curves at different temperatures for a 2% Co-doped ZnO film on Al_2O_3 (1$\underline{1}$02). The curve in the lower right panel and the red circle in the main frame were measured after cooling from 900K

3.4. Co-doped ZnO films grown in magnetic field

In this work Co-doped ZnO films were also grown in magnetic field of 1T that was applied during the growth process. Previously, ZnO films were grown by conventional MOCVD in 10T magnetic field [48]. The crystalline quality and morphology of these ZnO films changed upon application of strong magnetic field. The X-ray diffraction of the films was weaker when grown in magnetic field, reflecting the reduced film thickness by magnetic field. Morphology of the films remained similar, although, the size of leaf-like and plate-like crystallites was significantly smaller when grown in 10T. A similar magnetic field effect in grain size reducing has also been reported in MOCVD of $YBa_2Cu_3O_7$ at a magnetic field of 4 and 8T [49]. However, magnetic properties of doped ZnO films have never been studied before. For this reason, in our work Co-doped ZnO films were grown by PI MOCVD consequently in magnetic field and without magnetic field. The aim of this research was to investigate the influence of magnetic field on structural, crystalline and magnetic properties of the ZnO films.

3.4.1. Preparation of Co-doped ZnO films in magnetic field

It is very important to note, that the dimensions of the PI MOCVD reactor equipped with 1T permanent magnet are different from that used earlier for the growth of Co-doped ZnO films (refer to Chapter 2.2.2). Different reactor and furnace sizes mean that temperature gradients will be different. This might result in slightly different optimal deposition conditions from those that were found previously for Co-doped ZnO films (gas flow, deposition temperature and etc.). To find the optimal deposition temperature 2mol% Co-doped ZnO films were grown at different temperature (500°C, 525°C, 550°C, 575°C, 600°C) and their crystalline and structural properties were examined.

Once the optimal growth conditions were found the series of Co-doped ZnO films with different Co concentrations in precursor solution were prepared on Al_2O_3 (0001) and Al_2O_3 ($1\bar{1}02$) substrates. Co concentration in the precursor solution was increased from 1 mol% to 30 mol%. To test the influence of magnetic field, films for each Co concentration were first prepared without magnetic field and then consequently grown in 1T magnetic field whilst maintaining the same deposition conditions. In addition,

undoped ZnO films were also prepared with and without magnetic field and their structural, crystalline and magnetic properties were also examined.

Summarized optimal deposition conditions for Co-doped ZnO films are given in the Table 3.4.

Table 3.4 Deposition conditions for Co-doped ZnO films

Deposition temperature	550 °C
Evaporation temperature	90 °C
Carrier gas flow (Ar + O_2)	900 ml/min
Reactor pressure	5 mbar
Metalorganic precursors	$Zn(tmhd)_2$, $Co(tmhd)_3$
Solvent	1,2- dimethoxyethane
Zn/(Co+Zn) concentration in solution	0.025 mol/l
Co/(Co+Zn) concentration in solution	0, 1, 2, 5, 10, 15, 20%
Impulse frequency	2 Hz
Microdose mass	4 mg
Substrates	Al_2O_3 (0001)
Magnetic field	0T, 1T

3.4.2. Characterisation of Co-doped ZnO films

3.4.2.1. X-ray diffraction

All Co-doped ZnO films grown in PI MOCVD reactor equipped with 1T magnet reveal good crystalline quality even when doped with high Co concentrations. Similar to the previously grown Co-doped ZnO, films grown up to 10% Co in precursor solution exhibit high quality single crystalline (001) orientation perpendicular to the film plane. However, the presence of ZnO (110) reflection can be detected by XRD in films doped with 10% -20% Co which was not observed before in Co-doped ZnO films prepared by PI MCOVD on Al_2O_3 (0001) substrates. The films grown in 1T external magnetic field had identical crystalline orientations and similar reflection intensities as those grown without magnetic field. The results showing the X-ray diffraction patterns of ZnO films doped with different Co concentrations in and without magnetic field are given in Figure 3.23. This rules out a

possible effect of the external magnetic field on crystalline properties of the films, which contradicts with results found in work by M. Kasuga *et.al.* [48].

All films grown in PI MOCVD equipped with external magnet were also clear of any possible secondary phases as confirmed by XRD. The results are consistent with the earlier result for Co-doped ZnO films.

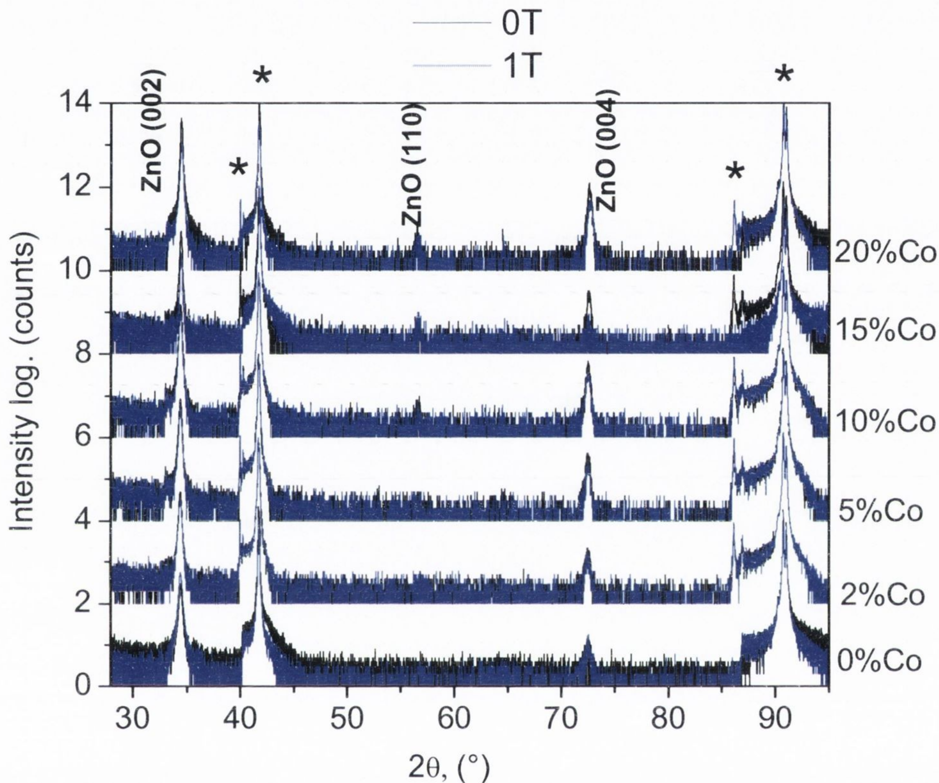

Fig. 3.23. X-ray diffraction analysis of Co-doped ZnO films grown in and without magnetic field showing very similar crystalline structure of the films independent on Co concentration or application of external magnetic field

The *c* and *a* lattice parameters of Co-doped ZnO films were also calculated and their change as a function of Co concentration was evaluated. All calculations were carried out according to the procedure described in Chapter 3.3.2.2. The results are shown in Figure 3.24.

We found that *c* lattice parameter of undoped ZnO film is slightly larger that the value of 5.206Å for bulk ZnO. The expected increase in *c* lattice parameter is observed

when films are doped with 2 and 5% Co due to substitution of larger Co^{2+} [41, 50]. However, when films are doped with larger Co concentration a sharp decrease in *c* lattice parameter is found with the values close to that of the bulk ZnO. The possible effect of not uniform Co distribution with the film thickness in heavily doped ZnO would be able to explain the observed decrease in *c* lattice parameter, rather than expected increase due to the substitution of larger Co^{2+}. If most of the substituted Co is concentrated on the surface of the films, especially when doped with larger Co concentration, then the increase in *c* lattice due to substitution of larger Co^{2+} would not be observed. In fact, larger Co concentrations were detected by SIMS analysis at the surface of the films in high concentrations Co doped ZnO films as discussed earlier (Chapter 3.3.2.1.).

In contrast to the earlier grown ZnO (a = 3.16Å), the a lattice parameter of undoped ZnO film grown in PI MOCVD reactor equipped with external magnet is only slightly larger than that of the bulk ZnO (3.25Å). Different *a* lattice parameter values for undoped ZnO films grown in different PI MOCVD reactors are more likely to arise due to changes in deposition conditions (such as temperature gradient, gas flow rate and etc) as a result of the change of the reactor geometry. There is no clear tendency in the change of *a* lattice parameter with Co concentration. Although, the lowest value of a lattice parameter was found for the films doped with 20% of Co. Again, this contradicts with the assumption that a lattice parameter of Co-doped ZnO films should increase with Co concentration due to substitution of larger Co^{2+}. The reason for this behaviour is again, most likely is a result of Co distribution through the film thickness, which is believed to be not uniform with larger Co content on the surface of the film. However, this has yet to be confirmed.

It is noted that films grown in external magnetic field have very similar lattice parameter values to those grown without magnetic field. This is consistent with the XRD results, since no effect was found on the crystalline properties of the films we did not expect to see any effect of magnetic field on *a* and *c* the lattice parameter values.

Finally, the average crystallite size calculated for all Co-doped ZnO films from ZnO(002) reflection using Scherrer's formula. With only one exception, all films showed gradual increase in crystallite size with Co concentration in a film. Again, this contradicts with our earlier results, where no clear dependence between average crystallite size and

Co concentration in a film was found. Typically, films with larger crystallites normally give rise to narrower FWHM. This is also observed in our Co-doped ZnO films. Table 3.5 summarises results for *a* and *c* lattice parameters, FWHM and average grain size.

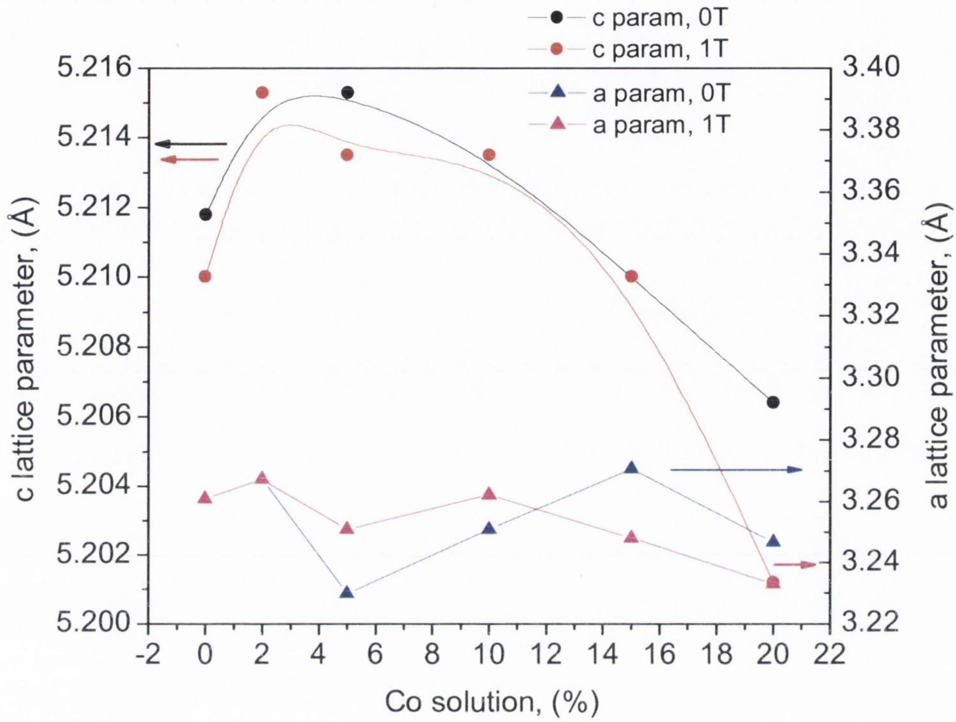

Fig. 3.24. The change of *c* and *a* lattice parameters in Co-doped ZnO films grown Al_2O_3 substrate as a function of Co concentration

Table 3.5. Summary of important parameters evaluated from XRD analysis for Co-doped ZnO films

Co concentration, (%)	**FWHM (002), (°)**	**c lattice parameter, (Å)**	**a lattice parameter, (Å)**	**Average crystallite size, nm**
		Al_2O_3 substrate		
0	0.2510	5.2118		33
0, 1T	0.2632	5.2100	3.2607	32
2	0.2352	5.2153	3.2671	35
2, 1T	0.2328	5.2153	3.2671	36
5	0.2087	5.2153	3.2298	40
5, 1T	0.2035	5.2135	3.2509	41

10	0.2006	5.2135	3.2509	42
10, 1T	0.2055	5.2135	3.2621	41
15	0.1727	5.2100	3.2704	48
15, 1T	0.1641	5.2100	3.2479	51
20	0.1628	5.2064	3.2465	52
20, 1T	0.1964	5.2012	3.2329	42

3.4.2.2. Film composition

Co concentration in Co-doped ZnO films was measured by EDAX technique. Each sample was measured in 6 different areas of $\sim 100 \mu m^2$ size. EDAX analysis revealed that Co is substituted into ZnO lattice (Figure 3.25). Co concentration in a film was found to be almost two times smaller than in precursor solution. Films grown in 1T external magnetic field had very similar Co concentration in a film. However, previously we have found that Co concentration in Co-doped ZnO films grown in PIMOCVD reactor without magnet is slightly larger than that in precursor solution. The obtained results signal the importance of the size of the reactor on film composition. Figure 3.26 shows the dependence of Co concentration in a film from Co concentration in precursor solution for the films grown in and without external magnetic field.

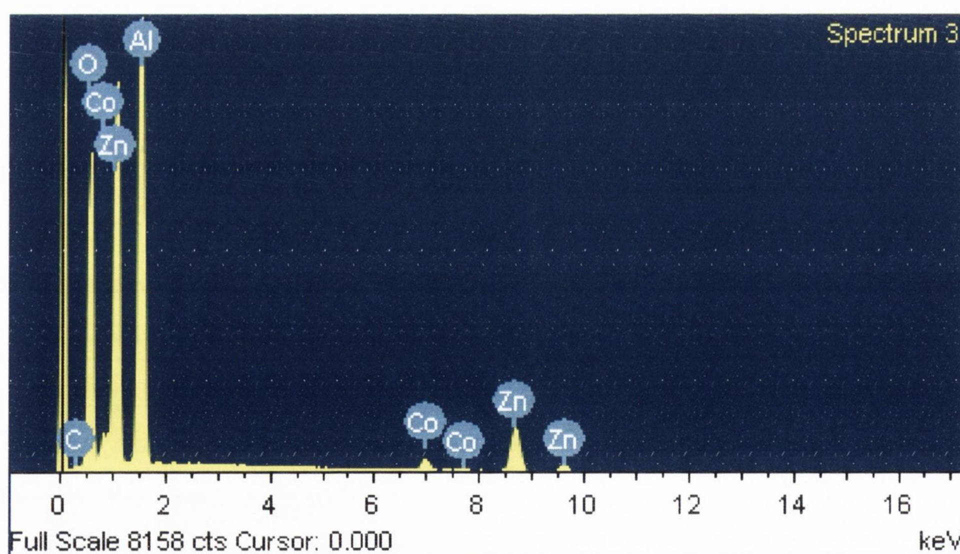

Fig. 3.25. EDAX spectrum of 15% Co-doped ZnO film showing the presence of Co and Zn elements in a film. Al peak is appearing in all spectra due to Al_2O_3 substrate

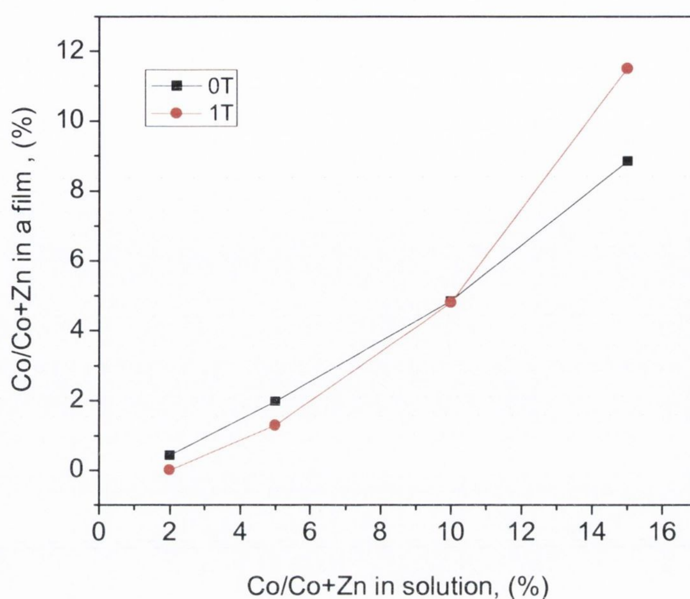

Fig. 3.26. Co concentration in Co-doped ZnO films versus Co concentration in precursor solution for the films grown in and without external magnetic field, showing smaller Co content in a film

3.4.2.3. Morphology of the films

SEM analysis revealed that all Co-doped ZnO films consisted of granules. The granules size was varying depending on Co concentration in the films. For the lower Co concentration (0-5%mol in precursor solution) the surface of the films consisted of approximately ~30-40 nm diameter granules. These results are very consisted with average crystallite size calculated from ZnO (002) reflection using Scherrer's formula. Slightly larger granules of approximately 40-50nm in diameter have been detected by SEM for 10% Co-doped ZnOfilms. The granulated crystallites of different sizes varying from 70 to 200nm have been found with further increase in Co concentration, which is larger than those calculated using Scherrer's formula. This is possibly a result of coalescence of smaller crystallites, which then form larger grains. Finally we found a slight decrease in crystallite size for the film grown at 20% Co in precursor solution which were approximately of ~60nm in diameter. The films grown with 20% Co in 1T external field was the only exception, which showed different surface morphology from those films grown without external magnetic field. It is noted that the surface morphology

of the films grown in a PI MOCVD reactor equipped with 1T magnet was quite similar to those grown earlier. The SEM micrographs of all Co-doped ZnO films grown in and without magnetic field with different Co concentrations are shown in Figure 3.27.

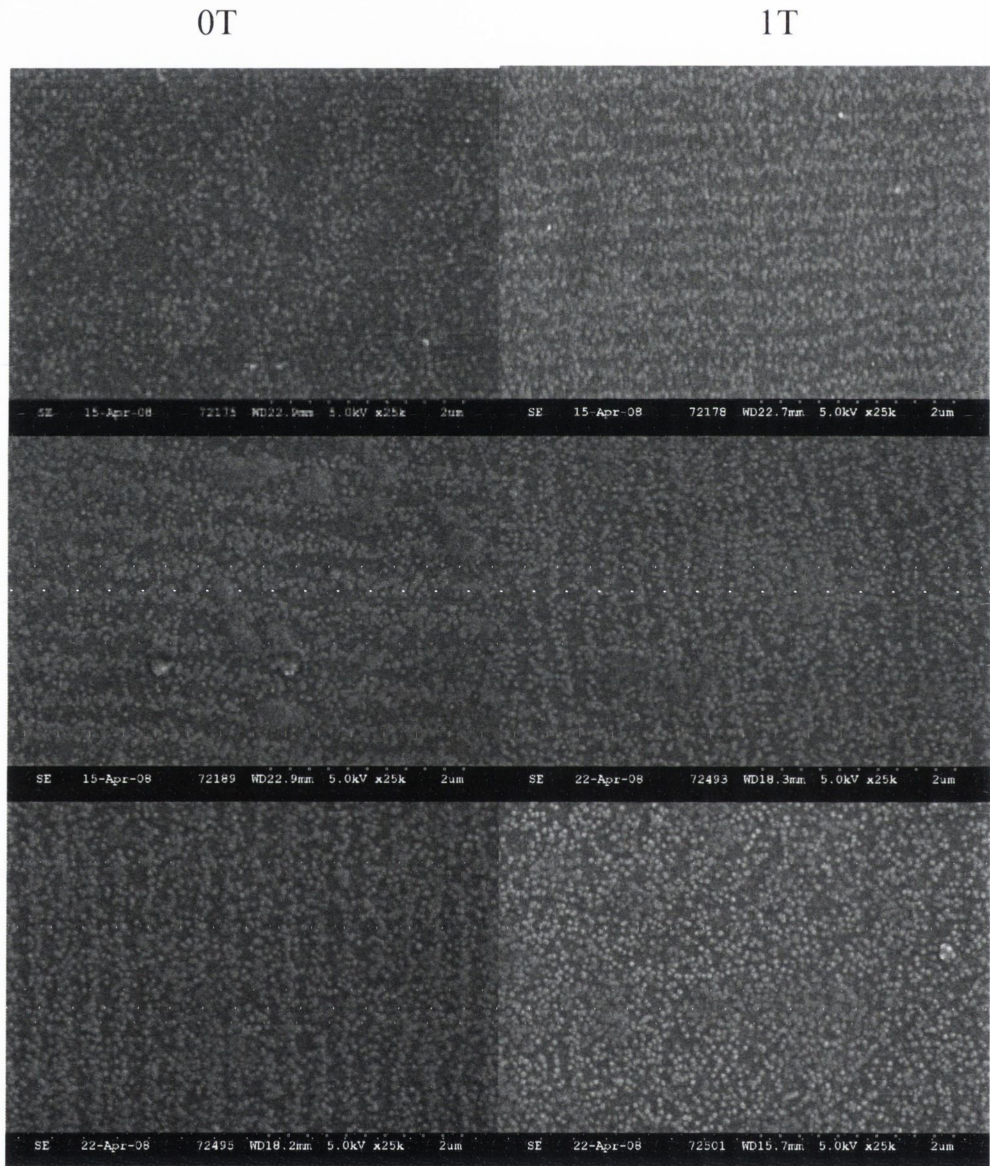

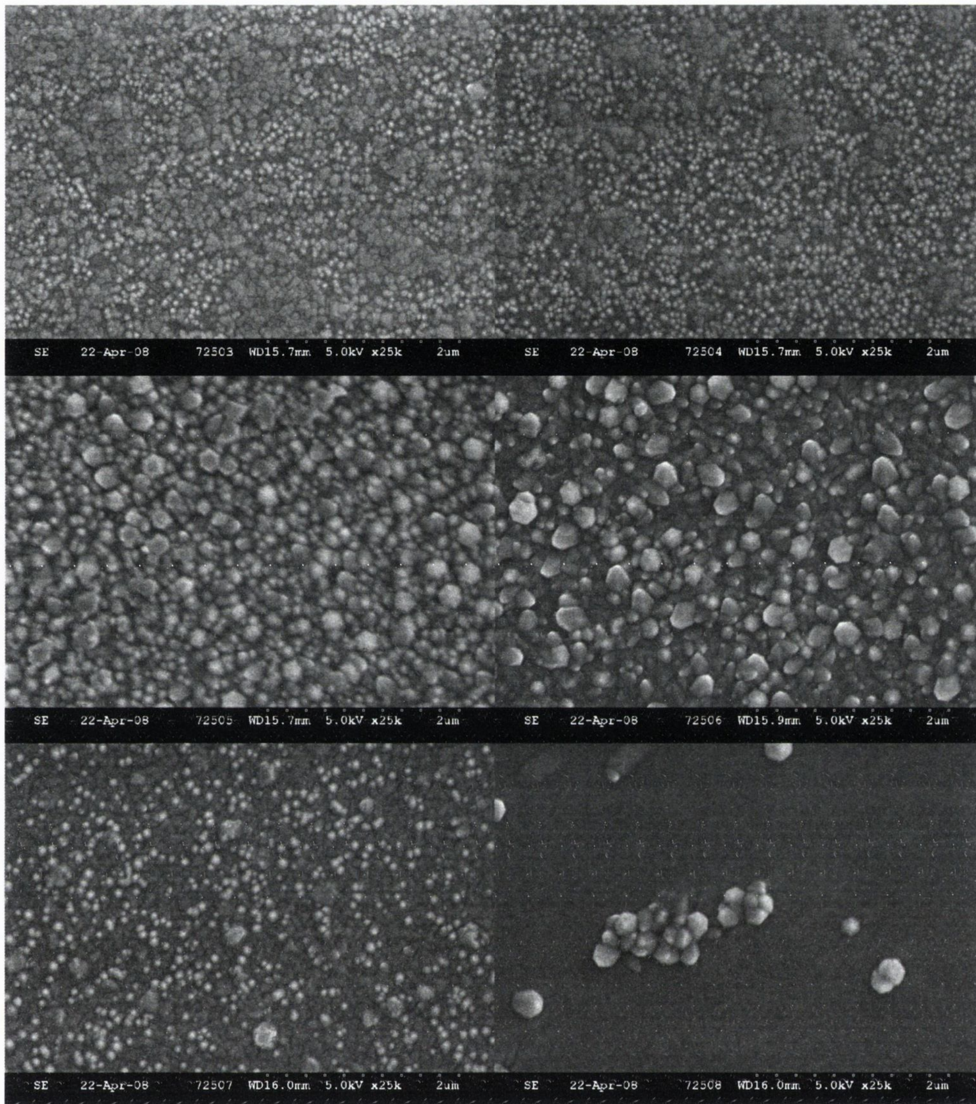

Fig. 3.27. SEM micrographs for Co-doped ZnO films with different Co concentrations. The left column represents films grown without external magnetic field and the right column represents films grown in 1T external magnetic field. The images are given with Co concentration increasing from top to bottom from 0, 2,5,10,15, and 20%

3.4.2.4. Magnetic properties

Squid magnetisation measurements were carried out on all samples at room temperature with 1T magnetic field applied perpendicular to the film plane. The idea was to reproduce earlier obtained giant magnetic moments in Co-doped ZnO films and also enhance the magnetic moment when films are grown in 1T external magnetic field.

Magnetisation measurements revealed that only five films (doped with 2, 5 and 20% Co) out of twelve showed ferromagnetic behaviour. This indicates that reproducibility of ferromagnetic properties in oxide based DMS is a big issue. These observations have also been mentioned in other works [28, 51]. The saturation magnetisation of five ferromagnetic Co-doped ZnO films was much lower than earlier found giant magnetic moments. However, Co-doped ZnO films doped with 2% Co in precursor solution (2% Co in precursor solution corresponds to ~0.3 % Co in a film) had the magnetic moment of 5.73 and 5.78 η_B/Co for the films grown without and in 1T magnetic field consequently. 5% Co-doped ZnO grown without external magnetic field showed only very weak ferromagnetic moment. No moment was found for 5% Co-doped ZnO grown in 1T external magnetic field. Finally, films grown with 20% Co in precursor solution had magnetic moments of only 0.2 and 0.15 η_B/Co for films grown without and in external magnetic field. As mentioned above the observed moments are much lower than the giant moments found earlier in our Co-doped ZnO films. The above results suggest there is still a big issue with the reproducibility of the magnetic moments and ferromagnetism on its own in oxide based DMS systems, particularly in Co-doped ZnO thin films. Moreover, opposite to expected, the external magnetic field did not enhance saturation magnetisation of Co-doped ZnO films grown in external magnetic field. SQUID magnetisation curves for all five ferromagnetic Co-doped ZnO films are shown in Figure 4.28.

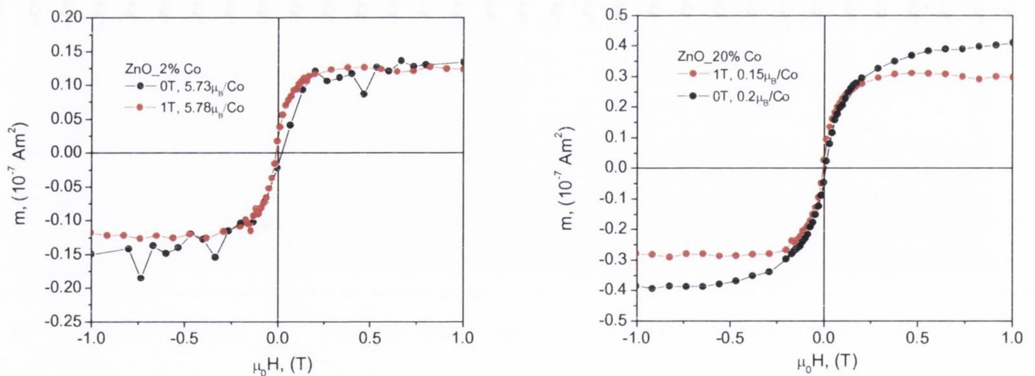

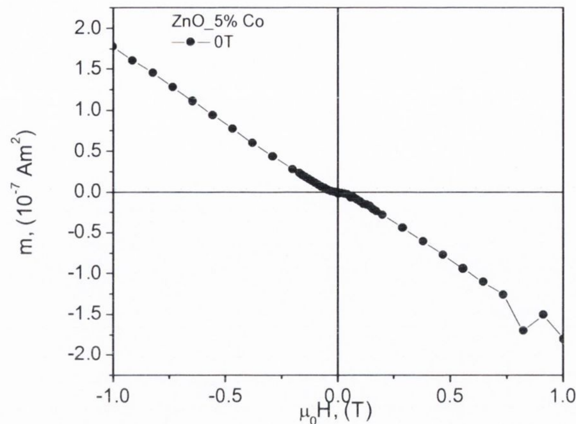

Fig. 3.28. SQUID magnetisation curves for Co-doped ZnO films grown in and without magnetic field

3.5. Conclusions

We have successfully deposited both undoped and Co-doped ZnO thin films on various substrates using PI MOCVD. Big novelty of this work was that ZnO and Co-doped ZnO films for the first time have been prepared using PI MOCVD method. Moreover, Co-doped ZnO films were also prepared in PI MOCVD reactor equipped with 1T permanent magnet.

Systematic optimisation of deposition conditions has shown that PI MOCVD is a suitable and versatile technique for the growth of highly (001) oriented ZnO films. The best quality ZnO films were obtained at 550 °C and 50% of O_2 in a total carrier gas mixture. Although an insignificant change in deposition temperature or oxygen concentration caused the decrease in the crystalline quality of ZnO films.

Highly crystalline (001) and (110) oriented C-doped ZnO films were deposited by PI MOCVD on (0001) and (1$\underline{1}$02) Al_2O_3 substrates, with Co concentration varying from 1 to 20 mol% in solution. An XPS study revealed that Co is substituted into ZnO lattice in a Co^{+2} valence state. No presence of metallic Co clusters was detected in the films by the XPS and XRD.

The inhomogeneous doping profile was confirmed by SIMS, indicating the coexistence of a thin highly doped surface layer and a ZnO film with a constant, but considerably lower, Co concentration.

The magnetic moment of Co-doped ZnO films was found to decrease with Co concentration and saturation magnetization was found to be highly anisotropic. A giant ferromagnetic moment of $14\mu_B$/Co was found for 1% Co. This is the largest moment observed in Co-doped ZnO ferromagnetic oxides to date. We suggest that magnetic moment in films grown by PI MOCVD, originates from a ferromagnetic/ antiferromagnetic ordering transition in a Co-doped ZnO layer.

The Co-doped ZnO films grown on Al_2O_3 (0001) in PI MOCVD reactor equipped with external magnet have developed ZnO (001) preferred orientation which is similar crystalline properties as to Co-doped ZnO discussed above. When doped with 15 and 20% of Co in precursor solution additional ZnO (101) reflection have appeared in XRD scans, which is different to our previous results. The morphology of the films grown was also very similar to those described above with the average calculated crystallite size matching those estimated from SEM micrographs. Finally, it was found that only five out of 12 prepared films are ferromagnetic at room temperature. The magnetic moments are lower than earlier observed giant magnetic moment in Co-doped ZnO film. In addition, opposite to expected, the preparation of the films in 1T external magnetic field did not induce the ferromagnetic ordering in Co-doped ZnO films, neither increase in the saturation magnetisation. The crystalline and structural properties of the films were identical when grown with and without magnetic field. Earlier, Kasuga *et.al.* [48] and Yanwei Ma *et.al.* [49] found that the growth rate of their ZnO and $YBa_2Cu_3O_7$ films was reduced and morphology was also different when grown in external magnetic field, however the magnetic field was much stronger than used in this work.

To summarise, it has been shown that PI MOCVD technique offers great potential for the preparation of room temperature ferromagnetic Co-doped ZnO films. Giant magnetic moments were measured for Co-doped ZnO films when doped with 1 and 2% Co. Different studies performed on structural and crystalline properties of the films confirm the intrinsic nature of observed ferromagnetism. The magnetic field applied during the growth of the films did not show the effect on structural, crystalline or magnetic properties of the films. We believe that PI MOCVD Co-doped ZnO films have great application perspectives in spintornic devices. However, the main drawback of these oxide based DMS is poor reproducibility of the magnetic properties.

References:

[1] H. L. Hartnagel, A. L. Dawar, A. K. J. and, C. Jagadish, **London 1995**.

[2] V. E. Wood, A. E. Austin, *Magnetoelectric Interaction Phenomena in Crystals*, Gordon and Breach, London, **1975**.

[3] A. A. J. A. C. S. 369, *Journal of American Ceramic Society* **1989**, *72*, 369.

[4] Y. Yan, S. B. Zhang, S. T. Pantelides, *Physical Review Letters* **2001**, *86*, 5723.

[5] A. F. Kohan, G. Ceder, D. Morgan, and C. G. Van de Walle, *Phys. Rev. B* **2000**, *61*, 15019.

[6] C. G. V. d. Walle, *Physica B* **2000**, *308–310,* 899

[7] S. Y. Myong, S. J. Baik, C. H. Lee, W. Y. Cho, and K. S. Lim, *Jpn. J. Appl. Phys.* **1997**, *36*, L1078.

[8] Ü. Özgür, Ya. I. Alivov, C. Liu, A. Teke, M. A. Reshchikov, S. Doğan, V. Avrutin, S.-J. Cho, a. H. Morkoçd, *Journal of Applied Physics* **2005**, *98*, 041301.

[9] D. C. Look, R. L. Jones, J. R. Sizelove, N. Y. Garces, N. C. Giles, a. L. E. Halliburton, *Phys. Status Solidi A* **2004**, *195*, 171.

[10] C. H. Park, S. B. Zhang, a. S.-H. Wei, *Phys. Rev. B* **2002**, *66*, 073202.

[11] A. Kobayashi, O. F. Sankey, and J. D. Dow, *Phys. Rev. B* **1983**, *28*, 946.

[12] J. Lu, Y. Zhang, L. W. Z. Ye, B. Zhao, and J. Huang, , **2003**, *57*, 3311.

[13] X. Wang, S. Yang, J. Wang, M. Li, X. Jiang, G. Du, X. Liu, and R. P. H. Chang, *J. Cryst. Growth* **2001**, *226*, 123.

[14] J. G. Ma, Y. C. Liu, R. Mu, J. Y. Zhang, Y. M. Lu, D. Z. Shen, and X. W. Fan, *J. Vac. Sci. Technol.B* **2004**, *22*, 94.

[15] Z. Z. Ye, J. G. Lu, H. H. Chen, Y. Z. Zhang, L. Wang, B. H. Zhao, a. J. Y. Huang, *J. Cryst. Growth* **2003**, *253*, 258.

[16] Y. Yan, S. B. Zhang, and S. T. Pantelides, *Phys. Rev. Lett.* **2001**, *86*, 5723.

[17] T. Dietl, H. Ohno, *MRS Bulletin* **2003**, *714*.

[18] X. M. Cheng, C. L. Chien, *Journal of Applied Physics* **2003**, *93*, 7876.

[19] U. Kenji, T. Hitoshi, K. Tomoji, *Applied Physics Letters* **2001**, *79*, 988.

[20] K. Ando, H. Saito, J. Zhengwu, T. Fukumura, M. Kawasaki, Y. Matsumoto, H. Koinuma, *Vol. 89*, AIP, **2001**, pp. 7284.

[21] J. Zhengwu, T. Fukumura, M. Kawasaki, K. Ando, H. Saito, T. Sekiguchi, Y. Z. Yoo, M. Murakami, Y. Matsumoto, T. Hasegawa, H. Koinuma, *Applied Physics Letters* **2001**, *78*, 3824.

[22] H. Saeki, H. Tabata, T. Kawai, *Solid State Communications* **2001**, *120*, 439.

[23] B. Beschoten, P. A. Crowell, I. Malajovich, D. D. Awschalom, F. Matsukura, A. Shen, a. H. Ohno, *Phys. Rev. Lett.* **1999**, *83*, 3073.

[24] Y. M. Kim, M. Yoon, I. W. Park, Y. J. Park, J. H. Lyou, *Solid State Communications* **2004**, *129*, 175.

[25] K. Rode, A. Anane, R. Mattana, J. P. Contour, O. Durand, R. LeBourgeois, *Journal of Applied Physics* **2003**, *93*, 7676.

[26] S. Ramachandran, A. Tiwari, and J. Narayan, *Appl. Phys. Lett.* **2004,** *84*, 5255.

[27] L. Hung-Ta, C. Tsung-Shune, S. Jhy-Chau, L. Show-Hau, H. Tzay-Ming, H. Rong-Tan, C. Fu-Rong, K. Ji-Jung, *Applied Physics Letters* **2004**, *85*, 621.

[28] D. P. Norton, M. E. Overberg, S. J. Pearton, K. Pruessner, J. D. Budai, L. A. Boatner, M. F. Chisholm, J. S. Lee, Z. G. Khim, Y. D. Park, R. G. Wilson, *Applied Physics Letters* **2003**, *83*, 5488.

[29] T. Wakano, N. Fujimura, Y. Morinaga, N. Abe, A. Ashida, and T. Ito, , *Physica C* **2001**, *10*, 260.

[30] B. S. Li, Y. C. Liu, Z. Z. Zhi, D. Z. Shen, Y. M. Lu, J. Y. Zhang, X. G. Kong, X. W. Fan, *Thin Solid Films* **2002**, *414*, 170.

[31] K.-H. Bang, D.-K. Hwang, S.-W. Lim, J.-M. Myoung, *Journal of Crystal Growth* **2003**, *250*, 437.

[32] J. Young Park, D. Ju Lee, Y. Su Yun, J. Ha Moon, B.-T. Lee, S. S. Kim, *Journal of Crystal Growth* **2005**, *276*, 158.

[33] S. G. Hammond, D. C. Nonhebel, C.-H. S. Wu, *Inorganic chemistry* **1963**, *2*, 73.

[34] X. Yang, G. Du, X. Wang, J. Wang, B. Liu, Y. Zhang, D. Liu, D. Liu, H. C. Ong, S. Yang, *Journal of Crystal Growth* **2003**, *252*, 275.

[35] P. A. Lane, P. J. Wright, M. J. Crosbie, A. D. Pitt, C. L. Reeves, B. Cockayne, A. C. Jones, T. J. Leedham, *Journal of Crystal Growth* **1998**, *192*, 423.

[36] Y. Ohno, D. K. Young, B. Beschoten, F. Matsukura, H. Ohno, D. D. Awschalom, *Nature* **1999**, *402*, 790.

[37] Y. D. Park, A. T. Hanbicki, S. C. Erwin, C. S. Hellberg, J. M. Sullivan, J. E. Mattson, T. F. Ambrose, A. Wilson, G. Spanos, B. T. Jonker, *Science* **2002**, *295*, 651.

[38] J. B. Torrance, M. W. Shafer, T. R. McGuire, *Physical Review Letters* **1972**, *29*, 1168.

[39] H. Ohno, *Science* **1998**, *281*, 951.

[40] L. Hyeon-Jun, J. Se-Young, C. Chae Ryong, P. Chul Hong, *Applied Physics Letters* **2002**, *81*, 4020.

[41] M. Venkatesan, C. B. Fitzgerald, J. G. Lunney, J. M. D. Coey, *Physical Review Letters* **2004**, *93*, 177206.

[42] W. Prellier, A. Fouchet, B. Mercey, S. Ch, B. Raveau, *Applied Physics Letters* **2003**, *82*, 3490.

[43] A. C. Tuan, J. D. Bryan, A. B. Pakhomov, V. Shutthanandan, S. Thevuthasan, D. E. McCready, D. Gaspar, M. H. Engelhard, J. W. Rogers, Jr., K. Krishnan, D. R. Gamelin, S. A. Chambers, *Physical Review B (Condensed Matter and Materials Physics)* **2004**, *70*, 054424.

[44] Z. Jin, M. Murakami, T. Fukumura, Y. Matsumoto, A. Ohtomo, M. Kawasaki, H. Koinuma, *Journal of Crystal Growth* **2000**, *214-215*, 55.

[45] D. Briggs, M.P. Seah, *Auger and X-ray Photoelectron Spectroscopy, Vol. 1*, Wiley, , New York, **1990**.

[46] N.S. McIntyre, D.D. Johnston, *Surf. Interface Anal.* **1990**, *15*, 265.

[47] S. Krishnamurthy, C. McGuinness, L. S. Dorneles, M. Venkatesan, J. M. D. Coey, J. G. Lunney, C. H. Patterson, K. E. Smith, T. Learmonth, P. -A. Glans, a. T. Schmitt, *Journal of Applied Physics* **2006**, *99*, 08M111.

[48] M. Kasuga, T. Takano, S. Akiyama, K. Hiroshima, K. Yano, K. Kishio, *Journal of Crystal Growth* **2005**, *275*, e1545.

[49] Yanwei Ma, Kazuo Watanabe, Satoshi Awaji, a. M. Motokawa, *Applied Physics Letters* **2000**, *77*, 3633.

[50] J. H. Kim, H. Kim, D. Kim, S. G. Yoon, W. K. Choo, *Solid State Communications* **2004**, *131*, 677.

[51] T. Dietl, H. Ohno, *Materials Today* **2006**, *9*, 18.

Chapter 4: Cr-doped In_2O_3 films

4.1. Introduction

In_2O_3 is a transparent n-type semiconducting oxide material (behaves as an insulator in stoichiometric form) with a wide band gap of ~3.6eV. Due to its unique properties, In_2O_3 found a variety of applications in microelectronic technologies. Tin doped In_2O_3 (ITO) is widely used as a transparent conductive electrode in various types of electronic devices, such as liquid crystal displays [1], solar cells [2], in tunnel junctions as a barrier layer [3] and as gas sensing material in gas sensors [4-6]. In semiconductors, In_2O_3 is used as a resistive element in integrated circuits [7]. When doped with tin dioxide, indium oxide forms indium tin oxide (ITO), which has high n-type conductivity and widely used in practice for transparent conductive coatings. In_2O_3 can serve as a semiconductor material, forming heterojunctions with p-InP, n-GaAs, n-Si, and other materials and used for manufacture of solar cells [2].

In_2O_3 doped with several atomic percent of transition metal was also considered as promising candidate for spintronics applications. The full review on recent progress on In_2O_3 is given in Chapter 1.4.3.2.

Up to date In_2O_3 films exhibiting high crystalline quality have been successfully prepared by MOCVD technique [8, 9]. However, up to date there are no publications on the preparation of In_2O_3 films and doped In_2O_3 films by PI MOCVD technique. Thus, the main aim of this part of the work is to prepare and characterise Cr-doped In_2O_3 films as possible candidates for spintronics applications using PI MOCVD method. Full characterisation of the films using XRD, XPS, SIMS, SEM and SQUID is provided in this chapter. In addition, Cr-doped In_2O_3 films are also prepared in magnetic field applied during the growth. The effect of applied magnetic field on magnetic and structural properties of Cr-doped In_2O_3 films is investigated.

4.2. Cr-doped In_2O_3 films

Thin films of Cr-doped In_2O_3 was recently reported to be a magnetic semiconductor displaying high-temperature ferromagnetism, single-phase crystal

structure, and semiconductor behaviour with high concentration of charge carriers [10]. Cr-doped In_2O_3 believed to be such a unique system, where the electrical and magnetic behaviour can be controllably tuned by the defect concentration. Being optically transparent and high temperature ferromagnetic, Cr-doped In_2O_3 appears as a viable candidate for the development of spin electronics. Another strong fact supporting suitability of In_2O_3 for the research of spintronics is based on the fact that magnetic ions when introduced into the lattice are distributed uniformly in the whole thickness of the film [11]. This is in contrast to the reported transition metal-doped ZnO, which was also experimentally observed in this work in Co-doped ZnO films.

4.2.1. Preparation of Cr-doped In_2O_3 films

Cr-doped In_2O_3 films were grown on c-cut and r-cut Al_2O_3 substrates using PI MOCVD technique. General deposition conditions are presented in the Table 4.1. Cr concentration in precursor solution was kept constant at 2 mol %. The substrate temperatures during deposition were increased every 50°C from 500 to 750°C. After deposition, the films were slowly cooled to room temperature in an oxygen pressure of 1 atmosphere. The thickness of the films, which was measured using scanning electron microscopy cross section, ranges from 270 nm to 400 nm depending on different substrate temperatures.

Table 4.1 Deposition conditions for Cr-doped In_2O_3 films

Deposition temperature	500 °C - 750 °C
Evaporation temperature	200 °C
Carrier gas flow (Ar + O_2)	800 ml/min
Reactor pressure	5 mbar
Metalorganic precursors	$In(acac)_3$, $Cr(acac)_3$
Solvent	1,2- dimethoxyethane
In/(Cr+In) concentration in solution	0.03 mol/l
Cr/(Cr+In) concentration in solution	2%
Impulse frequency	2 Hz
Microdose mass	4 mg
Substrates	Al_2O_3 (0001), Al_2O_3 $(1\underline{1}02)$

4.2.2. Characterisation of the Cr-doped In_2O_3 films

4.2.2.1. X-ray diffraction

XRD analysis was performed for all samples grown at different temperatures. The results for the XRD analysis for the Cr-doped In_2O_3 film on c-cut and r-cut sapphire are shown in Figure 4.1 and Figure 4.2, respectively. Films grown from $In(acac)_3$ at 500°C were mostly amorphous and had only very weak reflections from (222) and (400) planes. This fact indicates that 500°C is not sufficient temperature for precursor decomposition to occur on substrate surface, thus, resulting in the bad quality film (not shown in the graphs). All films deposited at 550°C-750°C on c-cut and r-cut sapphire substrates were polycrystalline and retained a cubic bixbyte structure. No secondary phases of metallic Cr or any other possible chromium oxides were detected by XRD.

For the films grown on Al_2O_3 (0001) substrate (222) and (400) orientations were dominant at all temperatures. Films deposited at 550 and 600°C also had other peaks, corresponding to (440), (600), (611), (622) orientations of In_2O_3. The intensity of (222) reflections increased with temperature, at the same time intensity of (400) reflections decreased. For the films grown at 750°C (222) preferential orientation was found to be dominant and only very weak reflection from (400) plane was observed. Similar change in preferred orientation from two (222) and (400) dominant orientations to more intense (222) orientation with the increase of substrate temperature was reported by Kostlin *et. al.*, in sprayed In_2O_3 films [12]. It was also reported that in the case of the films grown by chemical vapours the prevalence of the (222) orientation was observed [13, 14].

Films grown on Al_2O_3 ($1\underline{1}02$) substrate had (222), (400) and (440) preferred orientations. At lower deposition temperature all three reflections seem to be dominant along with very weak reflections from (622) plane. For Cr-doped In_2O_3 films grown at higher (650-750°C) temperature the intensity of (440), (222) reflection increased, but the intensity of (400) decreased, similarly as was observed for the films grown on Al_2O_3 (0001) substrate. Overall, it was found that growth of the films at higher temperatures on both substrate orientations had led to an improvement in the crystalline quality, confirmed by small values of FWHM.

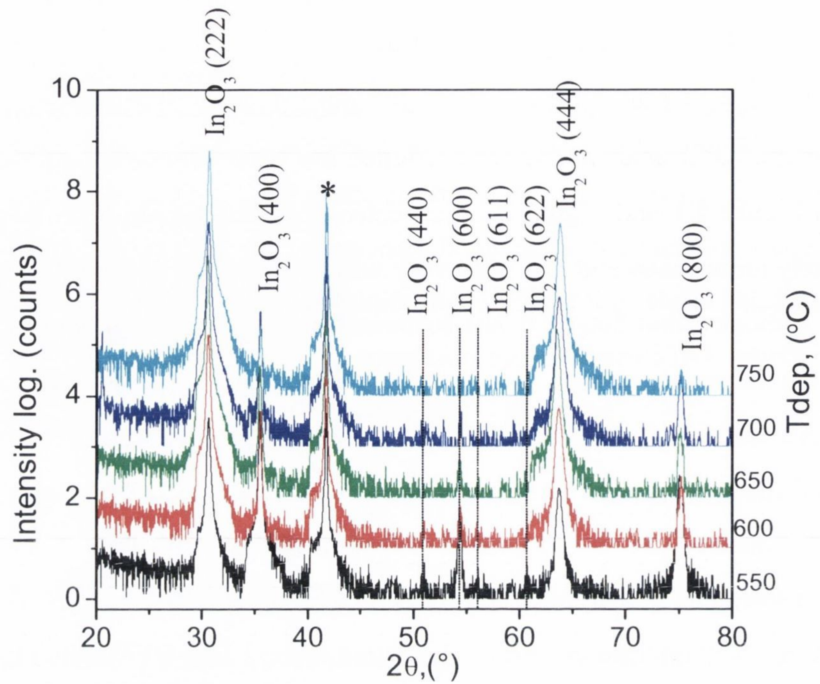

Fig. 4.1. XRD spectra for Cr-doped In_2O_3 films on Al_2O_3 (0001) at different deposition temperatures

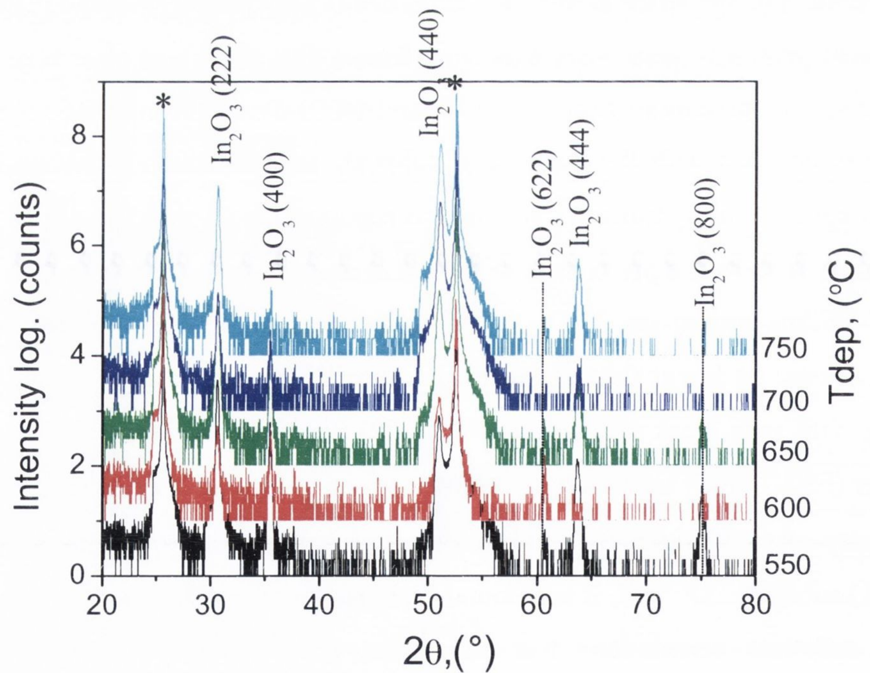

Fig. 4.2. XRD spectra for Cr-doped In_2O_3 films on Al_2O_3 ($1\underline{1}02$) at different deposition temperatures

The structural parameters such as lattice constant, crystallite size were calculated from the XRD data and their variation as a function of deposition temperature was studied. The *a* lattice parameter of cubic Cr-doped In_2O_3 films was calculated using the relation:

$$a = d\sqrt{(h^2 + k^2 + l^2)} \quad (29)$$

where *h, k, l* are the lattice planes and *d* is the interplanar spacing calculated from Bragg's equation. The *a* lattice parameter value was calculated from most intensive (222) reflection for films on Al_2O_3 (0001), and from (222), and (440) for the films on Al_2O_3 (1$\underline{1}$02) sapphire. Figure 4.3 shows the variation of the lattice parameter with the deposition temperature.

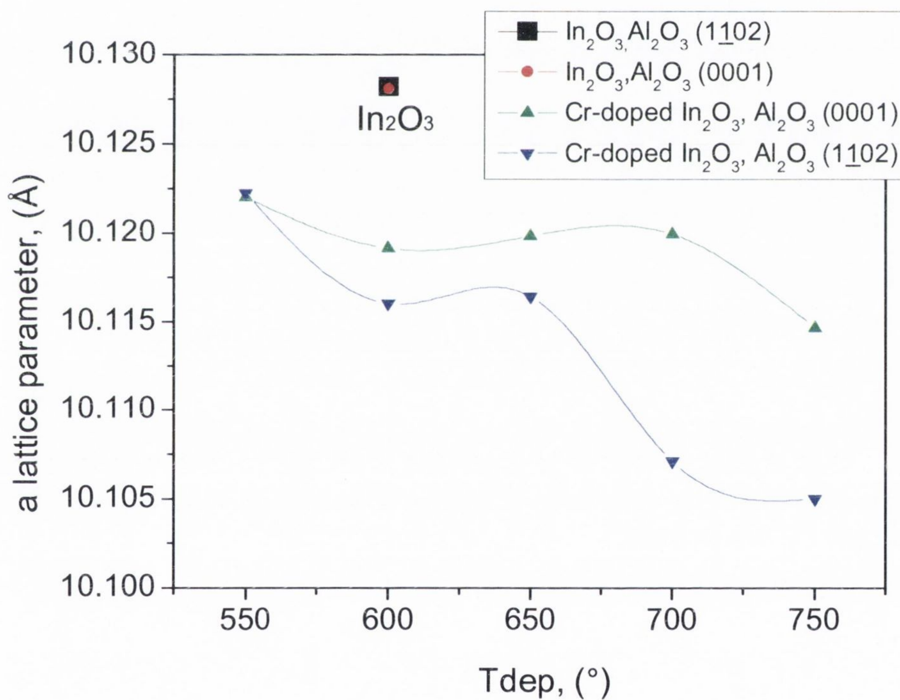

Fig. 4.3.Variation of a lattice parameter of Cr-doped In_2O_3 films with deposition temperature

The lattice parameter of undoped In_2O_3 on both substrates was slightly larger than the reported value[15] of 10.118Å for the cubic In_2O_3. 2% Cr-doped In_2O_3 films on two different substrates grown at lowest temperature had the highest lattice constant value of

10.128 Å. In both cases, a slightly smaller *a* lattice parameter values are expected for Cr-doped In_2O_3 films, since the smaller Cr atom substitutes for the larger In atom. For the films grown on Al_2O_3 (0001) the *a* parameter decreased from 10.128Å to 10.115Å as the substrate temperature increased and had the minimum value at 750°C indicating an improvement in the crystallinity. Similar change in lattice constant was found for the films on Al_2O_3 (1$\underline{1}$02), with the lowest value of 10.105Å at 750°C. Since the thickness of the films is well above 100nm we excluded the possibility that lattice mismatch between In_2O_3 and Al_2O_3 substrate, which is as high as 25%, is responsible for the observed changes in the lattice parameters. The above condition, where the strain effects play significant role in the change of lattice parameters may apply mostly for the films with thickness well under 100nm.

We found that the optimum temperature for the growth of 2% Cr-doped In_2O_3 films using PI MOCVD method is quite broad and lies within the range of 600-750°C.

The average crystallite size (D) of the films prepared at different substrate temperatures was calculated from the FWHM of the (222) peak reflection using Scherrer formula. The calculated values are given in Table 4.2. For the films grown on Al_2O_3 (0001) no correlation between deposition temperature and crystallite size was found. For the Cr-doped In_2O_3 films grown on Al_2O_3 (1$\underline{1}$02), the crystallite size increased with deposition temperature with the exception for the sample obtained at 550°C, which had the largest crystallites.

Table 4.2 The average crystallite size calculated using Scherrer formula for Cr-doped In_2O_3 film grown at different temperatures

T deposition (°C)	**Average crystallite size (nm), on Al_2O_3 (0001)**	**Average crystallite size (nm), on Al_2O_3 (1$\underline{1}$02)**
550	41	51
600	40	32
650	51	36
700	40	41
750	47	48

4.2.2.2. Morphology of Cr-doped In_2O_3 films

SEM and AFM analysis were carried out on all samples (Figures 4.4 and 4.5). The influence of deposition temperature on Cr-doped In_2O_3 films morphology was studied. SEM pictures revealed that surface morphology depends strongly on deposition temperature and it is consistent with the XRD results. Films grown at 500°C had very smooth surface. Referring back to XRD for the films deposited at 500°C it was suggested that SEM showed only the surface of the sapphire substrate and no film was formed at this temperature. Films deposited at 550°C consisted of densely populated crystallites with different preferred orientations. Increase in temperature to 750°C resulted in the growth of well ordered films having mainly In_2O_3 (222) and In_2O_3 (400) together with In_2O_3 (440) oriented crystallites on Al_2O_3 (0001) and Al_2O_3 ($1\underline{1}02$) substrates respectively. These crystallites tend to grow together at higher temperatures forming continuous film consisting of larger coalesce crystallites. Average crystallite size at 750°C ranged from 340nm - 450nm and 250 - 500nm for the films grown on Al_2O_3 (0001) and Al_2O_3 ($1\underline{1}02$) substrates respectively.

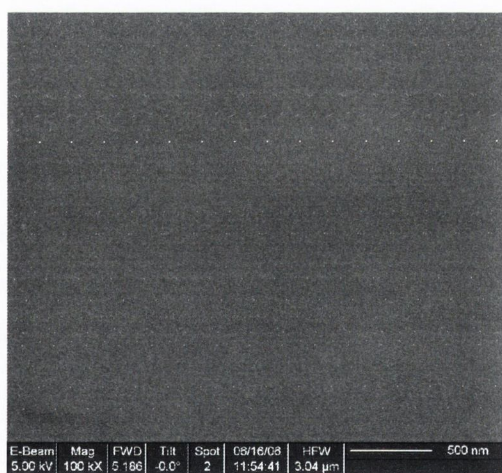

Tdep 500°C

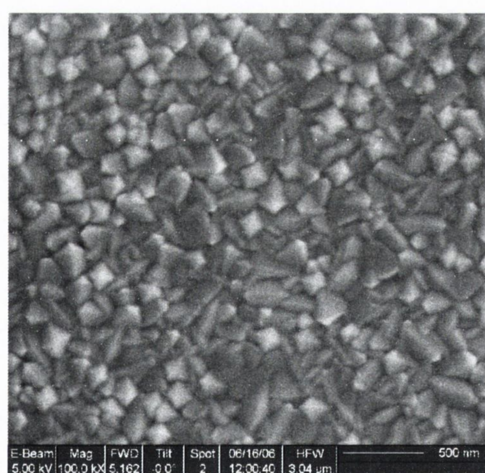

Tdep550°C

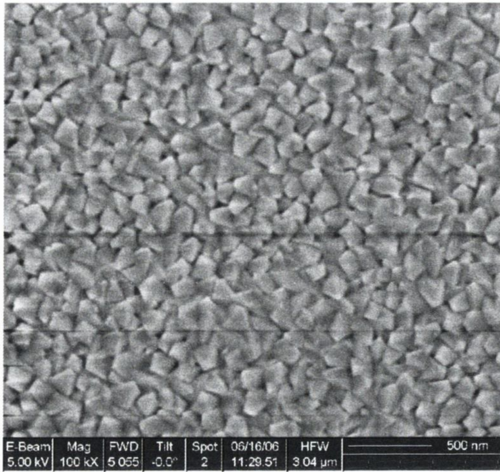

Tdep 600°C

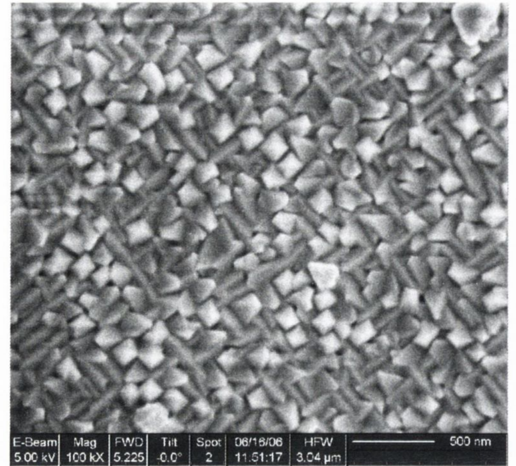

Tdep 650°C

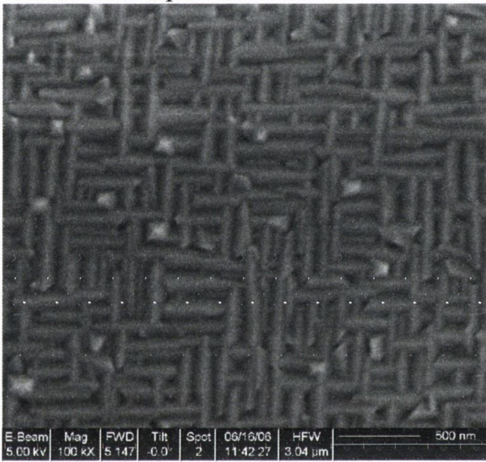

Tdep700°C

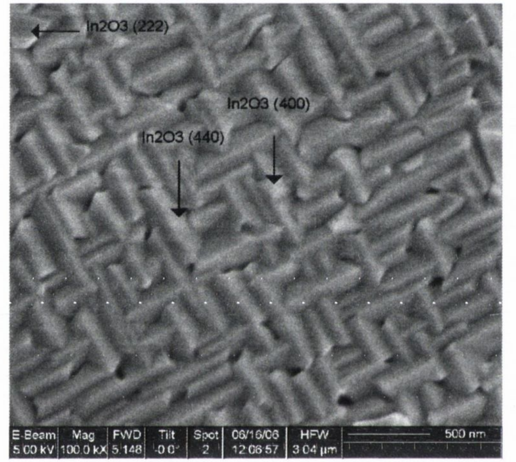

Tdep 750°C

Fig. 4.4 SEM images of Cr-doped In_2O_3 films on Al_2O_3 $(1\bar{1}02)$ substrate deposited at different temperatures

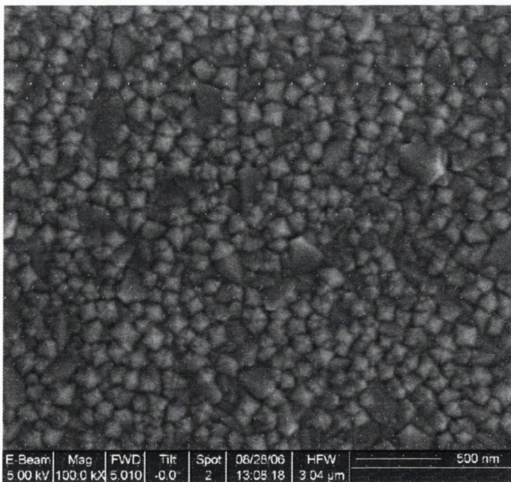

Tdep 550°C

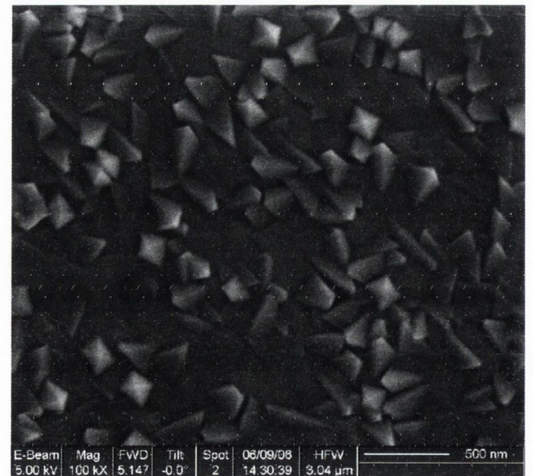

Tdep 600°C

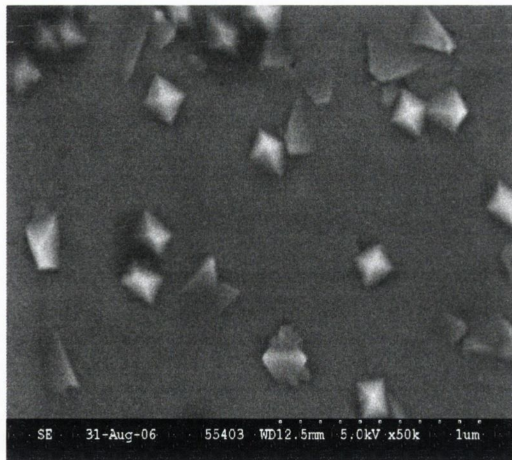

Tdep 650°C

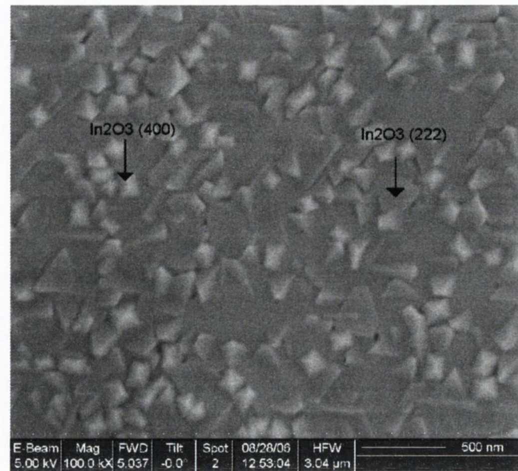

Tdep 700°C

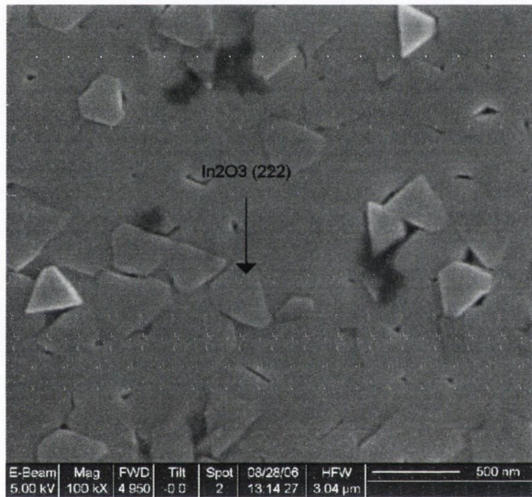

Tdep750°C

Fig. 4.5 SEM images of Cr-doped In_2O_3 films on Al_2O_3 (0001) substrate deposited at different temperatures

SEM cross-section analysis was also used to estimate the thickness of the Cr-doped In_2O_3 films. The example of SEM cross-section analysis is shown in Figure 4.6. The variation of films thickness with growth temperature is presented in Figure 3.7.

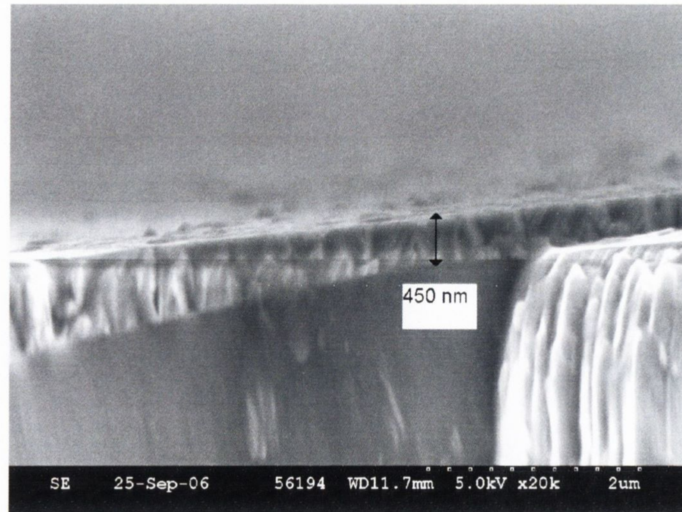

Fig. 4.6 SEM cross-section image for Cr-doped In_2O_3 film on Al_2O_3 (0001) grown at 750°C

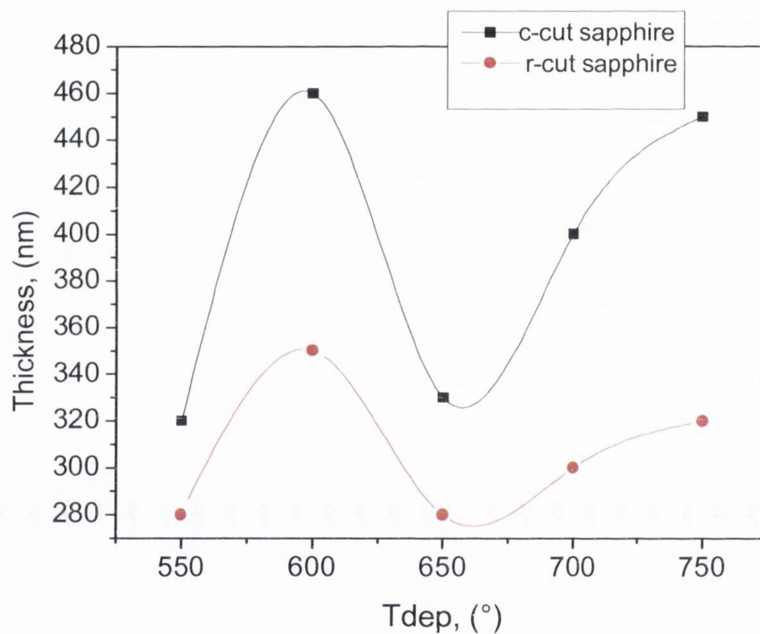

Fig. 4.7 The variation of Cr-doped In_2O_3 films thickness with growth temperature

From SEM cross section it was found that films thickness increased with deposition temperature with the exception for the films grown at 600°C on both substrates, which were the thickest. This inconsistency in the film thickness grown at 600°C could arise due to pulse instability during the injection of the precursor into the evaporation zone. The thickness increased from 320nm to 450nm and from 280 to 320nm

for the films on Al_2O_3 (0001) and Al_2O_3 $(1\underline{1}02)$ substrates respectively. In addition all films grown on Al_2O_3 (0001) were thicker than those grown on Al_2O_3 $(1\underline{1}02)$ substrate, which could be due to shifted deposition centre of the sample holder.

AFM micrographs of Cr-doped In_2O_3 deposited at different temperatures were recorded over the area of $5\mu m \times 5\mu m$. Figure 4.8 shows the AFM images of the films deposited at 750°C. AFM analysis confirmed the surface morphology of the films observed in SEM analysis. AFM also showed that films deposited at 550-700°C were very rough. The average surface roughness (Ra) ranged from 3.9 nm to 20.8nm for the Cr-doped In_2O_3 films on Al_2O_3 (0001). Films grown on Al_2O_3 $(1\underline{1}02)$ had smaller roughness deviation, which was found to decrease with deposition temperature form 13.5nm to 7.0 nm. Films grown at 750°C had the smallest Ra values of 3.9nm on Al_2O_3 (0001) and 7nm on Al_2O_3 $(1\underline{1}02)$ due to increase in films texture and coalescence of smaller crystallites.

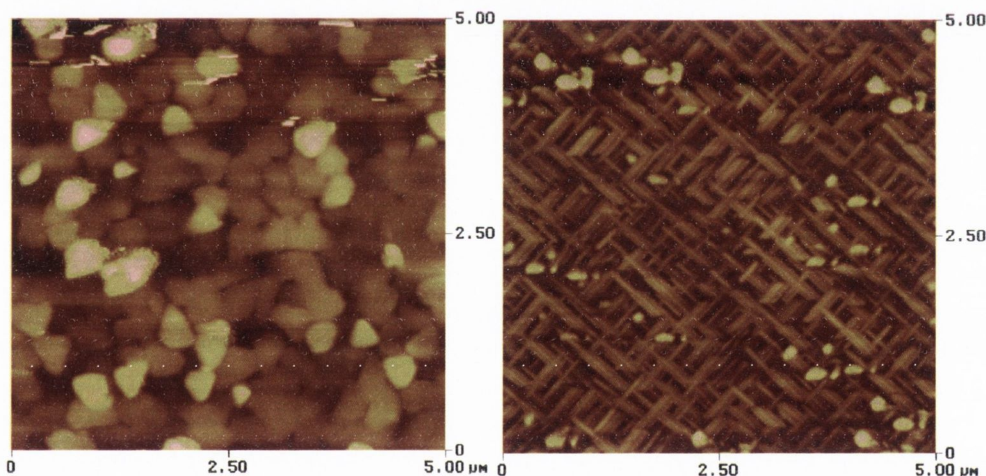

Fig. 4.8 AFM images of the Cr-doped In_2O_3 films deposited at 750°C. Left image- film grown on Al_2O_3 (0001), and right image for the film grown on Al_2O_3 $(1\underline{1}02)$ substrate

4.2.2.3. Composition of Cr-doped In_2O_3 films

EDAX was carried out on all Cr-doped In_2O_3 films. For all films the presence of aluminium, indium, chromium and oxygen was detected (Figure 4.9). The strong Al signal is coming from Al_2O_3 substrate. Weak Cr and very intensive In signals were

detected in all films. Measurements were carried out in 5 different regions of the film and the average value was estimated.

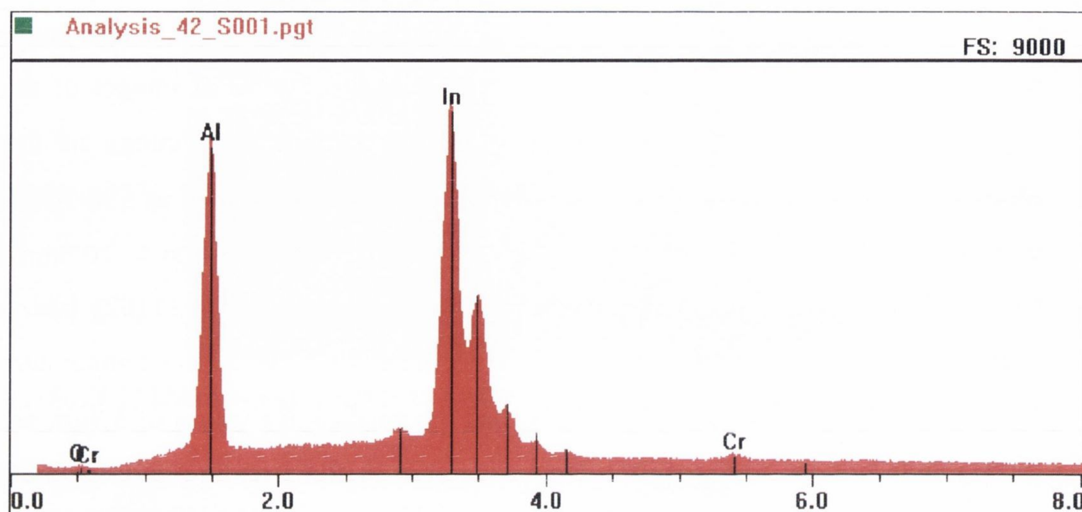

Fig. 4.9 Typical EDAX analysis spectra for Cr-doped In_2O_3 films grown on Al_2O_3 substrate

Cr concentration in a film was identified from relative intensities of In and Cr peaks by comparing them with peak intensities for the standards of In_2O_3 and Cr_2O_3. EDAX analysis revealed that Cr concentration in the films deposited at different temperatures was only slightly larger than that in precursor solution. The results are presented in Figure 4.10.

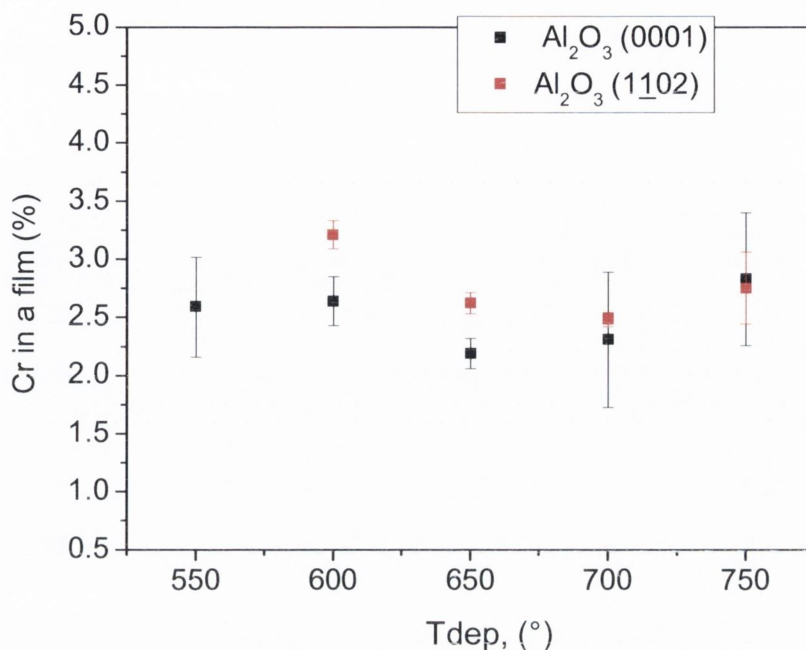

Fig. 4.10 Variation of Cr concentration in the 2% Cr-doped In_2O_3 films with deposition temperature

In order to determine the valence state of Cr ions in In_2O_3 matrix, core levels of XPS were measured. XPS analysis was performed on Cr-doped In_2O_3 films grown at 600 and 700°C on Al_2O_3 (0001) and Al_2O_3 ($1\underline{1}02$) substrates. Prior to XPS all samples were cleaned by sputtering the surface with Ar^+ ions to remove surface contamination. XPS measurements were obtained using Mg K_α line radiation (hν=1253,6 eV). Recording spectra a detail scan of ΔE=50meV was used. The binding energies of core electrons were corrected with the respect to the C 1s peak (284.6 eV).

$Cr2p_{3/2}$ peaks were obtained by subtracting the background from the recorded spectrum and then normalised. The Cr2p spectra of Cr-doped In_2O_3 films are shown in Figure 4.11. Vertical lines in the spectra indicate previously reported binding energies for Cr ions in the different valence states reported in [16-19] and Cr^0 corresponds to the binding energy of metallic Cr.

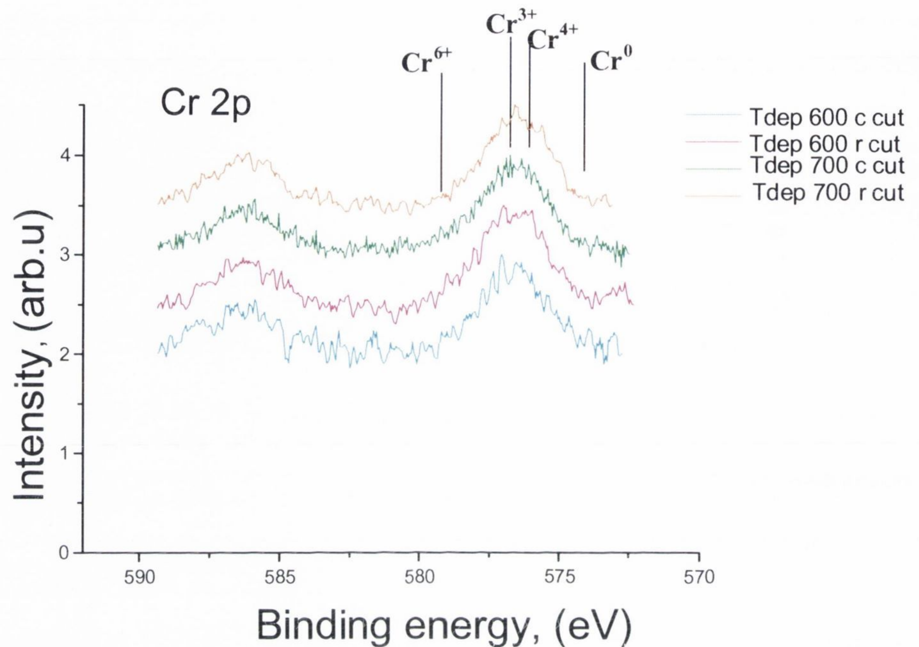

Fig. 4.11 XPS spectra of the Cr2p core level in the Cr-doped In_2O_3 films

Except for Cr, In, O and C elements, no other elements were found in the Cr-doped In_2O_3 films. It is believed that some amount of carbon may arise from the contamination on the surface of the films. The binding energy of the major $Cr2p_{3/2}$ core level contribution in all Cr-doped In_2O_3 films is about 576.0 ±0.3 eV, which is more consistent with the binding energy of Cr^{4+} (576.2-576.4eV) in CrO_2 [17, 18]. The accepted value of Cr^{3+} peak in $Cr2p_{3/2}$ spectra of Co_2O_3 lies in the energy interval of 576,6÷577eV [17, 18]. The position of Cr^{6+} ions in Cr2p binding energy spectrum of CrO_3 was in the range of 579,2÷580eV [16]. The Cr2p binding energy for Cr metal is at 574.2eV [16]. In XPS spectra measured for PI MOCVD grown Cr-doped In_2O_3 films no maximum is observed for the binding energy of Cr metal and Cr^{6+}, hence the presence of Cr^{6+} and formation of metallic Cr clusters is ruled out. The presence of Cr2p core level peak at 576.0 ±0.3 eV suggests that Cr in In_2O_3 matrix is present in Cr^{4+} state. However, the possibility that Cr in In_2O_3 is present in Cr^{3+} valence state cannot be excluded because the binding energies of Cr^{4+} and Cr^{3+} are

very close. Additional O1s XPS spectrum is required to differentiate between the Cr^{3+} and Cr^{4+}, like was found in the chromium oxide junctions [17]. XPS analysis also confirmed that Cr-doped In_2O_3 films were stoichiometric with O/(In+Cr) ratio ranging ~ 1.5 to 1.55.

SIMS analysis for the Cr-doped In_2O_3 films reveals a homogeneous distribution of Cr ions with the film depth without any surface or interface segregations in contrast to Co-doped ZnO films [20]. For example, in [21, 22] from Rutherford backscattering spectroscopy measurements was also found that Cu and Ni distribution in In_2O_3 is much more uniform than that in TiO_2 and ZnO. In general, as for the In_2O_3 host, it seems to be easier to get a uniform dopant distribution, in contrast to the case of doping transition metals for other host oxides such as ZnO. The results for SIMS depth profiles are shown in Figures 4.12 and 4.13. The position of the dashed line indicates the start of the registry of secondary ions and the black solid line indicates the moment when substrate surface is reached. Furthermore, Al^+ ions were observed through the whole thickness of the film, due to either diffusion of the Al into the film or due to the presence of holes in the films. Other SIMS registered ions were Na^+-23, O^+-16, In^+- 115, Cr^+-52, InO^+-131, CrO^+-68, Al^+-27. It is noted that some presence of Na^+ is always found on the surface of the samples due to contamination.

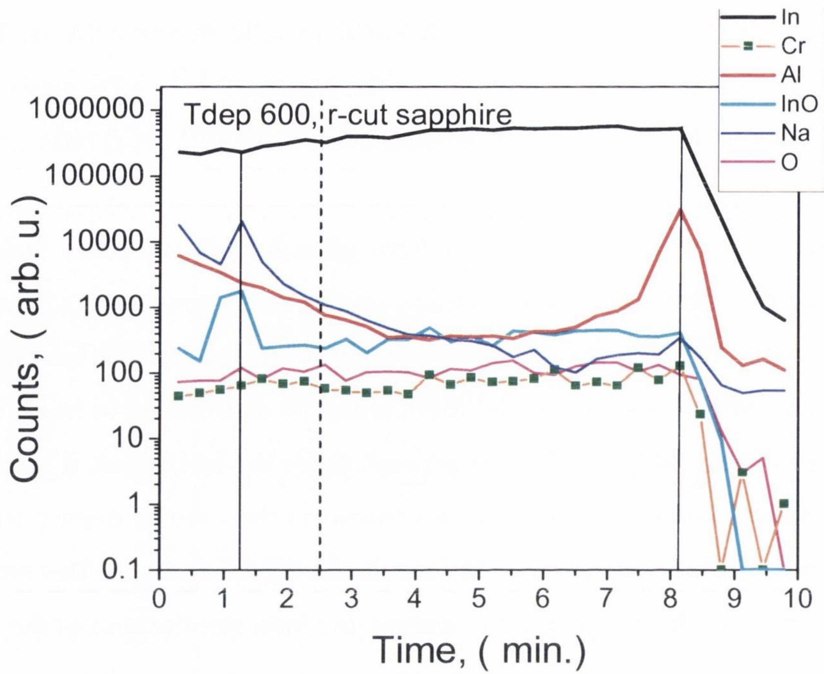

Fig. 4.12 SIMS depth profile as a function of milling time for 2% Cr-doped In_2O_3 film grown at 600°C on Al_2O_3 (1$\underline{1}$02) substrate

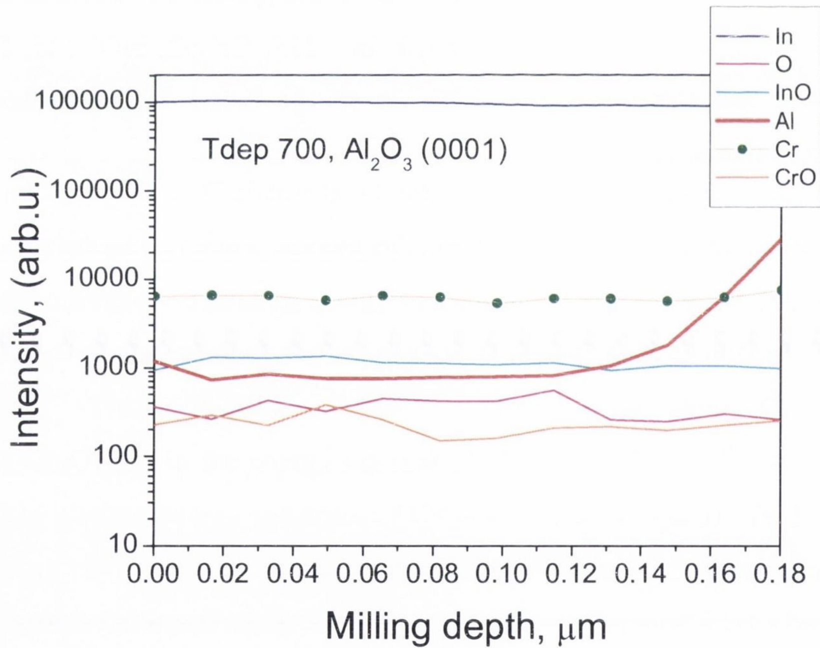

Fig. 4.13 SIMS depth profile as a function of milling depth for 2% Cr-doped In_2O_3 film grown at 700°C on Al_2O_3 (0001) substrate

4.2.2.4. Optical properties of Cr-doped In_2O_3 films

All Cr-doped In_2O_3 were transparent under visual examination. The optical transmission spectra were taken for the films grown at three different temperatures: 550°C, 650°C and 750°C, in the wavelength range between 300nm and 800nm. The results are shown in Figure 4.14. From the obtained spectra it is obvious that optical transmittance of the films is highly affected by the deposition temperature. The optical transmittance of the films was high and had the value of ~90%. However the films grown at 750°C had a sharp decrease in transmittance with decreasing the wavelength. The film grown at 650°C had better optical transmittance, although the best value was obtained for the film grown at 550°C. Generally, the high transmittance in the films is attributed to less scattering effects, structural homogeneity and good crystalline quality.

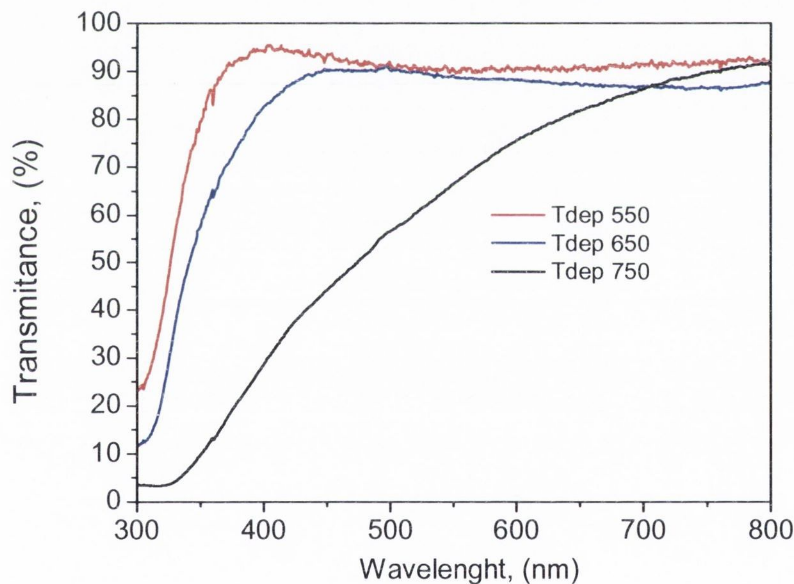

Fig. 4.14 Optical transmission spectra of 2%Cr-doped In_2O_3 grown at different temperatures

4.2.2.5. Magnetic properties of Cr-doped In_2O_3 films

Magnetisation measurements were carried on all Cr-doped In_2O_3 films using SQUID magnetometer. All measurements were performed at room temperature in 1 Tesla magnetic filed applied perpendicular and parallel to the film surface.

All films grown on Al_2O_3 (0001) substrate were found ferromagnetic at room temperature. Although, films grown on Al_2O_3 (1$\underline{1}$02) substrate did not show ferromagnetic behaviour at room temperature. Typical magnetisation curve for 2% Cr-doped In_2O_3 film on Al_2O_3 (0001) substrate is shown in Figure 4.15.

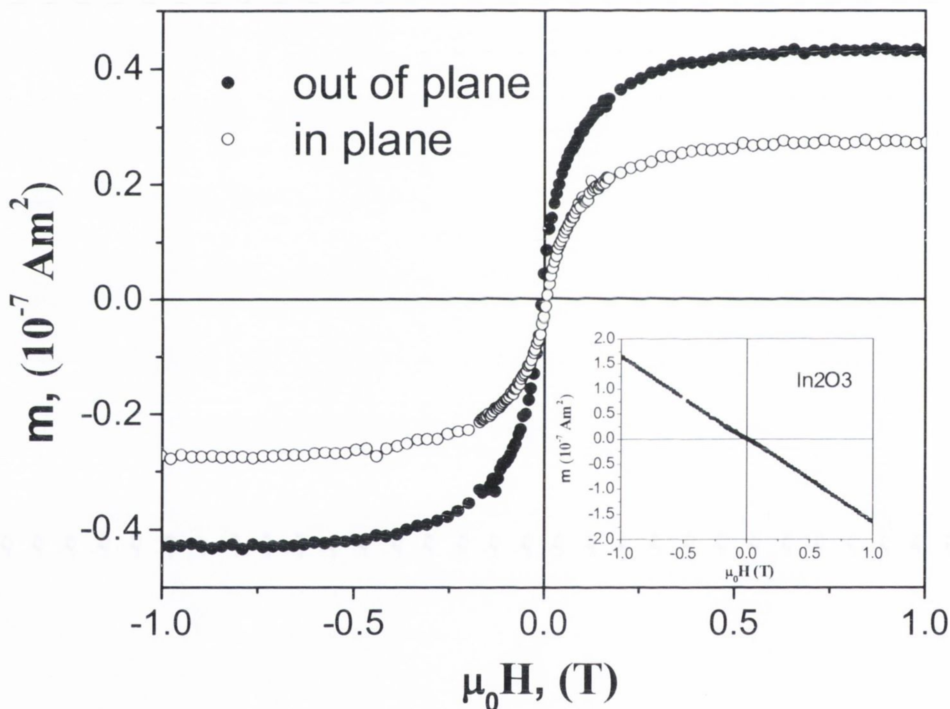

Fig. 4.15 SQUID magnetisation curve for 2%Cr-doped In_2O_3 film grown at 700°C on Al_2O_3 (0001) substrate. Inset in the figure shows magnetisation curve of undoped In_2O_3 film

The diamagnetic contribution from Al_2O_3 substrate is subtracted from the data. To rule out any contribution from magnetic impurities, which may arise during deposition process, undoped In_2O_3 film was also measured with SQUID. As expected, no magnetic moment was measured for undoped In_2O_3 (Figure 4.15, inset). Similar to Co-doped ZnO

films, all Cr-doped In_2O_3 films, except for the films grown at 600°C, which had very small anisotropy value, were found to be highly anisotropic having the highest magnetic moment when field is applied perpendicular to the film plane (Figure 4.16). The highest saturation magnetisation of $1.65\mu_B$/Cr assuming that all the Cr atoms contribute to the magnetisation, was found for the Cr-doped In_2O_3 film grown at 700°C. Overall, the saturation magnetisation did not change drastically with deposition temperature, except for the film grown at 600°C, which had the smallest magnetic moment of only $0.42\mu_B$/Cr. The absolute magnetic moment for the films grown at different temperatures is shown in the inset in Figure 4.16.

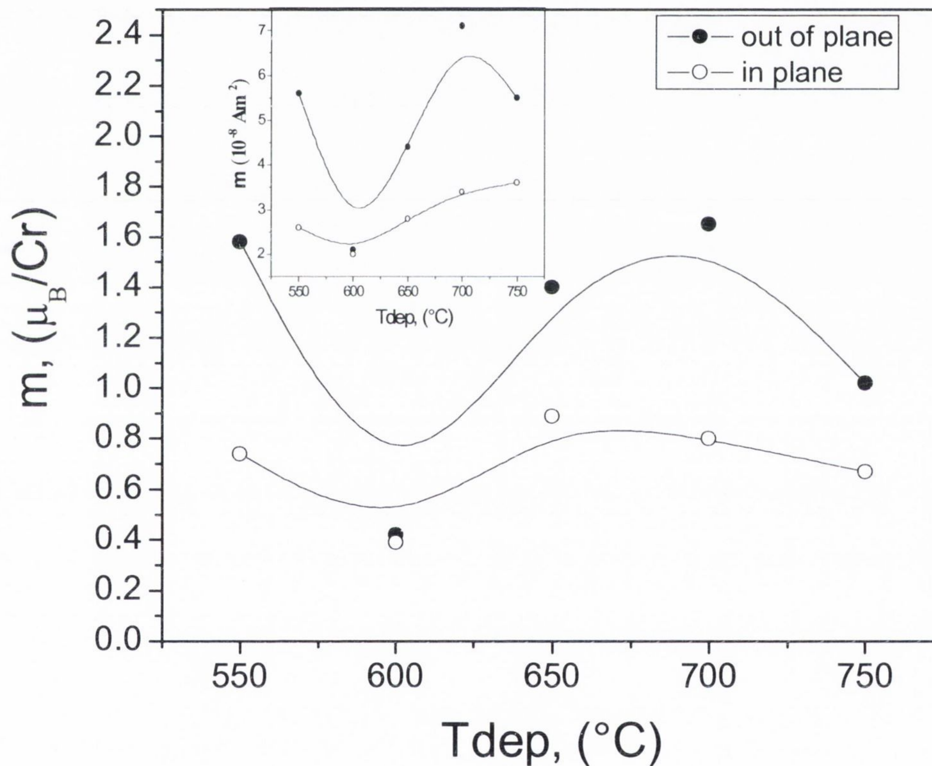

Fig. 4.16 Saturation magnetisation of Cr-doped In_2O_3 films expressed in μ_B/Cr atom as a function of deposition temperature, the inset shows the variation of absolute magnetic moment for Cr-doped In_2O_3 films as a function of deposition temperature

In addition to room temperature ferromagnetism and high anisotropy all films exhibited a small remanence of ~ 10% when field is applied perpendicular and ~ 15% for the parallel fields (Figure 4.17).

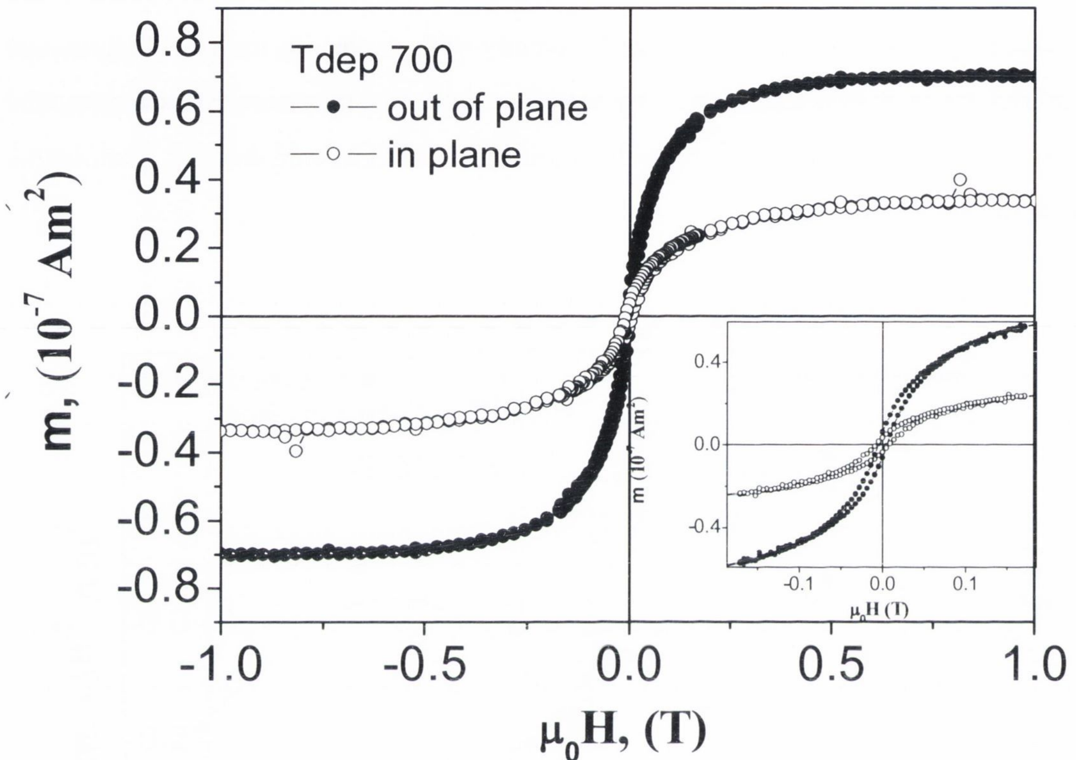

Fig. 4.17. Hysterisis curve for the Cr-doped In_2O_3 film grown at 700°C, graph inside shows magnified area of the hysterisis curves

Small coercive fields were found for all the samples. Coercive fields of up to 65 Oe together with saturation magnetisation of $1.5\mu_B$/Cr were also found in 2% Cr-doped In_2O_3 films prepared by reactive evaporation technique [10]. This results are consistent with the results obtained form our Cr-doped In_2O_3 films. The coercive field in PI MOCVD prepared films was higher when the magnetic field is applied parallel to the film surface with one exception for the film grown at 750°C. The measured coercive field values for both magnetic field directions are shown in Table 4.3.

Table 4.3 Calculated coercive fields for Cr-doped In_2O_3 films grown at different temperatures

Deposition temperature, (°C)	Coercive field, (Oe) for perpendicular direction of magnetic field	Coercive field, (Oe) for parallel direction of magnetic field
550	65	74
600	72	89
650	53	80
700	50	80
750	71	58

In this work, the variation of the magnetic moment of Cr-doped In_2O_3 films as function of time was also studied. It was previously found in our Co-doped ZnO films that magnetic moment is not stable and decreasing with time. For this reason, the magnetisation measurements of Cr-doped In_2O_3 films grown at 550°C and 750°C were carried out systematically over time. The results are shown in Figure 4.18. In both cases the as deposited films had the largest saturation magnetisation, nominally $5.6\times10^{-8}Am^2$ and $5.4\times10^{-8}Am^2$ for the films grown at 550°C and 750°C respectively, when field is applied perpendicular to the film surface. When films were repeatedly measured after 4 months, the out of plane saturation magnetisation decreased for films grown at 550°C and 750°C to $\sim4.5\times10^{-8}Am^2$ and $4.0\times10^{-8}Am^2$, respectively. Finally, when measured after 9 months, films had saturation magnetisation of $\sim4.5\times10^{-8}Am^2$ and $\sim3.4\times10^{-8}Am^2$. We found, that similar to Co-doped ZnO films, the saturation magnetisation in Cr-doped In_2O_3 film is not stable with time. Although, the decrease in saturation magnetisation for Cr-doped In_2O_3 films is significantly smaller (and even stabilises for the sample grown at 550°C) than that observed for Co-doped ZnO, where more than 50% decrease in magnetisation was measured just after 2 weeks. At the same time the in plane magnetisation changed differently for both samples. For the film grown at 550°C the in plane saturation magnetisation increased from $2.6\times10^{-8}Am^2$ to $3.7\times10^{-8}Am^2$ and $3.9\times10^{-8}Am^2$ when measured after 5 and 9 months, respectively. However, for the film grown at

750°C the in plane saturation magnetisation slightly decreased from $3.5\times10^{-8}Am^2$ to $3.4\times10^{-8}Am^2$ and $3.0\times10^{-8}Am^2$. Although, there is inconsistency in the changes of in plane saturation magnetisation with time, one common trend is observed for both samples: the magnetic anisotropy tends to decrease with time.

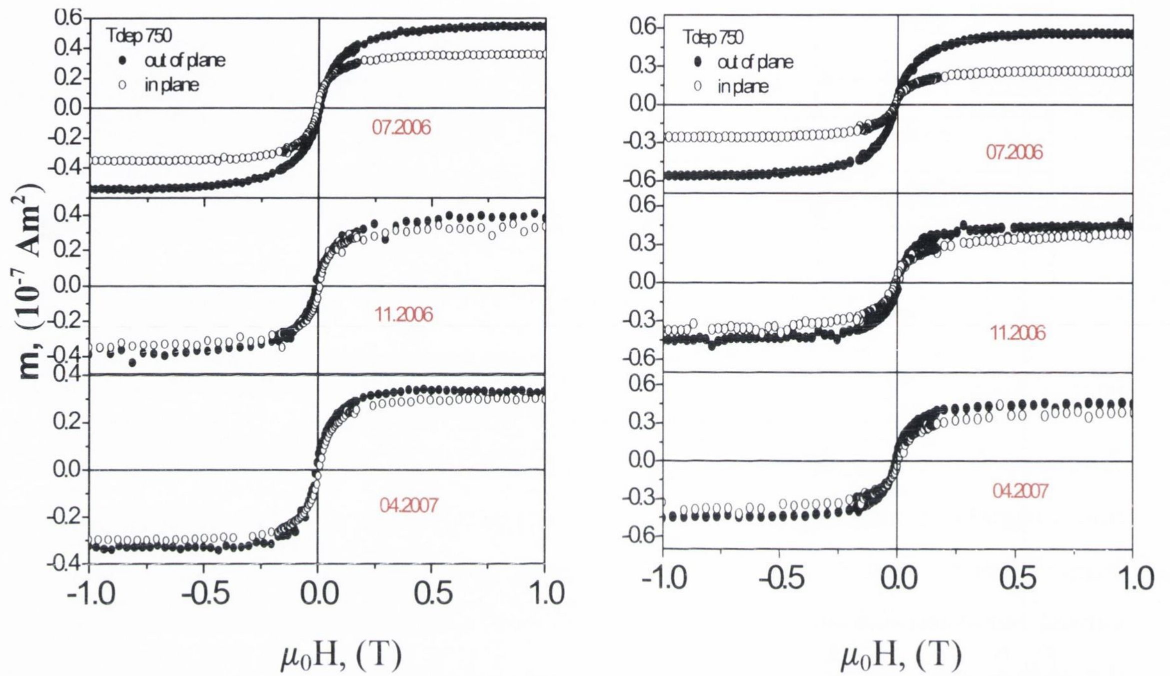

Fig. 4.18 The variation of out of plane and in plane saturation magnetisation with time for Cr-doped In_2O_3 films deposited at 550°C and 750°C

4.2.2.5.1. Effect of vacuum annealing on magnetic and structural properties

In most cases the observed ferromagnetism in TM-doped In_2O_3 films was found when films were semiconducting [23-26] or even showing some metallic behaviour [10], but not in insulating films [10, 24]. These results suggest Carrier-mediated model for ferromagnetism, in which the ferromagnetism is produced by *n*-type carriers that arise from oxygen vacancies in the sample. However, all our ferromagnetic Cr-doped In_2O_3 films prepared by PI MOCVD technique were insulating therefore it is hard to explain the observed ferromagnetism in these films.

To find out if induced oxygen vacancies could affect the ferromagnetic behaviour of our films, two samples were annealed in vacuum and their magnetic properties were investigated. Apart from magnetic properties of the films, their structural and crystalline properties were also investigated subsequently after annealing in vacuum (10^{-6} kg/cm^2). For this reason, two films grown on c-cut sapphire substrates at 600ºC and 700ºC were annealed in vacuum at 600ºC for 1 hour. The visual examination of the films showed that after vacuum annealing films retained its transparency. Annealing in vacuum also induced some conductivity in the films, as measured by multimeter, which was in the range of ~ 2kΩ and did not change with time. This means that annealing in vacuum induced oxygen vacancies in the films.

4.2.2.5.2. Conductivity measurements

In order to check the conductivity of vacuum annealed Cr-doped In_2O_3 film, two point DC conductivity measurements were carried out in School of Physics, Trinity College Dublin. Indium contacts were attached to the sample surface and served as electrodes. The current in the sample was measured as a function of applied voltage, which was varied from 0 to 0.05 at a rate of 0.005 volts per second at an interval of 10 points per second (Figure4.19). Knowing the samples thickness (*t*), width (*w*) and length (*l*) it is possible to calculate the conductivity using Formula 30.

$$\sigma = \frac{I}{V}\frac{l}{w \times t} \tag{30}$$

The film with the thickness of 460nm and 5mm length and width resulted in quite high conductivity value of 1876 S/m. Consequently; this gives the resisitivity value of 5.33^{-4} Ω/m for vacuum annealed Cr-doped In_2O_3 film.

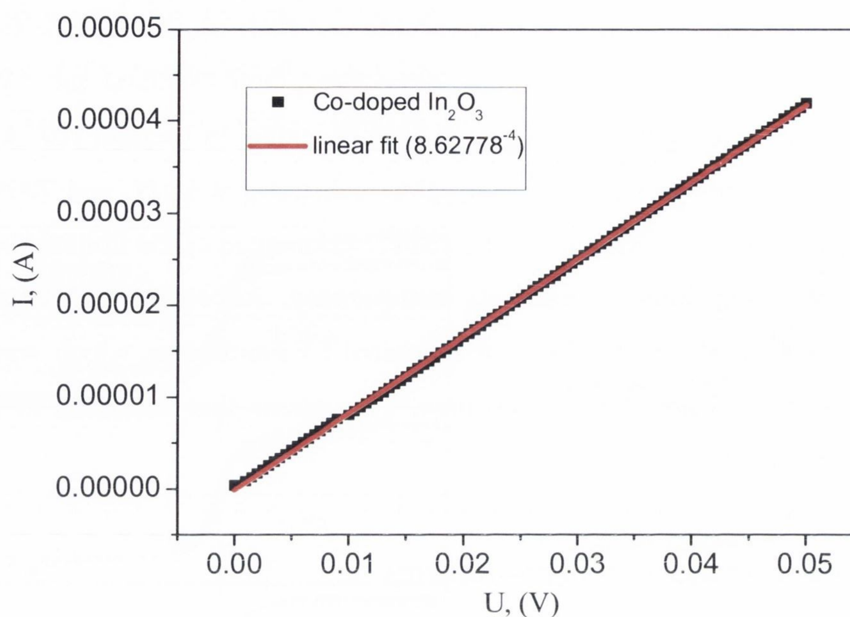

Fig. 4.19 Current (I) versus applied voltage in vacuum annealed Cr-doped In_2O_3 film showing the linear dependence as expected from Ohm's law

4.2.2.5.3. Structural properties and morphology of annealed films

It was crucial to investigate how vacuum annealing of the Cr-doped In_2O_3 films could affect its crystalline properties. For this reason, XRD analysis was performed on annealed samples and compared with the initial XRD data. The results of XRD analysis for annealed films are shown in Figure 4.20. X-ray diffraction analysis revealed that annealing in vacuum did not affect the crystalline quality of the films. In fact, film grown at 600°C had the same crystalline structure exhibiting (222) and (400) preferred orientations. The film grown at 700°C also showed similar crystalline structure with only one (222) preferred orientation as compared to (222) and (400) reflections prior to annealing in vacuum.

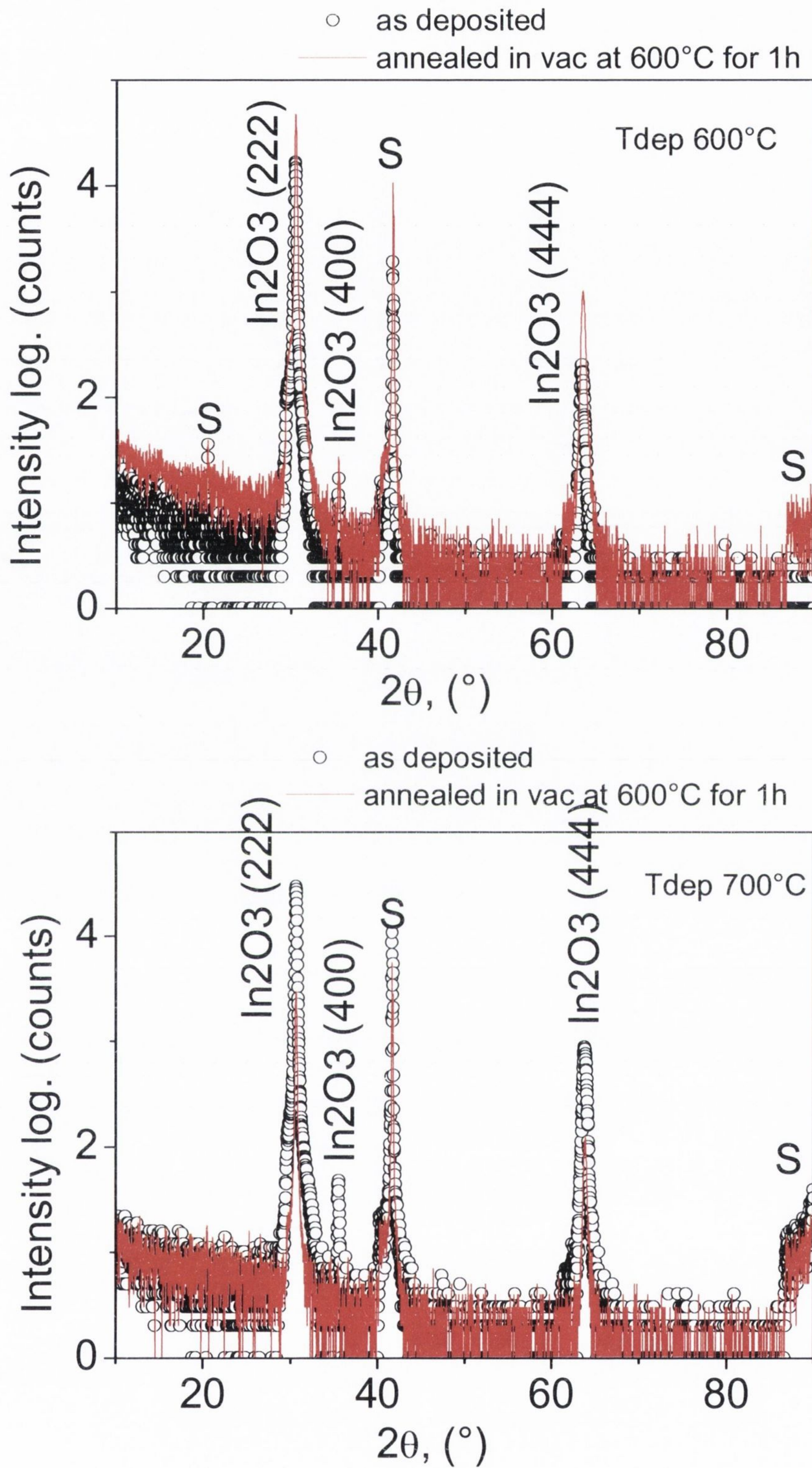

Fig. 4.20 Comparison of XRD spectra for Cr-doped In_2O_3 grown at 600℃ and 700℃ before and after annealing in vacuum

The morphology of the annealed films was studied using SEM and AFM analysis. The results for SEM analysis are shown in Figure 4.21. From SEM analysis it becomes obvious that vacuum annealing changes the morphology of the films. Before annealing films consisted of densely populated crystallites which grew together to form continuous film. Although, after annealing in vacuum the surface of the films changed significantly. For example, after annealing both films consisted of randomly populated crystallites separated by pores. AFM analysis also confirmed the structural changes in the films after annealing observed from SEM analysis.

As deposited ***Annealed in vacuum***

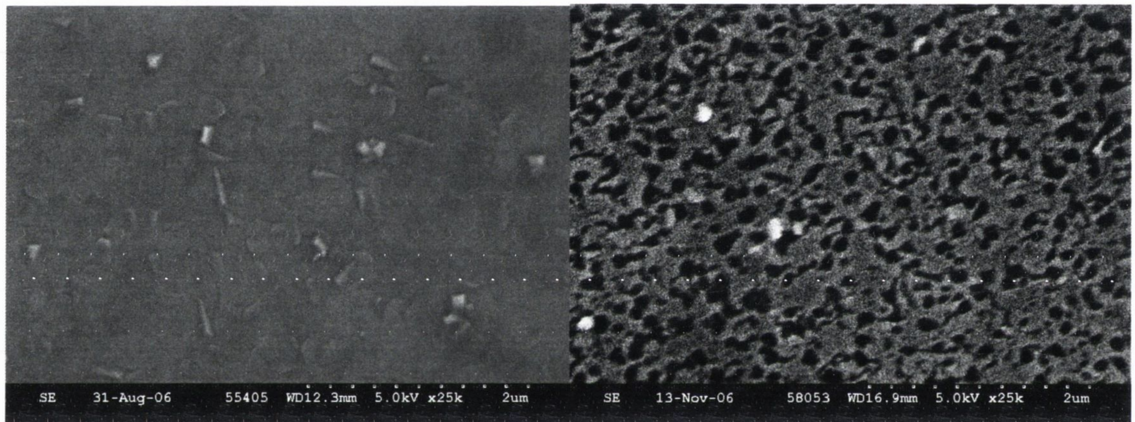

Tdep 600°C

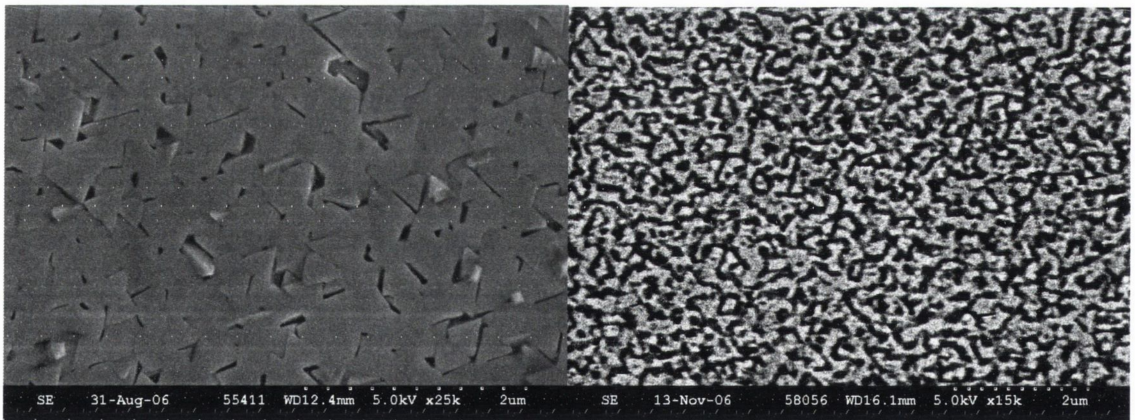

Tdep 700°C

Fig. 4.21 SEM micrographs of Cr-doped In_2O_3 films before and after annealing in vacuum

4.2.2.5.4. Magnetic properties of annealed films

Magnetic properties of annealed films were studied using SQUID magnetometer. Since the saturation magnetisation of Cr-doped In_2O_3 film was not stable with time the magnetisation data of annealed films was compared with the results obtained same day prior to vacuum annealing of the films. The changes in magnetisation with time for annealed films were also studied. The magnetisation results for vacuum annealed Cr-doped In_2O_3 are shown in Figure 4.22. The magnetisation data for the film grown at 600°C revealed that out of plane saturation magnetisation slightly increased from ~ $1.9\times10^{-8}Am^2$ to ~$2.3\times10^{-8}Am^2$ after vacuum annealing. The further increase (~$2.9\times10^{-8}Am^2$) was found when sample was repeatedly measured after 2 weeks. However, some inconsistency in the saturation magnetisation was found when the film was measured 2 and 6 months after annealing in vacuum. First, the saturation magnetisation slightly decreased to ~$2.3\times10^{-8}Am^2$ and then increased again to ~$2.8\times10^{-8}Am^2$. It is possible that during vacuum annealing some oxygen vacancies were introduced in the films, which contributed to the total magnetism of the film. Another possibility could arise due to the fact that sample was remounted for each measurement, so its position (parallel or perpendicular) could slightly change each time and introduce the error in the magnetisation readings. However, SQUID measurements taken for the sample grown at 700°C showed that the out of plane saturation magnetisation for this sample did not change after annealing in vacuum (Figure 4.22 f).). Overall, we can conclude that annealing in vacuum did not drastically change magnetic properties of the films.

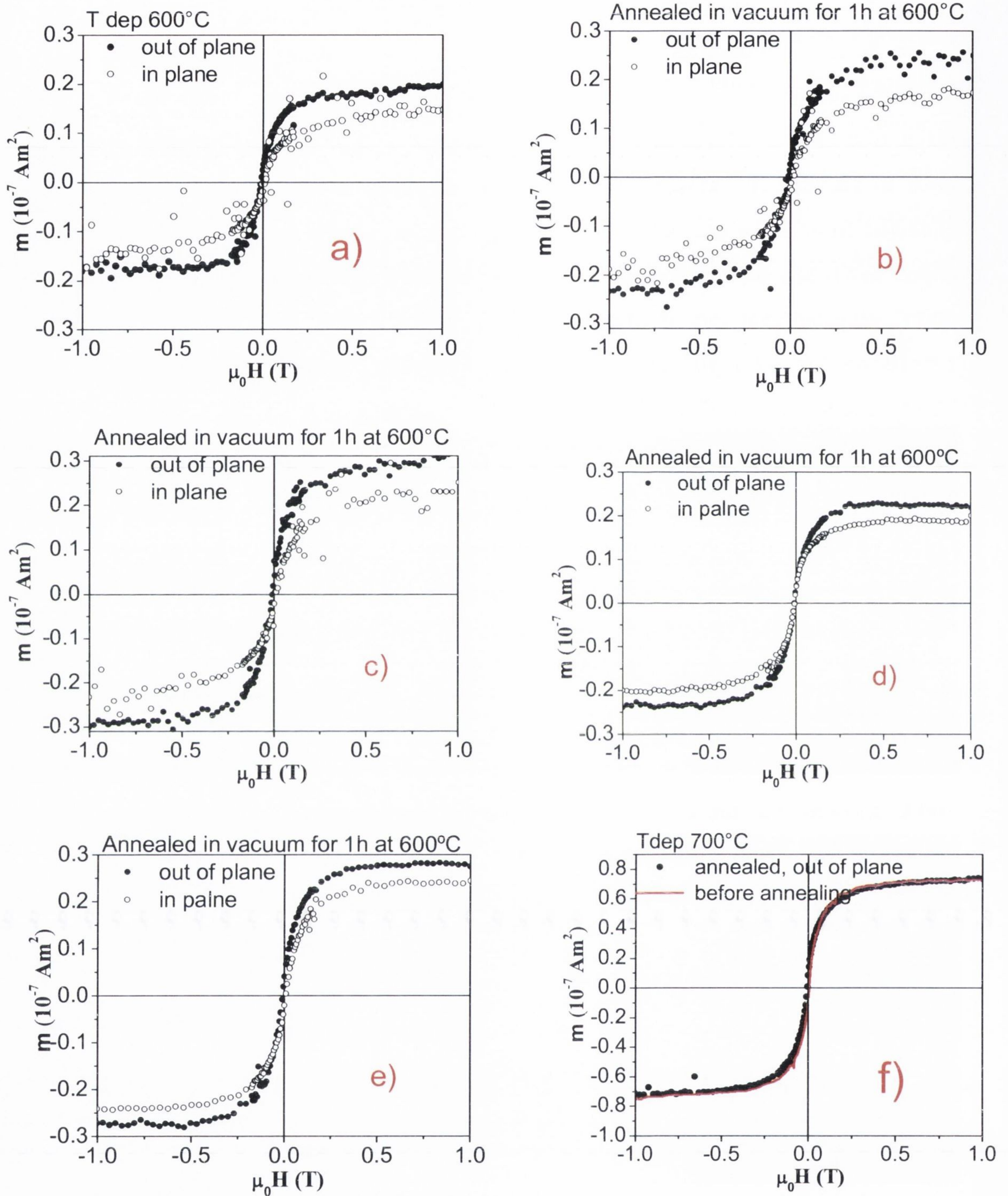

Fig. 4.22 SQUID magnetisation data for Cr-doped In_2O_3 grown at 600ºC, a) prior to annealing, b) immediately after vacuum annealing, c) 2 weeks after vacuum annealing, d) 2 months after vacuum annealing, e) 6 months after vacuum annealing, f) magnetisation data of the film grown at 700ºC

Additionally, the vacuum annealed Cr-doped In_2O_3 film grown at 700°C was annealed for 1 hour at 600°C in O_2 atmosphere. The magnetic properties together with structural properties of this film were studied. The results for magnetisation of the Cr-doped In_2O_3 film annealed in O_2 are shown in Figure 4.23. Magnetisation measurements revealed that after O_2 annealing film was no longer ferromagnetic at room temperature. To understand what factors could trigger the observed changes in magnetic properties of the film we looked at the structural properties of the annealed sample. The associated changes in X-ray diffraction and SEM analysis of the film, caused by O_2 annealing are shown in Figure 4.24.

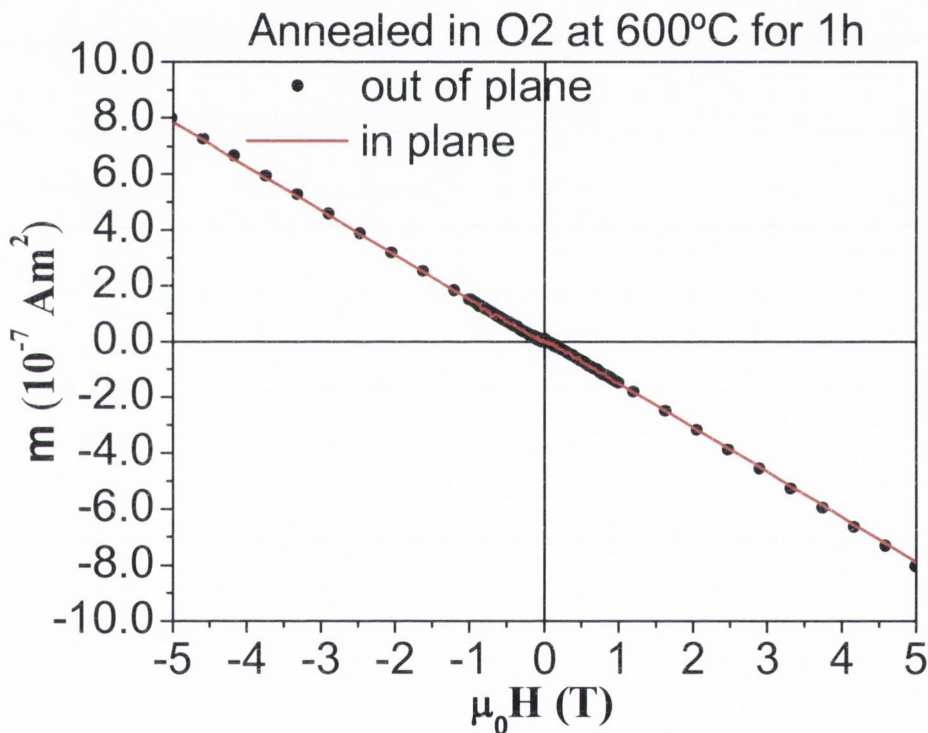

Fig. 4.23 SQUID magnetisation measurement for Cr-doped In_2O_3 film after annealing in O_2

Only very weak reflection from In_2O_3 (222) plane together with some fraction of amorphous phase was found from XRD analysis of the annealed sample, indicating that the crystalline structure of the film was significantly altered by O_2 annealing. Surface morphology of the film also changed after annealing in O_2 as evident from SEM

micrograph. The well ordered crystalline structure of the film's surface was completely destroyed.

The above results suggest that the observed ferromagnetism in Cr-doped In_2O_3 films is closely associated with the crystalline structure of the sample. The ferromagnetism vanishes, once the films are no longer crystalline.

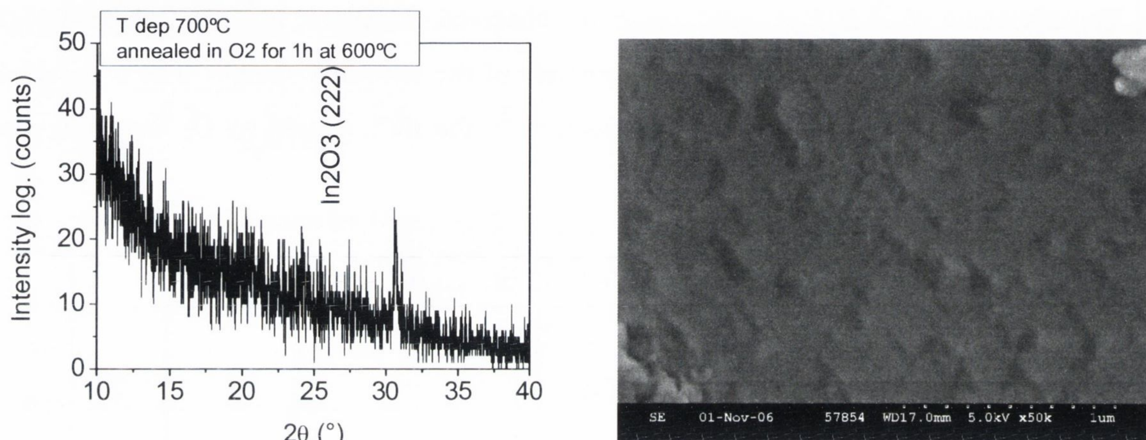

Fig. 4.24 XRD pattern (left) and SEM micrograph (right) of the Cr-doped In_2O_3 film after annealing in O_2

4.3. Growth of Cr-doped In_2O_3 films in magnetic field

In this work Cr-doped In_2O_3 films were also grown in magnetic field of 1T applied during the growth process. To the best of our knowledge magnetic properties of TM-doped In_2O_3 films have never been investigated before. We expect that the magnetic field applied directly during the growth of the Cr-doped In_2O_3 films could boost the magnetic properties and possibly increase the saturation moment. If this was achieved, it would be a very important step towards development of spintronic devices. For this reason, influence of magnetic field on structural, crystalline and magnetic properties of Cr-doped In_2O_3 films was carefully investigated using X-ray diffraction, SEM, AFM and SQUID magnetisation measurements.

4.3.1. Preparation of Cr-doped In_2O_3 films in magnetic field

The growth of the Cr-doped In_2O_3 films was carried out in the PI MOCVD reactor

equipped with 1 Tesla permanent magnet. Since the dimensions of the reactor differ from the PI MOCVD reactor without magnet, (for full details refer to Chapter 2.2.2) optimal deposition conditions differ from those described in Chapter 4.2.1. This time $In(tmhd)_3$ was chosen as the In precursor, since it produces the similar quality films as from $In(acac)_3$, but is more stable and does not precipitate from solution. The deposition conditions are shown in Table 4.4. Films with different Cr concentrations were subsequently grown without applied magnetic field and in 1T magnetic field on c-cut and r-cut sapphire substrates. The Cr concentration in precursor solution varied from 1 to 30 mol%. The substrate temperature during deposition was 650°C. After deposition, the films were slowly cooled to room temperature in an oxygen pressure of 1 atmosphere. The films grown in 1T magnetic field were also cooled in magnetic field. The thickness of the films, which was measured using XRR did not change upon applying magnetic field and only increased slightly with Cr concentration from 70nm for 1% Cr to 90nm for 30% Cr doped films.

Table 4.4 Deposition conditions for Cr-doped In_2O_3 films grown in PI MOCVD equipped with 1 Tesla magnet

Parameter	Value
Deposition temperature	650 ºC
Evaporation temperature	140 ºC
Carrier gas flow (Ar + O_2)	350 ml/min
Reactor pressure	5 mbar
Metalorganic precursors	$In(tmhd)_3$, $Cr(acac)_3$
Solvent	1,2- dimethoxyethane
In/(Cr+In) concentration in solution	0.015 mol/l
Cr/(Cr+In) concentration in solution	From 1% to 30%
Impulse frequency	2 Hz
Microdose mass	4 mg
Substrates	Al_2O_3 (0001) and Al_2O_3 $(1\underline{1}02)$

4.3.2. Characterisation of the Cr-doped In_2O_3 films grown in 1 Tesla

Characterisation of Cr-doped In_2O_3 films grown in and without magnetic field was carried out using different techniques, such as X-ray diffraction, SEM, EDX, AFM

and SQUID. All this techniques are very important in order to observe any possible changes in crystalline quality, morphology, and the most important in magnetic properties of the films caused by the application of magnetic field. All these characteristics of the films were carefully examined and subsequently compared for the samples grown without magnetic field and in 1T magnetic field.

4.3.2.1. Composition of Cr-doped In_2O_3 films

EDAX was carried out on all Cr-doped In_2O_3 films. Measurements were taken in 5 different regions of the film and the average Cr concentration in a film was estimated. Cr concentration in a film was identified from relative intensities of In and Cr peaks by comparing them with peak intensities for the standards of In_2O_3 and Cr_2O_3. The results for EDAX analysis of Cr-doped In_2O_3 films are shown in Figure 4.25. Cr concentration in Cr-doped In_2O_3 films linearly increased with Cr concentration in the precursor solution independent on substrate orientation or presence of magnetic field, as evident from EDAX. However, the actual Cr concentration in a film was almost twice as low as compared to Cr concentration in precursor solution. Thus, the 30mol% Cr in solution corresponded only to ~ 17% Cr in a film.

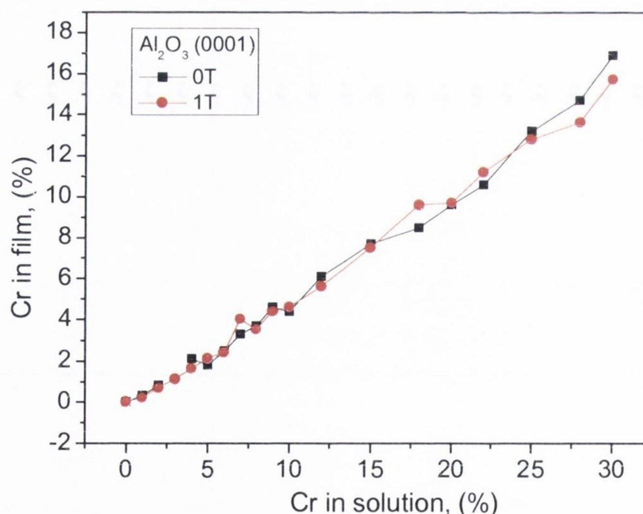

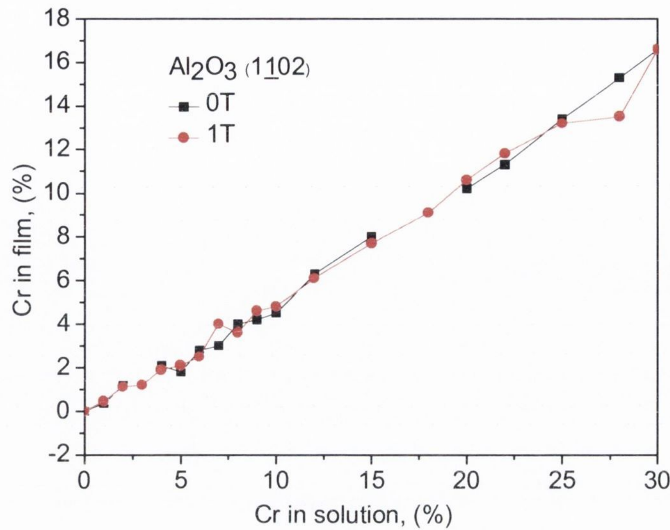

Fig. 4.25 Variation of Cr concentration in a film as a function of Cr concentration in precursor solution for Cr-doped In_2O_3 films

4.3.2.2. X-ray diffraction analysis

X-ray diffraction analysis was performed for all films deposited with different Cr concentrations with and without applied 1T magnetic field. The observed diffraction patterns for some Cr concentration in In_2O_3 are shown in Figure 4.26. The careful examination of the X-ray diffraction patterns for the Cr-doped In_2O_3 films showed that application of 1T magnetic field did not have any noticeable effect on crystalline properties of the films. XRD patterns were identical for the films grown with and without magnetic field. In fact, crystalline quality was found to change only with Cr content but not with the magnetic field. The In_2O_3 films with lower Cr (up to 10% in precursor solution) concentration had good crystalline quality. For the films on Al_2O_3 (0001) In_2O_3 (222) reflection is dominant together with weak reflections from In_2O_3 (400) and In_2O_3 (433) planes. For the films grown on Al_2O_3 (1$\bar{1}$02) In_2O_3(222) and In_2O_3 (440) reflection are dominant with weak reflection from In_2O_3(400) plane. With the increase of Cr concentration in precursor solution only one strong reflection from In_2O_3 (222) plane was found for the films grown on both substrate orientations indicating that addition of Cr into In_2O_3 lattice improved crystalline quality of the films. The improvement in crystalline quality of the films doped with higher Cr concentrations (10-15% in the

precursor solution) could be associated with less stress between substrate and In_2O_3 lattice mismatch (lattice mismatch between In_2O_3 and Al_2O_3 is +0.25%). Since, the ionic radius of Cr^{3+} is 0.76Å, much smaller as compared to 0.94Å for In^{3+}, the introduction of Cr into In_2O_3 would result in the reduction of lattice constant and consequently the reduction of lattice mismatch. The further increase in Cr concentration resulted in much poorer crystalline quality of Cr-doped In_2O_3 films. The intensity of In_2O_3 (222) reflection significantly decreased with further addition of Cr and the reflection from In_2O_3 (400) appeared again for the films on both substrate orientations. Moreover, the reflection from Cr_2O_3 peak was found for Cr concentrations higher that 25mol% for the films grown on Al_2O_3 (0001) substrates. This indicates that Cr solubility limit in In_2O_3 film is below 25mol% in precursor solution (or less than 14% in a film) for the films on Al_2O_3 (0001) substrate. However, the solubility of the Cr in In_2O_3 grown on Al_2O_3 (1$\underline{1}$02) is higher, since no formation of any Cr oxide secondary phases was found even for 30mol% Cr in precursor solution (or 17% in a films).

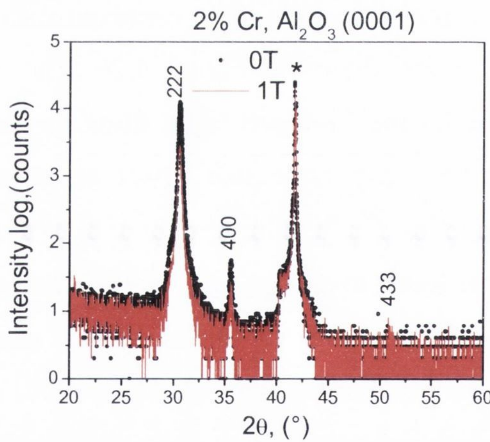

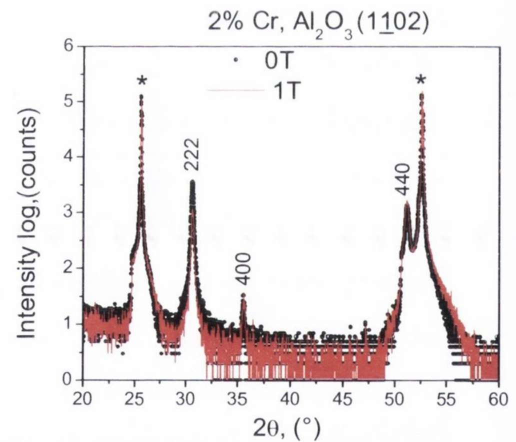

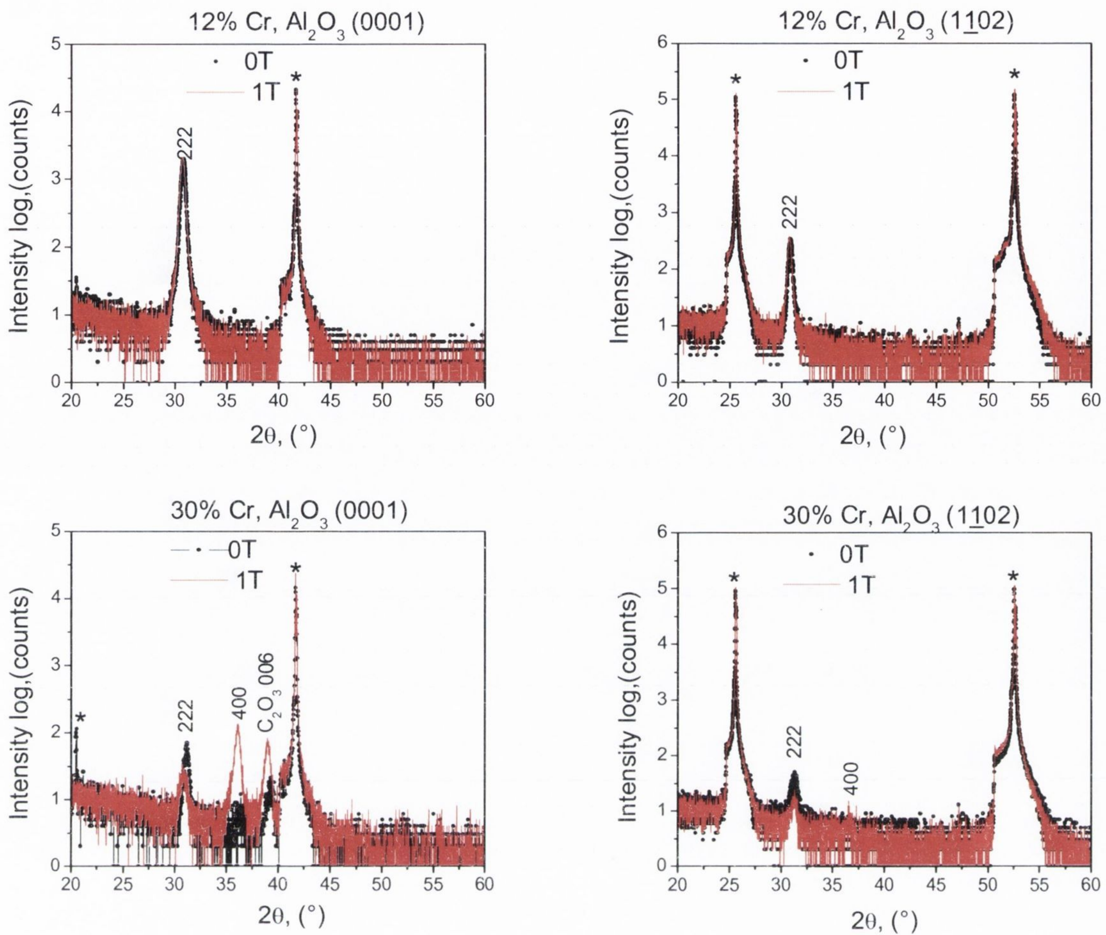

Fig. 4.26 XRD patterns for Cr-doped In_2O_3 films with different Cr concentrations and grown in and without 1T magnetic field

The lattice constant and crystallite size were also calculated from the XRD data for all Cr-doped In_2O_3 films using the same formula as described in Chapter 4.2.2.1. The variation of the lattice constant was studied as a function of Cr concentration. The influence of magnetic field on the lattice constant was also investigated. Figure 4.27 shows the variation of the lattice parameter with the Cr concentration in a film. The lattice parameter of undoped In_2O_3 films on both sapphire substrates was slightly lower (10.13Å) than the reported value [15] of 10.118Å for the cubic In_2O_3. This is easily explained by the induced stress due to lattice mismatch between thin film and sapphire substrate.

As expected, the lattice parameter of Cr-doped In_2O_3 films decreased with Cr concentration on both substrate orientations independent of magnetic field, with several exceptions at lower Cr concentrations. Although, for Cr concentrations above 14 atomic % in a film, the lattice parameter either decreased very insignificantly or even increased, for the films on both substrate orientations. This also confirms, that the solubility limit of Cr ions in the In_2O_3 cubic lattice for PI MOCVD grown films is ~14 atomic %.

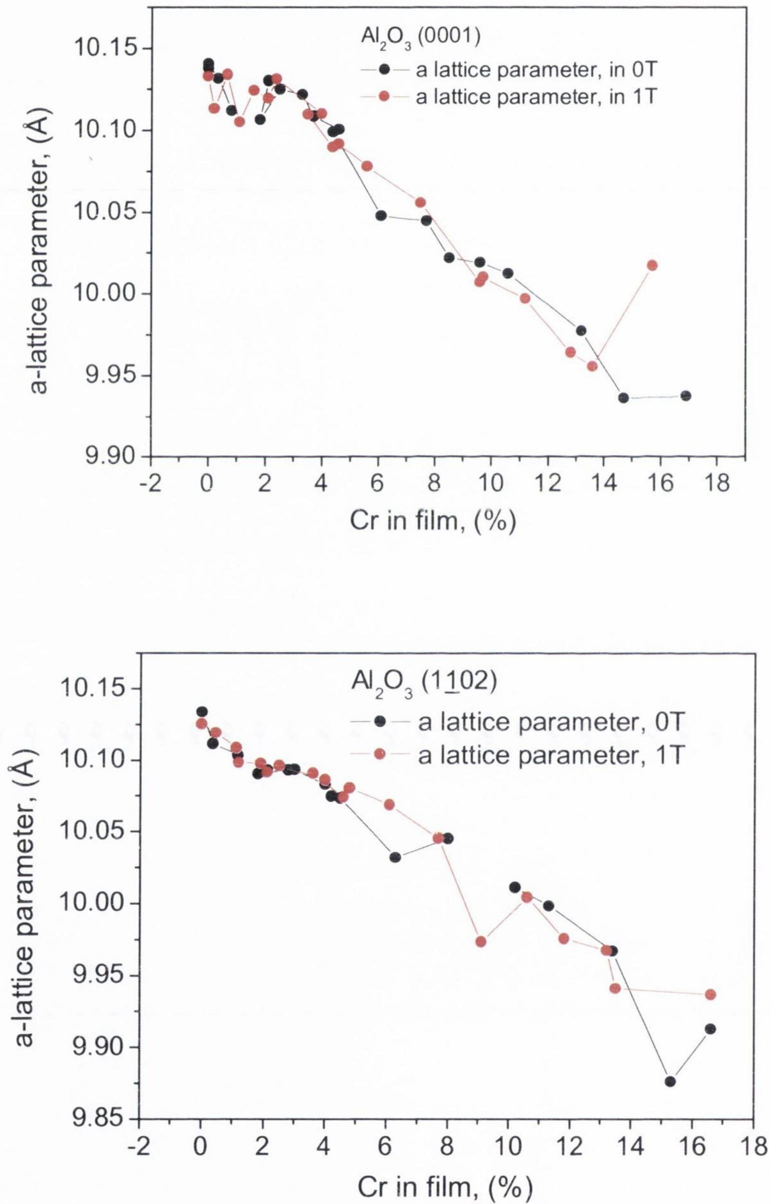

Fig. 4.27 The calculated lattice parameter of Cr-doped In_2O_3 films for different Cr concentrations

The average crystallite size (D) of the films with different Cr concentrations was calculated from the FWHM of the (222) peak reflection using Scherrer formula. The average crystallite size was studied as a function of Cr concentration in precursor solution and also as a function of applied 1T magnetic field. The calculated values are given in Table 4.5.

Table 4.5 The average crystallite size calculated using Scherrer formula for Cr-doped In_2O_3 film for different Cr concentrations in precursor solution for the grown in and without magnetic field

Cr in solution, (%)	Average crystallite size, (nm), Al_2O_3 (0001), 0T	Average crystallite size, (nm), Al_2O_3 (0001), 1T	Average crystallite size, (nm), Al_2O_3 $(1\underline{1}02)$, 0T	Average crystallite size, (nm), Al_2O_3 $(1\underline{1}02)$, 1T
1	29	31	32	30
2	33	28	42	39
3	28	32	35	38
4	28	30	35	35
5	29	30	33	34
6	21	23	29	31
7	22	22	29	24
8	21	22	27	26
9	19	22	26	26
10	20	21	25	23
12	21	20	23	24
15	19	18	20	25
18	18	17	38	29
20	19	18	17	23
22	15	18	21	19
25	17	19	16	16
28	21	19	24	16
30	13	26	14	29

From Scherrer formula we found that average crystallite size, with some exceptions, was largest for the films grown at lower Cr concentrations (up to 5mol%) and then slowly decreased with increasing Cr concentration. At the same time the average crystallite size depends on substrate orientation and was slightly larger for the films grown on Al_2O_3 $(1\underline{1}02)$ substrate. The average calculated particle size of Cr-doped In_2O_3 did not drastically change when films were grown in 1T, suggesting that magnetic field does not have the effect on the growth process and formation of crystallites in Cr-doped In_2O_3 films.

4.3.2.3. Morphology of Cr-doped In_2O_3 films

SEM analysis was done for all Cr-doped In_2O_3 films. The changes in film's morphology with Cr concentration were investigated. The morphology of the films grown with and without magnetic field for different Cr concentrations was also compared. The results for SEM analysis are shown in Figure 4.28. The films grown without Cr and with 1%Cr in precursor solution had similar morphology as Cr-doped In_2O_3 films shown in Chapter 4.2.2.2, grown at 650ºC. The morphology of those films is slightly different when grown in magnetic field, but as was later found this effect was arising more likely from the injection pulse instability rather than magnetic field effect. With Cr concentration increase (from 3%Cr in precursor solution) the crystallite size becomes smaller and is further decreasing with Cr concentration. For Cr concentration higher that 25% in precursor solution, the inclusions of bigger crystallites are found on the surface of the film. These crystallites could possibly be the secondary Cr_2O_3 phase, which is also observed in the XRD results. We found that magnetic field did not have any substantial visible effect on the film's surface morphology, as evident from SEM analysis.

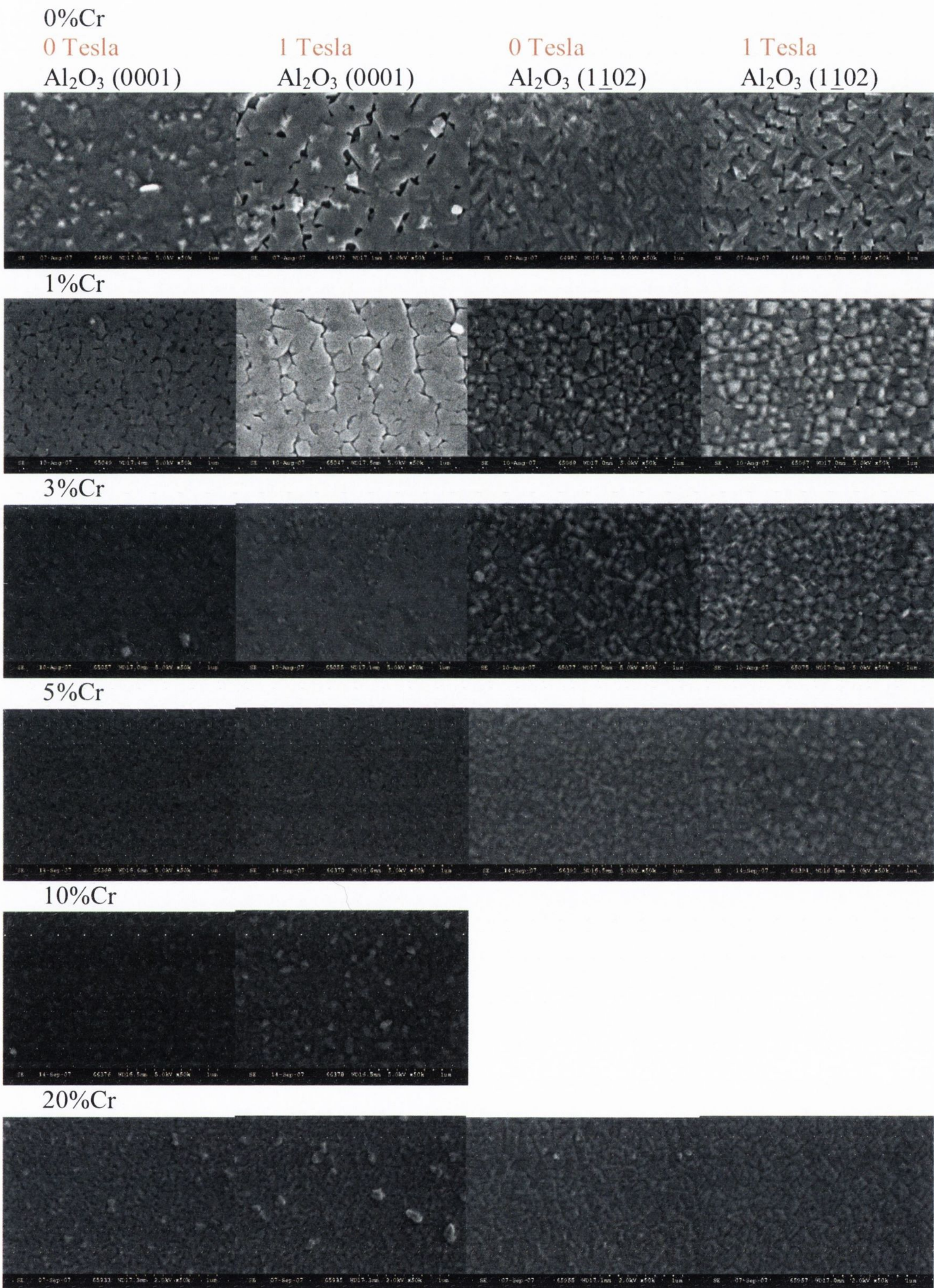
0%Cr
0 Tesla
Al_2O_3 (0001)
1 Tesla
Al_2O_3 (0001)
0 Tesla
Al_2O_3 (1$\bar{1}$02)
1 Tesla
Al_2O_3 (1$\bar{1}$02)
1%Cr
3%Cr
5%Cr
10%Cr
20%Cr

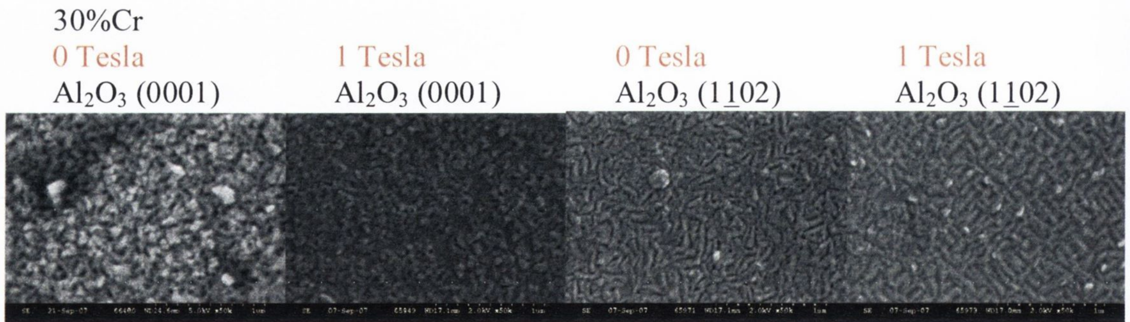

Fig. 4.28 SEM micrographs of Cr-doped In_2O_3 films with different Cr concentrations grown in and without magnetic field

4.3.2.4. Magnetic properties of Cr-doped In_2O_3 films

To test the samples for room temperature ferromagnetism all films (grown in and without magnetic field) were analysed using SQUID magnetometer. The measurements were performed at 300K in 1T magnetic field applied perpendicular and parallel to the film surface. Additionally, sapphire substrates were also measured using SQUID in order to test them for the presence of possible magnetic impurities. As expected, no ferromagnetic signal at room temperature was detected and only diamagnetic contribution from substrate was observed (Figure 4.29).

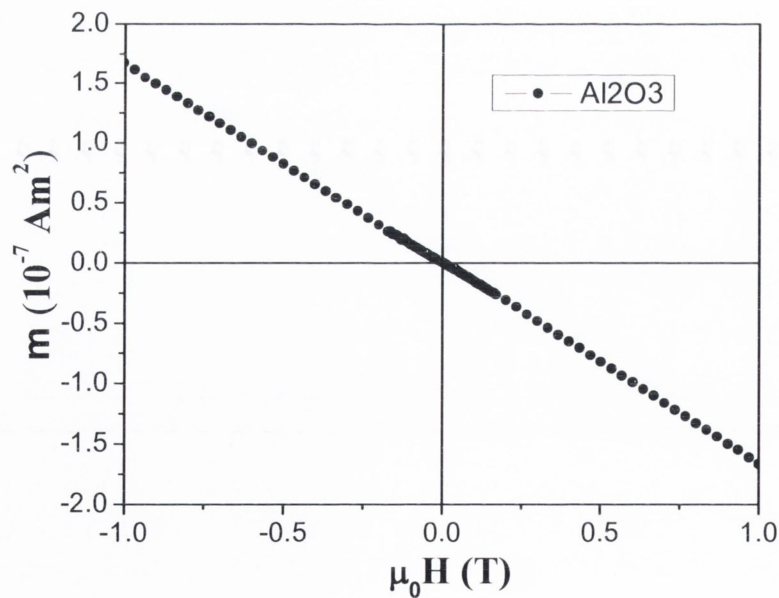

Fig. 4.29 Room temperature SQUID magnetisation of Al_2O_3 substrate

The magnetisation measurements revealed that all Cr-doped In_2O_3 films grown in a new reactor equipped with 1T magnet were not magnetic at room temperature, even the films with higher Cr concentrations. The magnetisation results for Cr-doped In_2O_3 films are shown in Figure 4.30. Moreover, films grown in 1T magnetic field also did not show the presence of room temperature ferromagnetism. These results suggest that the ferromagnetism in this system very strongly depends on the deposition conditions and even small shift in any of the deposition parameters can influence the ferromagnetic coupling and thus the reproducibility of the magnetic properties previously observed in Cr-doped In_2O_3 films.

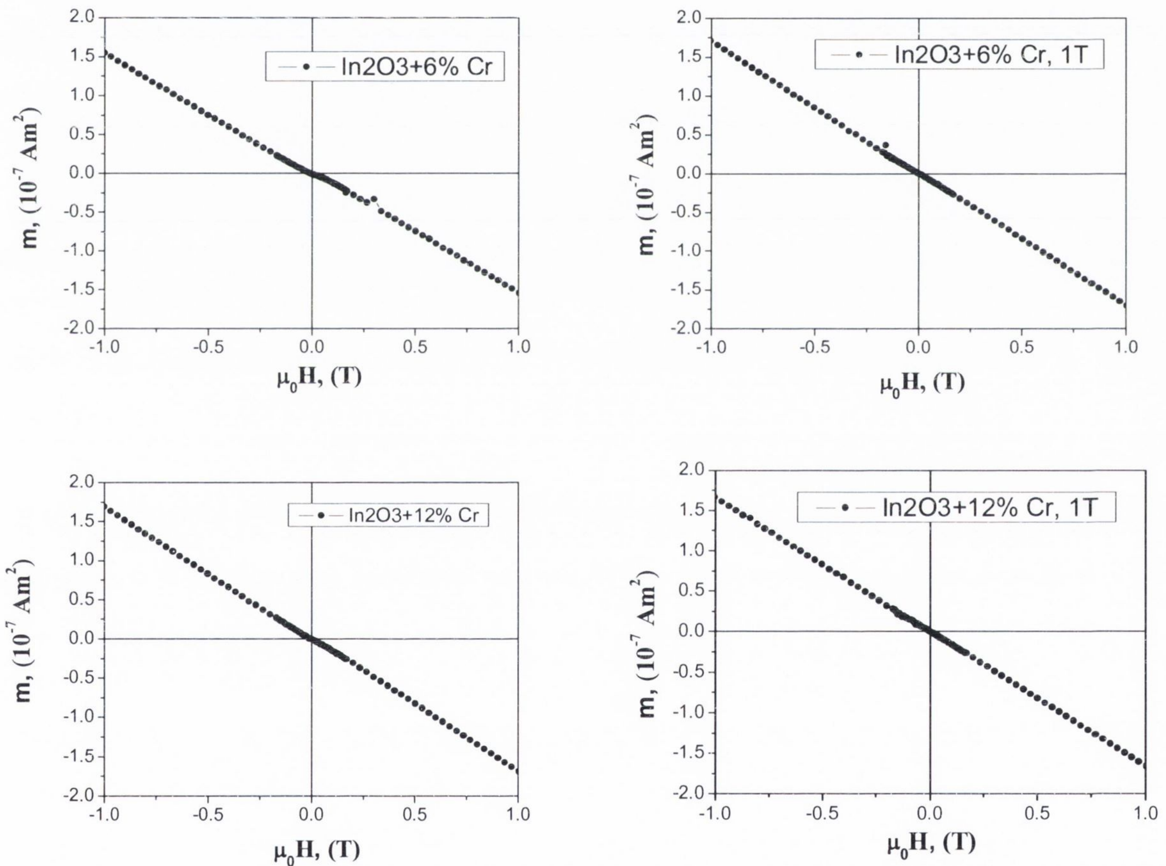

Fig. 4.30 SQUID magnetisation data for 6 and 12% Cr-doped In_2O_3 films grown on c-cut sapphire substrate in and without magnetic field

4.4. Conclusions

For the first time Cr-doped In_2O_3 films have been successfully prepared using PI MOCVD method. The crystalline properties, morphology and optical properties of the films strongly depend on deposition conditions including temperature and substrate orientation. The crystallographic structure of the films was highly influenced by the deposition temperature. The films grown at higher temperatures (700ºC and 750ºC) showed a strong (222) orientation on Al_2O_3 (0001) and (222) and (440) on Al_2O_3 ($1\underline{1}02$) substrate and exhibited a cubic structure. The films grown at lower temperature were randomly orientated. In addition, no formation of secondary phases was detected in 2%Cr-doped In_2O_3 films, as evident from XRD and XPS analysis. The SEM and AFM analysis indicated that surface topology was better for the films grown at 750ºC with average grain size and roughness values of 47nm and 48nm, and 3.9nm and 7nm for the films on Al_2O_3 (0001) and Al_2O_3 ($1\underline{1}02$) substrates respectively. Surprisingly, the films grown at lower temperatures (550ºC, 650ºC) showed the better transmittance of ~90% in the visible region, as compared to the film grown at 750ºC.

We found that Cr concentration in films is only slightly larger than that in precursor solution and that Cr is more likely to substitute for indium in In_2O_3 cubic lattice in Cr^{4+} oxidation state, however, the possibility of Cr^{3+} is not fully excluded. In contrast to Co-doped ZnO films, chromium ions distributed uniformly over the whole thickness of the films.

We found that magnetic properties of the Cr-doped films strongly depend on the substrate orientation, but not so much on neither deposition temperature nor crystalline quality. All 2% Cr-doped In_2O_3 films grown at different temperatures on Al_2O_3 (0001) substrate were room temperature ferromagnetic and insulating at room temperature, while films grown on Al_2O_3 ($1\underline{1}02$) were not magnetic. The magnetic moment of the films did not show any dependence on the deposition temperature and (with only one exception) did not change significantly. The highest magnetic moment of $1.65\mu_B$/Cr was found for the film grown at 700ºC which is comparable with the reported value of $1.5\mu_B$/Cr found for 2%Cr-doped In_2O_3 [10]. In addition, the saturation magnetisation was found to be highly anisotropic, with the highest magnetic moment when the magnetic field is applied perpendicular to the film surface. Similar, as was observed for Co-doped ZnO films, the

saturation magnetisation decreased with time, resulting in the decrease of the anisotropy of the films. However, the decrease in magnetic moment of Cr-doped In_2O_3 films was not so sharp as found for Co-doped ZnO films and seemed to stabilise after some period of time. By contrast to our results, other researchers found that only films, which show metallic or semiconducting behaviour, are room temperature ferromagnetic [10, 25]. The annealing of our ferromagnetic films induced conductivity, although magnetic properties of the annealed films did not change upon vacuum annealing. This suggests that some other mechanism, rather than proposed carrier induced magnetism is responsible for the observed ferromagnetic properties in our films. The origin of ferromagnetism in our samples is not quite clear. We ruled out that possibility of formation of secondary phases is responsible for observed ferromagnetism in our films, because it is known that metallic Cr is non-magnetic. In addition most of known Cr oxides are antiferromagnetic. We suggest double exchange mechanism between Cr^{4+} and In^{3+} ions as a possible origin of room temperature ferromagnetism in Cr-doped In_2O_3 films. Furthermore, there is always some degree of defects present in every lattice, which could also contribute to the observed room temperature ferromagnetism in our films.

The growth of the Cr-doped In_2O_3 films in 1T magnetic field did not have an obvious effect neither on the crystalline properties and morphology of the films nor on magnetic properties. Furthermore, all films grown in a new PI MOCVD reactor equipped with 1T permanent magnet did not show room temperature ferromagnetism. This result confirms that ferromagnetic ordering in DMS based oxide films is very sensitive to different deposition factors resulting in a very poor reproducibility also found in many other groups [10].

Finally we have shown that it is possible to obtain room temperature ferromagnetism in Cr-doped In_2O_3 films grown by pulse injection MOCVD on Al_2O_3 (0001) substrate. The high anisotropy and absence of secondary ferromagnetic phases suggest the intrinsic nature of room temperature ferromagnetism in our films. The observed ferromagnetism at room temperature in Cr-doped In_2O_3 films has confirmed that doping 2 mol % of Cr atoms into In_2O_3 may provide a promising magnetic material for new generation spin electronic devices.

References:

[1] K.A. Evans, A. J. D. (Ed.), *Chemistry of aluminium, gallium, indium and tallium*, Chapman and Hall, London, **1993**.

[2] C.G. Granqvist, *Applied Physics A* **1993**, *57*, 19.

[3] S. Kasiviswanathan, G. Rangarajan, *Journal of Applied Physics* **1994**, *75*, 2572.

[4] Y. Yasukawa, T. Seki, J. Muramatsu, S. Sugie, S. Tasaka, N. Inagaki, *Sens. Actuators, B, Chem.* **1993**, *13 - 14*, 613.

[5] T. Takada, H. Tanjou, T. Satio, K. Harrada, , *Sens. Actuators, B, Chem.* **1995**, 548.

[6] T. Takada, K. Suzuki, M. Nakane, *Sens. Actuators, B, Chem.* **1993**, *13–14*, 404.

[7] G. Peleckis, X. L. Wang, S. X. Dou, *Magnetics, IEEE Transactions on* **2006**, *42*, 2703.

[8] N. Kim, J. Myung, C. H. Kimm, P. S. S. Lee, A Appl. Res. , *Phys. Status Solidi, A Appl. Res.* **2005**, *202*, 108.

[9] T. Maruyama, L. T. Kitamura, *Journal of Applied Physics* **1989**, *28*, L1096.

[10] J. Philip, A. Punnoose, B. I. Kim, K. M. Reddy, S. Layne, J. O. Holmes, B. Satpati, P. R. LeClair, T. S. Santos, J. S. Moodera, *Nat Mater* **2006**, *5*, 298.

[11] U. Kenji, T. Hitoshi, K. Tomoji, *Applied Physics Letters* **2001**, *79*, 988.

[12] P. Prathap, G. G. Devi, Y. P. V. Subbaiah, K. T. Ramakrishna Reddy, V. Ganesan, *Current Applied Physics* **2007**, *In Press, Corrected Proof*.

[13] J.H. Lee, B.O. Park, *Surf. Coat. Technol.* **2004**, *184*, 102.

[14] F.O. Adurodija, L. Semple, R. Bruning, *Thin Solid Films* **2005**, *492*, 153.

[15] P. D. F. JCPDS: Joint Committee on Powder Diffraction Standards, International Center for Diffraction Data, in *card 44-1087*, Swarthmore, PA, **1997**.

[16] A. Maetaki, M. Yamamoto, H. Matsumoto, K. Kishi, *Surface Science* **2000**, *445*, 80.

[17] N. Pilet, C. Borca, A. Sokolov, E. Ovtchenkov, B. Xu, B. Doudin, *Materials Letters* **2004**, *58*, 2016.

[18] X. Zhang, Y. Chen, Z. Li, *Journal of Magnetism and Magnetic Materials* **2006**, *307*, 134.

[19] X. Liu, W. Su, Z. Lu, J. Liu, L. Pei, W. Liu, L. He, *Journal of Alloys and Compounds* **2000**, *305*, 21.

[20] Z. Anna, T. Arunas, D. Sebastiaan van, Y. K. Gun'ko, V. Kazlauskiene, *Applied Physics Letters* **2006**, *89*, 232503.

[21] H. Nguyen Hoa, S. Joe, H. Ngo Thu, B. Virginie, *Applied Physics Letters* **2005**, *87*, 102505.

[22] V. Brize, J. Sakai, N. Hoa Hong, *Physica B: Condensed Matter* **2007**, *392*, 379.

[23] G. Peleckis, W. Xiaolin, D. Shi Xue, *Applied Physics Letters* **2006**, *89*, 022501.

[24] T. Ohno, T. Kawahara, M. Murasugi, H. Tanaka, T. Kawai, S. Kohiki, *Journal of Magnetism and Magnetic Materials* **2007**, *310*, e717.

[25] P. Kharel, C. Sudakar, M. B. Sahana, G. Lawes, R. Suryanarayanan, R. Naik, V. M. Naik, *Vol. 101*, AIP, **2007**, p. 09H117.

[26] J. Stankiewicz, F. Villuendas, J. Bartolome, J. Sese, *Journal of Magnetism and Magnetic Materials* **2007**, *310*, 2084.

Chapter 5: Deposition and investigation of Fe_3O_4 oxide layers

5.1. Introduction

At room temperature magnetite (Fe_3O_4) is a soft ferromagnetic material and has an inverse spinel cubic structure. The tetrahedral **A** sites of Fe_3O_4 are occupied by one-third of the Fe^{3+} ions and the remaining Fe^{2+} and Fe^{3+} ions are located on the octahedral **B** sites with an average charge of 2.5 per formula unit. Ions at **B** sites are aligned ferromagnetically, but at the same time they are aligned antiferromagnetically with ions at **A** sites. This results, that magnetic moments of Fe^{3+} ions are cancelled out and the net magnetic moment in Fe_3O_4 is due to Fe^{2+} ions ($4\mu_B$), leading to the ferrimagnetic behaviour of magnetite. Apart from the interesting magnetic properties, magnetite has a structural transition at ~125K, known as the Verwey transition. At low temperature, below the Verwey transition the electrical conductivity of magnetite decreases by two orders of magnitude and Fe_3O_4 becomes insulating [1]. Above the Verwey transition temperature Fe_3O_4 behaves as a metallic conductor.

Since the discovery of magnetism in Fe_3O_4 it has a great impact on Materials Science due to its fascinating properties. Magnetite has also found a great number of applications, such as electric motors, electromagnets, transformers, video and audio adapters, magnetic inks, biomedical applications and etc [2].

Band structure calculations on Fe_3O_4 suggested that only minority spin (spin down) electrons present at the Fermi level, thus indicating the semi-metallic nature of Fe_3O_4. Therefore, for one spin orientation Fe_3O_4 acts as a metal, while for the opposite orientation it acts as an insulator [3]. This also means that the spin polarisation of Fe_3O_4 is 100%.

Semi-metallic magnetic oxides have recently attracted great attention for spintronics as they have high polarisation at the Fermi level and high T_C which are believed to benefit the injection of spin carriers into the semiconductors. Fe_3O_4 is one of the most potential semi-metallic oxides for spintronic applications due to its half metallicity, relatively low deposition temperatures and high T_C (~860K) [4] in comparison with other semi-metallic materials, such as $La_{1-x}Sr_xMnO_3$ (T_C=360K) or CrO_2 (T_C=395K). Thus, Fe_3O_4 offers a greater perspective for large TMR at room temperature [5]. The growth of these half-metallic oxides with higher T_C is still under progress. Prior

to application in real devices it is very important to be able to control the growth, magnetic and transport properties of Fe_3O_4 in the form of thin films. For example, the growth of the spinel Fe_3O_4 should be further optimised to prevent the formation of intrinsic growth defects of anti- phase boundaries that reduce the magnetic properties of thin epitaxial films [6]. These defects lead to some unusual features, the most remarkable being the non-saturation of magnetisation in thin films of Fe_3O_4, meaning that the properties of magnetite are very sensitive to the extrinsic or intrinsic defects.

Thin films of Fe_3O_4 have been well explored on single crystal MgO substrate that determines the epitaxial growth, since the lattice constant of magnetite ($a=8.397Å$) is twice as large as the lattice constant of MgO ($a=4.212Å$). Although, when depositing Fe_3O_4 on MgO, because of the different symmetry of Fe_3O_4, neighbouring growth islands can be shifted or rotated with respect to each other, resulting in anti-phase boundaries. The magnetic coupling over the large fraction of these boundaries is antiferromagnetic, thus acting as a barrier for the spin polarised conduction electrons [7, 8]. There are also few reports on thin film growth of Fe_3O_4 on other substrates, such as Al_2O_3, $SrTiO_3$, Si and GaAs [9, 10].

Various growth techniques have been used to fabricate single-crystalline Fe_3O_4 films including MBE [8, 11], PLD [12, 13], RF magnetron sputtering [14]. Up to date PI MOCVD have never been employed for the deposition of Fe_3O_4 films. Thus, the main aim of this part of our work is to deposit Fe_3O_4 films using PI MOCVD technique and investigate their magnetic properties. During deposition, 1T magnetic field was also applied. Until now, there are only very few examples of the utilisation of magnetic field during the fabrication of Fe_3O_4 films. For example, the magnetic field was applied during the growth of DC magnetron sputtered Fe_3O_4 films in order to define uniaxial magnetic anisotropy of the magnetic layer for using in spintronic devices [15]. The idea was to apply magnetic field during the growth of Fe_3O_4 films in order to enhance its magnetic properties. In the case of successful results, the PI MOCVD in an external magnetic field could be used in the fabrication of spintronic devices.

5.2. Preparation of Fe_3O_4 films

In this work the direct growth of iron oxide film in the form of Fe_3O_4 phase was achieved by using PI MOCVD technique and inert carrier gas. It is well know that α-

Fe_2O_3 is the most stable phase of iron oxide below 560°C. Normally, in reactive oxidising atmosphere most of the as-deposited iron oxide films are in α-Fe_2O_3 phase. Therefore frequently the second step is necessary to reduce this iron oxide phase by annealing at temperatures below 350°C for 3-5 hours in a H_2 (reducing) atmosphere to form a Fe_3O_4 phase. Here Fe_3O_4 films were grown in a single step reaction using $Fe(tmhd)_3$ as a precursor at different temperatures and employing two different carrier gas mixtures. The first series of films were grown using only Ar carrier gas and at deposition temperatures of 450°C, 500°C, 550°C, and 600°C. The second series of the Fe_3O_4 films were grown at 500°C and 550°C in reductive atmosphere using the mixture of Ar and H_2 gases. Each of the film growth process was consequently carried out without and in applied external magnetic field (1T) in order to compare the magnetic properties of the films and estimate the effect of external magnetic field. Films were grown on MgO(100) and Al_2O_3 (0001) substrates. In addition, to check the dependence of magnetic properties on the film thickness, six films were grown at 550°C on Al_2O_3 (0001). The thickness of the films was increased by increasing the number of injection pulses, from 1000 to 3000. The depositions were also repeated in 1T external magnetic field. After deposition, films were slowly cooled in vacuum to room temperature. The summary of the general deposition conditions is given in Table 5.1.

Table 5.1 General deposition conditions for Fe_3O_4 films

Deposition temperature	450°C - 600°C
Evaporation temperature	140 °C
Carrier gas flow	80 ml/min
Carrier gas	Ar, Ar+10% H_2
Reactor pressure	5 mbar
Metalorganic precursors	$Fe(tmhd)_3$
Solvent	1,2- dimethoxyethane
Fe concentration in solution	0.015 mol/l
Impulse frequency	2 Hz
Microdose mass	3 mg
Substrates	MgO(100), Al_2O_3(0001)

5.3. Investigation of Fe_3O_4 films

In our studies of Fe_3O_4 films we mostly focused on the magnetic properties of the films grown without and in external magnetic field. However, structural and crystalline properties of the films were also carefully examined and the optimal deposition conditions for the preparation of high quality Fe_3O_4 films were found.

5.3.1. Thickness of the Fe_3O_4 films

In this work, it was very important to determine the thickness of the films accurately, which is used to calculate the magnetic moment per formula unit or per mass unit for all Fe_3O_4 films. Then magnetic moments of the films grown in and without external magnetic field can be compared and the effect of the magnetic field can be estimated.

The thickness of Fe_3O_4 films was measured in four different areas using Zygo White Light Interferometry technique. The average value of four measurements was then used to estimate the thickness of the films. The thickness could not be estimated for the Fe_3O_4 grown at 500°C on Al_2O_3, due to bad adhesion of the films on the substrate surface. For this reason it is not possible to get good step of the film-substrate interface necessary for the accurate thickness measurement. Even though the sensitivity of the White Light Interferometer is very high (less than 1nm) there is ~5% uncertainty in the film thickness arising from the edge effect (the thickness of the films is lower at the edges of the substrates) in MOCVD grown films.

For both deposition methods (using Ar or Ar+H_2 atmosphere) films on MgO substrate are thicker than films grown on Al_2O_3 when grown at 450°C and 500°C. This could be due to the fact that optimal precursor decomposition/absorption and diffusion rate on MgO substrate is lying in this temperature range. Another reason is a possible gaseous phase turbulence resulting in the shift of the deposition centre on the substrate holder.

As expected, the increase in films thickness from ~60nm to ~140nm is found when the number of pulses during the deposition is increased from 1000 to 3000. All results are summarised in the Table 5.2.

Table 5.2. The average thickness of Fe_3O_4 films grown in different deposition conditions

Deposition temperature, (°C)	Thickness, (nm)	
	Al_2O_3 substrate	MgO substrate
Films grown in Ar atmosphere		
450	44	73
450, 1T	38	67.5
500	~100	140
500, cooled in 1T	~100	137
500, 1T	~100	144
550	46	45
550, cooled in 1T	50	39
550, 1T	45	31.5
600	40	25
600, 1T	24.5	21
Films grown in Ar+H_2 atmosphere		
500	30.5	55
500, 1T	28	52
550	92	134
550, 1T	89	129
Films grown with different pulse numbers		
1000	61	—
1000, 1T	59	—
2000	95	—
2000, 1T	94	—
3000	147	—
3000,1T	139	—

5.3.2. X-ray diffraction studies

5.3.2.1. Crystalline properties of Fe_3O_4 on Al_2O_3

X-ray diffraction structural characterisation of the films grown in Ar atmosphere on Al_2O_3 at different temperatures is shown in Figure 5.1. The main peaks of the films were compared with the JCPDS database and are corresponding to the Fe_3O_4 cubic inverse spinel structure. As evident from XRD patterns the Fe_3O_4 has developed (111) preferred orientation at all deposition temperatures. For the films grown at 450°C, 500°C and 550°C additional peaks at 39.3° were observed which corresponded to nonmagnetic α-Fe_2O_3 phase. The most intensive α-Fe_2O_3 reflection was found for the film grown at

500°C, while other films had only very weak reflection from α-Fe_2O_3 (600) phase. All films which had presence of α-Fe_2O_3 phase were brown-red in colour, rather than metallic dark colour typical for pure magnetite. In contrast, the film grown at 600°C had no evidence of other phases and had brown-grey colour with metallic shine. We also found that film grown at 600°C has very low resistance (in a range of ~ 150-350kΩ as measured by multimeter) typical for magnetite.

In addition, Fe_3O_4 has nearly the same structure and lattice parameter as maghemite (γ-Fe_2O_3) that is why they cannot be distinguished from each other only by XRD. To confirm the growth of Fe_3O_4 in the films Raman spectroscopy measurements were performed, which will be discussed later in the section 5.3.3.

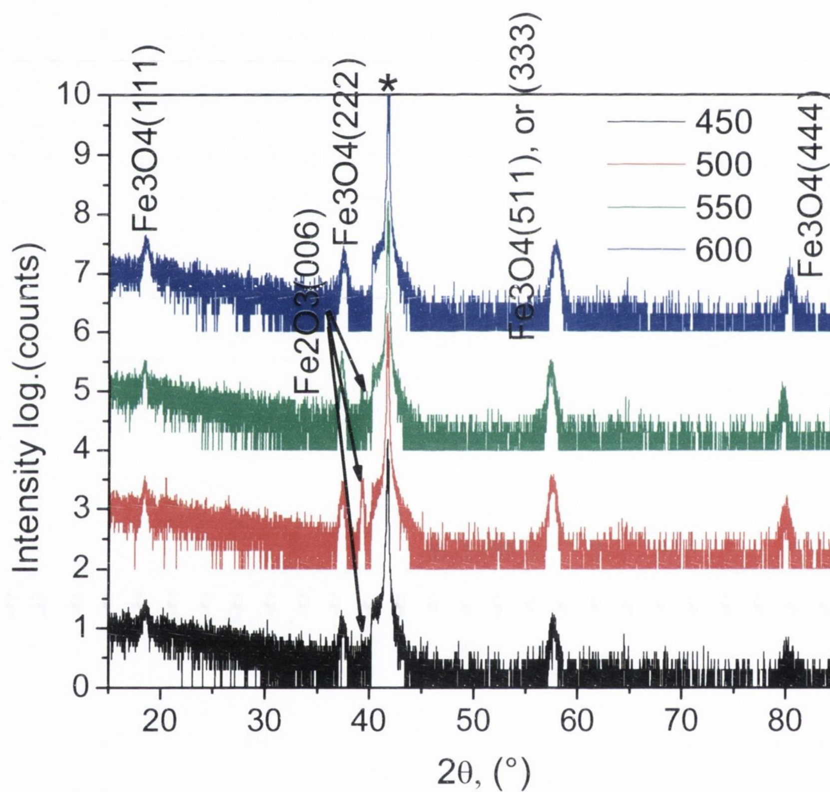

Fig. 5.1 XRD patterns (θ-2θ) of Fe_3O_4 films grown on Al_2O_3 at different deposition temperatures

The XRD patterns of the Fe_3O_4 films grown in Ar without external magnetic field were compared with those cooled in 1T external magnetic field (only for the films grown at 500°C and 550°C) and also grown in 1T magnetic field at all deposition temperatures. The results are shown in Figure 5.2. We did not observe any changes in crystalline properties of the films when cooled or grown in 1T external magnetic field. All films had

(111) preferred orientation regardless if films were grown in or without the presence of external magnetic field. We also did not find any consistent change in the intensity of the Fe_3O_4 peaks with application of external magnetic field. This allows us to suggest that 1T magnetic field does not have any significant effect on the crystalline properties of the PI MOCVD Fe_3O_4 films grown in Ar. In contrast to our films, Tang *et.al.* found that the preferred orientation of DC magnetron sputtered Fe_3O_4 films changes even upon applying 0.035T external magnetic field parallel to the film growth direction [15].

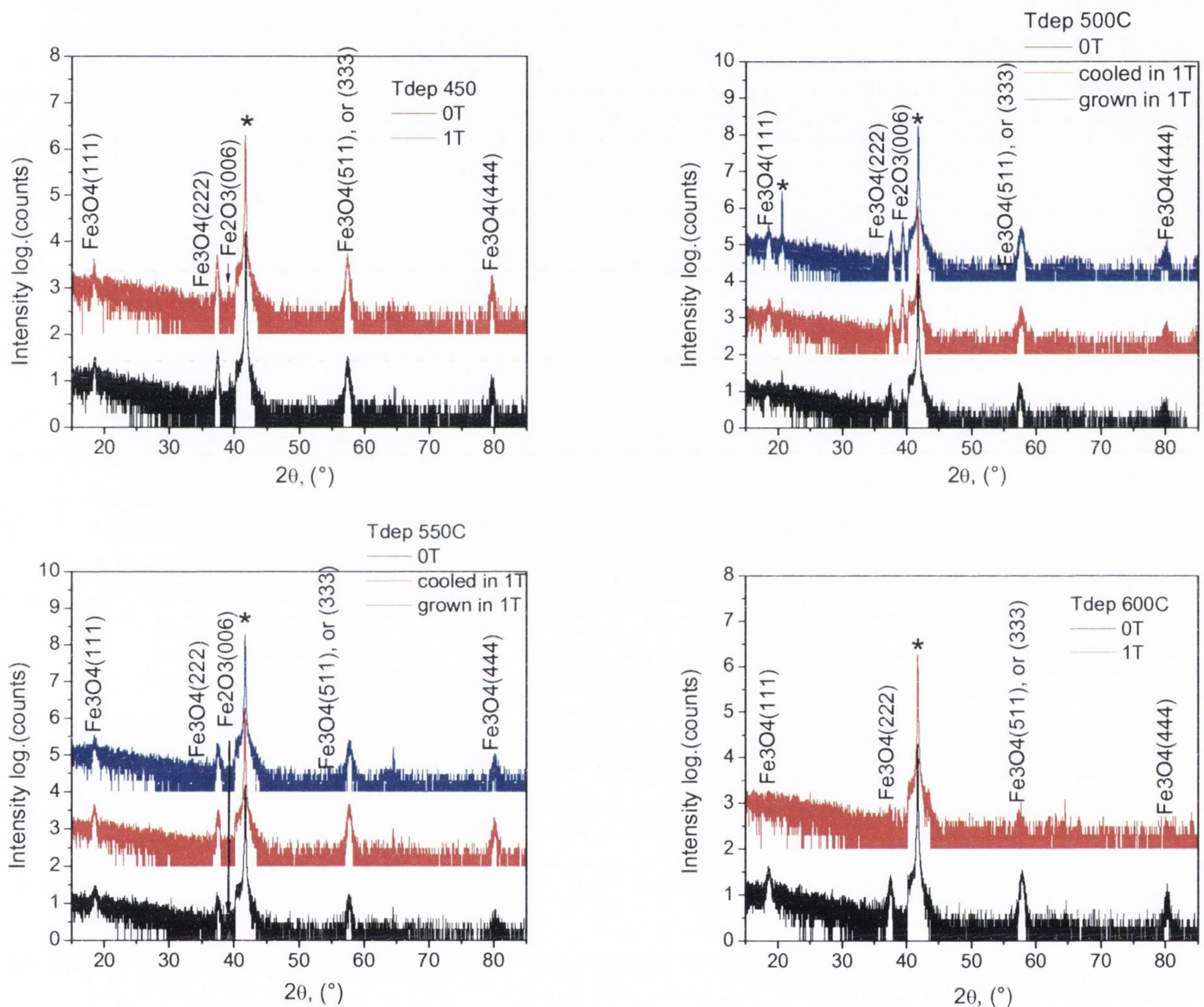

Fig. 5.2 The comparison of XRD patterns of Fe_3O_4 films grown in and without magnetic field on Al_2O_3 substrate, showing similar crystalline structure

The FWHM of (333) peak for Fe_3O_4 is lowest for the films grown at 450°C, and is ~0.57° and 0.52° for the films grown without and in external magnetic field, respectively, indicating a good crystalline quality of the films. The films grown at other temperatures

had an average FWHM of ~0.65° with slightly larger values for the films grown at 500°C and 550°C.

The XRD patterns of the Fe_3O_4 films grown on Al_2O_3 using Ar+H_2 as reactive atmosphere are shown in Figure 5.3. Similar to the films grown in Ar atmosphere all films have developed (111) preferred orientation. However, the films grown at 500°C had an additional weak reflection from Fe_3O_4 (400) plane. The films grown at 550°C were single crystalline. In contrast to the films grown in Ar, no secondary α-Fe_2O_3 phase was detected by XRD. Comparison of XRD patterns for the films grown in and without external magnetic proved to have no effect on crystalline properties.

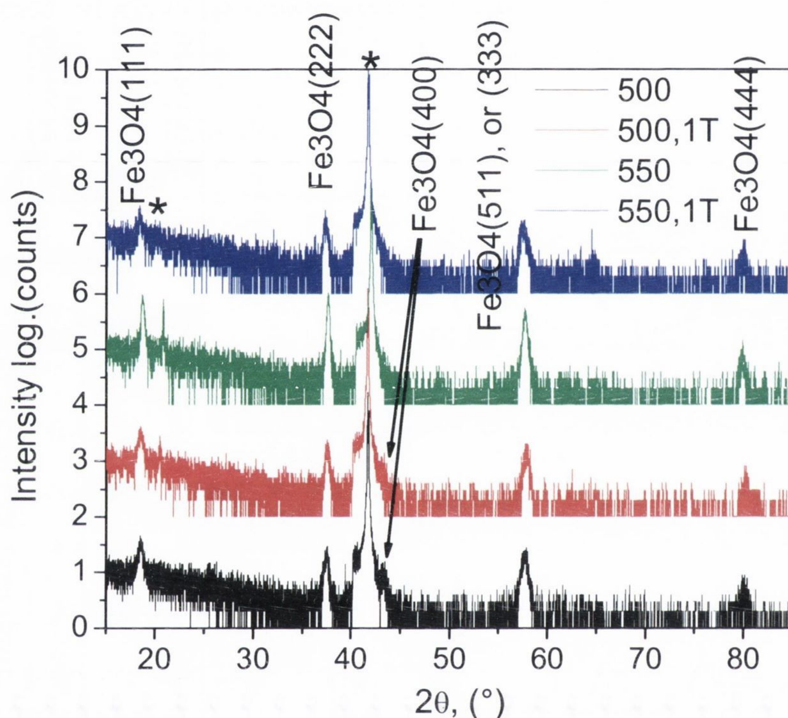

Fig. 5.3 XRD patterns of the Fe_3O_4 films grown on Al_2O_3 sapphire in Ar+H_2

The out of plane *a* lattice parameter of cubic Fe_3O_4 films grown on Al_2O_3 was calculated from (333) reflection and the variation of *a* lattice parameter as a function of deposition temperature was studied. We found that *a* lattice parameter of Fe_3O_4 films grown on Al_2O_3 substrate in Ar atmosphere was smaller than the accepted literature value of 8.397Å for the cubic Fe_3O_4. The films grown at 450°C and 500°C had quite similar value of *a* lattice parameter. Further increase in the deposition temperature resulted in the decrease of the *a* lattice parameter. Since the thickness of the Fe_3O_4 films is well below 100nm, we believe that the slight deviation in the lattice parameters of thin films on the

single crystal substrate may be due to the substrate induced strain in the film. In fact, it was found when Fe_3O_4 is grown on amorphous glass substrate its lattice parameter is very close to the bulk value [16], since amorphous glass does not provide any substrate induced strain and hence the films grow completely relaxed. Films grown at lower temperatures (450°C and 500°C) experienced less out of plane compressive strain than those grown at higher temperatures, and their lattice parameters differ less from that of the bulk value of Fe_3O_4.

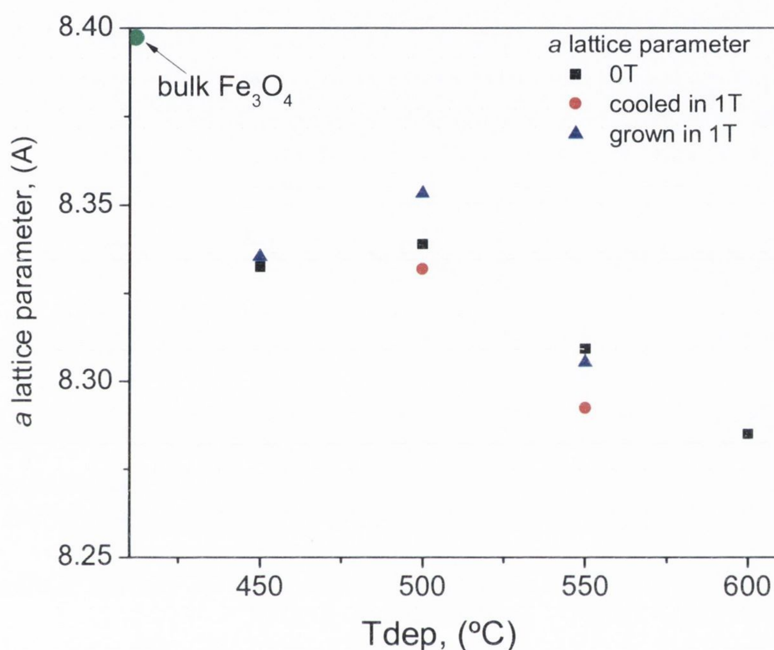

Fig. 5.4 The variation of lattice parameter (*a*) with deposition temperature for the Fe_3O_4 films grown on Al_2O_3 substrate in Ar atmosphere

The *a* lattice parameter of Fe_3O_4 films grown in $Ar+H_2$ reactive atmosphere at 500°C is slightly smaller than that of the films prepared in Ar atmosphere at the same temperature. Again, the decrease of *a* lattice parameter was also found with increase in deposition temperature to 550°C for the films grown in $Ar+H_2$ atmosphere. This is similar to the observed changes in lattice parameter in films grown in Ar atmosphere. The full summary of the results for *a* lattice parameter, FWHM and effective out-of-plane strain for Fe_3O_4 films grown on Al_2O_3 is shown in Table 5.3.

Table 5.3 The experimental values of FWHM, *a* lattice parameter and effective out-of-plane strain for Fe_3O_4 films grown in and without magnetic field at different temperatures

T deposition, (°C)	FWHM, (°)	a lattice parameter, (Å)	Effective out-of-plane strain, (%)
Fe_3O_4 grown in Ar atmosphere			
450	0.58	8.332	-0.78
450, 1T	0.52	8.335	-0.74
500	0.64	8.339	-0.70
500 cooled in 1T	0.71	8.332	-0.78
500, 1T	0.68	8.353	-0.53
550	0.64	8.309	-1.06
550 cooled in 1T	—	8.292	-1.27
550, 1T	0.60	8.305	-1.12
600	0.63	8.285	-1.35
Fe_3O_4 grown in $Ar+H_2$ atmosphere			
500	0.73	8.31	-1.04
500, 1T	0.56	8.309	-1.06
550	0.41	8.297	-1.21
550, 1T	0.80	8.297	-1.21

The *a* lattice parameter and associated strain was also calculated for the different thickness films grown with different pulse number. The results are shown in Table 5.4. All films had typical (111) dominant orientation regardless to the external magnetic field, similar to that for the films grown at 550°C in Ar. The FWHM of the film peak decreases with increasing film thickness. While, the *a* lattice parameter increased with film thickness (or number of pulses) and had the highest value of 8.367Å for the thickest film, indicating the relaxation of the substrate induced strain with the film thickness. The strain in the films was determined as the difference between measured and expected lattice parameter divided by expected lattice parameter value (taken from JCPDS database).

Table 5.4. The experimental values of FWHM, *a* lattice parameter and effective out-of-plane strain for the Fe_3O_4 films grown with different pulse numbers

Number of pulses	(111) FWHM, (°)	a lattice parameter, (Å)	Effective out-of-plane strain, (%)
1000	0.40	8.301	-1.16
1000, 1T	0.42	8.302	-1.14
2000	0.21	8.352	-0.54

2000, 1T	0.21	8.354	-0.51
3000	0.17	8.367	-0.36
3000, 1T	0.17	8.365	-0.38

The average grain size was calculated from XRD (333) reflection for Fe_3O_4 using Scherrer's formula. We found that average grain size of Fe_3O_4 films grown at different temperatures in Ar did not change very drastically and was lying in the interval of 12-18nm. The slightly smaller grain sizes were found for the films grown in $Ar+H_2$ reactive atmosphere. At the same time the films grown with different pulse numbers had larger grain size. However, the results we obtained using Fe_3O_4 (111) peak rather than (333) peak. The average grain sizes for all Fe_3O_4 films grown on Al_2O_3 substrate are shown in Table 5.5.

Table 5.5. The average grain size calculated for Fe_3O_4 films grown on Al_2O_3 substrate

Average grain size, (nm)			**Nr of pulses**	**Average grain size, (nm)**
T deposition, (°C)	**Grown in Ar**	**Grown in H_2+Ar**		
450	15.7	—	1000	20.9
450, 1T	17.4	—	1000, 1T	26
500	14.2	11.1	2000	23.4
500, cooled in 1T	12.7	—	2000, 1T	20.6
500, 1T	13.4	11.2	3000	22.5
550	14.1	12.3	3000	23.6
550, cooled in 1T	—	—	—	—
550, 1T	15.1	11.3	—	—
600	14.5	—	—	—
600, 1T	15.7	—	—	—

5.3.2.2. Growth of Fe_3O_4 on MgO substate

It was previously reported that the growth of Fe_3O_4 films on MgO(100) substrates results in highly oriented or epitaxial films [16]. Since Fe_3O_4 films on MgO (100) have a reported (100) preferential growth we could not detect the expected (400) peak at 43.052° because it was overlapping with much more intensive MgO (200) peak at 42.916°. For

this reason the X-ray diffraction structural characterisation of the Fe_3O_4 films on MgO(100) was performed by tilting the sample at *psi* angle of 15.79° between MgO(200) and Fe(511) and performing the *θ-2θ* scan in the angle range of 50°- 60° so as only the reflection for Fe_3O_4 (511) plane is observed at 56.9°. The typical XRD pattern for Fe_3O_4 films on MgO(100) substrate grown at different deposition temperatures is shown in Figure 5.5. As evident from XRD the Fe_3O_4 films deposited at different temperatures exhibited a single phase on (100) MgO substrate (Figure 5.5.b). In contrast to the films grown on Al_2O_3, Fe_3O_4 films on MgO did not show any presence of other iron oxide phases. All films had grey metallic colour and were highly conducting. The position of Fe_3O_4 (511) peak was shifted to larger angles indicating the presence of stress in the films.

The FWHM of the films was less than 1° indicating rather good quality. The films grown at 500°C had the lowest value of FWHM (Table 5.6.). The FWHM of the rocking curve, which is a measure of a mosaic spread in the films, was found to be less than 0.85°, with slightly smaller values for the films grown at higher temperatures.

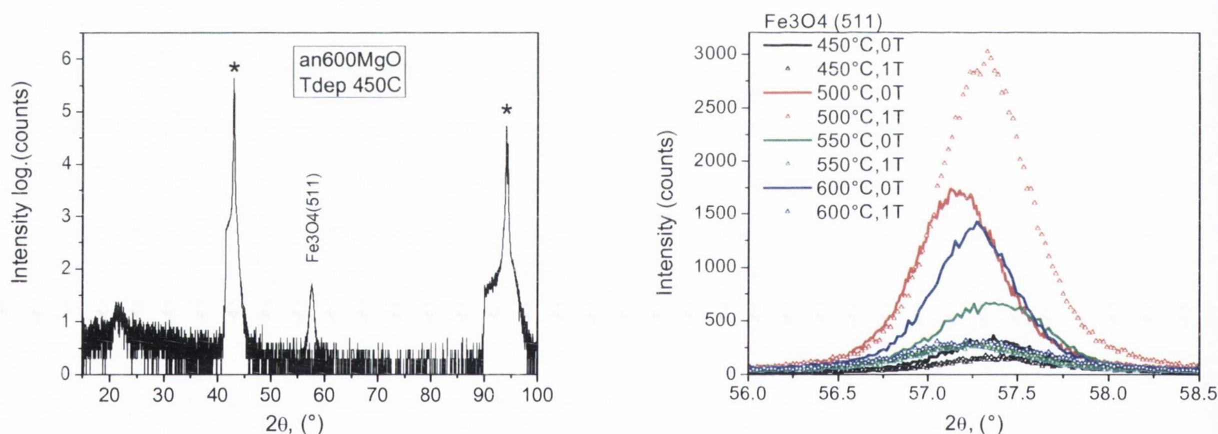

Fig. 5.5 Typical XRD pattern for the Fe_3O_4 film grown on (100) MgO substrate and Fe_3O_4 (511) reflection for the films grown at different temperature in and without external magnetic field (b)

We also found that all Fe_3O_4 films on (100) MgO are epitaxial. Figure 5.6 shows typical phi scan of the (511) reflection observed for the Fe_3O_4 films. Along the 360° sample in-plane rotation, four peaks of similar intensity are observed as expected for this particular reflection due to expected Fe_3O_4[100]/MgO[100] heteroepitaxial orientation.

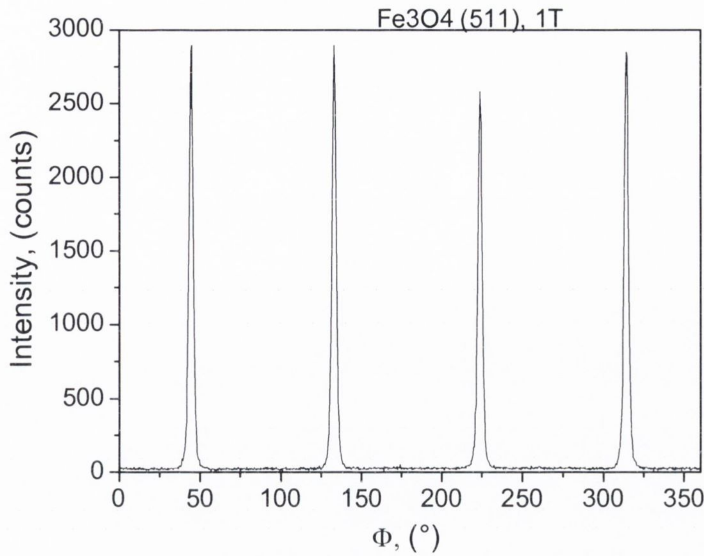

Figure 5.6 Phi scan performed for Fe_3O_4 (511) reflection, grown at 450°C showing four reflections

The Fe_3O_4 films grown in $Ar+H_2$ atmosphere were heteroepitaxial and had identical crystalline structure as films grown in Ar.

The *a* lattice parameter of Fe_3O_4 was smaller than that of bulk value, indicating that films grown on MgO experienced out of plane compression. The films grown in $Ar+H_2$ atmosphere had slightly larger values of a lattice parameter than those grown in Ar atmosphere and consequently experienced less substrate induced strain. Overall, Fe_3O_4 films grown at 500°C in $Ar+H_2$ had the best crystalline quality with lowest FWHM values and smallest lattice mismatch induced stress. For all films grown in two different atmospheres, the *a* lattice parameter increased with temperature decrease, suggesting that higher deposition temperatures result in formation of the films with larger stress (Figure 5.7.).

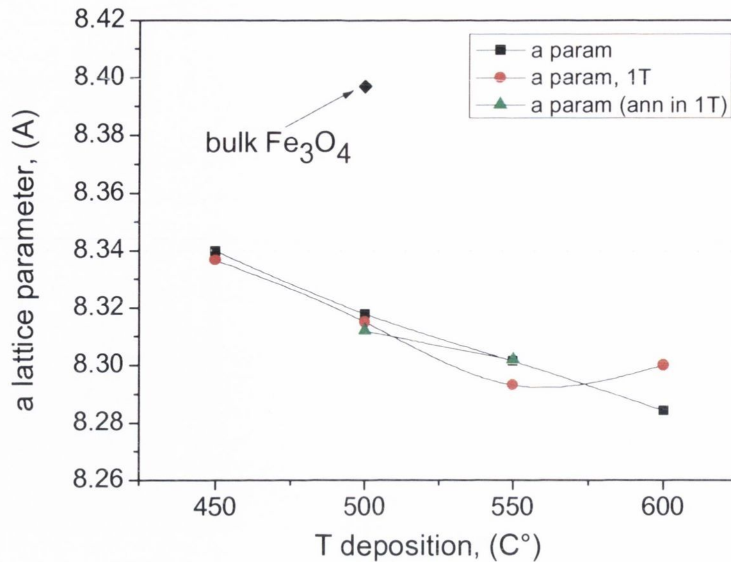

Fig. 5.7 The change of a lattice parameter with deposition temperature of Fe_3O_4 films on MgO substrate grown in Ar atmosphere

The average grain size calculated for the films had similar values as calculated for the films grown on the Al_2O_3. No dependence between deposition temperature and particle size was found for the Fe_3O_4 films grown on MgO substrate. All results for Fe_3O_4 films grown on MgO substrate are summarised in the Table 5.7.

It is noted that films grown in 1T external magnetic field have shown slightly larger FWHM values as those grown without magnetic field. The average grain size calculated for the films grown in external magnetic field is also slightly larger than those for the films grown without magnetic field. To be able to make conclusions it is necessary to grow more films and investigate the reproducibility of this effect. However, we do not exclude the possibility that external magnetic field applied during the growth of the films is responsible for the observed changes in FWHM and crystallite size in PIMOCVD grown Fe_3O_4 films.

Table 5.6 The FWHM, rocking curve, *a* lattice parameter, effective out-of-plane strain and average grain size values of the Fe_3O_4 films on MgO substrate

T deposition, (°C)	FWHM, (°)	Omega FWHM, (°)	a lattice parameter, (Å)	Effective out-of-plane strain, (%)	Average grain size, (nm)
Fe_3O_4 grown in Ar atmosphere					
450	0.66	0.68	8.340	0.68	13.7
450, 1T	0.72	0.84	8.337	0.72	12.5
500	0.56	0.83	8.318	0.95	16.1
500 cooled in 1T	0.53	0.79	8.315	0.97	17.2
500, 1T	0.58	0.79	8.312	1.02	15.6
550	0.72	0.56	8.301	1.16	12.5
550 cooled in 1T	0.69	0.68	8.293	1.25	13.0
550, 1T	0.79	0.64	8.302	1.14	11.5
600	0.53	0.66	8.284	1.36	17.1
600, 1T	0.93	0.68	8.300	1.17	9.8
Fe_3O_4 grown in $Ar+H_2$ atmosphere					
500	0.49	0.68	8.362	0.41	10.5
500, 1T	0.51	0.71	8.360	0.43	11.3
550	0.86	0.69	8.352	0.54	18.3
550, 1T	0.80	0.57	8.348	0.59	17.9

Finally, it is possible to conclude that the films grown in $Ar+H_2$ atmosphere have better crystalline quality than those grown in Ar only. The MgO substrate proved to be better choice for obtaining good quality epitaxial films of Fe_3O_4 prepared by PI MOCVD technique.

5.3.3. Raman spectroscopy studies

Room temperature Raman spectroscopy was performed in order to ascertain the Fe_3O_4 phase and also detect any other possible iron oxide phases. The excitation wavelength used was 514.5nm from an Ar^+ ion laser (Laser Physics Reliant 150 Select Multi-Line) with maximum power of ~10mW. In order to avoid an excessive heating and oxidation, ~3mW reduced laser power was used for all the measurements.

Generally, there are four actives modes for magnetite: A_{1g}, E_g and $3T_{2g}$ are Raman active modes, while; $4T_{1u}$ is an infrared active mode. The A_{1g} mode is the highest

frequency mode occurring at 670cm^{-1}. The E_g mode occurs at 306cm^{-1} and T_{2g} modes occur at 193cm^{-1} (T^1_{2g}), 540cm^{-1} (T^2_{2g}) and 490cm^{-1} for T^3_{2g} [17]. The magnetite thin films grown on Al_2O_3 substrate showed Raman shifts (A_{1g}) corresponding to Fe_3O_4 phase at ~667; 663, and 669cm^{-1} for the films grown correspondingly at 450, 500 and 550°C. The A_{1g} mode is directly linked to the structure of the magnetite system [18] and possesses the minimum FWHM for the film grown at 450°C, suggesting better crystalline quality of the film. The Raman bands are shifted to slightly lower wave number position in comparison with the values observed for bulk single crystal of Fe_3O_4 (which are 670cm^{-1}) and are representative of in-plane tensile strain [19]. The T^3_{2g} mode is observed only for the films grown at 500°C and 550°C at ~492cm^{-1}, while the E_g mode is not observed at all. There is also a presence of the peak at 297cm^{-1}, which suggests a beginning of oxidation, showed in studies by Dunnwald and Otto [20] and Hart *et al.* [21], especially when associated with the lines at 410-420cm^{-1}.In fact the Raman spectroscopy of our films shows two peaks at ~410cm^{-1} and 711cm^{-1}(the peak at 711cm^{-1} is observed for all films, while the peak at 410cm^{-1}only for films grown at 500°C and 550°C). These peaks belong to the characteristic signature of hematite [22, 23].

Raman measurements therefore confirm that films on Al_2O_3 have magnetite phase with the inclusion of secondary α-Fe_2O_3 phase found for the films prepared at 450°C, 500°C and 550°C. The results obtained from Raman measurements agree well with the XRD analysis of Fe_3O_4 films. Figure 5.8 shows Raman spectra for the films grown on Al_2O_3 substrate.

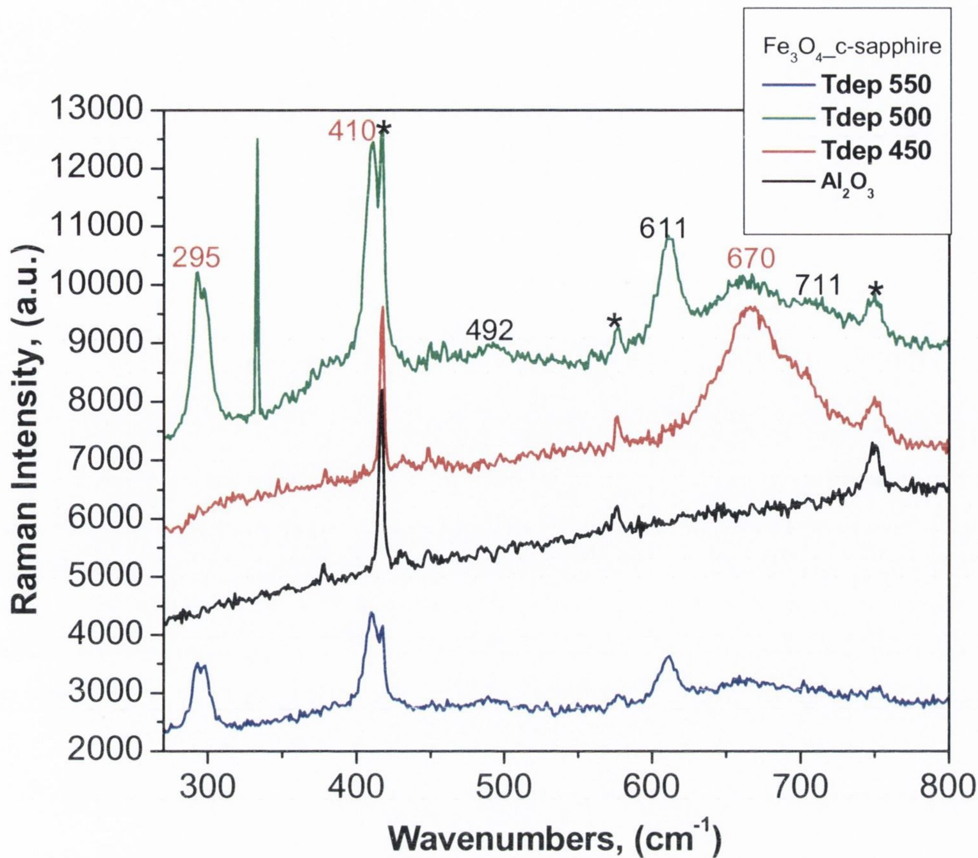

Fig. 5.8 Raman spectrum of Fe_3O_4 films, where * indicates substrate peaks, numbers in red indicate the approximate positions for Fe_3O_4 phase and in black indicate α-Fe_2O_3 phase

5.3.4. Investigation of surface microstructure

The surface microstructure of all Fe_3O_4 films was studied using SEM, AFM and MFM microscopy techniques. The changes in surface morphology were studied as a function of the deposition temperature, substrate, deposition atmosphere and the application of external magnetic field. It was previously reported, that the surface microstructure of superconducting films changes quite significantly under influence of external magnetic field [24]. It is quite possible that the effect of the magnetic field on the morphology could be even stronger when applied during the growth of ferromagnetic samples.

5.3.4.1. SEM

The SEM micrographs for the Fe_3O_4 films grown in Ar only atmosphere on c-cut sapphire substrate showed that the microstructure of the films strongly depends on the deposition temperature (see Figure 5.9). The magnetic field had no effect on the

microstructure of the films since all films had exactly the same surface morphology when grown in and without external magnetic field. For the growth temperature of 450°C, the surface resembled an aggregation of grains of about ~20nm in size. Similar morphology was found for the films grown at 550°C and 600°C but with grains forming smaller aggregations than at 450°C. The surface morphology of these films was relatively rough. This implied that a few defects, for example, small angle boundary existed in the grains [5]. Our films grown at 500°C are very rough, many crannies have appeared on the surface, which may be due to the thermal stress. It is believed that the boundary region may contain some voids, which would definitely increase the electrical resistivity of the films. In fact, the multimeter measurements proved that films grown at 500°C had the resistivity over 5MΩ.

We also studied the change in surface microstructure with the thickness of the films. The results can be found in Appendix 3. As expected, the film roughness and the grain size increased in diameter from ~25-35nm to ~100nm with the film thickness increasing from 60nm to 140nm.

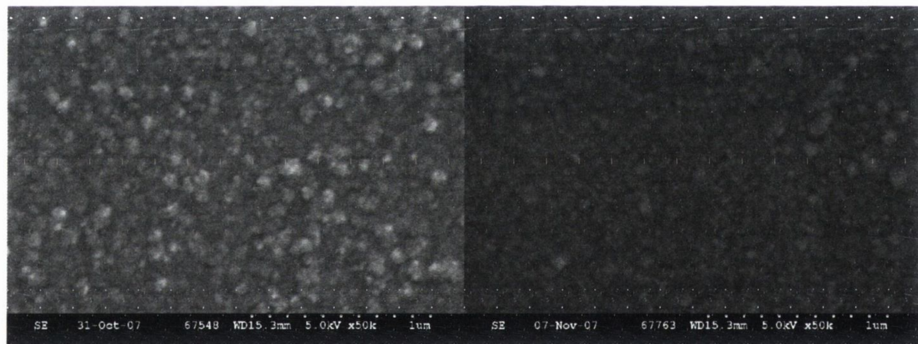

450°C 450°C,1T

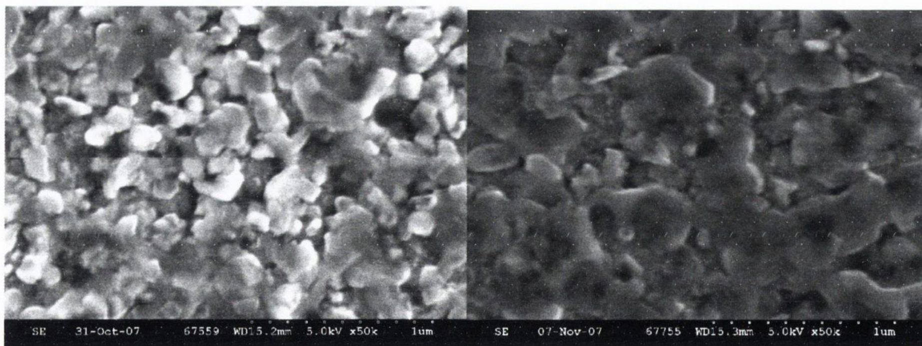

500°C 500°C,1T

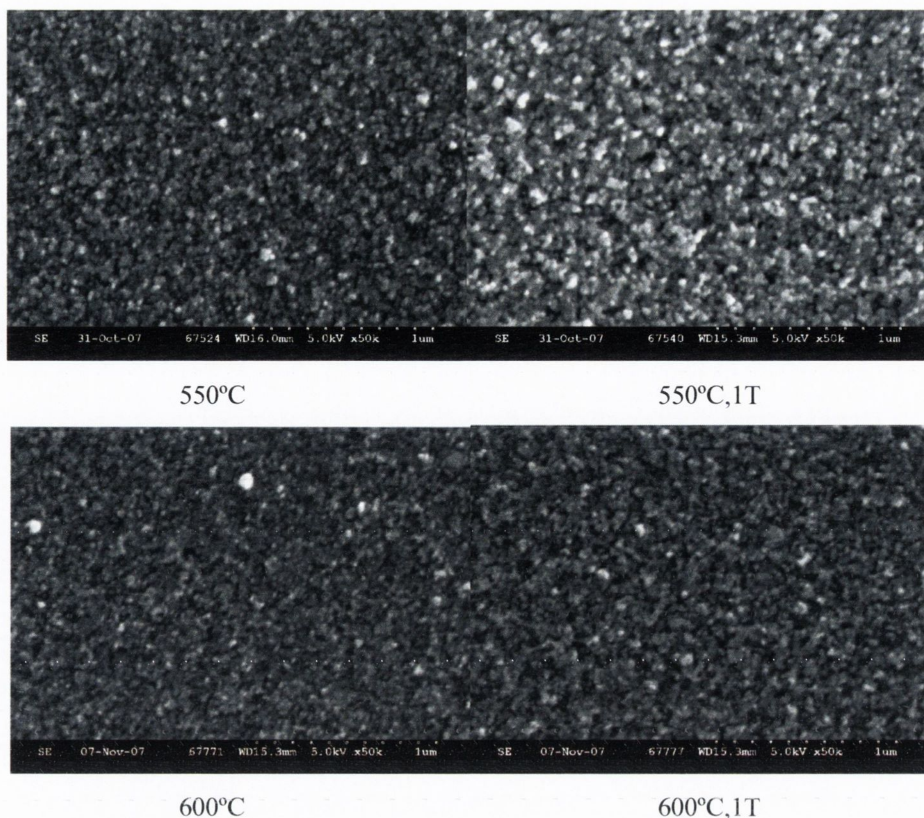

Figure 5.9. SEM micrographs of the Fe_3O_4 films on Al_2O_3 substrate grown in Ar atmosphere, showing different morphology of the films grown at different temperatures. The images in the left row are corresponding to films grown without magnetic field and in the right row in 1T external magnetic field

The surface microstructure of the magnetite films grown in Ar atmosphere on MgO(100) substrates is shown in Figure 5.10. When grown at 450°C films were smooth and consisted of particles forming small aggregates of approximately 25-35nm in size. The films grown at 550°C and 600°C possessed similar structure with slightly larger aggregates and are rougher. The films grown at 500°C had different structure and consisted of coalescent particles. It is noted, that in contrast to the films grown on Al_2O_3 at 500°C the films on MgO substrate had the lowest resistivity of ~50kΩ. The presence of the external magnetic field did not change the surface morphology of the magnetite films grown on MgO substrates.

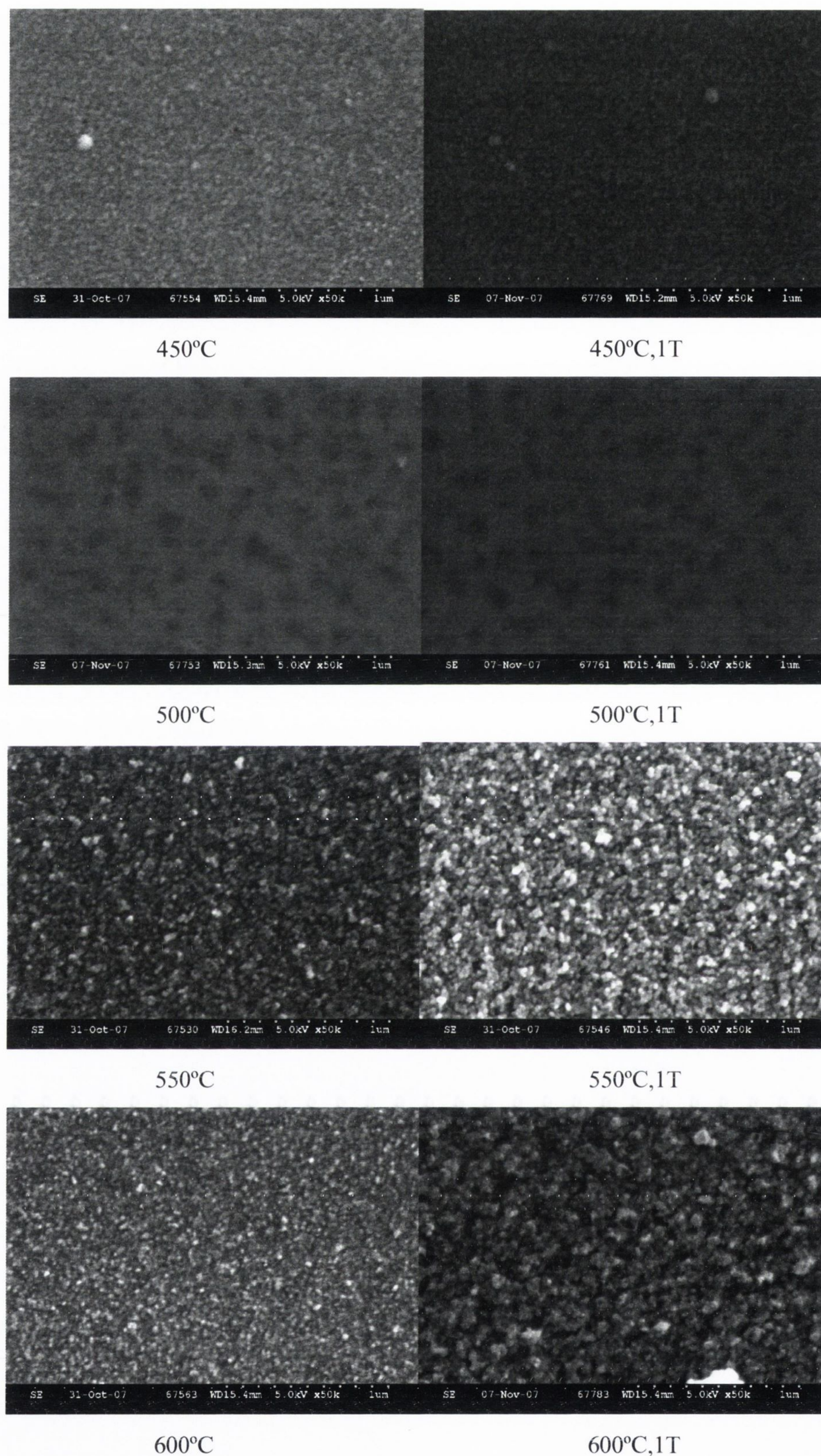

Fig. 5.10 SEM micrographs of the Fe_3O_4 films on MgO (100) substrate grown in Ar atmosphere. The films in the left row are grown without magnetic field and in the right row in 1T external magnetic field

The surface microstructure of the magnetite films grown in Ar+H_2 atmosphere was also studied. The results are shown in Figure 5.11. Films grown at 550ºC consisted

of approximately ~25-35nm aggregated grains and is very similar to that observed for the films grown in Ar atmosphere. However, the films on c-cut sapphire grown at 500°C had different microstructure and consisted of the large (~80nm) crystallites distributed over the smooth matrix. The different surface microstructure for those films is easily explained by the fact that those films have different XRD reflection (Fe_3O_4 (400)) not observed in other films, which results in this particular microstructure. Generally, films grown on Al_2O_3 substrate in Ar only and $Ar+H_2$ atmosphere at 500°C have much rougher surface consisting of randomly oriented grains than films grown at other deposition temperatures. We believe that this structure is a result of high saturation of precursor vapours near the substrate surface and low substrate temperature. This results in the rapid supply of reactants, but the low substrate temperature limits surface diffusion thus resulting in fewer nucleation sites.

At the same time, the surface of the films grown on MgO substrate at 500°C consisted of coalescent particles, similar to that found for the films grown at 500°C in Ar atmosphere on MgO substrates.

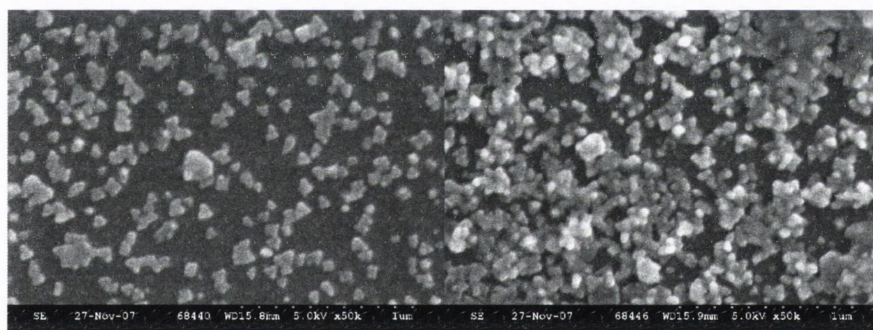

Al_2O_3, 500°C Al_2O_3, 500°C,1T

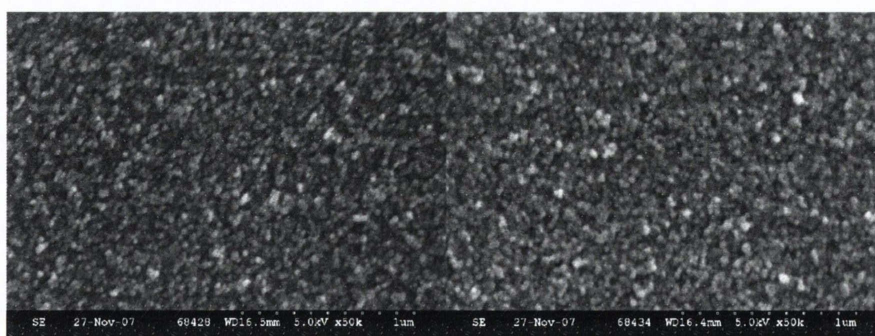

Al_2O_3, 550°C Al_2O_3, 550°C,1T

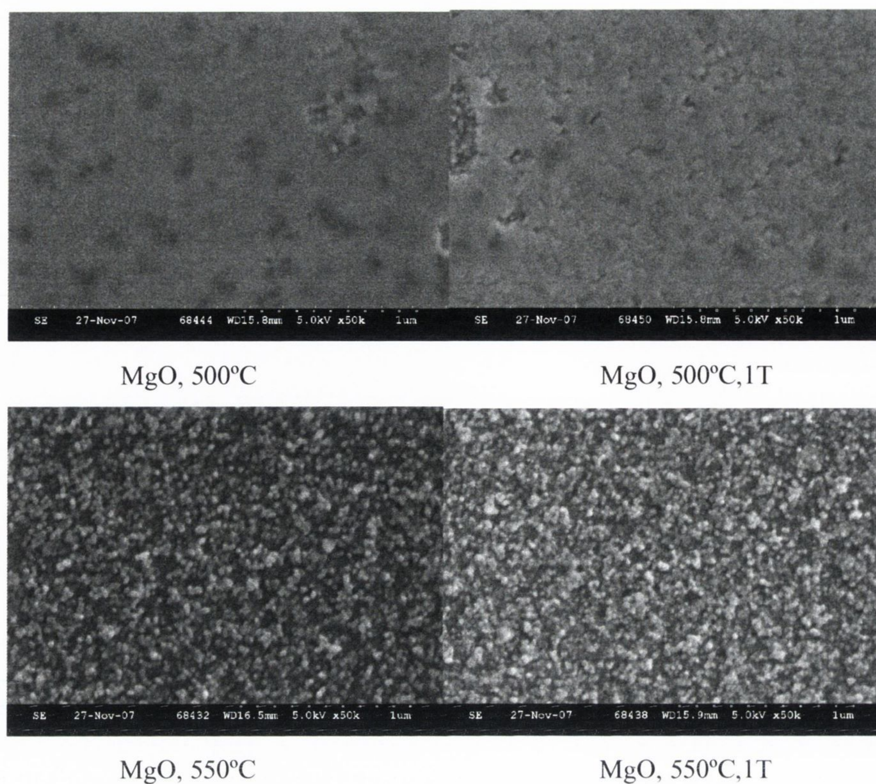

Fig.5.11. SEM micrographs of the Fe_3O_4 films grown in $Ar+H_2$ atmosphere

5.3.4.2. AFM

The AFM studies were done on some of the films in order to evaluate the change in films topology and roughness with deposition temperature. The AFM studies for surface roughness are consistent with the SEM studies. The average surface roughness (Ra) for some of the films is given in the Table 5.8. The smoothest films were obtained at 450ºC on both substrates indicating less stress in the films, also confirmed by XRD results. The smoothest films are obtained at 450ºC on MgO substrate. Together with good crystalline quality, good surface microstructure and low roughness it is possible to conclude that the best quality films are produced on MgO substrate at 450ºC. The roughness of the films grown at 500ºC is too high to be detected by AFM. Figure 5.12 shows examples of AFM images for the films grown at 550ºC on Al_2O_3 and MgO substrates.

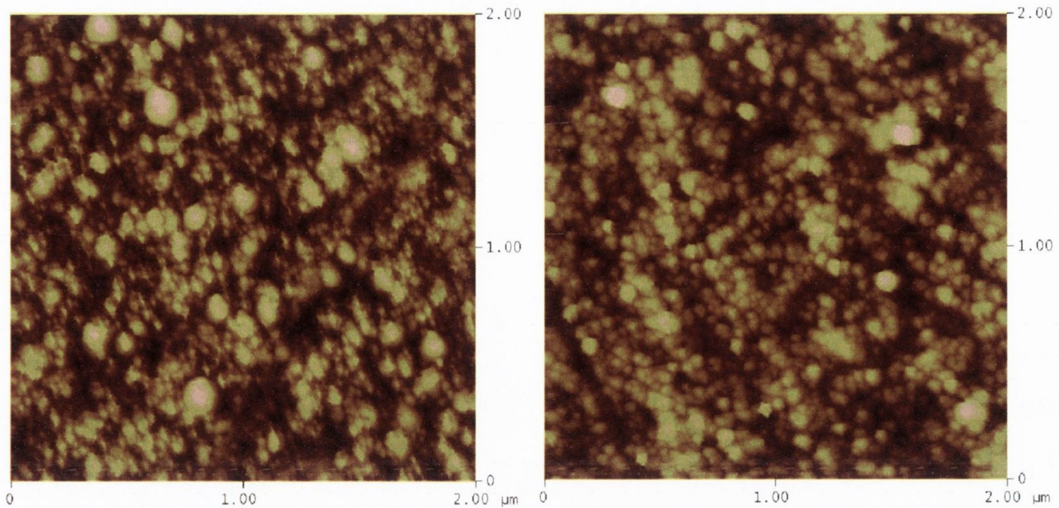

Fig. 5.12 AFM images of Fe_3O_4 films grown at 550°C on Al_2O_3 and MgO substrates. The dimensions of the square are 2μm

Table 5.7. The estimated Ra for the Fe_3O_4 films grown on c-cut sapphire substrate in Ar atmosphere

Deposition temperature, (°C)	Roughness average, Ra, (nm)	
	Al_2O_3	MgO
450	4.8	1.4
450, 1T	4.4	1.8
500	Very rough	Rough
500, 1T	Very rough	Rough
550	5.1	4.7
550, 1T	5.4	5.2
600	5.2	4.9
600, 1T	5.0	4.8

5.3.5. Magnetic force microscopy

The magnetic domain structure of the Fe_3O_4 films was investigated by magnetic force microscopy (MFM). The MFM measurements revealed that films have an irregular domain structure. J. Cheng *et.al.* found that the domain structure morphology of heteroepitaxial Fe_3O_4 films grown by MBE strongly depends on the substrate [25]. He found that the films grown on the $SrTiO_3$ substrate, which has the largest lattice mismatch with Fe_3O_4, have a nanoscale domain size of ~200nm. However when grown on MgO the films had the largest domain size. In contrast to the observed domain size increase with the decrease of the lattice misfit between Fe_3O_4 and the substrate, our PI

MOCVD grown magnetite films had similar domain structure when grown on c-cut sapphire and MgO substrates. The films grown in Ar atmosphere on Al_2O_3 substrate at 450°C showed well defined magnetic domains of approximately ~400-500nm in size. The films grown at 450°C on MgO substrate had similar domain structure, however it was not that well defined as on c-cut sapphire. The films retained the irregular shape domain structure with approximately 400-500nm then grown in different conditions, suggesting that growth parameters such as deposition temperature (550°C) or reactive atmosphere ($Ar+H_2$) do not have a major impact on the domain structure. The structure of the magnetic domains did not change either in size neither in shape when the external magnetic field was applied during the growth of the films. The MFM images for the Fe_3O_4 films are shown in Figure 5.13.

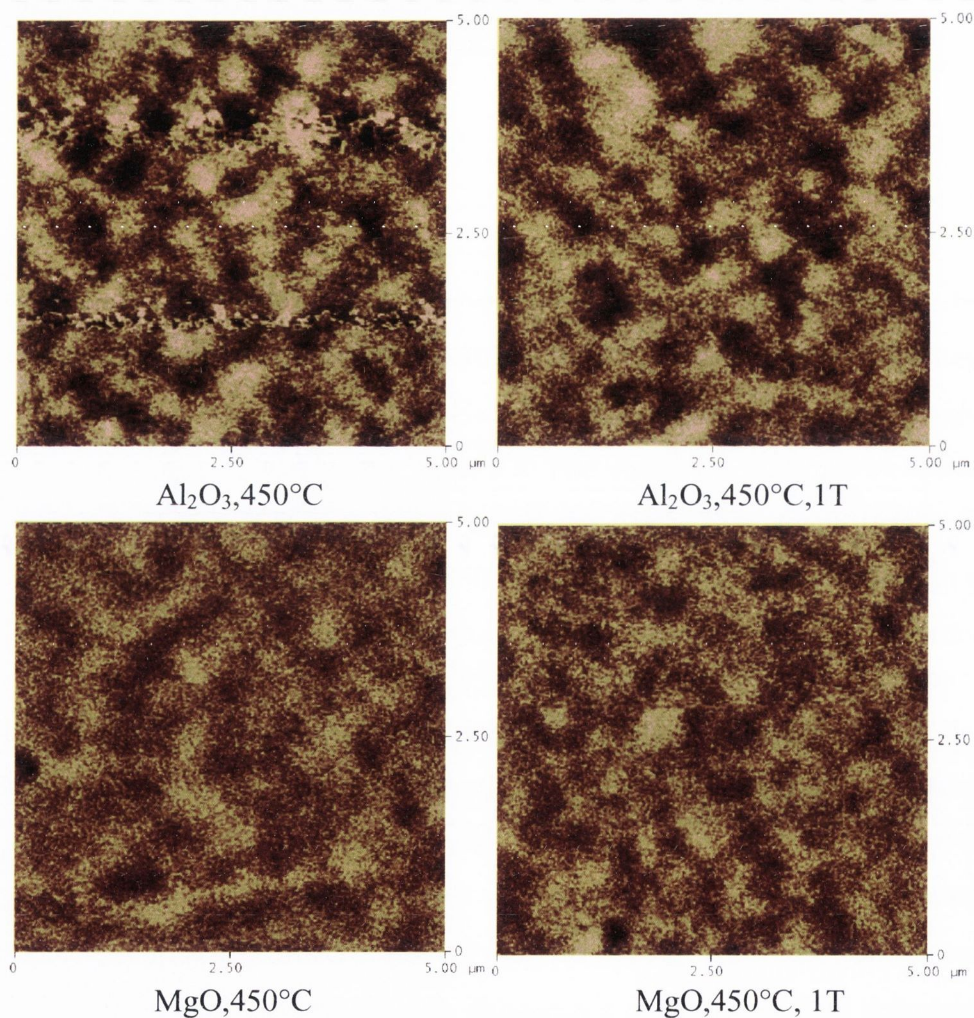

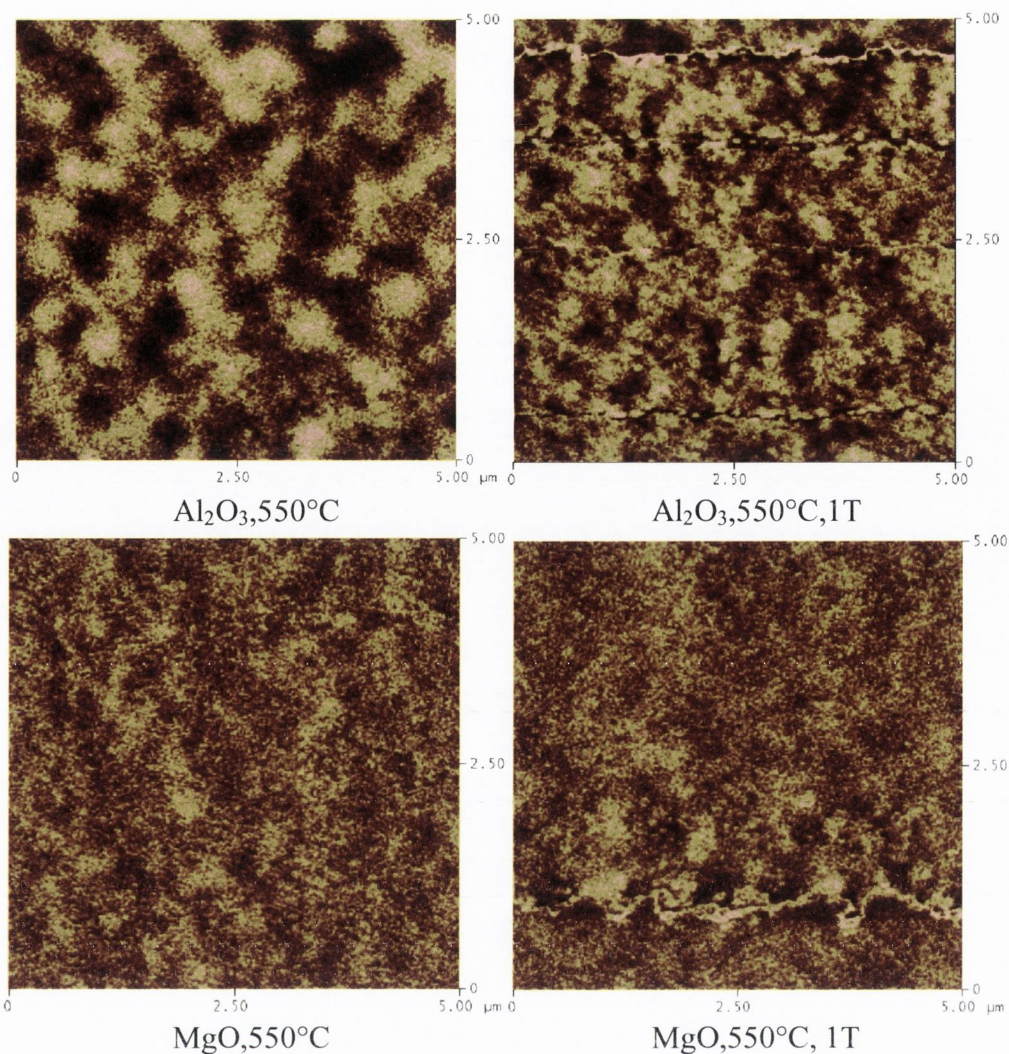

Fig. 5.13 MFM images for the Fe_3O_4 films grown in different conditions

5.3.6. Magnetisation measurements

The magnetic properties of the films, e.g. saturations magnetisation (M_s), remanence (M_R) and coercivity (H_C) were measured using superconducting quantum interference device (SQUID). Magnetic characterisation of the Fe_3O_4 films was carried out at 300K in 1T magnetic field applied parallel to the film surface. Some of the measurements for Fe_3O_4 grown on MgO substrates were also performed in 1T magnetic field applied perpendicular to the films surface and results were compared with those for the applied parallel field. It is noted, that the M_S are approximate values, because the raw measurements contain the substrate contribution and also due to the 5% uncertainty in the film thickness. The substrate contribution was determined by fitting the high-field data to a linear contribution and was subtracted from all experimental data in order to determine M_S.

5.3.6.1 Fe_3O_4 grown on Al_2O_3 substrate

For the Fe_3O_4 films grown in Ar atmosphere on Al_2O_3 substrate we observed a clear hysteresis nature confirming their room temperature ferromagnetic property. In contrast to the earlier reports all our films grown on Al_2O_3 substrate demonstrate a trend to saturate with a saturation field of ~0.5-0.6T, which is much lower than earlier reported saturation fields. For example, Tang *et al.* [26] reported non saturation of magnetisation in PLD grown Fe_3O_4 films on Si(001) substrate, which was attributed to the presence of anti-phase boundaries (APBs) in those films. The clear temperature dependence of the saturation magnetisation M_S was observed for the films grown on Al_2O_3 substrate. The saturation magnetisation of the Fe_3O_4 was lowest for the film grown at 450°C with the M_S value of only 227emu/cm^3. This is more than 50% lower than the value of 490emu/cm^3 reported for the single crystal Fe_3O_4 [7] or for the bulk Fe_3O_4 value, which is 471emu/cm^3 (or 4μ_B/f.u.) [27]. Increasing the deposition temperature from 450°C to 600°C resulted in the increase of M_S with the largest value of 372emu/cm^3 recorded for the films grown at 600°C. This result is better than the earlier reported M_S value of ~315emu/cm^3 for the magnetite films grown Al_2O_3 substrate[28]. The increase of the M_S with the deposition temperature in our films is attributed to the improvement in the crystalline quality. As previously discussed, the detected presence of the nonmagnetic α-Fe_3O_4 phase in the films grown on Al_2O_3 substrate decreased with the deposition temperature and completely vanished in the films grown at 600°C, thus resulting in the highest M_S value in those films. The only exception is the films grown at 500°C that had the largest fraction of secondary phase and the poorest morphology. Due to the difficulties of estimating the thickness of those films the magnetic properties are not evaluated.

It is also evident form Figure 5.14 that the external magnetic field applied during the growth has a significant effect on the magnetic properties of the deposited films. For all deposition temperatures the increase in both the M_S and M_R is observed when films are grown in 1T external magnetic field. Similar behaviour was earlier reported by Tang *et al.* [15], where an increase in M_S from 390emu/cm^3 to 420emu/cm^3 was observed for the Fe_3O_4 when grown in 350 Oe external magnetic field applied along the film plane. We also found a little increase in M_S values when films were cooled only to room temperature in 1T external magnetic field. For all deposition temperatures the M_R values were also largest when films are grown in external magnetic field. The M_S as high as 666 emu/cm^3 was obtained for the film grown at 600°C in 1T external magnetic field. This

value is much higher than 471emu/cm^3 estimated for the bulk Fe_3O_4. Keneddy *et.al.* [29] also observed a higher M_S value of 730emu/cm^3 in their Fe_3O_4 films on the GaAs substrate, which was accounted for by the presence of metallic Fe rich regions within the film. We did not find any presence of the metallic Fe in our films neither by XRD or Raman. The presence of the giant magnetic moment in our films was attributed to the external magnetic field applied during the growth.

On the other hand, one of the interesting aspects seen from Fig.5.14 for the Fe_3O_4 films grown at 600°C in 1T external magnetic field is that the hysteresis curve shows extra structures. During the magnetic reversal extra steps on the magnetisation appear and the hysteresis curve becomes double loop. From XRD and Raman spectrum no indication of other phase is found. At this moment the origin of those magnetic steps is not clear, but one of the possible explanations is the formation of an in-plane strained interface layer.

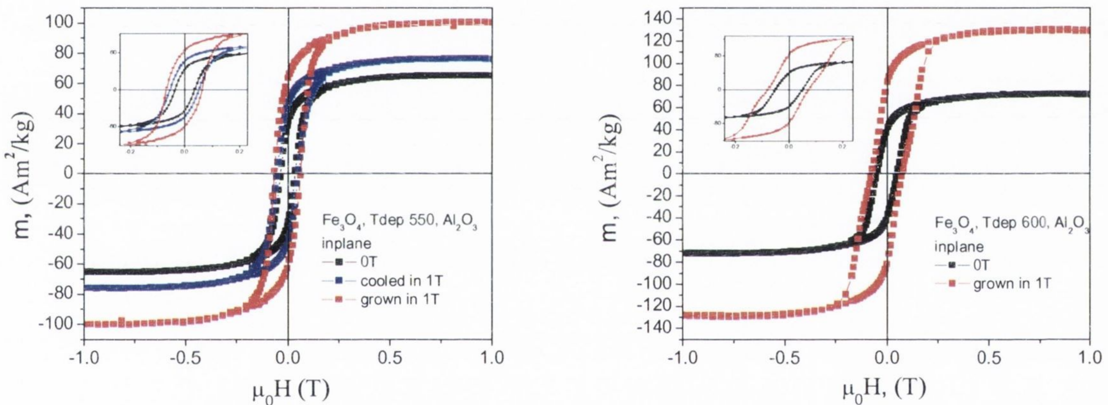

Fig. 5.14 Hysteresis curves of the Fe_3O_4 films grown in and without external magnetic field on Al_2O_3. The blue line indicates the effect of cooling the film in 1T external magnetic field

The magnitude of the coercive fields, H_C, for the films prepared with and without an external magnetic field was different. All the films grown in the external magnetic field had larger H_C. Moreover, the increase in H_C with the deposition temperature was also found with the largest value of ~700Oe obtained for the film grown at 600°C in an external magnetic field.

Different results were obtained for the Fe_3O_4 films grown in a reductive Ar+H_2 atmosphere on Al_2O_3. The giant M_S values are observed for the films grown at 500°C, while for the films grown at 550°C the M_S dropped to 1/3 of its bulk value, but H_C values are still quite large. The magnetic field effect was also not that significant, and the M_S

increased by very small amount when the films were grown in the external magnetic field. It was previously reported that the magnetic parameters of the Fe_3O_4 films prepared by LPCVD technique deteriorate on H_2 reduction, possibly due to the creation of the oxygen deficiency in H_2 reduced Fe_3O_4 or the formation of antiferromagentic metastable FeO phase [30]. Although, this assumption cannot explain the giant M_S and large H_C or M_R values for the films grown in reductive atmosphere at 500°C. Generally, the films grown at 550°C have slightly poorer crystalline quality and larger lattice mismatch induced strain, which could lead to enhanced growth related defects. We suggest that the increased density of the APBs in our films gown at 550°C could result in low M_S values. To better observe the changes in the M_S values with deposition temperature for the films grown in and without external magnetic field the results were plotted in Figure 5.15 and also tabulated in Table 5.8.

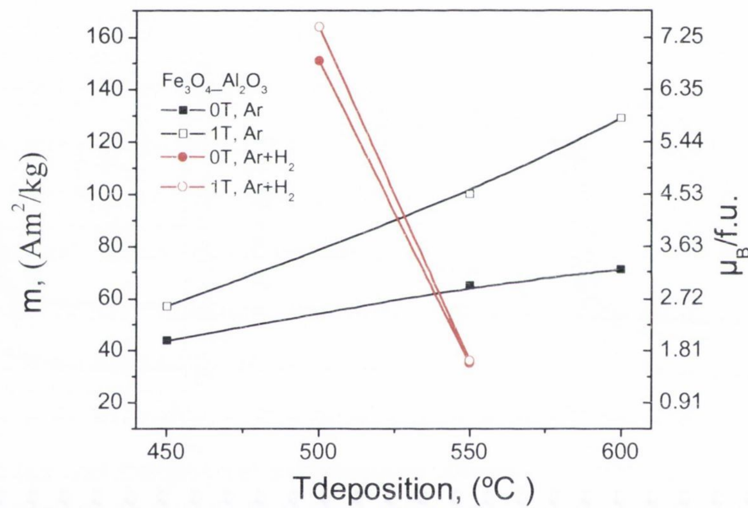

Fig. 5.15 The M_S and μ_B/f.u. values versus deposition temperature for the films on Al_2O_3 grown in and without external magnetic field

Table5.8. The magnetic properties of Fe_3O_4 films grown on Al_2O_3 at different deposition parameters

Al_2O_3	Magnetic parameters				
	Specific (mass) magnetisation, σ,(emu/g or Am^2/kg)	Magnetisation, M_S (emu/cm^3 or 10^3A/m)	Remanence, M_R (emu/g or Am^2/kg)	Coersive field, H_C, (Oe or 10^{-4}T)	Magnetic moment per f.u. (μ_B/f.u.)
Grown in Ar only atmosphere					
450	44	227	20	206	1.82
450,1T	57	296	29	240	2.37
550	65	337	34	360	2.70

550, cool. 1T	76	393	45	502	3.15
550, 1T	100	518	62	640	4.15
600	72	372	40	500	2.94
600,1T	130	666	81	705	5.34
Grown in Ar+H_2 atmosphere					
500	152	781	95	520	6.26
500, 1T	160	841	99	640	6.74
550	35	182	21	480	1.45
550,1T	37	189	19	540	1.51

We also found that magnetisation of the films changes upon changing the film thickness (Figure 5.16). The largest M_S values have been observed for the Fe_3O_4 films grown at 2000 pulses (~95nm) and decreased again at 3000 pulses (~140nm). This is quite unexpected. The increase in the M_S with film thickness was expected due to decrease in disordered Fe_3O_4 phase atoms at the grain boundaries and better crystallinity. We suggest that possible error in the thickness estimation for the films grown from 3000 pulses could result in the lower M_S values. The increased M_S values were also observed for three different film thicknesses when grown in external magnetic field.

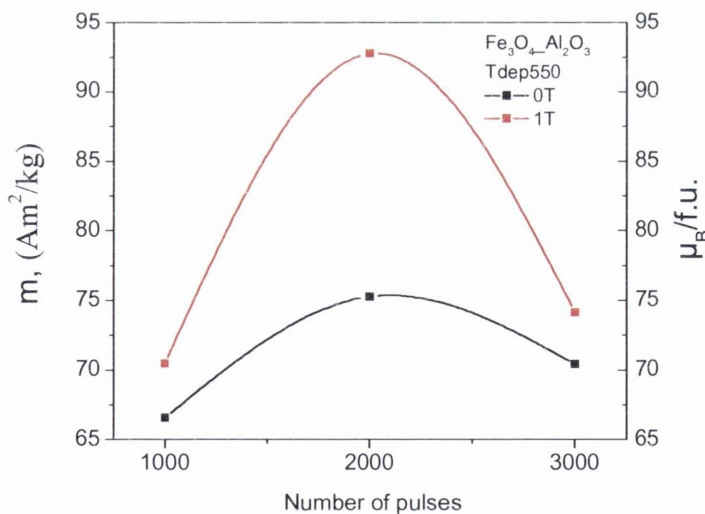

Fig. 5.16 The M_S values of the Fe_3O_4 films versus film thickness (number of pulses)

5.3.6.2. Fe_3O_4 films grown on MgO substrate

Figure 5.17 shows the magnetic hysteresis curves for the Fe_3O_4 films prepared on MgO (100) substrate. We found that the magnetisation of all films saturates at ~0.6-0.8T, which is slightly larger than for the films grown on Al_2O_3. The phenomenon reported by Marguiles *et al.* [31] where the magnetisation did not saturate in the applied fields as high as 7T is not observed in our films. Similar as was found for Fe_3O_4 films on Al_2O_3 the M_S of the films on MgO substrate increased with the deposition temperature. Similar trend where the M_S of Fe_3O_4 on MgO substrate increases with the deposition temperature is reported in other work [32]. The increase in M_S was also found then the films are grown in external magnetic field. However, the estimated M_S values were much lower than for the films on Al_2O_3. For example, the Fe_3O_4 grown at 450°C on MgO has the saturation magnetisation value of only 82emu/cm^3 as compared to 227emu/cm^3 for the same film grown on Al_2O_3. This value is almost 6 times smaller than the bulk value for Fe_3O_4 (471emu/cm^3). The highest M_S values of 457emu/cm^3 were obtained for the film grown at 600°C in 1T magnetic field. It was discovered, that physical properties of epitaxial Fe_3O_4 films deviate from those of the bulk, such as a larger electrical resistivity [33], magneto-resistance [34, 35] and magnetisation which does not saturate in high magnetic fields [31]. These differences are attributed to the presence of antiphase boundaries (APBs), which are natural defects occurring during growth of Fe_3O_4/MgO thin films [31, 36]. It is well known that epitaxial Fe_3O_4 films grown on a single crystal MgO substrate possess a high density of APB defects arising because of the double lattice parameter of Fe_3O_4 (8.397Å) as compared to that of the MgO substrate (4.213 Å) and lower symmetry of Fe_3O_4 compared to MgO. In the first stages of growth islands of Fe_3O_4 are deposited on MgO, however, because of the difference in unit cell parameter and crystal symmetry, the different islands can be related by a shift vector, which is not a lattice translation vector [31, 37]. APBs are formed when islands of Fe_3O_4 on MgO surface coalesce and the neighbouring islands are shifted with respect to each other [8]. We believe that much lower M_S values observed for the films on MgO substrate can be accounted to the presence of APBs.

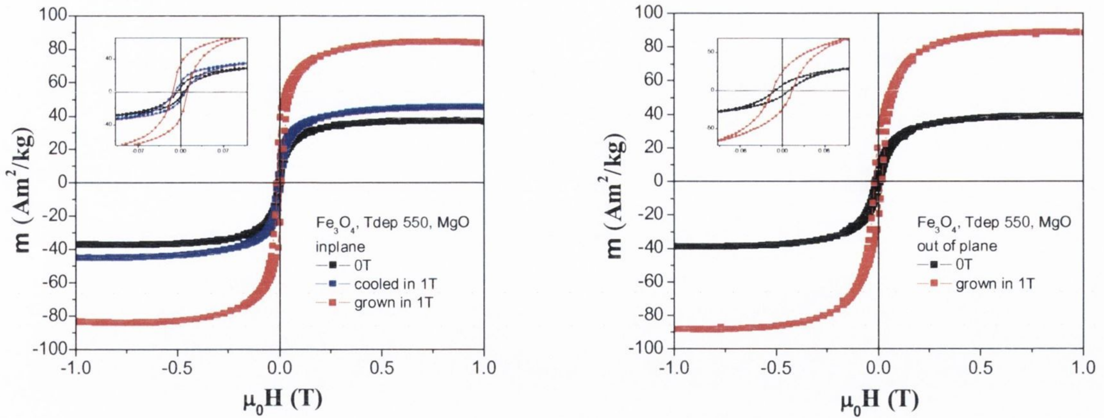

Fig. 5.17 Hysteresis curves for Fe_3O_4 films on MgO substrate grown in and without external magnetic field. The blue line indicates the effect of cooling the film in 1T external magnetic field

The magnitude of the H_C for the Fe_3O_4 films on MgO is much lower and does not follow the trend observed for the films on Al_2O_3. This can be attributed to differences in surface roughness when films grown on different substrates. It was shown by Cheng *et al.* that for magnetic films with similar thicknesses, coercivity is proportional to surface roughness [25]. Indeed, all our Fe_3O_4 films grown on MgO substrate had slightly smaller average roughness than those grown on Al_2O_3 substrate.

For the Fe_3O_4 grown on MgO substrate we can also find that the magnetic easy axis lies on the film plane, as shown in Figure 5.18. Thus, the larger H_C is expected when the magnetic field is applied perpendicular to the film plane, which is consistent with our results.

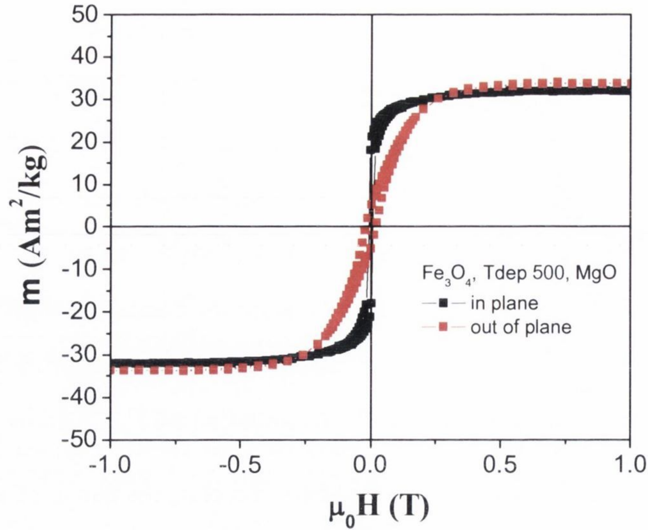

Fig. 5.18 Hysteresis curves of the Fe_3O_4 film with magnetic field applied parallel to the film plane (black squares) and perpendicular to the film plane (red squares)

Again, the saturation magnetisation and other magnetic parameters of the Fe_3O_4 films, grown on MgO in Ar/H_2 atmosphere exhibit similar behaviour to those grown on Al_2O_3. However, the M_S of the films grown in external magnetic field is improved very little as compared to the films grown in Ar atmosphere. The M_S of the 50nm Fe_3O_4 grown at 500°C was much higher than that of the bulk. Similar and even 25% larger M_S were also observed in the work done by Arora *et al.* [38] where 5nm thick films exhibited a giant M_S of 922emu/cm^3, although the origin of giant moments in the films is not quite clear. When grown at 550°C the M_S value of our films (together with the H_C and M_R) decreased and was only 1/8 of its bulk value. The increased density of APBs in the films grown at 550°C could possibly play a major factor in the decrease of magnetic properties. This is supported by the fact that the lattice mismatch induced strain and grain size (roughness) are larger for the films grown at 550°C which could lead to the increased density of the APBs and consequently decline in magnetic properties.

To better observe the changes in the M_S values with deposition temperature for the films grown in and without external magnetic field the results were plotted in Figure 5.19 and also tabulated in Table 5.9.

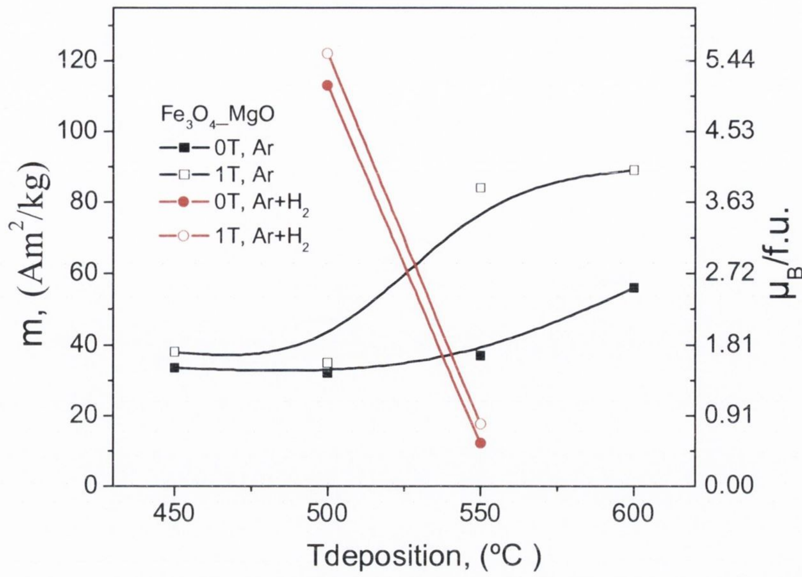

Fig. 5.19 The M_S and μ_B/f.u. values versus deposition temperature for the films on MgO, grown in and without external magnetic field

Table5.9. The magnetic properties of Fe_3O_4 films grown on MgO at different deposition parameters

MgO	Magnetic parameters				
	Specific (mass) magnetisation, σ (Am²/kg)	Magnetisation, M_S (emu/cm³ or 10³A/m)	Remanence, M_R (Am²/kg)	Coersive field, H_C, (Oe or 10⁻⁴T)	Magnetic moment per f.u.
Grown in Ar only atmosphere					
450	16	82	6.8	100	0.66
450,1T	21	107	9.3	100	0.86
500	32	166	19.6, (4.8⊥)	83, (185⊥)	1.33
500, cool. 1T	31	159	18.1, (5.2⊥)	145, (220⊥)	1.27
500, 1T	35	181	22.2, (6.3⊥)	120, (210⊥)	1.45
550	37	191	5, (6.8⊥)	47, (130⊥)	1.53
550, cool. 1T	45	233	10	90	1.87
550, 1T	83	430	31, (24⊥)	118, (185⊥)	3.45
600	57	296	6.1, (11.3⊥)	52, (153⊥)	2.37
600,1T	89	457	13.6, (9.1⊥)	35, (60⊥)	3.66
Grown in Ar+H_2 atmosphere					
500	114	592	61	126	4.74
500, 1T	122	630	70	90	5.05
550	12	63	3.5	89	0.51
550, 1T	18	71	4.1	68	0.73

5.4. Conclusions

Thus we have shown that Fe_3O_4 thin films can be successfully prepared by using PI MOCVD and $Fe(tmhd)_3$ precursor in a single step.

The crystalline quality morphology and magnetic properties of the films strongly depend on deposition conditions. All films grown on Al_2O_3 have developed (111) preferred orientation, regardless to the deposition temperature and reactive atmosphere. However, only films grown at 600ºC in Ar atmosphere had no presence of secondary phases, while films grown at lower temperatures showed XRD peak corresponding to α-Fe_2O_3 phase. The presence of secondary phase was also confirmed by Raman measurements. In contrast, Ar+H_2 reductive atmosphere promoted the formation of cubic Fe_3O_4 phase with no evidence of secondary phases, as confirmed by XRD measurements. At the same time, films grown on MgO substrate at different deposition temperatures in both Ar/Ar+H_2 atmospheres are epitaxial and no presence of secondary phase can be seen from XRD in those films. The XRD analysis revealed that lattice mismatch related stress, i.e. in plane compressive strain is present in all films, regardless to the substrate. We found that stress in the films increases with increase in deposition temperature due to the contribution of thermal stress.

The SEM and AFM analysis showed that when films are grown in Ar atmosphere the smoothest surface is obtained at 450ºC on both Al_2O_3 and MgO substrate. Generally, low substrate temperature results in low surface diffusion and supersaturation of precursor vapours near the surface, thus leading to fewer nucleation centres and rougher surface microstructure. However we believe that 450ºC could be low enough to slow down the decomposition of precursor and consequently slow down the heterogeneous reaction near the substrate surface. This would provide more time for nucleation centres to form in low diffusion conditions than at slightly higher temperatures and thus resulting in smoother surface morphology.

Smoother surface and smaller stress means that there are less defects and consequently less antiphase boundaries present in those films, which are responsible for larger coercivity. In contrast to literature reports [15], we did not observe any changes in morphology neither crystalline properties of Fe_3O_4 films when films are grown in 1T external magnetic field. This implies, that external magnetic field does not have any visible effect on the structural and crystalline properties of the films. Magnetic force

microscopy also confirmed that magnetic field does not have the effect on shape and the size of magnetic domains in Fe_3O_4 films.

The saturation magnetisation and coercive field of the films are found to depend on crystalline and structural properties of the films. The saturation magnetisation increased with the deposition temperature and was largest for all Fe_3O_4 films in Ar atmosphere prepared at 600°C. However, the saturation magnetisation of the films grown in $Ar+H_2$ atmosphere was larger for 500°C rather than 550°C. In both case the increase in saturation magnetisation is related with the improvement in crystalline quality of the films. The coercive field was also changing with the deposition temperature. The changes in coercive field of the films on Al_2O_3 are associated with the strains in the films, where larger coercive values are found in films with larger stains. However, the coercivity of the films on MgO does not follow this trend and is a result of several factors like surface roughness, lattice mismatch induced strains and also the presence of antiphase boundaries. These results show that magnetic properties of thin films are very different from that of bulk the Fe_3O_4. Much more investigation needed in order to understand the magnetic behaviour of thin Fe_3O_4 films grown on different substrates and in different deposition conditions.

Here we have shown that saturation magnetisation of Fe_3O_4 can be tuned by introducing an external magnetic field during the growth process. The increase in saturation magnetisation was achieved in all Fe_3O_4 films grown in external magnetic field. These results suggest that external magnetic field can be very effectively used to tune magnetic properties of Fe_3O_4 thin films during PI MOCVD growth. We believe that this approach can be useful for the preparation of various spintronic devices.

References:

[1] W. B. Mi, J. J. Shen, E. Y. Jiang, H. L. Bai, *Acta Materialia* **2007**, *55*, 1919.

[2] Y.B. Xu, E. Ahmad, J. S. Claydon, Y. X. Lu, S. S. A. Hassan, I. G. Will, B. Cantor, *Journal of Magnetism and Magnetic Materials* **2006**, *304*, 69.

[3] Z. Zhang, S. Satpathy, *Phys. Rev. B* **1991**, *44*, 13319.

[4] J.M. De Teresa, A. Fernandez-Pacheco, L.Morellon, J. Orna, J. A.Pardo, D. Serrate, P. A. Algarabel, M. R. Ibarra, *Microelectronic Engineering* **2007**, *84*, 1660.

[5] G. Zhang, C. Fan, L. Pan, F. Wang, P. Wu, H. Qiu, Y. Gu, Y. Zhang, *Journal of Magnetism and Magnetic Materials* **2005**, *293*, 737.

[6] J. F. Bobo, D. Basso, E. Snoeck, C. Gatel, *Eur. Phys. J. B* **2001**, *24*, 43.

[7] D. T. Marguilies, F. T. Parker, M. L. Rudee, F. E. Spada, J. N. Chapman, P. R. Aitchison, A. E. Berkowitz, *Phys. Rev. Lett.* **1997**, *79*.

[8] T. Himba, F. C. Voogt, L. Niesen, P. A. A. van der Heijden, W. J. M. de Jonge, *Journal of Applied Physics* **1999**, *85*, 5291.

[9] S. B. Ogale, K.Ghosh, P. R. Sharma, l. R. Greene, R. Ramesh, and T. Venkatesan, *Phys. Rev. B* **1996**, *57*, 7823.

[10] M. Ishikawa, H. Tanaka, and T. Kawai, *Appl. Phys. Lett.* **2005**, *86*, 222504.

[11] W. Kim, K. Kawaguchi, N. Koshizaki, M. Sohma, T. Matsumoto, *Journal of Applied Physics* **2003**, *93*, 8032.

[12] C.A. Kleint, H.C. Semmelhack, M. Lorenz, J. M. M.K. Krause, M. M. 725., *Journal of Magnetism and Magnetic Materials* **1995**, *725*, 140.

[13] E.J. Preisler, J. Brooke, N.C. Oldham, T.C. McGill, *J. Vac. Sci. Technol. B* **003**, 1975.

[14] J.P. Hong, S.B. Lee, Y.W. Jung, J.H. Lee, K.S. Yoon, K.W. Kim, C.O. Kim, C.H. Lee, *Appl. Phys. Lett.* **2003**, *83*, 1590.

[15] X.-L. Tang, H.-W. Zhang, H. Su, Z.-Y. Zhong, Y.-l. Jing, *Journal of Solid State Chemistry* **2006**, *179*, 1618.

[16] S. Tiwari, R. Prakash, R. J. Choudhary, D. M. Phase, *Journal of Physics D-Applied Physics* **2007**, *40*, 4943.

[17] O. Shebanova, a. P. Lazor, *Journal of Solid State Chemistry* **2003**, 424.

[18] R. Gupta, A.K. Sood, P. Metcalf, a. J. M. Honig, *Phys. Rev. B* **2002**, *65*, 104430.

[19] L. V. Gasparov, D. B. Tanner, D. B. Romero, H. Berger, G. Margaritondo, a. L. Forro, *Phys. Rev. B* **2000**, *62*, 7939.

[20] J. Dunnwald, A. Otto, *Corros. Science* **1989**, *29*, 1167.

[21] T. R. Hart, S. B. Adams, H. Tempkin, in *3rd International Conference on Light Scattering in Solids* (Ed.: S. Porto), Flammarion, Paris, **1976**, p. 254.

[22] M. J. Massey, U. Baier, R. Merlin, W. H. Weber, *Phys. Rev. B. Condens. Matter* **1990**, *41*, 7822.

[23] S. H. Shim, T. S. Duffy, *American Mineral.* **2002**, *87*, 318.

[24] Yanwei Ma, Kazuo Watanabe, Satoshi Awaji, a. M. Motokawa, *Applied Physics Letters* **2000**, *77*, 3633.

[25] J. Cheng, G. E. Sterbinsky, B. W. Wessels, *Journal of Crystal Growth* **2008**, *310*, 3730.

[26] J. Tang, K. Y. Wang, a. W. Zhou, *Journal of Applied Physics* **2001**, *89*, 7690.

[27] I. Chamritski, a. G. Burns, *journal of Phys. Chem. B* **2005**, *109*, 4965.

[28] A. M. Bataille, A. Tagliaferri, S. Gota, C. d. Nadai, J. B. Moussy, M. J. Guittet, K. Bouzehouane, F. Petroff, M. Gautier-Soyer, N. B. Brookes, *Physical Review B (Condensed Matter and Materials Physics)* **2006**, *73*, 172201.

[29] R. J. Kennedy, P. A. Stampe, *Journal of Physics D: Applied Physics* **1999**, *32*, 16.

[30] S. Dhara, B. R. Awasthy, A. C. Rastogi, B. K. Das, N. V. Gelfond, N. E. Fedotova, A. F. Bykov, I. K. Igumenov, *Journal of Magnetism and Magnetic Materials* **1994**, *134*, 29.

[31] D. T. Margulies, F. T. Parker, M. L. Rudee, F. E. Spada, J. N. Chapman, P. R. Aitchison, A. E. Berkowitz, *Physical Review Letters* **1997**, *79*, 5162.

[32] S. Soeya, J. Hayakawa, H. Takahashi, a. K. Ito, *Appl. Phys. Lett.* **2001**, *80*, 823.

[33] W. Eerenstein, T. T. M. Palstra, T. Hibma, a. S. Celotto, *Phys. Rev. B* **2002**, *66*, 201101.

[34] W. Eerenstein, T. T. M. Palstra, S. S. Saxena, a. T. Hibma, *Phys. Rev. Lett.* **2002**, *88*, 247204.

[35] J. M. D. Coey, A. E. Berkowitz, Li. Balcells, F. F. Putris, a. F. T. Parker, *Appl. Phys. Lett.* **1998**, *72*, 734.

[36] S. Celotto, W. Eerenstein, a. T. Himba, *Eur. Phys. J. B* **2003**, *36*, 271.

[37] F. C. Voogt, T. T. M. Palstra, L. Niesen, O. C. Rogojanu, M. A. James, a. T. Himba, *Phys. Rev. B* **1998**, *57*, 08107.

[38] S. K. Arora, W. H-C, R. J. Choudhary, I. V. Shvets, O. N. Mryasov, H. Yao, a. W. Y. Ching, *Phys. Rev. B* **2008**, *77*, 134443.

Chapter 6: Deposition and investigation of $CoFe_2O_4$ layers

6.1. Introduction

$CoFe_2O_4$ has the similar inverse spinel structure as Fe_3O_4, but in contrast to Fe_3O_4 is a hard ferrite rather than a soft ferrite. In $CoFe_2O_4$ the octahedral **B** sites are occupied by eight Co^{2+} and eight Fe^{3+} cations, while tetrahedral **A** sites are occupied by the remaining Fe^{3+} cations. $CoFe_2O_4$ is also a half metallic material with a smaller saturated magnetic moment of $3.7\mu_B$/f.u. Co^{2+} ions on the **B** sites of the spinel $CoFe_2O_4$ give rise to large anisotropies [1]. In thin film form the magnetic anisotropy of $CoFe_2O_4$ strongly depends on the amount of strain. For example, by selecting substrates with different lattice constants or depositing films at different substrate temperatures it is possible to change their preferred orientation, the amount of stress in the films and hence their magnetic properties [2].

From practical point of view ferrite thin films offer great potential applications, as they are good candidates for magneto-optical devices. Particularly, $CoFe_2O_4$ thin films have attracted much attention in recent years due to their unique physical properties, such as high T_C, large magnetic anisotropy, moderate magnetisation and excellent chemical stability [3]. These properties were exploited in high-density magnetic recording and magneto-optical recording devices. More recently, $CoFe_2O_4$ has also been used In magnetoelectric composite thin films [4, 5], due to its magnetostriction.

Recently much attention has been paid to the material systems with ferroelectric and magnetic composites known as multiferroics, in which the mechanical deformation of the magnetostrictive phase results in polarisation in the piezoelectric phase through the interphase elastic interactions [6, 7]. $CoFe_2O_4$ is a potentially good candidate for fabrication of multiferroic composites, polycrystalline bilayers or multilayers [8-10]. Also, the hard ferromagnetic $CoFe_2O_4$ thin films have been used to act as a strong unidirectional exchange biasing for soft ferrite films [11]. The strong exchange coupling between single-crystalline spinel structure ferrite thin films have been found at room temperature [12]. The magnetic interlayer coupling between $Co_xFe_{1-x}O_4/Fe_3O_4$ bilayer and Fe_3O_4 layer isolated by MgO was already researched [13]. The purpose of $Co_xFe_{1-x}O_4$ base layer was to increase the coercive field of Fe_3O_4 layer.

$CoFe_2O_4$ thin films have been fabricated using different techniques like sol-gel [14], sputtering [15-17], CVD [18], MBE [19], PLD [20] and other. An important task is to make $CoFe_2O_4$ that meets the requirement of high coercivity for high-density recording media and also other applications by using the technology that is as simple as possible. The focus of this work is to prepare $CoFe_2O_4$ films using PI MOCVD technique. Similarly to Fe_3O_4 films we plan to apply the external magnetic field during the growth of $CoFe_2O_4$ films. Our main objective is to obtain the good quality $CoFe_2O_4$ thin films and investigate their magnetic properties when films are grown in and without external magnetic field. The obtained results are to be compared with those of Fe_3O_4.

6.2. Preparation of $CoFe_2O_4$ films

$CoFe_2O_4$ films were grown on Al_2O_3 (0001) substrates in $Ar+O_2$ gas mixture using PI MOCVD technique. After the deposition all films were slowly cooled to room temperature in O_2 atmosphere. All films were grown in and without external magnetic field in order to estimate the effect of magnetic field on the structural and magnetic properties of the films.

To prepare stoichiometric $CoFe_2O_4$ films the $Co(tmhd)_2$ concentration in $Co(tmhd)_2$ +$Fe(tmhd)_3$ precursor mixture was varied. The films were grown at 10%, 20%, 30% and 40% $Co(tmhd)_2$ concentration in precursor solution while maintaining $Fe(tmhd)_3$ concentration fixed and the optimal Co precursor concentration was found. To evaluate the optimal deposition temperature $CoFe_2O_4$ films were grown at different deposition temperatures. The magnetic and structural properties of those films were investigated as a function of deposition temperature. To check the reproducibility of the magnetic properties of $CoFe_2O_4$ the films were repeatedly grown on two Al_2O_3 (0001) and two MgO substrates at the optimal deposition conditions. The deposition was repeated under the same conditions with applied 1T external magnetic field. The summarised deposition conditions are given in the Table 6.1.

Table 6.1 General deposition conditions for $CoFe_2O_4$ films

Deposition temperature	500°C - 700°C
Evaporation temperature	140°C
Carrier gas flow	80 ml/min
Carrier gas	Ar, O_2
Reactor pressure	5 mbar
Metalorganic precursors	$Fe(tmhd)_3$, $Co(tmhd)_2$
Solvent	1,2- dimethoxyethane
Fe concentration in solution	0.015 mol/l
Impulse frequency	2 Hz
Microdose mass	~3 mg
Substrates	MgO, Al_2O_3 (0001)

6.3. Characterisation of $CoFe_2O_4$ films

6.3.1. Thickness measurements

The thickness of all films was estimated from X-ray Reflectivity (XRR) measurements. In contrast to Fe_3O_4 all $CoFe_2O_4$ films possessed high density (comparable to that of 5.3g/cm^3 for the bulk $CoFe_2O_4$). This gave us the possibility to measure thickness using XRR technique rather than white light interferometry used for Fe_3O_4 films. The obtained XRR measurement was simulated using Philips X'Pert program and the thickness was estimated. The simulation error for all measurements is not greater than 2%.

The maximum thickness was found for the films grown at 600°C indicating that at this temperature the precursor decomposition and films growth rate is optimal. The films thickness slightly decreased when grown at temperatures lower or higher that 600°C. The results for film thickness grown at different deposition temperatures, in and without magnetic field are shown in Figure 6.1

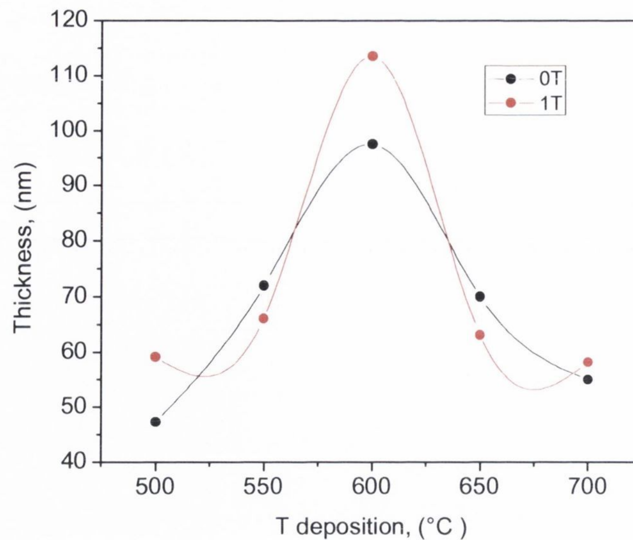

Fig. 6.1 Thickness of $CoFe_2O_4$ films versus deposition temperature for the films grown in and without external magnetic field on Al_2O_3 (0001)

Preliminary, the average film roughness and density were also estimated from XRR measurements. It was found that all films have very high density, which is comparable to that of the bulk $CoFe_2O_4$ value of 5.3g/cm^3. All films also have very smooth surface with the average roughness values as low as ~1nm, except for the films grown at 500°C with the roughness of~5nm.

6.3.2. X-ray Diffraction studies

6.3.2.1. Co concentration influence

To evaluate the optimal Co concentration in precursor solution, the X-ray diffraction was carried out on the films prepared with different Co concentrations. The results are shown in the Figure 6.2. All the films showed the presence of cubic $CoFe_2O_4$ phase developed in (111) preferred orientation. For the films grown with 10% Co in precursor solution the additional peaks can be found which do not belong to $CoFe_2O_4$ phase. The peak at 39.6° is attributed to α-Fe_2O_3 phase. The extra peak at 38.1°, which looks to be splitting of the (222) $CoFe_2O_4$ peak is also found for the films grown with 10% and 20% Co in precursor solution. The splitting of $CoFe_2O_4$ is also observed for (333) and (444) reflections. The possible origin of the peak splitting could be the presence of other iron oxide phase, however due to similar structure and lattice

parameters it is hard to distinguish them from each other only by XRD. The other possibility is that due to the lattice mismatch and misorientation between $CoFe_2O_4$ and Al_2O_3 substrate causing the peak to split. Because of the difference in the lattice mismatch induced stress different regions of the film under different strains are formed (higher stress is induced at the substrate/film interface). Consequently those regions will have slightly different *d*-lattice spacing, which will result in the shift (or splitting) of the X-ray diffraction peak. As for example, the studies on 4H-doped SiC epilayers by high resolution XRD proved that the peak splitting is occurring due to the misorientation, caused by the tilt against substrate by small tilting angles [21]. The films grown with 30% and 40% of Co in precursor solution had no presence of secondary phases or peak splitting. However, the intensities of the main peaks of $CoFe_2O_4$ were higher as well as FWHM of the peaks was smaller when grown with 30% Co indicating better crystalline quality of the films compared to those grown with 40% Co. Relying on the results obtained from X-ray diffraction all further $CoFe_2O_4$ films prepared at different temperatures were grown with 30% Co in precursor solution.

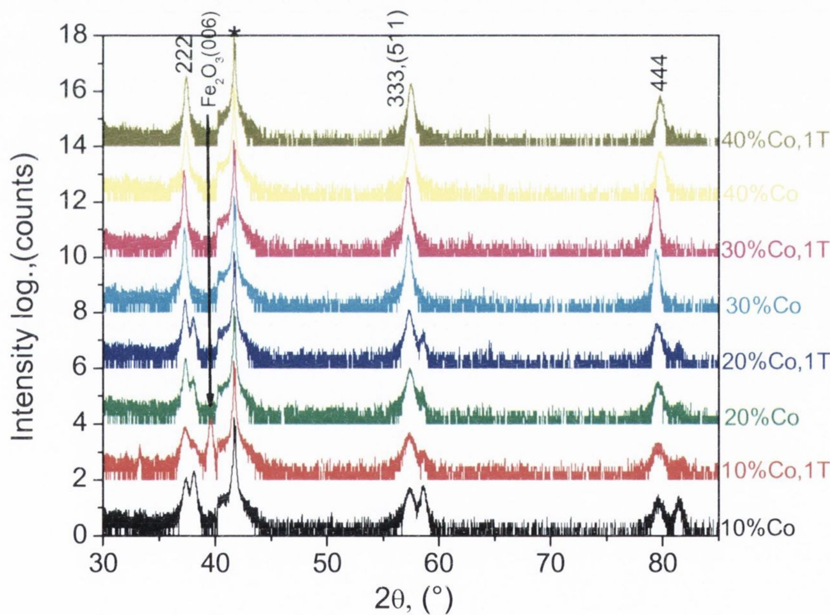

Fig. 6.2 X-ray diffraction of $CoFe_2O_4$ films grown at 600°C on Al_2O_3 with different Co concentrations in precursor solution

The FWHM, calculated *a* lattice parameter and associated strain are shown in the Table 6.2. We have also calculated the *a* lattice parameter and strain for the splitting XRD peak in the films prepared with 10% and 20% Co in precursor solution.

It was estimated that the FWHM of $CoFe_2O_4$ (111) peak decreases with the Co concentration in precursor solution and has the smallest value of ~0.1271° for the film grown with 30% Co. The slight increase in FWHM is found when films are deposited with 40% Co. The decrease of FWHM indicates the improvement in crystalline quality of the $CoFe_2O_4$ films with the Co concentration increase up to 30%. This suggests that at 30% Co in precursor solution the closest to stoichiometric Co/Fe ratio in the film is achieved, thus resulting in good crystalline quality.

The out of plane *a* lattice parameter of cubic $CoFe_2O_4$ films grown with different Co concentrations on Al_2O_3 was calculated from (222) reflection. For all Co concentrations in precursor solution the *a* lattice parameter of the films is smaller than the accepted literature value of 8.392Å for the cubic $CoFe_2O_4$. The closest to its bulk value *a* lattice parameter of 8.364Å and the smallest out of plane stress was found for $CoFe_2O_4$ film grown with 30% Co. This result signals that the film grown with 30% Co in precursor solution has either stoichiometric or very close to stoichiometric Co/Fe ratio in the film. Similar to Fe_3O_4 films all $CoFe_2O_4$ films grown with different Co concentration experienced substrate induced out of plane strain. As expected, the *a* lattice parameter calculated from the splitting (222) $CoFe_2O_4$ peak was almost 2.5% smaller than the bulk value for $CoFe_2O_4$ due to $Al_2O_3/CoFe_2O_4$ interface lattice mismatch induced stress.

The average grain size was calculated from $CoFe_2O_4$ (222) reflection using Scherrer's formula. It was found that the average grain size slightly increased with Co concentration and was largest for 30% Co in precursor solution.

For all films grown with different Co concentrations the FWHM, *a* lattice parameter or grain size did not change upon application of 1T external magnetic field, suggesting that external magnetic field does not affect the crystalline properties of the $CoFe_2O_4$ films grown by PI MOCVD technique.

Table 6.2 Summary of experimental values of FWHM, *a* lattice parameter, effective out-of-plane strain and average grain size for $CoFe_2O_4$ films grown with different Co concentrations on Al_2O_3 substrate. The ^{1} indicates the main peak, and ^{2} indicates the splitting (222) peak

Co conc. in solution, (%)	FWHM[1] (222)/FWHM[2], (°)	a^1/a^2 lattice parameter, (Å)	Effective out-of-plane strain, (%)	Average crystallite size, (nm)
10%	0.2632/ 0.2708	8.332/ 8.185	-0.71/ -2.46	32/ 31
10%, 1T	0.2577/ -	8.350/ 8.173	-0.50/ 2.61	33
20%	0.1823/ 0.2351	8.340/ 8.198	-0.62/ 2.31	46/ 34
20%, 1T	0.2173/ 0.2515	8.350/ 8.197	-0.50/ 2.32	39/ 33
30%	0.1271	8.362	-0.36	47
30%, 1T	0.1151	8.364	-0.33	46
40%	0.1717	8.323	-0.82	34
40%, 1T	0.1726	8.326	-0.79	35

6.3.2.2. Deposition temperature influence

The X-ray diffraction patterns of the $CoFe_2O_4$ films grown at different deposition temperatures on Al_2O_3 substrate with 30% Co are given in Figure 6.3. All as deposited films have good crystalline quality and are formed in a single phase with (111) preferred orientation. It is noted, that the peak intensity increases with deposition temperature and is highest for the films grown at 600°C and 700°C. The increase in intensity is mainly attributed to the formation of larger grains. In general, the films grown at higher temperatures (600°C and higher) developed better crystalline quality with smaller FWHM and smaller lattice mismatch associated stress. The best results were obtained for the film grown at 600°C which has FWHM as low as ~0.12° and the lattice parameter value of 8.36Å matching the best as compared to its bulk value of 8.392Å [19, 22]. All films grown on Al_2O_3 substrate exhibit an out of pane compressive strain and a corresponding in plane tension regardless to the deposition temperature. The effective out of plane strains, FWHM and *a* lattice parameters are determined from XRD and shown in Table 6.3. It is been previously reported that the strain induced by substrate could give rise to significant effects on the magnetocrystalline anisotropy [23]. This will be discussed below in the section dealing with magnetic properties of the $CoFe_2O_4$ films.

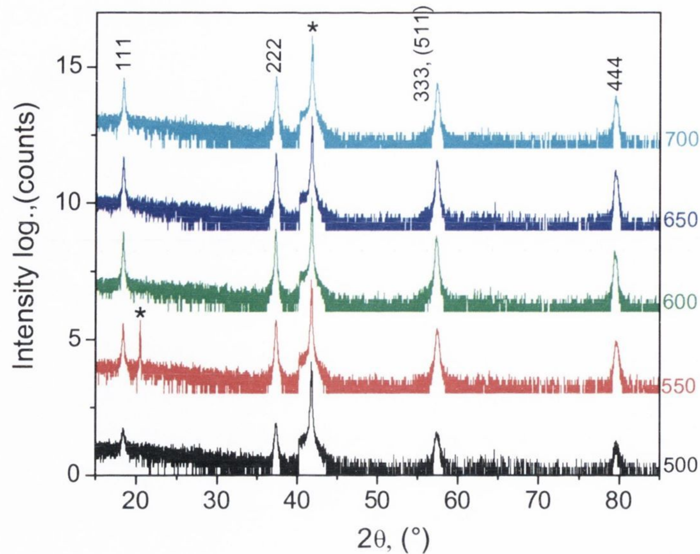

Fig. 6.3 X-ray diffraction patterns for $CoFe_2O_4$ films grown on Al_2O_3 substrate at different temperatures

Similarly as to Fe_3O_4 films cubic $CoFe_2O_4$ is expected to grow epitaxially on MgO(100) substrates due to small lattice mismatch between film and substrate [23, 24]. The X-ray diffraction was performed following the same procedure as described for the Fe_3O_4 films on MgO(100) substrate. The X-ray diffraction revealed the epitaxial growth of $CoFe_2O_4$ films on MgO(100) substrate with $CoFe_2O_4$[100]/ MgO[100] heteroepitaxial orientation as evident from the *phi* scan. The results are shown in Figure 6.4, inset shows the *phi* scan around $CoFe_2O_4$(511) which reveals four expected peaks of similar intensities.

The FWHM measured for $CoFe_2O_4$ (333) reflection on MgO is between 0.6-0.66°. This is three times larger than the one found for films grown on Al_2O_3, however, it is not possible to compare the FWHM for two different substrates. For the films grown on Al_2O_3 the (111) reflection was used to estimate the FWHM and (333) reflection was used for the films grown on MgO, where the third order peak FWHM is always larger.

The calculated *a* lattice parameter of $CoFe_2O_4$ was smaller than that of the bulk value, indicating that films grown on MgO experienced out of plane compression. The effective out of plane strain for the films grown on MgO is compatible with that for the films grown on Al_2O_3 at 650°C and 700°C. The summary of all experimental values for

$CoFe_2O_4$ grown on MgO and Al_2O_3 substrates obtained from XRD measurements can be found in Table 6.3.

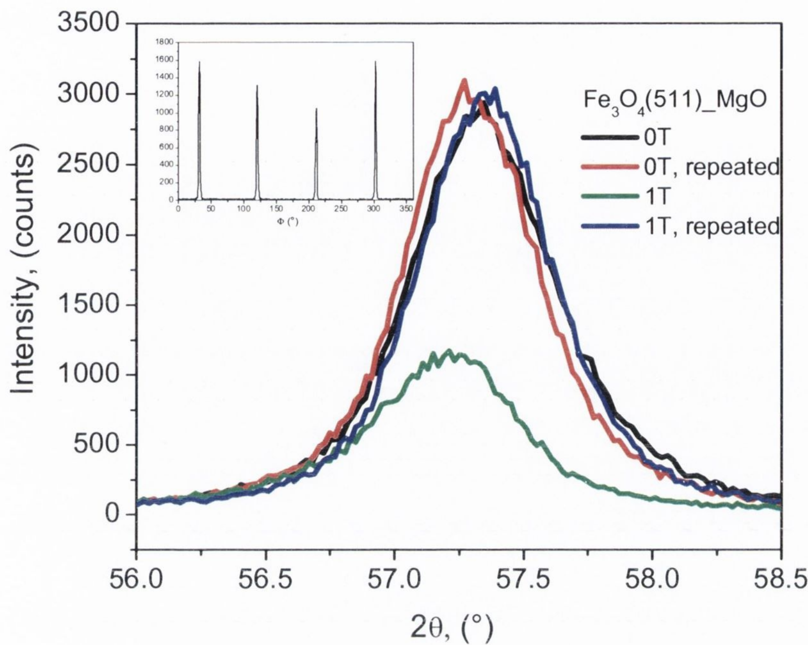

Fig. 6.4. X-ray diffraction of $CoFe_2O_4$ (511) reflection grown on (100) MgO substrate at 600°C in and without external magnetic field. The inset is showing phi scan around $CoFe_2O_4$ (511) reflection evidencing the epitaxial relation between film and MgO substrate

The average crystallite size was calculated for all $CoFe_2O_4$ films. The crystallite size increased with deposition temperature and had the maximum average value of ~63nm - ~70nm for the films grown at 600°C. The slight decrease in average crystallite size with further increase in deposition temperature was then observed. These results are quite expected, since the larger crystallites produce a higher intensity peaks in Θ/2Θ scan. Therefore the films grown at 600°C with highest peak intensity have the largest crystallites. The films grown on MgO at 600°C had much smaller crystallite size than those grown on Al_2O_3. Judging from small (~15nm) crystallite size it is expected that $CoFe_2O_4$ film have very smooth surface morphology when grown MgO substrate.

Table 6.3. Summary of experimental values of FWHM, *a* lattice parameter, effective out-of-plane strain and average grain size for $CoFe_2O_4$ films grown at different temperatures on Al_2O_3 and MgO substrates

T deposition, (°C)	FWHM (111), (°)	a lattice parameter, (Å)	Effective out-of-plane strain, (%)	Average crystallite size, nm
		Al_2O_3 substrate		
500	0.2855	8.357	-0.42	28
500, 1T	0.2577	8.291	-1.20	31
550	0.1560	8.344	-0.57	52
550, 1T	0.1707	8.348	-0.52	47
600	0.1271	8.362	-0.36	63
600, 1T	0.1151	8.364	-0.33	70
650	0.1535	8.355	-0.44	52
650, 1T	0.1632	8.356	-0.43	49
700	0.1762	8.354	-0.45	46
700, 1T	0.1667	8.353	-0.46	48
		MgO (substrate)		
600	0.6469/0.6569	8.356/8.355	-0.43/-0.44	15/14
600,1T	0.6425/0.6520	8.36/8.354	-0.38/-0.45	14/15

All $CoFe_2O_4$ films grown in 1T external magnetic fields exhibited similar crystalline structure to those films prepared without external magnetic field. Thus, we concluded that external magnetic field does not have any noticeable effect on the crystalline properties of $CoFe_2O_4$ films.

6.3.3. EDAX measurements

EDAX analysis revealed that Co concentration in $CoFe_2O_4$ films grown at 600°C is almost corresponding to the one in precursor solution. The only exception is the film grown with 10% Co in precursor solution, which has slightly larger Co amount in the film (Figure 6.5).

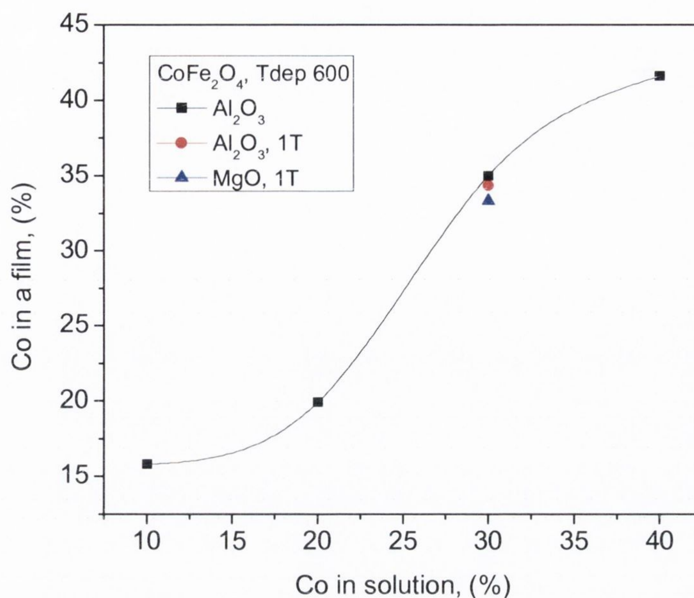

Fig.6.5. Variation of Co concentration in the film with Co concentration in precursor solution for $CoFe_2O_4$ films grown on Al_2O_3 substrate. Red triangle denotes Co concentration for the film grown in 1T on Al_2O_3 substrate and blue square for the films grown on MgO substrate

From Figure 6.3 it is easy to estimate that stoichiometric Co concentration (Co/Fe = ½) in a $CoFe_2O_4$ film grown at 600°C is achieved at ~30% Co in precursor solution. These results coincide well with the X-ray diffraction analysis of $CoFe_2O_4$.

6.3.4. Raman spectroscopy studies

Room temperature Raman spectra were recorded to confirm the presence of $CoFe_2O_4$ phase. The excitation wavelength used was 514.5nm from an Ar^+ ion laser (Laser Physics Reliant 150 Select Multi-Line) with maximum power of ~10mW. In order to avoid an excessive heating and oxidation, ~3mW laser power was used for all the measurements.

The Raman spectra of cobalt ferrite do not differ much from the Raman spectra of magnetite. The same five optical active Raman modes (A_{1g}+ E_g+$3T_{2g}$) characteristic of the cubic inverse spinel structure are generally observed [25].

It was observed that all $CoFe_2O_4$ films grown at different temperatures present similar Raman spectra given in Figure 6.4. The films grown on Al_2O_3 substrate showed four out of expected five Raman shifts at 305, 470, 620 and 690cm^{-1}. Except from the downshifts observed in all Raman peaks, the spectrum showed in Figure 6.6 is similar to

the spectrum of bulk maghemite presented in [26]. The observed downshift is due to the larger Co-atom mass compared to the Fe atom mass. The similarities between the Raman features of the $CoFe_2O_4$ films and bulk maghemite suggest that our films present the crystal structure of cobalt modified γ-Fe_2O_3 reported in the literature [27]. Raman measurements therefore confirm that all films have developed cubic inverse spinel $CoFe_2O_4$ structure.

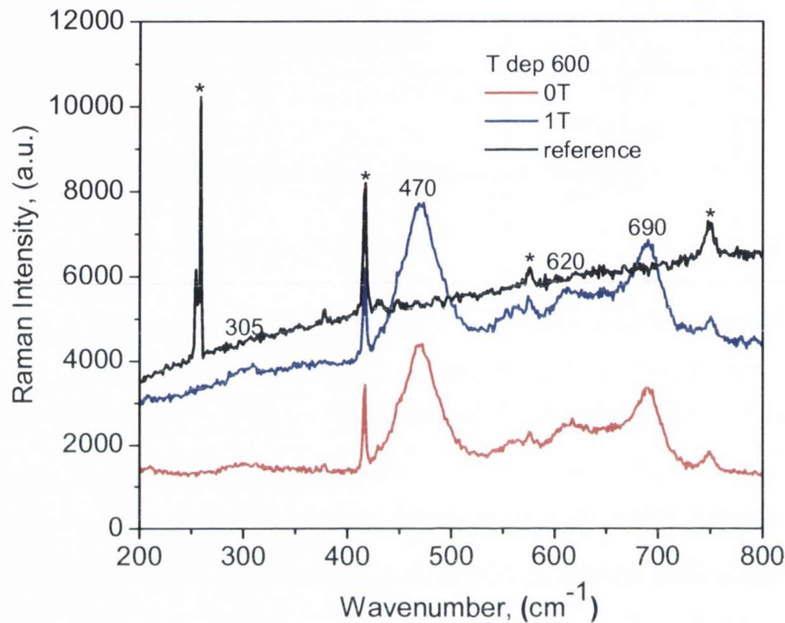

Fig. 6.6 Raman spectrum of $CoFe_2O_4$ films, where * denotes substrate peaks, numbers denote the approximate positions for $CoFe_2O_4$ phase

6.3.5. Investigation of surface microstructure

6.3.5.1. SEM

SEM micrographs of the $CoFe_2O_4$ films grown Al_2O_3 substrate are shown in Figure 6.7. It is noted, that the microstructure of the films depends on the deposition temperature. As, when grown at 500°C, the surface of the films is rough and consists of smooth matrix with an aggregation of large, approximately ~70nm in size crystallites. With the increase in deposition temperature the surface becomes less rough and presents a very smooth matrix with only few impurities. The decrease in surface roughness with deposition temperature indicates that films develop less growth related defects. However, these results disagree with the previously obtained from X-ray diffraction, where the largest crystallites were calculated for the films grown at higher deposition temperatures.

The possible explanation is that at lower deposition temperature films morphology consists of large aggregates formed from smaller crystallites, while for the higher deposition temperatures crystallites do not form aggregates but rather spread uniformly on the surface. The magnetic field showed to have no visible effect on the microstructure of the films since all films had exactly the same surface morphology when grown in and without external magnetic field.

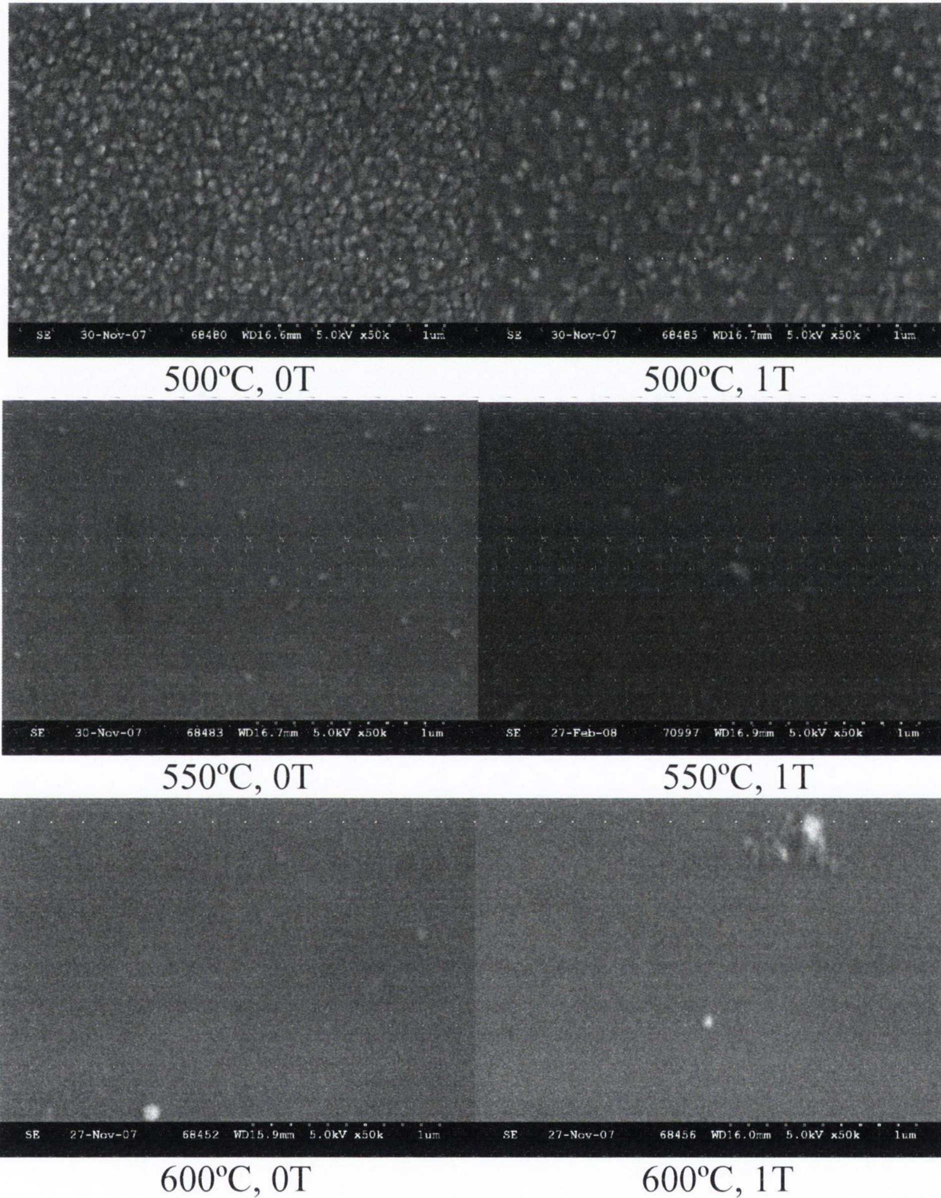

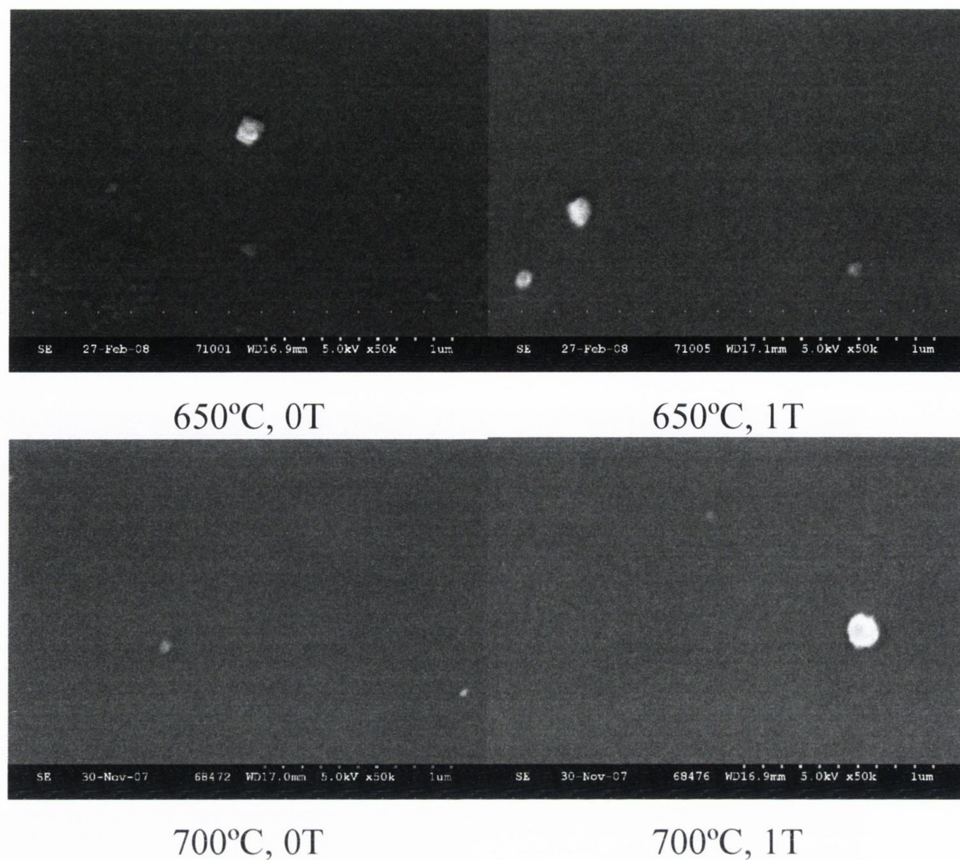

Fig. 6.7. SEM micrographs of $CoFe_2O_4$ films grown at different deposition temperature in and without external magnetic field

6.3.5.2. AFM microscopy

Surface morphology of $CoFe_2O_4$ films grown on MgO substrate was studied using AFM microscopy. The films prepared at 600°C revealed a very smooth surface roughness, Ra of only ~ 0.182nm and ~ 0.190nm when grown without and in 1T external magnetic field respectively.

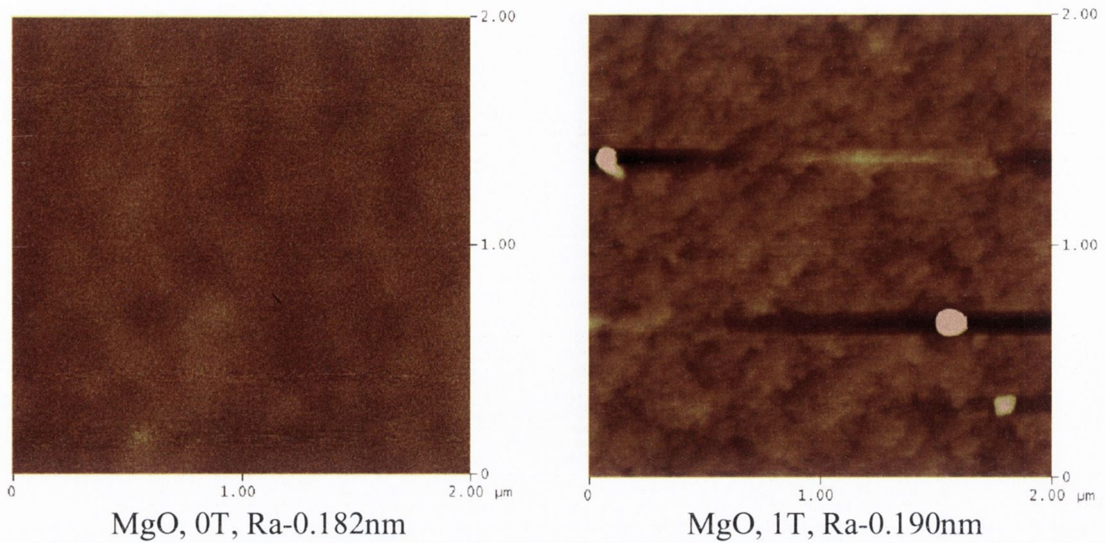

Fig. 6.8.AFM images of $CoFe_2O_4$ films grown on MgO substrate

6.3.6. Magnetic force microscopy

The MFM have been employed to reveal the magnetic domain structure of $CoFe_2O_4$ films. MFM images were taken in zero fields at room temperature. The out of plane domain images for the $CoFe_2O_4$ grown at 600°C on Al_2O_3 and MgO substrates are shown in Figure 6.9. The recorded domain images were also compared with the ones obtained for the films grown in 1T external magnetic fields. The observed domain image is of very high contrast consisting of cluster-like domains of various shapes, where the magnetisation is confined up and down. Similar irregular domain structure was reported in epitaxial $CoFe_2O_4$ films grown on $SrTiO_3$ substrate. Moreover, very similar domain structure was found in our Fe_3O_4 films although the contrast of the domains was much smaller, especially for the films grown on MgO substrates. Magnetic domain structure or size did not change when grown on different substrates or in 1T external magnetic field.

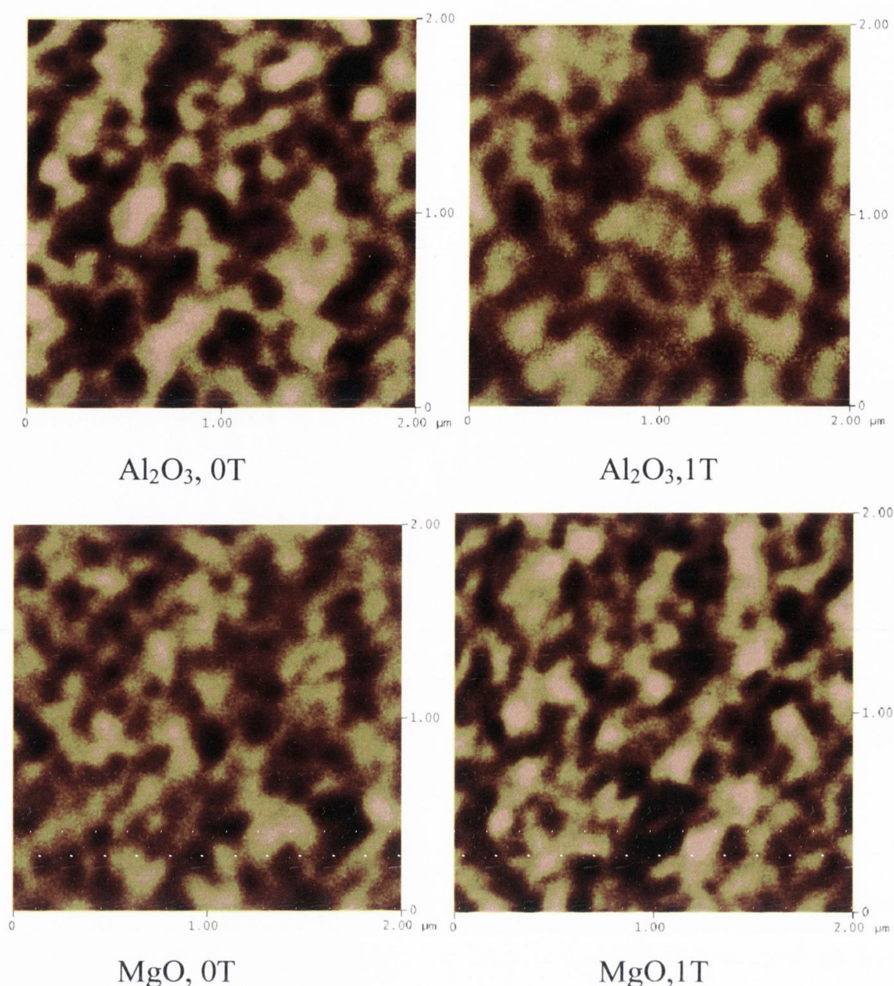

Fig. 6.9 Magnetic domain structure of $CoFe_2O_4$ films grown at 600°C. The scale is 2μm

6.3.7. Magnetisation measurements

The magnetic properties of the films, e.g. saturations magnetisation (M_s), remanence (M_R) and coercivity (H_C) were measured using superconducting quantum interference device (SQUID). Magnetic properties of $CoFe_2O_4$ films were measured at room temperature with a maximum magnetic field of 5T applied parallel to the film surface. Some of the measurements were also performed in 5T magnetic field applied perpendicular to the films surface to study the magnetic anisotropy of the films. Like for Fe_3O_4 films the calculated M_S are approximate values, because the raw measurements contain the substrate contribution and also due to the 5% uncertainty in the film thickness. The substrate contribution was determined by fitting the high-field data to a

linear contribution and was subtracted from all experimental data in order to determine M_S.

6.3.7.1. Co concentration influence on magnetic properties

The magnetic hysteresis curves of $CoFe_2O_4$ films grown at 2 different Co concentrations and magnetic field applied parallel to the film surface are shown in Figure 6.10. The shape of the hysteresis curves is rather different from that of the Fe_3O_4 films. The $CoFe_2O_4$ films are magnetically much harder than the Fe_3O_4 films.

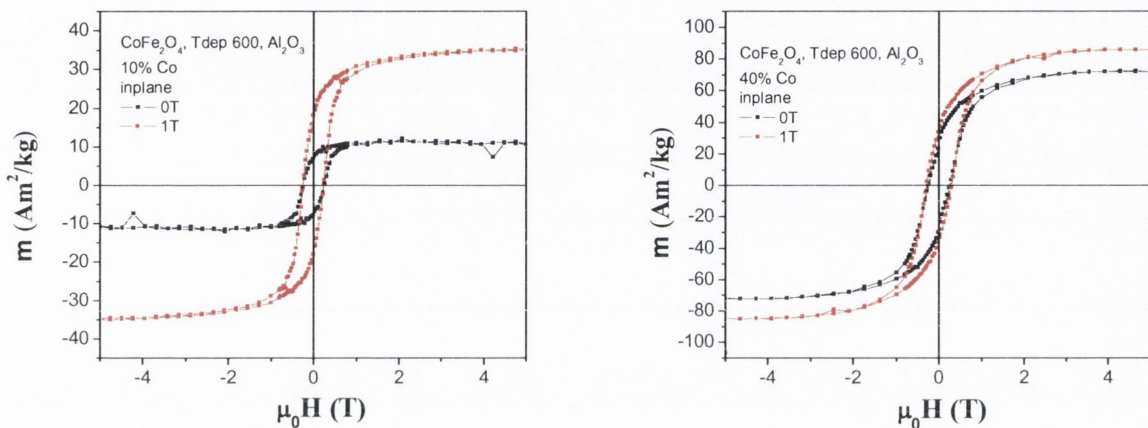

Fig. 6.10. Hysteresis curves for $CoFe_2O_4$ films grown in and without magnetic field on Al_2O_3 substrate with 10 and 40% Co

The dependence of the saturation magnetisation from Co concentration in precursor solution for $CoFe_2O_4$ films is shown in Figure 6.11. The saturation magnetisation of the films grown with 10% Co in precursor solution was quite small as compared to the saturation magnetisation of ~69Am^2/kg for a bulk $CoFe_2O_4$. Low saturation magnetisation value was expected; since a non-magnetic α-Fe_2O_3 phase was detected in films grown with 10% Co. Depending on the amount present in a film α-Fe_2O_3 phase would significantly reduce the magnetic moment of $CoFe_2O_4$. An increase in saturation magnetisation with Co concentration was observed for the films grown in 1T external magnetic field. The largest value of ~85Am^2/kg was found for the film grown with 40% Co in 1T external magnetic field. This value is larger than the saturation magnetisation found for bulk $CoFe_2O_4$, the origin of these large M_S values is not very clear. While for the films grown without magnetic field the sharp increase in saturation magnetisation is found for 20%Co. However the saturation magnetisation slightly decreases with further increase in Co concentration (Refer to Table 6.4). All films except

those grown at 20% showed larger saturation magnetisation when grown in 1T external magnetic field following the same trend as observed for Fe_3O_4 films.

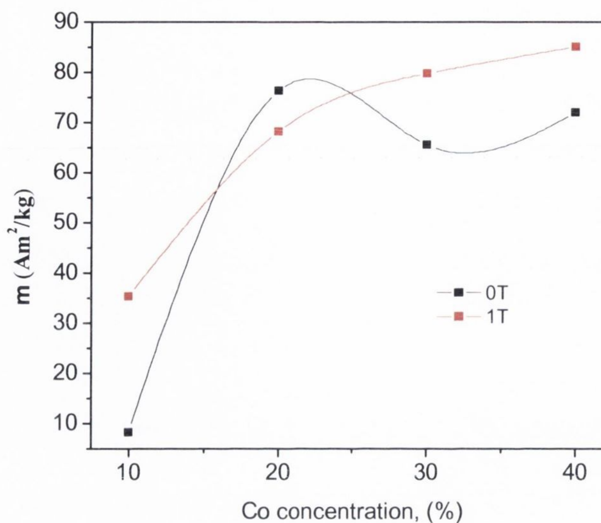

Fig. 6.11. M_s values of $CoFe_2O_4$ films grown with different Co concentrations with and without external magnetic field

Table 6.4. The magnetic properties of $CoFe_2O_4$ films grown on Al_2O_3 with different Co concentrations

Co concentration, (%)	Magnetic parameters				
	Specific (mass) magnetisation, σ,(emu/g or Am^2/kg)	Magnetisation, M_S (emu/cm³ or 10^3A/m)	Remanence, M_R (emu/g or Am^2/kg)	Coersive field, H_C, (Oe or 10^{-4}T)	Magnetic moment per f.u.
At different Cr concentrations					
10%	8.2	41	7.3	2480	0.47
10%, 1T	35.3	270	18	2440	1.48
20%	76.4	405	19.6	1620	3.2
20%, 1T	68.2	361	18.1	1960	2.9
30%	65.6	348	22.4	2260	2.76
30%, 1T	80	423	31.8	1920	3.9
40%	72	383	26.9	2510	3
40%, 1T	85	453	35.3	2930	3.6

The change in coercivity of the films with Co concentration was also studied. We found that films grown with 10 and 40% Co in precursor solution have the largest coercivity values. The lowest coersivity was found for the film grown with 20% Co. Such changes in coercivity values could be related to the stress in the films and also to the

crystallite size. It has been found that coercivity of $CoFe_2O_4$ films increases with the increasing grain size and reaches maximum value for the grain with diameter of about 40nm [28]. Grains more than 40nm divide into domains and domain wall movements result in reduced coercivity with increasing size. Similar phenomenon was also observed in work done by Y.C.Wang *et al.* [[17]]. Indeed, the grain size of our films grown with 30% is slightly larger than 40nm. Therefore, lower coercivity for the films grown with 30%Co could be associated with the larger grain size, more than 40nm. On the other hand the large lattice mismatch induced stress in the films result in high coercivities. Thus, the films that have more stress (with 10% and 40%Co) have larger coercivities as compared to those, which have lower stress (20, 30% Co). The large coercivity values found in our films are comparable to those previously reported by different groups [29-31].

6.3.7.2. Deposition temperature influence on magnetic properties

The change of M_S value in our films was studied as a function of deposition temperature. The summarised results are shown in Figure 6.12. The M_S value of $CoFe_2O_4$ films grown without external magnetic field was largest (~81Am^2/kg) for the film grown at 500°C. This value is larger than the bulk value of ~69Am^2/kg for $CoFe_2O_4$. The films grown at 550 °C and 600°C had almost ideal M_S value of the bulk $CoFe_2O_4$. However, the M_S values dropped with further increase in deposition temperature. The film grown at 700°C had only ¼ of the bulk $CoFe_2O_4$ M_S value. Similar results were found in $CoFe_2O_4$ films grown by PLD where saturation magnetisation decreased for the films grown at temperatures above 600°C, with a very low M_S value observed for the film grown at 700°C [32]. Generally, $CoFe_2O_4$ show the saturated moment of approximately 1/3 of that of Fe_3O_4. According to the local moment theory, the magnetisation is determined by the distribution of metal ions in two different sites of spinel. As was mentioned earlier, $CoFe_2O_4$ form inverse spinel and Co^{2+} is assumed to replace Fe^{2+} at octahedral **B** site. The magnetic moment of $CoFe_2O_4$ should drop to about ¾ of the M_S of Fe_3O_4. The decrease of the magnetic moment is due to the fact that Co^{2+} has smaller magnetic moment ($3\mu_B$) compared to Fe^{2+} ($4\mu_B$), thus replacing Fe by Co tends to reduce magnetic moment [23]. However, the saturated moment of $CoFe_2O_4$ films does not always follow this prediction, which is also the case of our films.

The M_S value of the $CoFe_2O_4$films grown in 1T external magnetic field was rather different from that when grown without magnetic field. The largest saturation magnetisation of $80Am^2/kg$ was observed for the film grown at 600°C. This value is larger than the one obtained for the films grown at 600°C, but without external magnetic field. This is in good agreement with the results of Fe_3O_4 films, where an enhancement of M_S values was obtained for the films grown in 1T external magnetic field as compared to those grown without external magnetic field. However the saturation magnetisation of $CoFe_2O_4$ grown at other deposition temperatures in external magnetic field was even four times smaller (another exception is a films grown at 700°C, which has both M_S values of ¼ of the bulk value with slightly larger M_S value when grown in external magnetic field), than when films are grown without external magnetic field (Figure 6.9, red symbols).

We also found that the trend for Ms in 1T field is very similar to the trend in thickness shown in Fig.6.1. It is quite possible that the effect of external magnetic field depends on the thickness of $CoFe_2O_4$ films.

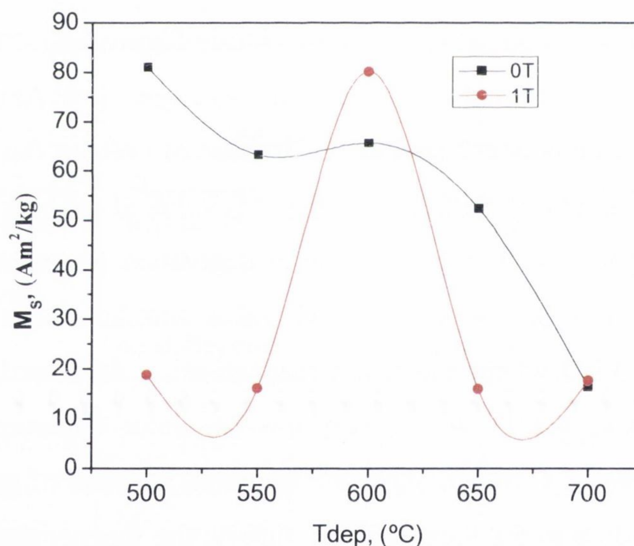

Fig. 6.12 M_S of $CoFe_2O_4$ grown at different deposition temperature with and without external magnetic field

Like for Fe_3O_4 films, the enhancement of the magnetic properties was expected for the $CoFe_2O_4$ grown in external magnetic field. As opposite, significant reduction of magnetic properties of $CoFe_2O_4$ is achieved when films are grown in external magnetic field for all deposition temperatures except 600°C. It is hard to explain such magnetic field effect. The hysteresis loops of $CoFe_2O_4$ and the influence of the external magnetic

field on magnetic properties of the films grown at different deposition temperatures can be seen in Figure 6.13.

One can see that all $CoFe_2O_4$ films have high coercivity. The coercivity value does not seem to change drastically with the applications of external magnetic field. Films grown at 500°C had the largest coercivity, which then decreased with increasing deposition temperature. Similar behaviour was observed for $CoFe_2O_4$ films grown by sol-gel and PLD methods [30]. J.P. Zhou et al. found the opposite, where the increase in H_C with deposition temperature was attributed to a high planar stress caused by the thermal expansion mismatch between $CoFe_2O_4$ and substrate [32]. High coercivities in $CoFe_2O_4$ are known to arise due to the stress induced by substrate lattice mismatch. In fact, our films grown at lower deposition temperatures have larger stress as calculated from *a* lattice parameter values than those grown at higher deposition temperatures, thus the high H_C values are expected.

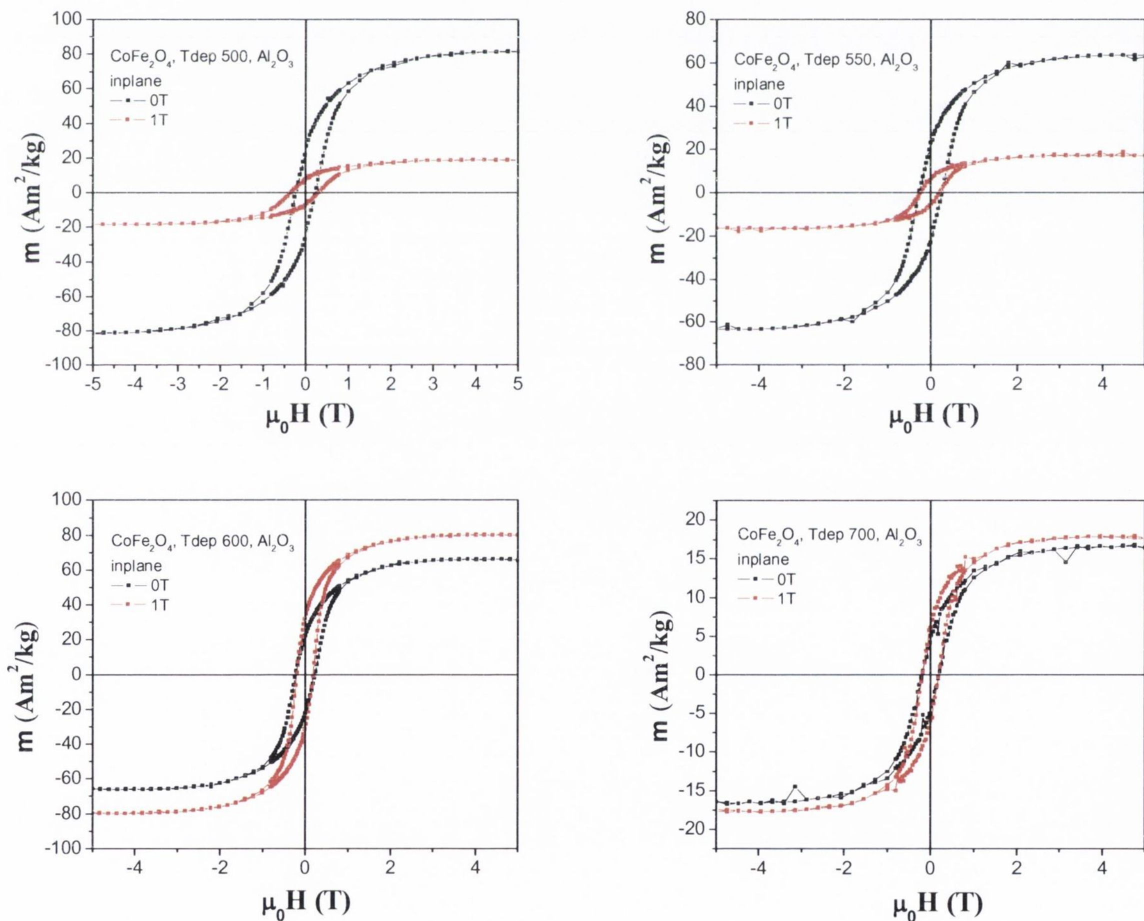

Fig. 6.13. Hysteresis loops showing the influence of magnetic field on magnetic properties of $CoFe_2O_4$ films grown on Al_2O_3 substrate at different deposition temperatures

The coercivity values at higher deposition temperature could also be reduced due to larger crystallite size (over 40nm). This effect was already discussed when studying coercivity changes in films grown with different Co concentrations in precursor solution. In spite of the fact that parallel H_C is rather large for all films, perpendicular H_C is always larger, so even larger H_C values are expected when magnetic field is applied perpendicular to the film surface. In this work the hysteresis loop of $CoFe_2O_4$ with magnetic field applied in perpendicular and in plane directions were also measured. The results are shown in Figure 6.14. The in plane and perpendicular coersivity has the same value (2140 Oe) and hysteresis curve shows similar shape. In several works it was suggested that this occurs due to the randomly orientated easy axes of the ferrite films, because the $CoFe_2O_4$ films were grown without any preferred growth direction [29, 30]. Yet, this suggestion cannot be applied for our films, since all films grown on Al_2O_3 substrate showed (111) preferred orientation. Basically, these results seem to indicate that the magnetic easy axis no longer lies on the film plane for the $CoFe_2O_4$ film. This effect in our samples is possibly caused by both magnetic anisotropy and shape anisotropy. The in plane direction is an easy magnetisation direction in consideration of the shape anisotropy. However, the hardest magnetic axis is along (110) directions, which is mainly parallel to the film surface in consideration of the stress effects on the magnetic anisotropy [33].

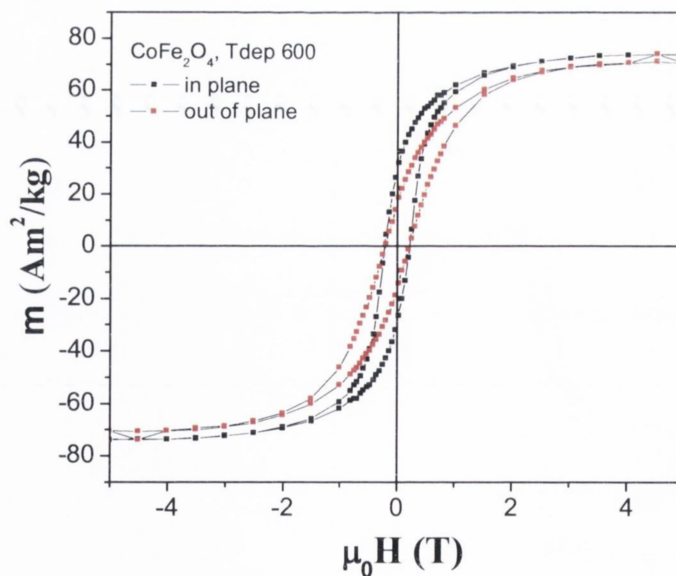

Fig. 6.14 shows quite similar hysteresis curves for $CoFe_2O_4$ films with magnetic field applied perpendicular and parallel to the films surface

Table 6.5. Summary of the magnetic properties for $CoFe_2O_4$ films grown on Al_2O_3 and MgO substrates at different deposition temperatures

Al_2O_3	**Magnetic parameters**				
	Specific (mass) magnetisation, σ (Am^2/kg)	**Magnetisation, M_S (emu/cm^3 or $10^3 A/m$)**	**Remanence, M_R (emu/g or Am^2/kg)**	**Coersive field, H_C, (Oe or 10^{-4}T)**	**Magnetic moment per f.u.**
500	81	430	25	2320	3.4
500, 1T	18.7	99	7	3280	0.78
550	63.2	336	23	2650	2.65
550, 1T	16.0	85	5.6	2150	0.67
600	65.6	348	32	2270	2.76
600, 1T	80	423	22	1920	3.35
650	52.4	282	17	1800	2.20
650, 1T	15.8	83	2.8	1800	0.67
700	16.4	89	6	1930	0.69
700, 1T	17.5	94	4.6	1970	0.74
Tdep 600°C					
MgO	45.3/43.6	240/234	2.5/2.8	420/510	1.90/1.84
MgO, 1T	40/49	213/265	2.5/3.5(20⊥)	430/520 (6040⊥)	1.7/2.08
Al_2O_3, repeated	63.8/19.7	340/105	19/6.6	2140	2.68/0.83
Al_2O_3, repeated, 1T	68.6/73.6	365/391	21/29 (16⊥)	1780/2140, (2140⊥)	2.88/3.09

6.3.7.2.1. Magnetic properties of $CoFe_2O_4$ on MgO substrate

Hysteresis curve of $CoFe_2O_4$ grown on MgO substrate showed rather different shape from those grown on Al_2O_3. $CoFe_2O_4$ films had very small coercive fields of approximately ~400-500 Oe when magnetic field applied parallel to the film surface. These H_C values are only half of that measured for bulk $CoFe_2O_4$ (~900 Oe) [32]. However, H_C value increased more than 11.5 times when magnetic field is applied perpendicular to the film surface. The H_C value for magnetic field applied perpendicular to the films surface increased to 6040 Oe as compared to only 430 Oe when field is applied parallel (Figure 6.15.a). Obviously, this signals that the hysteresis loops of $CoFe_2O_4$ on MgO exhibit strong magnetic anisotropy with magnetic easy axis lying on

the film plane. The anisotropic property has often been observed in strained structures. Lisfi *et al.* has found that the magnetic anisotropy is sensitive to the film thickness in $CoFe_2O_4$ films on MgO [34]. Liu *et al.* also investigated the anisotropy induced by residual strain in $CoFe_2O_4$ powders [35]. Although, the mechanism responsible for the strong magnetic anisotropy of $CoFe_2O_4$ films is not yet well understood, the strain induced strong ferromagnetic behaviour has been found in many magnetic thin films such as $((La,Ca)MnO_3$ [36] and $(La,Sr) MnO_3$ [37]. When transition metal ions with an orbitally degenerate ground state, such as $Fe^{2+}(3d^6)$ or $Co^{2+}(3d^7)$ are incorporated into the ferrite lattice, the degeneracy of the ground state is lifted by the local crystalline field, the exchange interactions and the spin-orbit coupling, thus leading to energy levels which depend on the direction of magnetisation. Such effects enhance magnetocrystalline anisotropy and the anisotropy of the magnetostriction. Y. Suzuki *et al.* found very similar perpendicular anisotropy in single crystalline $CoFe_2O_4$ films grown on MgO substrate and explained his observations using magneto-elastic theory [11]. However more magnetic measurements needs to be provided to evidence the dominant role of strain in the observed magnetic anisotropy of our films. Until then the possibility of the other factors like shape anisotropy and antiphase boundaries influence cannot be excluded.

The effect of magnetic field on magnetic properties of $CoFe_2O_4$ films grown on MgO substrate was also studied. Figure 6.15b shows hysteresis curves for four $CoFe_2O_4$ films grown at 600°C with magnetic field applied perpendicular to the film plane. It is noted that we found that magnetic moment is reproduced for two films grown in the same conditions during the same deposition process. At the same time the magnetic moment was not reproduced for two films grown in 1T external magnetic field during the same deposition process. This signals that it is very hard to judge if magnetic field causes the increase of the magnetic moment of $CoFe_2O_4$. Further investigations are necessary in order to confirm the magnetic field effect on the magnetic properties of $CoFe_2O_4$ films.

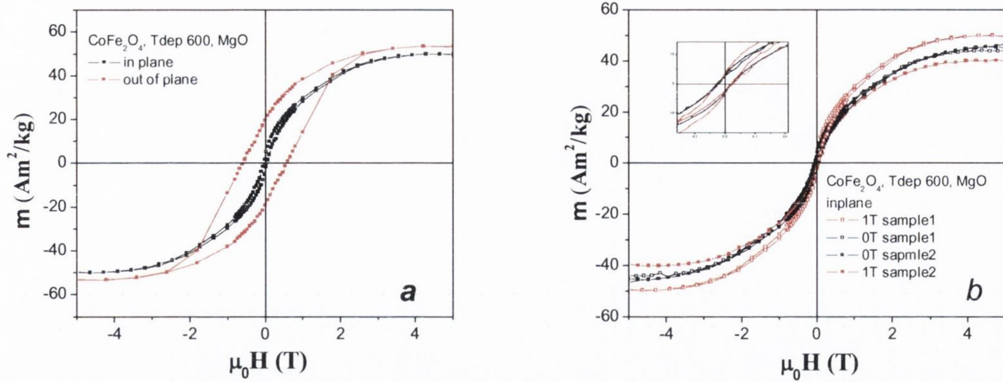

Fig. 6.15. a) Hysteresis curves for $CoFe_2O_4$ films with magnetic field applied parallel and perpendicular to the film surface, showing huge magnetic anisotropy effect; b)

6.4. Conclusions

In summary, it was shown that highly crystalline $CoFe_2O_4$ films could be grown by PI MOCVD technique. To the best of our knowledge this is for the first time when PI MOCVD was applied for the growth of $CoFe_2O_4$ films.

In order to find the optimal deposition conditions for $CoFe_2O_4$ films a series of tests were carried out. This involved deposition of the films with different Co concentrations in precursor solution and also deposition at different temperatures on two different of substrates (hexagonal Al_2O_3(0001) and cubic MgO (111)). The optimal $CoFe_2O_4$ growth was achieved at 600°C with 30% Co in precursor solution. These deposition conditions resulted in a high quality $CoFe_2O_4$ film with stoichiometric Co content. Under these conditions films produced on Al_2O_3 substrates were single crystalline and developed (111) preferred orientation. The films grown on MgO substrates were epitaxial. The surface morphology of the films grown at optimal deposition conditions is very smooth (Ra is in the order of ~0.2nm), which is a good factor for practical applications in electronic devices. The lattice parameter of all films was slightly smaller than the accepted value of ~8.392Å for cubic $CoFe_2O_4$, meaning that all films experience out of plane compressive strain and a corresponding in plane tension regardless to the deposition temperature or substrate. It is well known that lattice mismatch induced strains in the ferrite films can be responsible for large magnetic anisotropies [34].

The magnetic properties of the films studied as a function of Co concentration in precursor solution showed that saturation magnetisation strongly depends on Co

concentration. The saturation magnetisation was very low for films grown with 10% Co, which is related to poorer crystalline properties of those films having inclusions of nonmagnetic α-Fe_2O_3 phase. The high presence α-Fe_2O_3 is believed to be responsible for small magnetic moment of $CoFe_2O_4$ film grown with 10% Co. Films grown with 20, 30 and 40% Co had much larger saturation magnetisation, comparable to the bulk value for $CoFe_2O_4$ (~72Am^2/kg). The increase in saturation magnetisation with Co concentration is due to an improved crystalline structure of the films, with all films displaying Co content close to stoichiometric. The coercivity of the films grown at different Co concentration was largest for the films grown with 40 and 10% Co in precursor solution. The variation in coercivity values in our films is most likely to be related to the combination of two factors. First factor is a lattice mismatch induced stress in the films which is largest for the films grown with 10 and 40% Co and is well known to significantly increase the coercivity. The second factor is possibly related to the size of the crystallites, as it was shown previously in several reports [17, 28], that $CoFe_2O_4$ films with larger crystallites have reduced coercivity. Consequently, $CoFe_2O_4$ films grown with 20 and 30% Co, which have larger crystallites of around 40nm and smaller stains show smaller coercivity. Films grown with 10 and 40% Co, however have larger coercivity due to larger stress and smaller crystallites.

The magnetic properties of $CoFe_2O_4$ films studied as a function of deposition temperature revealed that saturation magnetisation decreases with deposition temperature. The largest saturation magnetisation value was obtained for the film grown at 500°C. The in plane coercivity value was largest for the films grown at 500°C and 550°C. High H_C in those films is associated with the large lattice mismatch induced stress. The magnetic measurements of the films performed with magnetic field applied in plane and out of plane directions revealed that coercivity of the films is almost the same. This suggests that magnetic anisotropy in our films grown on Al_2O_3 substrate is not pronounced. This effect is most likely caused by both magnetic and shape anisotropy in the films.

Very unexpected results were obtained when growing $CoFe_2O_4$ in 1T external magnetic field. The magnetic field effect was opposite to that observed in Fe_3O_4 films. The significant reduce (almost four times) of magnetic moment is found when films are grown in external magnetic field. The exception is the film grown at 600°C, which have slightly larger saturation magnetisation when grown in external magnetic field. The film grown at 700°C also has slightly larger saturation magnetisation, but the actual value is so

small that the effect can be neglected. It is not quite clear why the external magnetic field caused the drop in saturation magnetisation of $CoFe_2O_4$ films and not an increase as was observed for Fe_3O_4.

The magnetic properties of $CoFe_2O_4$ films prepared at 600°C are different when grown on MgO substrate. First of all, the saturation magnetisation is ~1/3 times smaller than that of $CoFe_2O_4$ on Al_2O_3 even though the films were grown during the same deposition process. Secondly, the hysterisis of the films on MgO is more than four times smaller when magnetic field is applied parallel to the film surface. At last, in the contrast to the films grown on Al_2O_3 the magnetic properties of $CoFe_2O_4$ on MgO substrate have very large out of plane anisotropy with measured coercive field of more than 6000 Oe. The large anisotropy and slightly lower saturation magnetisation of the films on MgO is attributed to the strains in the films and possibly to the presence of antiphase boundaries, which are very common for epitaxial Fe_3O_4 films.

Different magnetic properties are found for $CoFe_2O_4$ prepared at 600°C on MgO. First of all, the saturation magnetisation of those films is about 1/3 times smaller than found for the films on Al_2O_3. Moreover, the in plane coercive field of the films on MgO is more than four times smaller. Finally, films grown on MgO substrate showed huge out of plane magnetic anisotropy with coercive field of more than 6000 Oe for magnetic field applied perpendicular to the film plane. The reduced saturation magnetisation and large anisotropies of the films grown on MgO are most likely to be due to the strains in the lattice and the presence of antiphase boundaries very often reported for the Fe_3O_4 films and discussed in Chapter 5.

The effect of external magnetic field on magnetic properties of $CoFe_2O_4$ on MgO substrate tested on two samples is not very clear. For one sample the increase in saturation magnetisation is found when grown in external magnetic field. However, the slight decrease in saturation magnetisation is found for the second sample grown in external magnetic field. This means that reproducibility of magnetic properties of $CoFe_2O_4$ films is poor.

To summarise, we have shown that external magnetic field applied during the growth of $CoFe_2O_4$ films on Al_2O_3 and MgO substrates can be achieved. This could be effectively used for future practical applications, by employing films with large saturation magnetisation and also large coercive fields. However, the effect is not only "positive" but also "negative", resulting in the decrease of saturation magnetisation. To check reproducibility of magnetic properties it is necessary to produce large numbers of the

films under the same deposition conditions and measure its magnetic properties. In order to understand what triggers "negative" magnetic field it is necessary to produce a larger series of the films under different deposition conditions and also investigate their magnetic properties.

References:

[1] R. M. Bozorth, E. F. Tilden, A. J. Williams, *Phys. Rev. B* **1955**, *99*.

[2] S. Chikazumi, *Physics of Ferromagnetism*, Oxford University Press, New York, **1997**.

[3] J. H. Jin, J. Ding, J. S. Chen, X. S. Miao, *Journal of Magnetism and Magnetic Materials* **2006**, *303*, e387.

[4] H. Zheng, J. Wang, S. E. Lofland, Z. Ma, L. Mohaddes-Ardabili, T. Zhao, *Science* **2004**, *303*, 661.

[5] J. G. Wang, X. W. Wang, Y. J. Wu, M. Zeng, Y. Wang, H. Jiang, *Appl. Phys. Lett.* **2005**, *86*, 122501.

[6] H. Zeng, *Science* **2004**, *303*, 661.

[7] T. Wu, *Phys. Rev. B* **2006**, *73*, 134416.

[8] W. H. Wang, X. Ren, *Journal of Crystal Growth* **2006**, *289*, 605.

[9] J. P. Zhou, H. C. He, Z. Shi, C. W. Nan, *Appl. Phys. Lett.* **2006**, *88*, 013111.

[10] K. S. Chang, *Appl. Phys. Lett.* **2004**, *84*.

[11] Y. Suzuki, R. B. van Dover, E. M. Gyorgy, J. M. Phillips, V. Korenivski, D. J. Werder, C. H. Chen, R. J. Cava, J. J. Krajewski, W. F. Peck Jr., K. B. Do, *Appl. Phys. Lett.* **1996**, *68*, 714.

[12] Y. Suzuki, R. B. van Dover, E. M. Gyorgy, J. M. Phillips, R. J. Felder, *Phys. Rev. B* **1996**, *53*, 14016.

[13] P. A. A. van der Heijden, P. J. H. Bloemen, J. M. Metselaar, R. M. Wolf, J. M. Gaines, J. T. W. M. van Eemeren, P. J. v. d. Zaag, *Phys. Rev. B* **1997**, *55*, 11569.

[14] J. G. Lee, J. Y. Park, *Journal of Applied Physics* **1998**, *84*, 2801.

[15] J. Ding, Y. J. Chen, Y. Shi, S. Wang, *Appl. Phys. Lett.* **2000**, *77*, 3621.

[16] J. EchiGoya, W. Asano, A. Yamaguchi, *Phys. Status Solidi A* **2002**, *191*, 359.

[17] Y. C. Wang, J. Ding, J. B. Yi, B. H. Liu, *Appl. Phys. Lett.* **2004**, *84*, 2596.

[18] A. G. Fitzgerald, T. G. May, *Thin Solid Films* **1976**, *35*, 201.

[19] S. A. Chambers, R. F. C. Farrow, S. Maat, *Journal of Magnetism and Magnetic Materials* **2002**, *246*, 124.

[20] Y. Kitamoto, S. Kanatake, *Journal of Magnetism and Magnetic Materials* **1999**, *193*, 97.

[21] R. S. Okojie, T. Holzheu, X. Huang, a. M. Dudley, *Appl. Phys. Lett.* **2003**, *83*, 1971.

[22] G. Hu, J. H. Choi, C. B. Eom, V. G. Harris, Y. Suzuki, *Phys. Rev. B* **2000**, *62*, R776.

[23] L. Horng, G. Chern, M. C. Chen, P. C. Kang, D. S. Lee, *Journal of Magnetism and Magnetic Materials* **2004**, *270*, 389.

[24] M. C. Terzzoli, S. Duhalde, S. Jacobo, L. Steren, C. Moina, *Journal of Alloys and Compounds* **2004**, *369*, 209.

[25] B. Ammundsen, G. R. Burns, M. S. Islam, H. Kanoh, J. Roziere, *Journal of Phys. Chem. B* **1999**, *103*, 5175.

[26] D. L. A. de Fria, S. Venancio Silva, M. T. de Oliviera, *Journal of Raman Spectrosc.* **1997**, *28*, 873.

[27] T. Maruyama, L. T. Kitamura, *Journal of Applied Physics* **1989**, *28*, L1096.

[28] C. N. Chinnasamy, B. Jeyadevan, K. Shinoda, K. Tohji, D. J. Djayaprawira, M. Takahashi, R. J. Joseyphus, A. Narayanasamy, *Appl. Phys. Lett.* **2003**, *83*, 2862.

[29] J. G. Lee, K. P. Chae, J. C. Sur, *journal of Magnetism and Magnetic Materials* **2003**, *267*, 161.

[30] J. G. Lee, H. M. Lee, C. S. Kim, Y. J. Oh, *journal of Magnetism and Magnetic Materials* **1998**, *177-181*, 900.

[31] M. S. Lee, T. Y. Kim, C. S. Lee, J. C. Park, Y. I. Kim, D. Kim, *Journal of Magnetism and Magnetic Materials* **2004**, *268*, 62.

[32] J. P. Zhou, H. C. He, C. W. Nan, *Applied Surface Science* **2007**, *253*, 7456.

[33] Y. Suzuki, G. Hu, R. B. van Dover, R. J. Cava, *Journal of Magnetism and Magnetic Materials* **1999**, *191*, 1.

[34] A. Lisfi, C. M. Williams, *Journal of Applied Physics* **2003**, *93*, 8143.

[35] B. H. Liu, J. Ding, *Appl. Phys. Lett.* **2006**, *88*, 042506.

[36] Y. M. Xiong, *Journal of Applied Physics* **2005**, *97*, 083909.

[37] J. Dho, *Appl. Phys. Lett.* **2003**, *82*, 1434.

Chapter 7: Conclusions and Future Work

7.1. Conclusions

In this work we have prepared and investigated a number of magnetic oxide materials, which could have potential applications in a new generation of spintronic devices.

We have demonstrated that PI MOCVD technique offers a great potential for the preparation of wide range high quality oxide thin films. Together with the ease of use and low cost PI MOCVD has a great advantage over more complex and expensive thin film preparation techniques.

The new PI MOCVD equipped with 1T external magnet was developed in this work. This gave us the possibility for the first time to study the effect of external magnetic field on the structural and magnetic properties of the films.

Extensive studies have been performed on Co-doped ZnO films. It was shown that films grown on Al_2O_3 (0001) and Al_2O_3 (1$\underline{1}$02) substrates by PI MOCVD exhibit room temperature ferromagnetism and found to be highly anisotropic. The films doped with 1% Co in precursor solution showed the largest ferromagnetic moments reported for this system to date. The absence of metallic Co clusters as confirmed by XRD and XPS studies together with monotonic decrease of magnetic moment with Co concentration all suggest the intrinsic origin of ferromagnetism in Co-doped ZnO films.

We have also successfully prepared Cr-doped In_2O_3 films and studied their magnetic properties. We found that all films prepared on Al_2O_3 (0001), but not on Al_2O_3 (1$\underline{1}$02), at different temperatures were room temperature ferromagnetic when doped with 2% Cr in precursor solution. All films were found to be highly anisotropic with largest saturation magnetisation found when magnetic field is applied perpendicular to the film plane. The magnetic moment of Cr-doped In_2O_3 films was found to slightly decrease with time and then stabilised after some certain period. This is different to what was previously found for Co-doped ZnO films where the saturation magnetisation was monotonically decreasing with time. The absence of the secondary ferromagnetic phases also proposes the intrinsic nature of room temperature ferromagnetism in Cr-doped In_2O_3 films. The annealing of the films in vacuum revealed that there is no correlation between conductivity and ferromagnetism of the films as opposite to the proposed in [1]. All this suggests that

the proposed mechanism of carrier-mediated magnetism in Cr-doped In_2O_3 films cannot be fully applicable for our PI MOCVD grown films.

The studies of the external magnetic field effect on magnetic properties of oxide based DMS have also been examined. Unfortunately the expected enhancement of magnetic properties in Co-doped ZnO films and Cr-doped In_2O_3 films has not been achieved. We also have not found any significant effect of magnetic field on the structural or crystalline properties of the films. Moreover, sometimes it was very hard to reproduce the earlier obtained magnetic moments in the films even upon application external magnetic field. All these suggest that the reproducibility of the magnetic properties in oxide based DMS systems is still a big issue and drawback for the possible application of these oxide based DMS in spintronic devices. However, in overall we have found evidence for an intrinsic origin for the ferromagnetism in studied Co-doped ZnO and Cr-doped In_2O_3 films. The observed ferromagnetism cannot be fully explained in conventional terms, thus a novel theoretical explanation is urgently needed.

We have also successfully prepared high quality ferromagnetic Fe_3O_4 and $CoFe_2O_4$ films using PI MOCVD technique. The structural and crystalline properties of the films were studied when films are prepared without and in external magnetic fields. We found that calculated average particle size slightly smaller when films are grown in external magnetic field. Moreover, the magnetic properties of the films were also found to strongly depend on the presence of the external magnetic field. Very promising results were achieved for Fe_3O_4 films grown in external magnetic field with all films showing the enhancement of the magnetic moment. With some exceptions the opposite magnetic field effect causing the reduction of the magnetic moment was found in $CoFe_2O_4$ films grown in external magnetic field. We believe that it is also possible to achieve the positive magnetic field effect in $CoFe_2O_4$ films by testing under different deposition conditions.

To conclude, it has been shown that external magnetic field could be successfully utilised during the MOCVD growth of Fe_3O_4 and $CoFe_2O_4$ films to tune their magnetic properties. We believe that this approach can be useful for the preparation of various spintronic devices.

7.2. Future work

The future work will include further research on oxide based DMS and magnetic oxides. We plan to investigate the effect of external magnetic field on structural and magnetic properties of the films over wide range of deposition conditions. We expect to find certain deposition conditions when $CoFe_2O_4$ films grown in magnetic field would exhibit an improvement of magnetic moment rather than earlier found decrease. We also plan to develop Mn_3O_4 and Co_3O_4 thin films and investigate their magnetic and structural properties in external magnetic field over wide range of deposition conditions.

We also aim to increase the strength of external magnetic field (to use stronger magnets), thus expecting to observe even larger magnetic field impact on the magnetic properties of the films.

7.2.1. Preparation of Mn_3O_4 films

The success of enhancement of saturation magnetization in Fe_3O_4 and $CoFe_2O_4$ films when grown in external magnetic field has been encouraging. One of the future challenges will be to study the effect of external magnetic field in antiferromagnetic systems.

Mn_3O_4 (hausmannite) is an antiferromagnetic oxide with its ferrimagnetic Curie point at ~42K. By applying the external magnetic field during the growth of Mn_3O_4 films we expect tune its magnetic properties. Preliminary studies carried on Mn_3O_4 have showed that films can be successfully grown in PI MOCVD reactor over wide temperature range of 550-850°C. Two different Mn precursors: $Mn(tmhd)_3$ synthesized in Trinity College and $Mn(acac)_2HOC_2H_4NMe$ donated by SLU (Uppsala) in Sweden, were tested for the preparation of Mn_3O_4 films. The resultant films were prepared in and without external magnetic field. We found that Mn_3O_4 films have developed good crystalline quality with (101) preferred orientation independent on precursor type or magnetic field. Figure 7.1 shows preliminary XRD studies of Mn_3O_4 films grown at 600°C on Al_2O_3 (0001) substrate.

Preliminary studies of the surface morphology of the films grown in and without magnetic field have been also preformed (Figure7.2.). Even though we found that for the films grown at 600°C the surface morphology does not change visibly with the application of external magnetic field we expect that saturation magnetization

of the films could be tuned. For this reason systematic studies of crystalline, structural and magnetic properties of Mn_3O_4 films are planned to be carried out in the future.

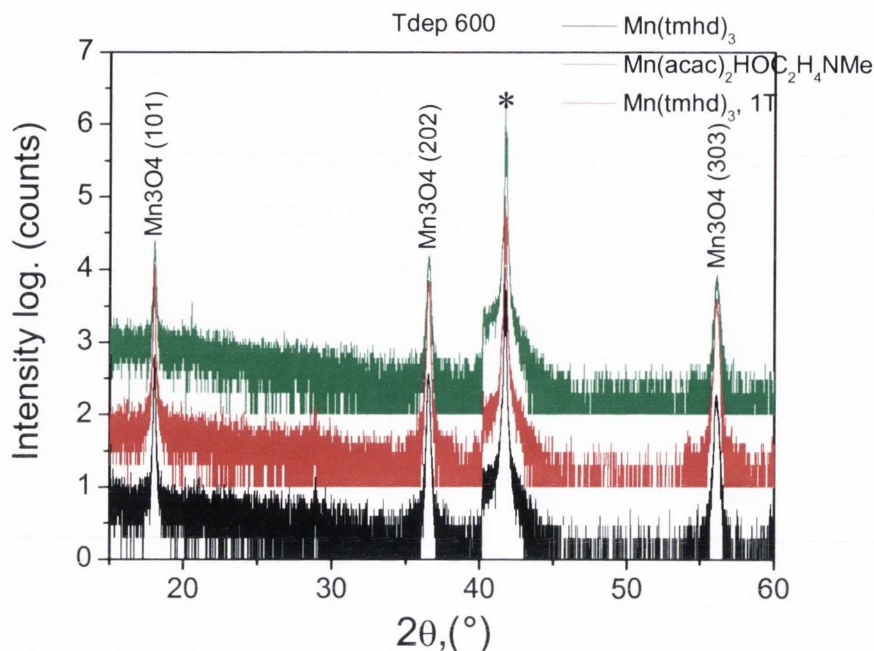

Fig. 7.1. X-ray diffraction patterns of Mn_3O_4 films grown at 600°C on Al_2O_3 (0001) substrate from two different precursors showing similar crystalline quality independent on the precursor choice or presence of external magnetic field

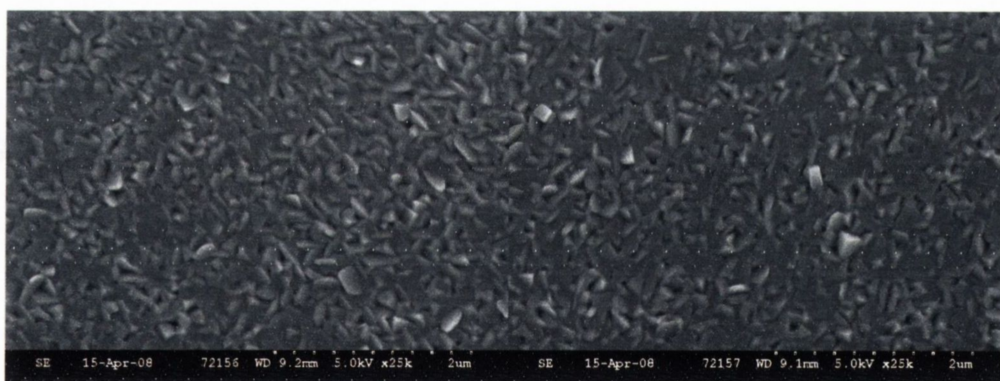

Fig. 7.2. SEM micrographs of Mn_3O_4 films prepared in (right image) and without (left image) external magnetic field (1T), showing similar surface morphology

7.2.2. Preparation of Co_3O_4 films

An antiferromagnetic oxide that is planned to be studied is Co_3O_4 with Neel temperature of ~30K. We have already prepared several Co_3O_4 samples by PI

MOCVD in and without external magnetic field. Our preliminary XRD studies have showed that all films have developed good crystalline quality showing (111) preferred orientation (Figure 7.3.). The preliminary SEM studies performed for the films grown in and without external magnetic field are given in Figure 7.4.

We hope that by carefully testing and selecting different deposition conditions the crystalline, structural and magnetic properties of Co_3O_4 films could be possibly tuned by external magnetic field.

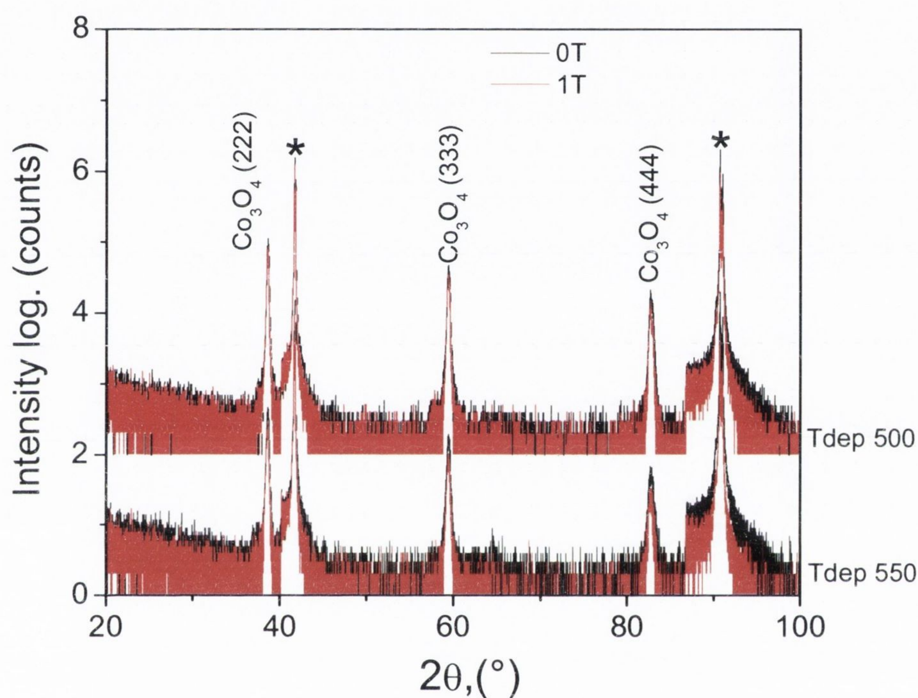

Fig. 7.3. X-ray diffraction patterns of Co_3O_4 films showing good crystalline quality, independent on the presence of external magnetic field

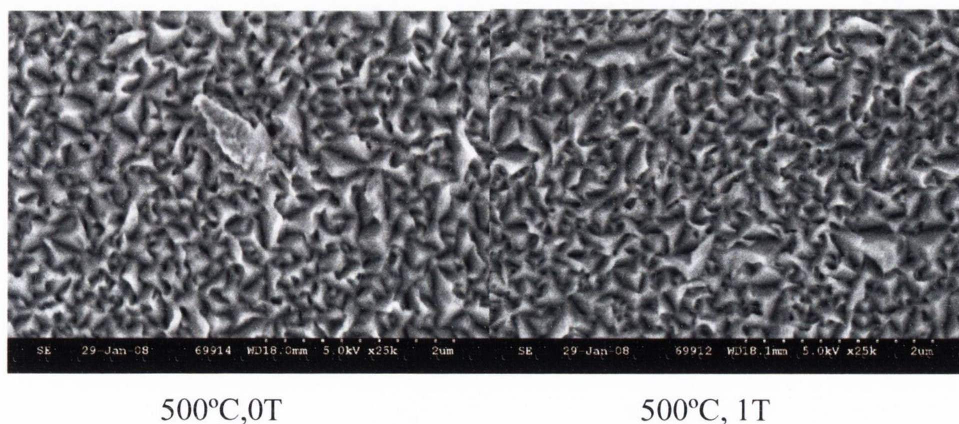

500°C,0T 500°C, 1T

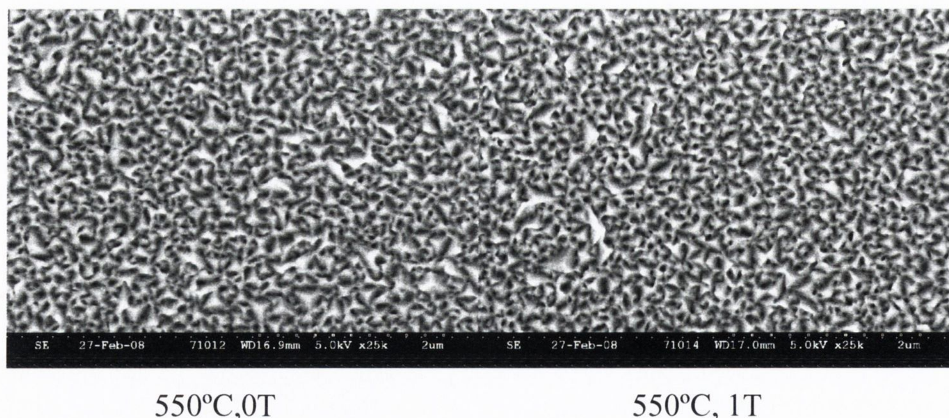

550°C,0T 550°C, 1T

Fig. 7.4. SEM microhraphs of Co_3O_4 films prepared in and without external magnetic field

We expect that our approach to growth oxide films by PI MOCVD in external magnetic can be utilised to prepare a number of various magnetic oxide based materials with controlled magnetic properties. We believe that in the long term this research will contribute usefully to further development of MOCVD technology and new oxide based magnetic and electronic devices.

References

[1] J. Philip, A. Punnoose, B. I. Kim, K. M. Reddy, S. Layne, J. O. Holmes, B. Satpati, P. R. LeClair, T. S. Santos, J. S. Moodera, *Nat Mater* **2006**, *5*, 298.

Chapter 8: Appendices

Appendix 1: AFM images of Cr-doped In_2O_3 films deposited on Al_2O_3 (0001) substrate at different deposition temperatures

550°C

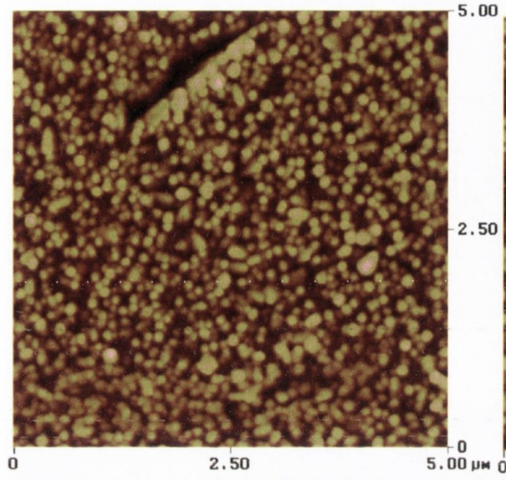

600°C

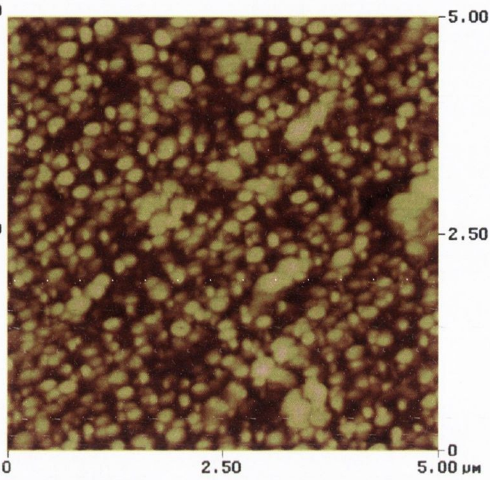

650°C

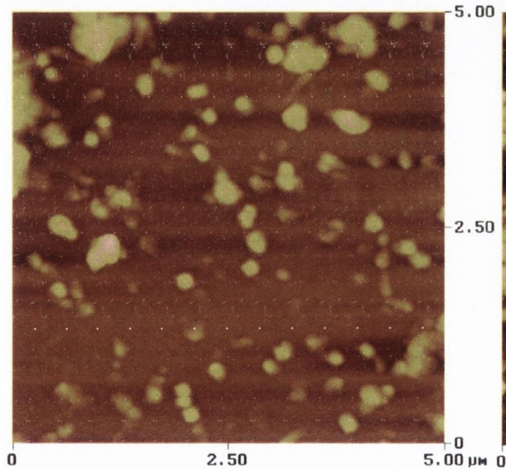

700°C

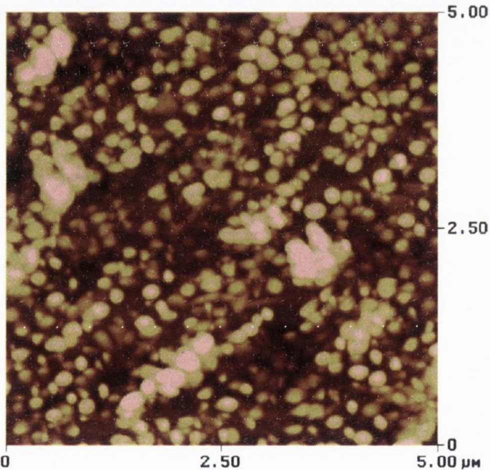

Appendix 2: AFM images of Cr-doped In_2O_3 films deposited on Al_2O_3 $(1\underline{1}20)$ substrate at different deposition temperatures

550°C

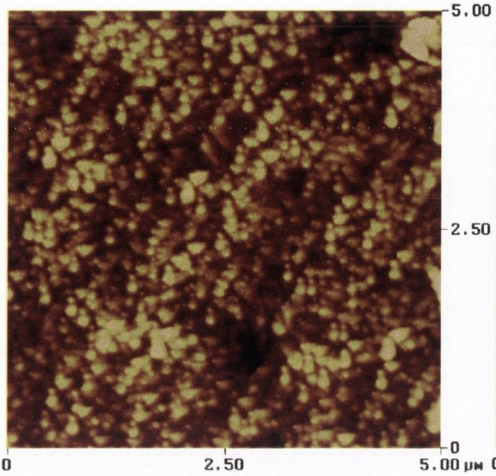

600°C

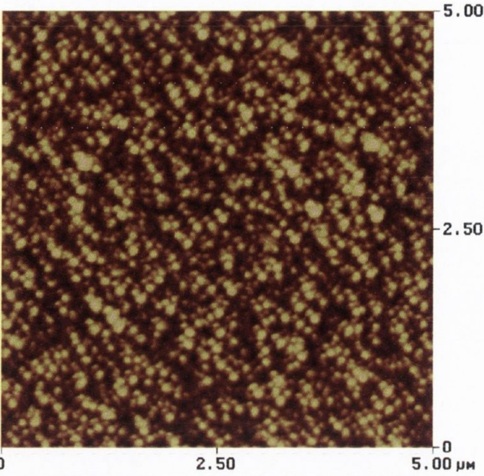

650°C

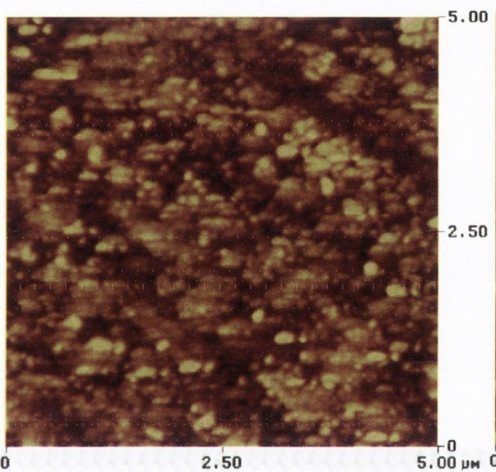

700°C

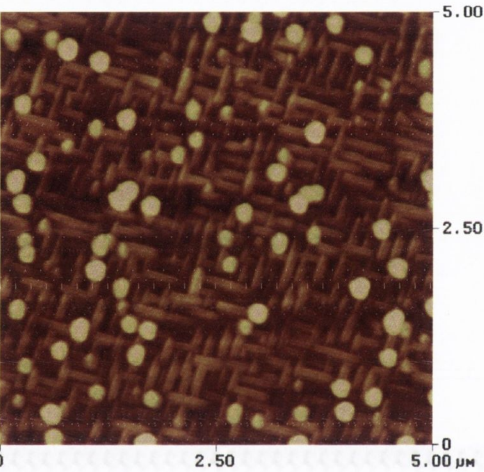

Appendix 3: SEM micrographs of Fe_3O_4 films on Al_2O_3 (0001) grown at 550ºC in Ar atmosphere with different number of pulses

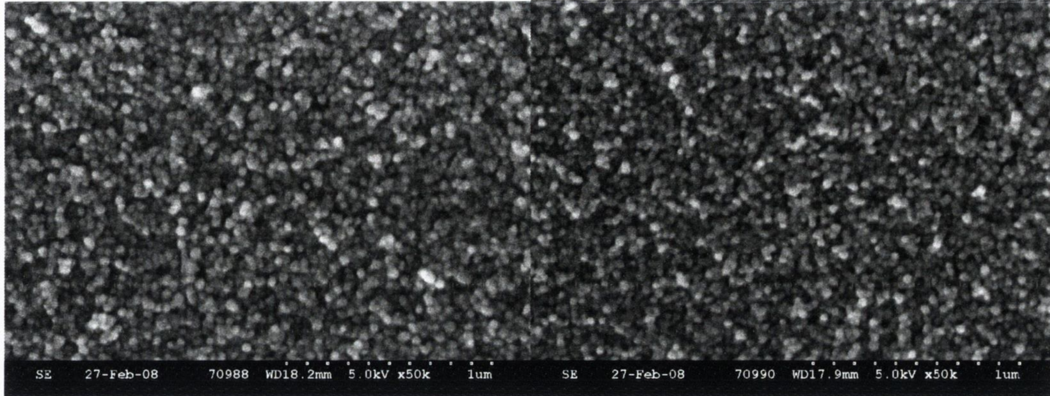

1000 pulses 1000 pulses, 1T

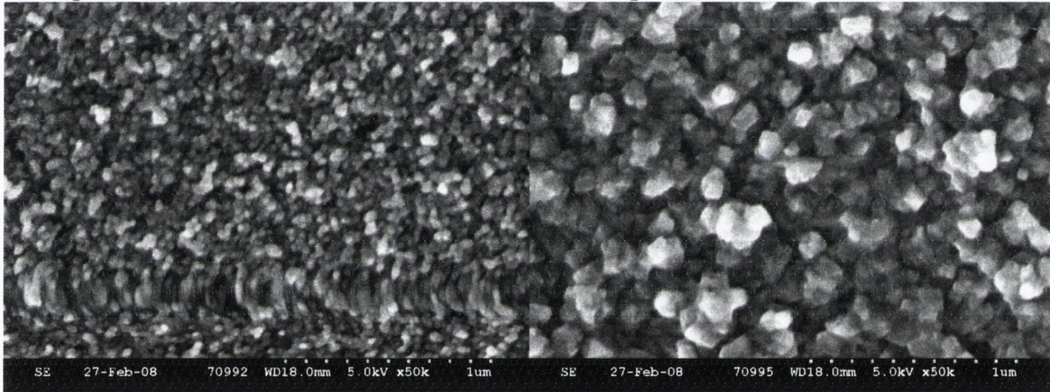

2000 pulses 2000 pulses, 1T

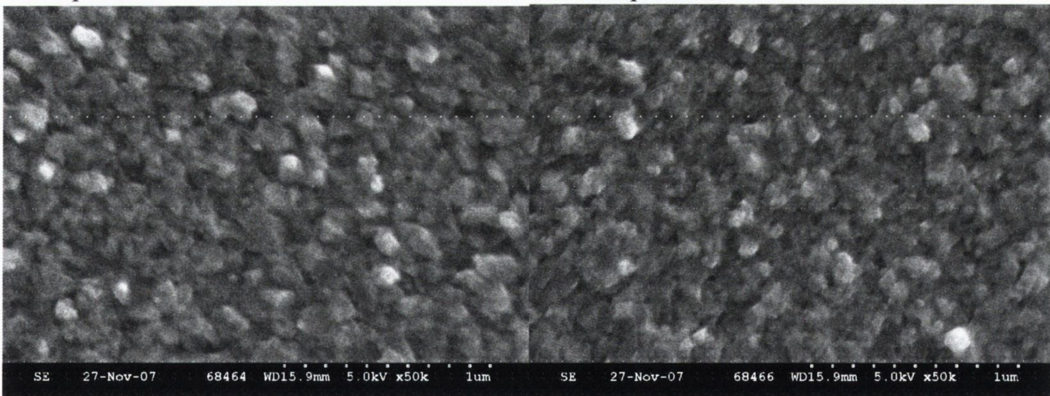

3000pulses 3000 pulses, 1T

Publications

1. Anna Zukova, Arunas Teiserskis, V. Kazlauskiene, Y.K. Gun'ko and Sebastiaan van Dijken. *Structural and magnetic properties of Co-doped ZnO films grown by pulse-injection MOCVD.* Journal of Magnetism and Magnetic Materials, Volume **316**, Issue 2, September 2007, Pages e203-e206
2. Anna Zukova, Arunas Teiserskis, Sebastiaan van Dijken, Y. K. Gun'ko, and V. Kazlauskiene. *Giant moment and magnetic anisotropy in Co-doped ZnO films grown by pulsed-injection metal organic chemical vapor deposition technique.* Appl. Phys. Lett. **89**, 232503 (2006)
3. Arunas Teiserskis, Anna Zukova, Yurii K. Gun'ko, Sergei Grudinkin, Tatiana S. Perova and Robert A. Moore. *Investigation of alumina–silica films deposited by pulsed injection metal–organic chemical vapour deposition.*Thin Solid Films, Volume **515**, Issue 4, 5 December 2006, Pages 1830-1834
4. Abrutis, A. Bartasyte, Z. Saltyte, A. Zukova, S. Donet and F. Weiss. *Thick SmBCO layers and SmBCO/YBCO structures grown by pulsed injection MOCVD* Physica C: Superconductivity, Volume **415**, Issues 1-2, 1 October 2004, Pages 21-28

Conference oral and poster presentations

1. "VIII Latin American Workshop on Magnetism, Magnetic Materials and their Applications", Rio de Janeiro, Brazil, 12-16 August, 2007
   Conference poster presentation: "Structural and magnetic properties of Cr-doped In_2O_3 films grown by pulse-injection MOCVD"
2. "III Joint European Magnetic Symposia", San Sebastian, Spain, 26-30 June, 2006. Conference poster presentation: "Structural and magnetic properties of Co-doped ZnO films grown by pulse-injection MOCVD" Publications
3. CVD Ireland meeting, Dublin College University, Dublin, Ireland, 20 October, 2006. Oral presentation: "MOCVD *of magnetically doped ZnO layers*".